2018-10-01

Development and Use of Lipidomics and Proteomics Methods to Identify and Measure Pro-Survival Metabolic Pathways in Cancer

Monique Merilyn Speirs
Brigham Young University

BYU ScholarsArchive Citation

Speirs, Monique Merilyn, "Development and Use of Lipidomics and Proteomics Methods to Identify and Measure Pro-Survival Metabolic Pathways in Cancer" (2018). *Theses and Dissertations*. 7601.
https://scholarsarchive.byu.edu/etd/7601

Development and Use of Lipidomics and Proteomics Methods to Identify and Measure Pro-Survival Metabolic Pathways in Cancer

Monique Merilyn Paré Speirs

A dissertation submitted to the faculty of
Brigham Young University
in partial fulfillment of the requirements for the degree of

Doctor of Philosophy

John C. Price, Chair
Joshua L. Andersen
Kenneth A. Christensen
Sean Warnick
Julianne House Grose

Department of Chemistry and Biochemistry

Brigham Young University

ABSTRACT

Development and Use of Lipidomics and Proteomics Methods to Identify and Measure Pro-Survival Metabolic Pathways in Cancer

Monique Merilyn Paré Speirs
Department of Chemistry and Biochemistry, BYU
Doctor of Philosophy

Throughout society's continual war against cancer, we have attempted pharmacological intervention only to find that tumors develop modes of resistance. It is well known that genetics play an integral role in cancer. Technological advances have greatly improved our ability to study cancer biochemistry beyond the genome by measuring changes in the expression and activity of RNA, proteins, and lipids in experimental models and human patients. As our techniques and technology to perform cancer research progresses, it is becoming more evident that cancer cells develop stress tolerance mechanisms at multiple levels within the central dogma, including altering mRNA expression, enzyme concentrations, and functional activity of cellular proteins and lipids.

In the first chapter, I review previous discoveries demonstrating the importance of metabolic reprogramming in cancer cells and how shifts in metabolic pathways contribute to cancer progression and therapeutic challenges. I discuss how mass spectrometry is a multifunctional research tool that can be used to identify global shifts in gene expression, identify oncogenic roles of specific metabolites and corresponding metabolic pathways, conduct enzyme activity assays, and understand the effects of drugs on cell signaling and metabolic flux through specific pathways. While metabolic reprogramming is a complex and multifaceted concept, the following chapters focus on two specific stress tolerance pathways of lipid and protein metabolism we have shown to significantly promote cancer cell evolution, proliferation, and drug resistance in models of human pancreatic and colon cancer. I describe novel mass spectrometry-based lipidomics and proteomics methods we developed to measure and determine the biological impact of these pathways in each model. I discuss the contributions we have made toward increasing general knowledge of metabolic reprogramming networks in cancer and how they may be targeted in more specific and effective manners to sensitize cancers to therapeutic drugs.

Specifically, the second chapter entails our study of a pro-survival lipid metabolic pathway driven by the sphingolipid modifying enzyme sphingosine kinase in a panel of differentially reprogrammed pancreatic cancer subclones. The third chapter describes our novel kinetic proteomics approach to identify how the cellular degradation system autophagy is used to selectively remodel the proteome of colon tumor cells in a xenograft mouse model of colon cancer. Lastly, I discuss how these and other projects completed during my graduate work lay a foundation for ongoing research to further our fundamental understanding of cancer metabolism and treatment development.

Keywords: foundational cancer research; metabolic reprogramming; clonal evolution; sphingolipid signaling; selective autophagy; mass spectrometry; kinetic proteomics

ACKNOWLEDGEMENTS

I acknowledge the BYU Department of Chemistry and Biochemistry new investigator star-up funds, Ronald K. Robins Graduate Research Fellowship, Fritz B. Burns Funds for Cancer Research, and the BYU Simmons Center for Cancer Research for funding this research. I am very grateful for members of other laboratories both at BYU and the University of Utah, who allowed me to use their facilities and provided incredible assistance and advice for my research, especially the Andersen Lab at BYU directed by Dr. Joshua L. Andersen, BYU Proteomics Core Facility directed by Dr. Daniel Mortensen, BYU DNASC in the Department of Biology under the direction of Dr. Michael F. Whiting and managed by Dr. Edward Wilcox, BYU Mass Spectrometry Facility directed by Bruce Jackson, University of Utah Proteomics and Metabolomics Core under the direction of James E. Cox and John Alan Maschek, University of Utah Preclinical Research Resource Faculty directed by David H. Lum.

I acknowledge my fellow graduate students in the Price Lab, including Bradley Naylor, Andrew Mathis, Adam Swensen, Lavender Hsien-Jung Lin, Richard Carson, and Rusty Denton as well as my undergraduate assistants Peter Maxfield Jones, John Connor Holman, Emily Cannon, McCall Briggs Harris, Prinelsa Encarnacion, and Brittany Johnson for assisting me in many of my wet lab experiments and data analysis. I am most grateful to my lab mates for continually offering kind words of support and for the life-long friendships I have made during my time working in the Price Lab.

I sincerely thank my incredible mentor Dr. John C. Price. Every time I talk to Dr. Price, I learn something new! He is the most intelligent and hard-working scientist I have ever met. Even if he doesn’t know the exact answer to one of my crazy questions, he uses his extensive knowledge of biochemistry to figure out the answer or design an experiment to figure it out. I am

grateful for his stalwart example of persistence and diligence and grateful to him for continually challenging me to undergo difficult feats in my research. I am especially grateful for him assisting me through each one of those challenges with great concern and care. He has been so patient with me throughout the ups and downs of my research and graduate school experience. Dr. Price will never cease to inspire me to be a better scientist and a more faithful latter-day saint through his shining example of diligence, sacrifice, and love.

I sincerely thank my family for their constant support and concern for me. I thank my husband Kyle Speirs for encouraging me to be positive and optimistic when I was stressed and discouraged about setbacks in my research. I am grateful for the continual support and inspiration of my mother DonnaMarie Paré. She is the kind of person who works as hard as she possibly can, and then works a little bit more. She was the first in her family to obtain an advanced degree and has become one of the best in her field of occupational therapy. She always encouraged me to get as much formal education as I can and provided all of the resources I needed to achieve my goals. Her magnificent example of hard work and deep passion for higher education have pushed me to be more diligent in my studies and strive for excellence in my graduate work and future career. Cancer took my father, Philip Paré I, from this earth far too early in both of our lives. He was tremendously strong in mind and spirit throughout his life and battled his disease to the point where he could barely walk but continued working as a veterinarian up until just two weeks before his passing. His stalwart example of persistence and stamina inspired me to complete every step of my research with full energy of heart. I pray that one day we will find a way to eliminate this life-destroying disease.

I thank my parents-in-law Troy and Brenda Speirs for being the most loving and supportive representatives of parents for me while I'm far from home. Whenever I have needed them for anything, they have rushed to my aid and cared for me like their own daughter. I thank my siblings and siblings-in-law Ryan Sheaparé, Rhiannon Sheaparé, Philip Paré II, Annette Paré, Britney Baker, Josh Baker, and Kortney Speirs for their kindness, advice, support, and for helping me enjoy life even when I'm completely overwhelmed with school and life challenges.

I thank my Heavenly Father for answering numerous prayers exclaimed both silently and audibly in the lab, over the computer, during my commutes to and from BYU, and at my bedside. He has helped me figure out solutions to seemingly impossible problems in my research almost immediately before saying "amen" and pushed me in the most loving and encouraging ways whenever I'm tempted to give up. I also thank Him for placing so many wonderful co-workers, friends, and family members in my life who have served as ministering angels to me throughout my experience at BYU.

TABLE OF CONTENTS

TITLE PAGE i

ABSTRACT ii

ACKNOWLEDGEMENTS iii

TABLE OF CONTENTS vi

LIST OF TABLES xii

LIST OF FIGURES xiii

1. Introduction to metabolic reprogramming and omics methods for cancer research 1

   Metabolic reprogramming in cancer cells results from and enhances tolerance to intrinsic and environmental stress 1

   Dynamic reprogramming of interconnected glucose, nucleic acid, lipid, and protein metabolic pathways enhances cancer cell viability and growth in unfavorable conditions 3

   Metabolic reprogramming contributes to therapeutic challenges and provides opportunities for drug target discovery and treatment development 5

   Mass spectrometry can be used to identify metabolic pathways and drug targets in cancer 8

   My contributions toward improving omics applications and understanding mechanisms of pro-survival metabolism in cancer 12

2. Sphingosine kinase 1 signaling is maintained as a core proponent of a cancerous phenotype in spite of metabolic pressure and epigenetic drift 21

   Chapter Summary 21

      Authors in Order of Contribution 21

Contributions of Authors 21
ABSTRACT 22
Motivation 22
Results 23
Data Availability.. 23
INTRODUCTION... 24
RESULTS.. 32
PDAC subclones and healthy controls displayed variations in cell size and morphology.... 32
DNA fingerprints were identical in distinct PDAC clonal populations 33
PDAC subclones exhibited distinct nscSNP profiles relative to healthy control cells, but were virtually isogenic relative to one another... 34
Isogenic PDAC subclones displayed global variations in mRNA expression relative to one another and to healthy control cells 37
Isogenic reprogrammed PDAC subclones displayed global shifts in protein expression relative to one another and to healthy control cells 38
Isogenic reprogrammed PDAC clones displayed global shifts in lipid expression networks including altered metabolism of bioactive sphingolipids S1P and C16 Cer 42
Sphingolipid focused LC-MS confirmed that both global lipid expression and S1P/C16 Cer metabolism were modified in PDAC subclones relative to the healthy control................... 45
Extracellular lipid profiles of PDAC subclones mirrored the intracellular lipid profiles 53

Pathway specific Lipidomics and RNA-Seq analyses suggest a parallel shift in S1P/C16 Cer metabolism in PDAC subclones driven by Sphingosine Kinase 1 55

SK1 activity is modulated by different combinations of concentration and MAPK1-mediated phospho-activation in pancreatic cancer subclones 58

SK1 inhibition effectively normalized S1P/C16 Cer levels in distinct PDAC subclones..... 64

Selective inhibition of SK1 reduced PDAC cell proliferation in a dose-dependent manner 66

PDAC subclones displayed different levels of drug resistance but selective SK1 inhibition sensitized all subclones to mitochondria mediated apoptotic signals.................................. 71

DISCUSSION 76

MATERIALS AND METHODS 87

Experimental Design 87

Cell Size/Morphology Analysis.. 89

STR Profiling... 89

RNA-Seq Analysis 89

SNP Analysis/SNP Profiling and Data Analysis 90

RNA Expression Profiling and Data Analysis 90

Protein Expression Profiling and Data Analysis 91

Shotgun Lipidomics Assay Development and Data Analysis 92

Intra/extracellular Lipidomics LC-MS Analysis 95

Western Blot Analysis 97

Targeted S1P/C16 Cer Quantitative Analysis and SK1 Activity Assay 97

Cell Proliferation Assay.. 99

Flow cytometry cell death assays 100

Quantitation and statistical tests 100

SUPPLEMENTAL TABLES.. 101

ABBREVIATIONS... 104

ACKNOWLEDGEMENTS 105

FUNDING... 105

3. Autophagy targets mitochondria specifically in tumors, but not the liver of HCT116 xenograft mice 106

Chapter Summary.. 106

Authors in Order of Contribution 106

Contributions of Authors 106

ABSTRACT 107

Motivation 107

Results 108

Data Availability... 108

ABBREVIATIONS... 108

INTRODUCTION... 109

EXPERIMENTAL PROCEDURES 114

Experimental Design and Statistical Rationale 114

Measurement of deuterium enrichment 117

In vivo cell proliferation assay 117

Sample preparation for quantitative and kinetic proteomics analyses 118

LC-MS data acquisition 120

Peptide identification 121

Quantitative proteomics data analysis 121

Kinetic proteomics data analysis 122

Immunofluorescence analysis 124

Calculation of individual protein degradation rates 124

RESULTS AND DISCUSSION 126

Autophagy inhibition reduced *in vitro* cell proliferation and sensitized CRC cells to chemotherapy 126

Autophagy inhibition did not significantly reduce *in vivo* cell proliferation 126

In vivo protein concentrations changed in response to autophagy inhibition in the tumor and liver 128

In vivo protein turnover changed in response to autophagy inhibition in the tumor and liver 130

Protein functional categories responded to CQ treatment differently in the tumor and liver 133

Immunofluorescence supported mitochondrial targeting by autophagy in the xenograft ... 138

Drug metabolism enzymes increased in the liver during CQ treatment 140

Degradation of mitochondria is sensitive to autophagy inhibition in xenograft tumors 141

CONCLUSION 143

Future Directions 145

ACKNOWLEDGEMENTS 147

4. Conclusions and future directions toward understanding metabolic mechanisms of cancer and chemoresistance 148

Chapter Summary 148

CONCLUSIONS FROM PUBLISHED WORK 148

FUTURE DIRECTIONS 153

Amino acid metabolism is a potential chemosensitizing drug target in triple negative breast cancer cells 153

Generation of chemoresistant colon cancer cell line 161

Bibliography 166

LIST OF TABLES

Supplemental Table 2-1 Comparison of components in cell growth mediums used to feed pancreatic cancer groups (pA, pB, pC, pD) during subculturing experiment............................ 101

Supplemental Table 2-2 STR Profile Reports of healthy control and pancreatic cancer cells before and after subculturing experiment. 103

LIST OF FIGURES

Figure 1-1 General workflow used to conduct omics experiments throughout my graduate research. 10

Figure 2-1 General localization of lipids and cancer-promoting roles in the cell. 26

Figure 2-2 Structures and metabolism of pro-apoptotic C16 Cer and pro-survival S1P. 29

Figure 2-3 Schematic of experimental workflow used to generate isolated pancreatic cancer subclones from a common genetic origin and identify pro-survival pathways. 31

Figure 2-4 Pancreatic cancer subclones and healthy control cells displayed variations in cell size and morphology. 33

Figure 2-5 Genome-wide nscSNP Analysis PSN-1 subclones and healthy control cells. 36

Figure 2-6 RNA, protein, and lipid expression profiling suggest global shifts in transcription and metabolism between pancreatic cancer subclones and relative to the healthy control. 39

Figure 2-7 Shotgun lipidomics suggests global shifts in lipid metabolism including conserved differences in pro-survival S1P and pro-apoptotic C16 Cer levels among pancreatic cancer subclones relative to healthy control cells. 43

Figure 2-8 Representative elution profiles of C16 Cer, S1P, and corresponding deuterated internal standards. 45

Figure 2-9 Representative MS/MS fragmentation spectra of C16 Cer and corresponding internal standard C16 Cer-d7 measured by LC-MS of pancreatic cell lipids. 46

Figure 2-10 Representative MS/MS fragmentation spectra of S1P and corresponding internal standard S1P-d7 measured by LC-MS of pancreatic cell lipids. 47

Figure 2-11 Data derived from lipidomics and RNA-Seq assays suggest a conserved shift in signaling sphingolipid metabolism in pancreatic cancer subclones relative to the healthy control driven in part by SK1. 50

Figure 2-12 SK1 enzyme activity assay reveals SK1 as a key driver of the conserved S1P:C16 Cer imbalance in pancreatic cancer subcultures, which may be corrected by SKI-II treatment. . 51

Figure 2-13 S1P and C16 Cer levels were altered in pancreatic cancer subclones relative to the healthy control but may be corrected in part by SKI-II treatment. 52

Figure 2-14 Comparison of mRNA expression of enzymes directly involved in S1P/C16 Cer metabolic pathway. 56

Figure 2-15 SK1 expression and/or ERK2-mediated phosphorylation was increased in pancreatic cancer subclones relative to healthy control cells. 59

Figure 2-16 Cytoplasmic actin mRNA and protein levels were reduced in pancreatic cancer subclones relative to the healthy control. 61

Figure 2-17 Fatty Acid Synthase mRNA and protein levels were increased in pancreatic cancer subclones relative to the healthy control. 62

Figure 2-18 SK1 inhibition significantly slowed pancreatic cancer cell proliferation relative to the healthy control and each cancer subclones displayed a distinct level of dose-dependent SKI-II sensitivity. 67

Figure 2-19 Results of growth experiments of pancreatic cancer subclones and healthy control cells treated with increasing concentrations of SKI-II. 69

Figure 2-20 Pancreatic cancer subclones displayed different drug sensitivities yet SKI-II effectively sensitized each subclone to mitochondria-mediated apoptotic signals. 72

Figure 2-21 SK1 inhibition significantly sensitized pancreatic cancer subclones to mitochondria-mediated apoptotic signals. 75

Figure 2-22 Divergence tree of genotypic and phenotypic analyses of isolated pancreatic cancer subcultures (pA, pB, pC, pD) and healthy control cells (hT) revealing nongenetic heterogeneity and a conserved, pro-cancer sphingolipid metabolic pathway mediated by SK1........ 77

Figure 2-23 Schematic model of pro-survival S1P signaling in pancreatic cancer cells (left) followed by a shift in the sphingolipid rheostat toward C16 Cer-driven pro-apoptotic signaling induced by SKI-II treatment (right). 87

Figure 3-1 In vivo autophagy flux measurement workflow. 113

Figure 3-2 Autophagy inhibition slowed colon cancer cell proliferation and enhanced chemosensitivity. 127

Figure 3-3 Effects of CQ induced autophagy inhibition on global protein concentrations in the tumor and liver. 129

Figure 3-4 Effects of CQ induced autophagy inhibition on global protein turnover in the tumor and liver. 132

Figure 3-5 Effects of CQ treatment on turnover of autophagy related proteins and substrates relative to the observed global proteome in the tumor and liver. 136

Figure 3-6 Effects of CQ treatment on concentrations of autophagy related proteins and substrates relative to the observed global proteome in the tumor and liver........ 137

Figure 3-7 Accumulation of LC3-II autophagy markers in tumor and liver tissues of HCT116 xenograft mice treated with CQ relative to vehicle controls. 139

Figure 3-8 Effects of CQ treatment on drug metabolism in the liver. 141

Figure 3-9 Protein degradation rates in the tumor and liver of xenograft mice........ 142

Figure 3-10 Schematic model of autophagy substrate selection in the tumor versus liver tissue in colon cancer xenograft mouse. 145

Figure 4-1 Effects of chemotherapy on sensitive versus resistant TNBC cells. 154

Figure 4-2 Effects of chemotherapy on mitochondrial morphology in sensitive and resistant TNBC cells 155

Figure 4-3 Chemoresistance and chemotherapy reduced respiratory oxygen flux (mitochondrial activity) in TNBC cells. 156

Figure 4-4 Amino acid metabolism was modified in chemoresistant TNBC cells 158

Figure 4-5 Kinetic model of amino acid and protein metabolism in sensitive versus resistant TNBC cells 159

Figure 4-6 Protein turnover measurement in TNBC cells using 15N-based metabolic labeling. 160

Figure 4-7 Comparison of cell proliferation rates of Wild-Type versus oxaliplatin resistant cell line (ROXY-HCT116) treated with 0.625µM oxaliplatin. 164

Figure 4-8 Differentially expressed genes in chemoresistant versus wild type CRC cells. 165

1. Introduction to metabolic reprogramming and omics methods for cancer research

Metabolic reprogramming in cancer cells results from and enhances tolerance to intrinsic and environmental stress

Cellular metabolism is defined as the process of catabolizing nutrients and building new components in order to maintain life. Cellular metabolism is made up of a complex network of enzyme mediated chemical reactions driven by intrinsic and environmental signals. Metabolic pathways are highly regulated at multiple checkpoints throughout the lifetime of a cell in order to maintain sufficient levels of energy and molecular material in healthy cells and either correct or dispose of potentially damaging cells [1]. Shifts in the acquisition and metabolism of proteins, lipids, carbohydrates, and nucleic acids lead to changes in cellular phenotypes and behavior. Tumor cells commonly exhibit shifts metabolic pathways involved in bioenergetics, anabolism, and redox homeostasis [2]. Corresponding regulatory systems are often used to achieve these metabolic modifications, allowing malignant cells to circumvent quality control checkpoints, divide, and proliferate uncontrollably [1].

Regulatory and signaling molecules are commonly mutated in cancer cells due to both stochastic and conserved genetic aberrations such as single nucleotide polymorphisms (SNPs), translocations, amplifications and deletions [3]. A number of non-genetic factors, such as epigenetic modifications to the DNA, interactions with neighboring tumor or benign cells, progressive stages of the tumor, cytotoxic stress, and nutrient availability have also been shown to influence cancer cell metabolism and behavior [2,4]. In addition to the basic energy and biosynthetic needs of resting cells to maintain homeostasis, rapid proliferation imparts significant intracellular stress by dramatically increasing metabolic demands [5-7]. Because each cell division entails the doubling of cellular contents, cancer cells require continuous sources of carbohydrate, amino acid and fatty acid substrates to produce new DNA, RNA, proteins, and lipids [7,8]. Cancer cells increase nutrient consumption and metabolic flux to promote *de novo* biosynthesis in order to enhance supply of metabolic intermediates [1]. Elevated levels of biosynthesis and metabolism must be fueled by overactive ATP production which in turn leads to other significant sources of intracellular stress, including mitochondrial overuse and damage as well as high levels of cytosolic reactive oxygen species (ROS) [9].

Cell stress levels are further heightened by pressures from the tumor microenvironment. Unlike normal cells, tumor cells are enclosed within a harsh, nutrient-poor microenvironment and must readily adapt to such conditions in order to survive. Due to reduced blood supply and increased metabolic activity of neighboring cells, tumor cells are subjected to hypoxia, depleted nutrient availability, and increased environmental ROS [8,10]. In normal cells, oxidative and other cytotoxic stresses trigger pro-apoptotic signaling pathways [7,9]. On the other hand, intrinsic and environmental stress promote pro-*survival* signaling cascades in cancer cells, allowing them to completely evade natural growth arrest signals [7,9]. Cancer cells modify gene expression, signaling cascades, and multiple metabolic pathways to strategically acquire and utilize limited nutrients from the environment and even their own cellular material, enabling them to both maintain homeostasis and build new biomass for cell division.

While regulatory tumor suppressor genes such as p53 are inactive in over 50% of patients due to loss of function mutations [11], cancer cells overexpress growth and transcription factors and/or their corresponding receptors such as transforming growth factor-β (TGFβ), c-MYC, insulin like growth factor (IGF), SREBP-1, and hypoxia inducible factor (HIF-1) [1,12]. Growth and proinflammatory transcription factors have been shown to upregulate pro-growth signaling cascades and machinery such as MAPK, the PI3K/Akt/mTOR axis, and Ras GTPases, which in turn activate metabolic pathways most essential for survival during nutrient stress, enabling cancer cells to bypass normal metabolic checkpoints for proliferation and apoptosis [7].

Dynamic reprogramming of interconnected glucose, nucleic acid, lipid, and protein metabolic pathways enhances cancer cell viability and growth in unfavorable conditions

Since the "Warburg Effect" was discovered nearly a century ago [13], the complexity of metabolic reprogramming and its effects on cancer cell evolution and behavior is increasingly evident. Warburg proposed that cancer cells upregulate uptake of glucose and flux through anaerobic glycolysis due to dysfunctional mitochondria [13]. His discovery prompted an increased interest in cancer metabolism and inspired research endeavors beyond the level of the genome. Since then, various characteristics of pro-cancer metabolism have been identified. Prior to earlier beliefs, recent research indicates that increased glucose metabolism via glycolysis is not necessarily a fixed metabolic feature of cancer cells [14]. When oxygen levels are limiting, HIF-1 upregulates anaerobic glycolysis through PI3K/Akt signaling to boost ATP levels in highly proliferative cells [12]. Since the pentose phosphate pathway branches from glycolysis, increased glycolytic flux also promotes production of ribose for DNA synthesis and NADPH required for scavenging ROS to maintain a reductive cellular environment [15]. However, intermittent and staggered switching between anaerobic and mitochondrial oxidative phosphorylation in populations of slower cycling as well as highly proliferative cells throughout the tumor promotes overall tumor progression and metastasis [14]. Indeed, high levels of aerobic oxidative phosphorylation and other mitochondrial metabolic processes such as the TCA cycle are required for tumor growth [2].

AKT stimulates *de novo* fatty acid synthesis and overexpression of Fatty Acid Synthase enzymes to support new membrane production during rapid cell division [16,17]. Alternatively, when energy and acetyl-CoA levels are low, cancer cells have been shown to upregulate fatty-acid oxidation; elevated levels of β-oxidation provide ATP as well as acetyl-CoA to accelerate citrate oxidation, a significant energy source for proliferating cells [18]. Enzyme mediated shifts in the metabolism and concentrations of bioactive sphingolipids promotes proliferative signaling cascades that mediate stress tolerance and proliferation [19].

Another common feature of cancer cells is increased metabolism of amino acids such as glutamine (glutaminolysis). Myc transcription factors promote expression of glutamine transporter proteins and glutaminase, leading to increased glutamine uptake and glutaminolysis [12]. Elevated glutaminolysis has been shown to promote pro-survival signaling and provides a nitrogen source for synthesizing new amino acids, proteins, and nucleic acids necessary for cell division [20,21]. Meanwhile, elevated levels of HIF-1 promote glycine metabolism, an amino acid which serves a precursor for *de novo* purine synthesis [1]. While extracellular soluble protein abundant in plasma and interstitial fluid is generally not utilized as a source of amino acids for cellular biosynthesis, Ras-transformed cells internalize extracellular proteins through large, heterogeneous vesicles called macropinosomes from which they recover free amino acids for new protein synthesis via lysosomal protein degradation [22]. Cancer cells commonly upregulate cytosolic protein recycling *via* autophagy or “self-eating”; increased mTOR mediated autophagy flux promotes cell viability in nutrient poor conditions, perhaps by degrading excess proteins and organelles, thereby providing free amino acids for macromolecular synthesis [23,24]. All in all, metabolic pathways are selectively coordinated in response to a variety of stress stimuli, enabling cancer cells to maintain survival and growth in an ever-changing microenvironment.

Metabolic reprogramming contributes to therapeutic challenges and provides opportunities for drug target discovery and treatment development

Metabolic plasticity leads to complex clinical challenges such as inter- and intratumor heterogeneity and multidrug resistant phenotypes [25-27]. Tumors are made up of a diverse range of cell types, including both cancerous cells and stromal cells like neurons, vascular endothelial cells, fibroblasts, and adipocytes [28]. Even so, cellular heterogeneity is palpably present in *pure* tumor cell populations derived from a common tissue type (intertumor heterogeneity) and even in cancer cells derived from the exact same tumor (intratumor subclonal heterogeneity) [28]. Indeed, no two tumors have been shown to exhibit matching genetic or metabolic aberration profiles [27,28].

Peter Nowell was the first to formally recognize cancer as an evolutionary physiological process [29]. His theory has repeatedly been validated by the identification of intratumor subclonal heterogeneity and evolutionary selection in many human cancers including pancreatic and colorectal [25,27,28,30,31]. The hierarchical model of cancer stem-like cells (CSCs) is often used to explain tumor heterogeneity [32]. CSCs display stem-cell like phenotypes such as plasticity in the transition between resting (G_0 phase) and proliferative (S phase) states, thereby providing both transient amplifying cells and differentiated non-CSCs used to establish the basis of the tumor [28,32]. Recent research indicates that metabolic reprogramming is vital for CSCs to retain self-renewal potential and adapt to stressful stimuli including chemotherapy [28].

Chemotherapy currently remains the first line of defense for most tumor types [1]. Conventional chemotherapeutic drugs such as alkylating agents and nucleoside analogs act by interfering with DNA integrity and/or synthesis in all cells they come into contact with, thereby inhibiting the cell cycle and proliferation [1]. Treatment failures commonly result due to acquired/adaptive drug resistance [1,28], which is currently among the greatest challenges in cancer treatment [14] and contributes to high patient mortality rates [1]. Radiation and chemotherapeutics themselves act as potent sources of cytotoxic stress and can therefore heighten defense mechanisms or trigger alternative metabolic stress tolerance mechanisms in cancer cells [26,33,34]. This greatly limits the clinical value of current therapeutic approaches and the ability to predict treatment outcomes [27]. The fact that previously and newly established cells throughout the architecture of the tumor differentially adapt their metabolism in response to genotoxic stress introduces major challenges for precision cancer medicine [27,28]. Indeed, metabolic heterogeneity underlies the failure to achieve a global therapeutic effect on the tumor using conventional chemotherapeutic approaches [28].

Chemotherapy induced genotoxic stress promotes the adaptive CSC phenotype and reprogramming of specific metabolic pathways in both cancer and surrounding cells [1]. Shifts in mitochondrial, protein, and lipid metabolism throughout the tumor have been shown to boost energy levels and promote metabolic mechanisms of chemoresistance [1,28]. Increased expression of genes that regulate mitochondrial function, autophagy mediated protein degradation, lysosome degradation, and mitochondrial respiration have been reported as important features of pro-survival metabolism in chemoresistant CSCs [28,35]. In addition, hierarchal metabolic heterogeneity throughout the tumor enables metabolic symbiosis between neighboring cells, further enhancing adaptation to cytotoxic changes in the microenvironment during chemotherapy [28]. For example, epithelial cancer cells have been shown to induce a "reverse" Warburg effect in surrounding fibroblasts, causing them to adopt a "pseudo-hypoxic" state and generate abundant levels of lactate [36]. This allows neighboring cancer cells to remain fully oxygenated and continue to produce high levels of ATP and metabolic intermediates by feeding off the mitochondrial fuel lactate produced by surrounding fibroblasts [36].

CSCs in colon and pancreatic tumors displaying increased levels of *de novo* fatty acid and cholesterol synthesis as well as increased uptake of exogenous lipids and lipoproteins are highly resistant to chemotherapy [5]. Ovarian cancer cells under genotoxic stress have been shown to readily take up free fatty acids released by neighboring adipocytes to use as an abundant source of ATP, promoting bioenergetics and chemoresistance [5]. Increased production of bioactive lipid metabolites such as sphingosine-1-phosphate (S1P) enhances resistance to cytotoxic drugs and radiation while suppression of S1P signaling sensitizes various cancer cell models to apoptosis [19]. These types of metabolic adaptations to chemotherapy make it very difficult to predict treatment outcomes and achieve long-lasting effects in aggressive tumors [1,27].

Another disadvantage of conventional treatments is that chemotherapeutics are systemically toxic, lack specificity for cancer tissue, and are accordingly associated with debilitating side effects [1]. Current research efforts are geared toward developing more potent and tumor-specific treatment regimes in order to enhance cytotoxic effects in the tumor while minimizing chemotherapy dosages and off target effects. For example, combinatorial treatments whereby multiple drugs with different molecular targets are being used more commonly in attempt to reduce clonal selection and enhance global effects of the treatment across heterogeneous tumors [1]. Anti-cancer drug combinations include both conventional chemotherapeutics as well as newly identified, more targeted drugs that suppress growth factors, cell surface receptors, and enzymes involved in pro-survival signaling [37,38]. Because metabolic reprogramming is such a critical response to cytotoxic stress in cancer, cancer metabolism has emerged as a promising drug target in recent years [1]. Altered metabolic pathways may suggest novel therapeutic targets for combination drugs to enhance treatment specificity and destabilize metabolic mechanisms of chemoresistance [1].

Mass spectrometry can be used to identify metabolic pathways and drug targets in cancer

The transition from a normal to a cancer cell is not caused by a single event. The reason cancer research and treatment is so challenging is because numerous cellular pathways made up of thousands of genes and metabolites are systematically altered to achieve a cancerous phenotype. DNA sequencing technology has facilitated the identification of genetic mutations that contribute to pathways underlying cancer pathogenesis and genetic evolution [39]. However, DNA sequencing provides limited information about changes in gene *expression* caused by epigenetic and metabolic reprogramming events, which can play equally important roles in cancer pathogenesis and drug resistance [1,4,5,26,28,40]. Therefore, a holistic or systems biology approach that can measure multiple pathways of gene expression at a time is necessary to increase understanding of key pathways amid the unique biochemical context of a given cancer cell population [1,40,41].

Analytical techniques such as RNA-Sequencing and mass spectrometry (MS) can be used to simultaneously quantify thousands of different molecules in a single biological sample [1]. Such techniques are recognized as a field of systems biology known as high-throughput omics technologies [41]. Omics experiments made up of a combination of “wet” and “dry” lab experiments [1] can be used to identify and measure up to thousands of mRNA molecules (transcriptomics), proteins (proteomics), and lipids (lipidomics) throughout the cell. The wet lab experiments carried out for my research followed a consistent strategy: 1) apply treatments to experimental groups, 2) extract and purify cellular molecules of interest, e.g. RNA, proteins, or lipids, and 3) acquire high-throughput data by running samples on an analytical instrument such as a gene sequencing system or a mass spectrometer using an acquisition method appropriate for the desired results.

Wet lab protocols are followed by dry experiments, which involve multiple data analysis steps that typically make up the bulk of the work, though can be made more efficient with the assistance of computational and mathematical tools. Omics data analysis for my research was made up of three phases: 1) use computational tool to convert high throughput data into interpretable terms, e.g. assign protein or lipid identities to raw mass spectral signals by comparing raw data to proteomics/lipidomics databases, 2) establish statistical filters, perform a quality control check, and remove data that do not meet statistical criteria, 3) normalize data to total signal or internal standards, 4) perform literature search to generate hypotheses and identify potential pathways of significance, 5) use bioinformatics tools to categorize molecules into functional groups or pathways, 6) implement statistical tests to compare pathways and compounds of interest between different experimental groups 7) interpret results and infer biological significance of altered pathways and/or biochemical effects of treatments (**Figure 1-1**).

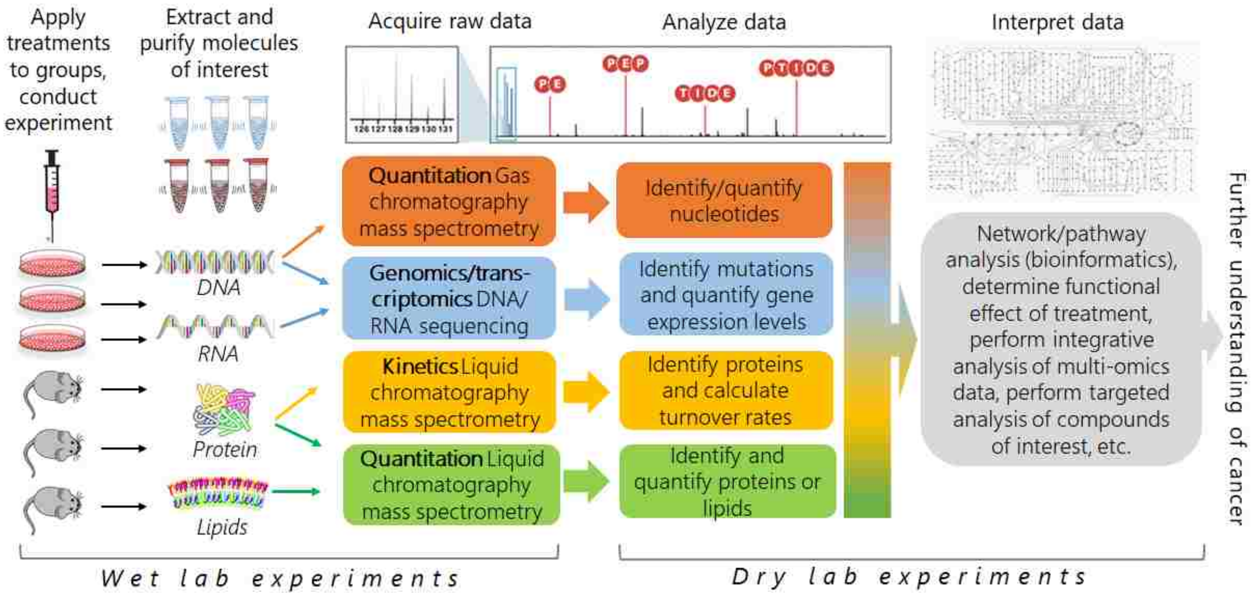

Figure 1-1 General workflow used to conduct omics experiments throughout my graduate research.

Moreover, mass spectrometry facilitates proteomics and lipidomics experiments by measuring the mass, charge, and intensities of a diverse range of analytes extracted from cell and tissue samples, providing data that can be used to identify and measure the relative concentrations of proteins produced by genes and a diverse range of lipid species produced and expressed in a given cancer model [1,41]. Quantitative proteomics and lipidomics data can thus be used generate vast protein/lipid concentration profiles or “signatures” of experimental groups, providing information about global differences in macromolecular expression and metabolism between healthy and cancerous cells types or groups treated with a drug versus controls [1]. As mentioned above, global data can be further analyzed using bioinformatics techniques to identify specific metabolic and signaling pathways that may be modified depending on cell type or treatment [42,43].

Proteomics and lipidomics methods can also be performed in a targeted manner to identify and measure specific metabolites of interest as well as determine whether they are present or absent in a particular sample or have increased or decreased in concentration in response to a certain stimulus such as chemotherapy or enzyme inhibition. In this way, proteomics and lipidomics techniques can be used as a tool to conduct enzyme and drug activity assays and determine the effects of such stresses on specific compounds and metabolic reactions or pathways. Specific changes can then be compared to global shifts in the lipidome or proteome to infer the targeted and general biological effects of a drug on an organism. In recent years, MS technologies have become increasingly sensitive and recently provided a means to measure *in vitro* and *in vivo* metabolic flux in cell culture and animal models treated with dietary heavy isotopes such as ^{13}C amino acids or heavy water (D_2O) that serve as metabolic tracers as they are incorporated into proteins via protein synthesis [44-49]. Mass spectrometry is then used to measure rate of isotope incorporation into each protein over time, which serves as a metric of protein turnover [44]. This method is referred to as kinetic proteomics and when combined with quantitative data provides information about how the synthesis and degradation rates of specific proteins and cellular structures are modified by a certain treatment.

Despite being at an early stage relative to other biochemistry techniques, quantitative and kinetic omics studies have already provided insight into disease related metabolic mechanisms, paving the way for drug target discovery [1,48-52]. Novel applications of systems biology facilitated by continually improving analytical instruments can be used to generate robust transcriptomic, proteomic and lipidomic data that provide key insight into previously discovered and novel metabolic and drug resistance mechanisms in cancer [1]. The use of mass spectrometry in studying cancer evolution and metabolism is expected to significantly improve our understanding and ability to treat patients with aggressive, heterogeneous, and drug resistant tumors [1,27].

My contributions toward improving omics applications and understanding mechanisms of pro-survival metabolism in cancer

My graduate work merges the two emerging fields of cancer metabolism and systems biology. My studies integrated large scale ‘omics’ technologies as well as traditional biochemistry techniques to study manifestations of cellular metabolic reprogramming in models of pancreatic and colon cancer. Some of this work is finalized and compiled in Chapters 2-3, respectively entitled “Sphingosine kinase 1 signaling is maintained as a core proponent of a cancerous phenotype in spite of metabolic pressure and epigenetic drift” and “Autophagy targets mitochondria specifically in tumors, but not the liver of HCT116 xenograft mice”. As shown in these chapters, the overall focus of my graduate work has been to investigate how modified metabolic pathways contribute to the aggressive and drug resistant natures of cancer. Both studies suggest ways to sensitize metabolically dynamic cancer cells to drug treatment and improve specificity of cytotoxic treatments toward malignant cells, providing promising ways to destabilize pro-survival metabolism in tumor tissue while minimizing off target effects in surrounding healthy cells. Each study highlighted an emerging concept of cutting-edge cancer metabolism research, including sphingolipid signaling and autophagy.

Previous research has shown that nongenetic switching between phenotypes and stress induced “stemness” are fundamental characteristics of cancer cells that severely reduces the predictability of treatment outcomes, enhances tumor heterogeneity, and promotes drug resistance pathways in pancreatic adenocarcinoma (PDAC) [25,27,53]. The aims of my first project (Chapter 2) were to identify pro-survival metabolic and signaling pathways of significance among differentially reprogrammed subclones of PDAC from a common genetic origin. Four isolated cancer subcultures were exposed to the basal or new dietary conditions to encourage differential reprogramming of metabolic and/or stress signaling pathways. We used multiple techniques including RNA-Seq, STR and SNP analyses, quantitative proteomics, lipidomics, and cell behavior assays to compare the genomic and phenotypic profiles of the PDAC subclones to one another and relative to a healthy immortalized control cell line.

One of the major challenges of this study was to develop a method that consistently and accurately measured the concentrations of two lipid targets of interest, C16 Ceramide (d18:1/16:0) and S1P (d18:1) along with the remainder of the lipidome. We were interested in these two lipids above others due to their apparent roles in cell-fate signaling in various models of cancer [19,54-57]. Ceramides are often considered pro-death signals due to multiple potential functions in inducing apoptosis and senescence in many different experimental systems [58,59]. On the other hand, S1P promotes optimal cell growth in response to growth factors and contributes to various processes including angiogenesis, stress response, suppression of apoptosis, and cell motility that altogether promote cancer cell survival and proliferation [19].

One of the benefits and challenges of mass spectrometry is its ability to identify specific lipid structures in complex mixtures such as whole cell lysates. The ability to distinguish one lipid type from another is very important and has introduced significant challenges for research because lipids with high structural similarity that appear similar on a mass spectrum can play very different roles *in vivo*. For example, hundreds of different ceramide species are expressed in a given cell; ceramide production and biological activities are heavily determined by the length of their fatty acid chain [59]. Long-chain ceramides (C14:0-C20:0) for instance, tend to be linked with apoptotic processes whereas some *very*-long-chain ceramides (C22:0-C26:0) have been shown to play pro-proliferative roles [59]. Advances in MS technology are promoting studies to determine exactly how the functions of specific bioactive ceramides with different chain lengths differ in the cell. Thus far, most studies agree that intracellular accumulation of C16 Ceramide (C16 Cer) promotes apoptosis [57,59-62].

As another important example, some research suggests sphingosine (d18:1) may serve as a key physiological regulator by inhibiting protein kinase C and inducing cell-cycle arrest [63]. A simple addition of a phosphate group to sphingosine by the enzyme Sphingosine Kinase 1 (SK1) leads to S1P formation, which as previously mentioned is firmly established as an *anti*-apoptotic signal that promotes cancer survival and growth [19,56,63-70]. Although the challenge of distinguishing between the structures and functions of architecturally similar sphingolipids remains quite pertinent, liquid chromatography (LC) coupled to tandem mass spectrometry (MS/MS) has evolved to become the method of choice for identifying and quantifying sphingolipid metabolites in biological samples due to its high sensitivity and specificity [71].

Certain lipids including our targets of interest C16 Cer and S1P were difficult to detect and quantify due to biological factors such as low abundance relative to other lipid species in complex samples, as well as experimental complications such as pressure issues, sample carryover, poor chromatography, uninterpretable fragmentation patterns, data analysis inefficiency, low signal/noise levels, insufficient instrument sensitivity, and inability to mobilize lipid targets via electrospray ionization (ESI). After troubleshooting each one of these issues using multiple chromatography columns, buffer combinations, elution gradients, sample preparation techniques, acquisition methods, ESI source parameters, and mass spectrometers on campus and at the University of Utah Metabolomics and Proteomics Core Facility [72] and with much guidance from Dr. John C. Price at BYU and Dr. John Alan Maschek at the U of U, I came up with reverse phase (RP) LC-MS/MS lipidomics and targeted techniques to quantify the global lipidome along with consistent and accurate measurements of both sphingolipid targets using deuterated internal standards (C16 Cer-d7 and S1P-d7). In addition, I used the S1P/C16 Cer targeted RP-LC-MS/MS techniques to carry out a novel method of measuring SK1 metabolic activity by comparing between the concentrations of S1P and C16 Cer in each cell group treated with a selective inhibitor of SK1 relative to vehicle controls.

The lipidomics RP-LC-MS/MS method, sample preparation protocol, and data analysis workflows I established during this study are now being used as the standard method of choice for analyzing lipid samples in the BYU Mass Spectrometry Core Facility under the direction of Dr. Daniel Mortensen. These techniques are helping students in the Price lab and throughout the Chemistry and Life Science Departments study lipid biochemistry in aging and disease models. While kinetic proteomics studies have been performed by multiple research groups [44-47,49,50,52,73], increased instrument sensitivity and improved data analysis tools underway in our lab are making kinetic lipidomics a possibility. Students in the Price lab are currently using my quantitative lipidomics methods along with our metabolic-labeling tools [44] as a basis to measure lipid turnover in cells and tissue models of cancer and Alzheimer's.

While the wet lab experiments and LC-MS method development steps required significant amounts of careful work at the lab bench and in various MS facilities, the bulk of my time was spent on data analysis. For example, I went through each MS-1 and MS/MS spectra of our targeted LC-MS data by hand to verify the quality of the chromatography and fragmentation patterns of each lipid target relative to their corresponding internal standards. Another major challenge of the pancreatic cancer study was integrating the data from our multiple omics analyses and cell based assays to determine the physiological significance of the molecular differences observed between groups. Remarkably, global and targeted data from each assay pointed toward SK1 as an important driver of cancerous behaviors in the PDAC subclones, including rapid proliferation and defense against mitochondria mediated apoptosis.

The genomic aberration, transcriptomic, proteomic, and lipidomic profiles of all of the cancer groups were significantly perturbed relative to the healthy control, indicating that PDAC cells alter gene sequence and expression at multiple levels to promote the cancer phenotype. Although the cancer subclones were confirmed as isogenic, they exhibited significant differences in sensitivity to anti-cancer drugs. This seems to be due to a shift in signaling S1P/C16 Cer metabolism conserved across all four phenotypically disturbed cancer subclones. The concentration of pro-survival S1P relative to its pro-apoptotic metabolic precursor C16 Cer was elevated to different extents in each subclone relative to the healthy control. Moreover, each subclone exhibited variations in expression and MAPK1 mediated phospho-activation levels of SK1. Selective SK1 inhibition was sufficient to normalize growth rates relative to the slower growing healthy control and sensitized all four cancer subclones to drug-induced apoptosis. The results of this study indicate that omics techniques can not only be used to identify oncogenic roles of specific lipids and corresponding metabolic pathways and regulatory proteins, but also serves as a tool to conduct enzyme activity assays. My work expounds on previous research by increasing understanding of how bioactive sphingolipids are regulated epigenetically to enhance stress resistance and proliferation of heterogeneous PDAC subclones and how SK1 may be used as a cancer cell-specific drug target to improve treatment efficacy in metabolically adaptive cancers.

The purpose of my second project (Chapter 3) was to develop and utilize a kinetic proteomics method to increase understanding of how autophagy is used to promote metabolism and viability in cell and animal models of cancer. Autophagy is the process by which portions of the cytosol are encapsulated within membrane-bound vesicles called autophagosomes and delivered to lysosomes for destruction [74]. Cancer cells exhibit increased autophagy-driven turnover of the cellular proteome and this increase is linked to stress tolerance and chemoresistance [74-76]. Chloroquine (CQ) is a nonselective autophagy inhibitor that functions by suppressing lysosomal activity which stalls degradation of autophagosomes [77,78]. CQ is a potential anti-cancer agent because it reduces cancer cell proliferation and sensitizes cancer models to chemotherapy [77,78]. However, surrounding healthy tissues that depend on autophagy and lysosomal activity for natural mechanisms of protein homeostasis may be sensitive to CQ and damaged by combined chemotherapy [78]. The beneficial contribution of autophagy to cancer and the cytosolic substrates of consequence are unknown [23]. In normal cells, autophagy is a nonselective bulk degradation system used to tolerate nutrient starvation [74]. A growing body of work suggests that autophagy also selectively clears *specific* proteins[75,79,80][75, 79, 80][75, 79, 80][75, 79, 80][75, 79, 80][75, 79, 80][75, 79, 80][75, 79, 80][75, 79, 80](Johansen and Lamark 2011, Mathew, Khor et al. 2014, Mathew and White 2015) in response to certain stress stimuli [74-76,79,81,82]. Identifying whether autophagy is selective for specific proteins and organelles is crucial to understand how autophagy provides a metabolic advantage in cancer and may be used as a more selective drug target [23].

Targeting pathways of cancer cell autophagy rather than nonspecific autophagy may facilitate more selective tumor inhibition, yet remains to be explored, in part due to the challenge of measuring this highly dynamic process *in vivo* [83]. I used a novel application of mass spectrometry-based metabolic flux experiments to investigate substrate selection in the tumor. Specifically, I employed kinetic proteomics techniques to measure changes in the concentrations and turnover rates of hundreds of different protein types in tumor and healthy tissues derived from a xenograft mouse model treated with CQ. Each group was also exposed to a low percentage of dietary D_2O, which allowed us to monitor the incorporation of heavy isotopes into proteins over time via LC-MS and calculate changes in protein turnover rates resulting from autophagy inhibition.

Multiple sample preparation techniques and analytical instruments were used to maximize the breadth and accuracy of our kinetic and quantitative data. In the process, I developed protocols new to our lab using methods introduced by recent scientific literature as a basis to isolate cytosolic and mitochondria enriched fractions using density-gradient centrifugation on a sucrose cushion [84] and implement an MS sample preparation technique using a stable isotope dimethyl label for each protein in the sample, which ultimately provides more accurate quantitative proteomics data compared to standard label-free methods [85]. The MS preparation protocol I created using dimethyl labeling has been used for other proteomics research projects in my lab and as a part of the CHEM 584/586 teaching curriculum. I also carried out immunofluorescence experiments to detect changes in the concentrations of autophagy markers caused by drug-induced shifts in autophagy flux in both tumor and healthy tissues. As in my first study, the data analysis portion of this project entailed the bulk of the work. I performed an extensive ontology analysis by matching protein identifications from the kinetic and quantitative data sets with multiple databases to accurately categorize autophagy substrates based on function and subcellular location. Lastly, I performed statistical tests to compare turnover rates and concentrations of the global proteome as well as specific autophagy substrates in CQ treated tissues versus corresponding vehicle controls.

These assays showed that pharmacological autophagy inhibition significantly reduced CRC cell growth and sensitized cells to chemotherapy. Short-term CQ treatment also reduced tumor and healthy liver cell proliferation in the xenograft mice and increased the concentrations and turnover rates of drug metabolism enzymes. These results indicate that autophagy enhances cancer cell viability and growth and that CQ mediated inhibition of autophagy has cytotoxic effects on both cancer and healthy surrounding tissues. CQ treatment significantly reduced global protein turnover and concentrations in the tumor. The turnover rates of mitochondrial proteins were significantly more sensitive to autophagy inhibition relative to other autophagic substrates and the only substrate that significantly increased in concentration relative to the global proteome. This suggests that autophagy plays an important role in controlling the turnover of mitochondrial proteins relative to the global proteome and other autophagic substrates in CRC tumor cells, a phenomenon known as mitophagy [81].

In the liver, CQ slightly reduced global protein turnover and significantly increased global protein concentrations. Unlike the tumor, the decrease in average turnover rate of mitochondrial proteins was much like the global proteome and other autophagic substrates in the liver. Ribosomal proteins displayed the greatest decrease in turnover relative to other autophagy substrates and increased in concentration, suggesting that the ribosome may be selectively targeted by autophagy under basal conditions in the liver as opposed to the mitochondria in the tumor. In addition, the fold increase in mitochondrial protein concentrations was significantly *lower* relative to the global lipidome after CQ treatment, suggesting that both synthesis and degradation of the mitochondria in the liver were suppressed by the cytotoxic effects of CQ. This study represents a novel application of kinetic proteomics techniques to measure the effects of pharmacological suppression of autophagy flux on the global proteome and specific substrates selectively degraded by the autophagy pathway. At the same time, this study contributes to cancer metabolism research by increasing understanding of how autophagy is used to remodel the proteome in cancer cells relative to healthy tissues.

Autophagy is a promising yet risky drug target due to its roles in proteome quality control and maintenance in both healthy and cancerous tissues in experimental models as well as humans. My study suggests that targeting mitophagy rather than nonspecific autophagy may facilitate more selective tumor inhibition and reduce side effects in surrounding cells. Moreover, the D_2O based metabolic labeling technique I used to measure autophagy flux in this study can potentially be implemented in human subjects. D_2O is a safe and cost-effective metabolic label that can be used to measure protein turnover in human tissue specimens such as plasma much like in experimental models [47]. Immense progress is being made by my lab and in other groups to further develop data analysis methods that will facilitate kinetic proteomics studies in human subjects. Integration of omics technology and cancer medicine is becoming increasingly prevalent through the development of mass spectrometers intended for use in clinical settings [86]. I demonstrated a novel and relatively efficient analytical technique that has immense potential for applications in human cancer patients. D_2O-based kinetic proteomics may serve as a sensitive and efficient way to monitor drug induced changes in the flux and functions of specific metabolic pathways, potentially leading to personalized clinical information to improve the precision of diagnostic and treatment strategies [86].

2. Sphingosine kinase 1 signaling is maintained as a core proponent of a cancerous phenotype in spite of metabolic pressure and epigenetic drift

Chapter Summary

This chapter is the extended manuscript of our multi-omics study of a panel of metabolically reprogrammed human pancreatic cancer cells. It was submitted to *Oncotarget* in September 2018 and was accepted for publication in November 2018.

Authors in Order of Contribution

Monique Paré Speirs*[1], Adam C. Swensen*[1], Tsz Yin Chan[1], Peter Maxfield Jones[1], John Connor Holman[1], McCall Harris[1], John Alan Maschek[2], James E. Cox[2], Richard H. Carson[1], Jonathon Hill[3], Joshua L. Andersen[1], John T. Prince[1], John C. Price[1]

Author affiliations: 1. Department of Chemistry and Biochemistry, Brigham Young University, Provo, Utah 84602; 2. Health Sciences Cores-Metabolomics, University of Utah, Salt Lake City, Utah 84112; Department of Physiology and Developmental Biology, Brigham Young University, Provo, Utah 84602.

Contributions of Authors

I developed and performed all the steps for the LC-MS lipidomics assays, performed all steps for the proteomics assay, developed and performed all steps for the SK1 activity assay, designed and performed all steps of the cell proliferation experiments, prepared samples for the RNA-Seq assay, analyzed and interpreted data achieved from all omics and cell-based assays, constructed all of the figures, and wrote the entire manuscript. Adam C. Swensen developed and performed the shotgun lipidomics method and cell death assays and analyzed and interpreted data from these assays. Tsz Yin Chan performed and quantified the SK1 western blot assays. Peter Maxfield Jones and John Connor Holman maintained cell cultures, contributed to LC-MS and cell morphology data analysis and method development, and assisted in instrument maintenance, data analysis and interpretation, figure development, lipidomics and RNA sample preparation, and manuscript editing. McCall Harris maintained cell cultures and assisted in sample collection and sample preparation for LC-MS lipidomics experiments and assisted in data analysis and interpretation. John Alan Maschek developed and optimized the S1P targeted QqQ method and provided vital insight for sample preparation and data analysis. James E. Cox provided the instrument and facility for QqQ method development and data collection. Jonathan Hill calculated the densities for the global SNP analysis, performed the SNP principle component analysis, and provided vital insight for genomic and transcriptomic data analysis and interpretation. Richard H. Carson and Jonathan Hill performed statistical analysis of RNA-Seq data. Josh Andersen guided experimental design of cell based assays. John C. Price provided guidance and direction for all experimental designs and data analysis procedures; assisted in developing and performing all MS methods, genetics and cell based assays, interpreted data, and edited the manuscript.

ABSTRACT

Motivation

Rapid proliferation and microenvironmental stresses promote random and selective shifts in cell signaling cascades. Subpopulations derived from a single cancer cell can exhibit distinct phenotypes while conserving vital pro-survival pathways. We aimed to identify significant

drivers of cell-fate in pancreatic adenocarcinoma (PDAC) by subculturing in standard or new growth conditions to encourage differential metabolic reprogramming.

Results

The genetic and phenotypic expression profiles of each subclone were analyzed relative to a healthy control cell line (hTert-HPNE). The subclones exhibited distinct variations in gene expression and lipid metabolism. We observed, relative to hTert-HPNE, PSN-1 subclones uniformly maintained modified sphingolipid signaling and specifically retained elevated sphingosine-1-phosphate (S1P) to C16 ceramide (C16 Cer) ratios. Each clone utilized a different perturbation to this pathway, but maintained this perturbed signaling to preserve the cancerous phenotypes of rapid proliferation and defense against mitochondria-mediated apoptosis. Although the subclones were unique in their sensitivity, inhibition of the kinase that makes S1P (sphingosine kinase, SK1) significantly reduced the ratio of S1P/C16 Cer, slowed proliferation, and enhanced sensitivity to apoptotic signals. This reliance on S1P signaling identifies this pathway and SK1 specifically as a potential drug-sensitizing target that may be used to normalize S1P/C16 Cer metabolism consistently across uniquely reprogrammed PDAC clones.

Data Availability

All supplemental databases from this study are available on the Price Lab research network drive and will also be included online upon publication of the manuscript. Raw data are stored on the Price lab Synology data repository.

INTRODUCTION

Cancer development is a highly dynamic biochemical process driven by both neutral evolution and natural selection [30]. Due to the combined influences of stochastic and selective factors like genetic instability and metabolic stress, a single originating cancer cell can give rise to heterogeneous clonal populations with distinct genetic and/or phenotypic profiles [87]. Inter- and intra-tumor heterogeneity introduces major clinical challenges by enhancing drug resistance and limiting the predictability of cancer prognosis [8,10,27]. Alternatively, multiple subclones may exhibit parallel evolution, whereby specific adaptations or pro-cancer pathways are selectively *maintained* amid other complex changes displayed throughout tumor progression [31]. These conserved pro-cancer pathways provide a degree of evolutionary predictability [27], potentially serving as ubiquitous drug targets among heterogeneous cancer subclones [33,88]. Predicting which pathways are retained so that subclones will consistently respond to treatments versus those that are modifiable remains limited in most tumor types [27].

Pancreatic ductal adenocarcinoma (PDAC) is an unusually aggressive form of cancer displaying frequent, severe levels of inter- and intra-tumor heterogeneity driven by successive genetic and epigenetic modifications in early and metastatic stages [25]. Chemotherapy is effective in some patients, but most tumors develop resistance mechanisms and efforts to improve standard chemotherapeutic procedures have failed clinical trials [89]. An increased foundational understanding of the conserved pathways during PDAC cell evolution at the genomic, transcriptomic, and metabolic levels will pave the way for novel therapeutic opportunities [25].

One potentially conserved pathway is the balance between pro-survival versus pro-apoptotic signaling metabolites within and directly surrounding the cancer cell. These signals largely determine whether a cell is sensitive or resistant to anti-cancer drugs and has the potential of giving rise to drug resistant clonal populations [90]. Investigating changes in the expression and metabolism of signaling lipids and the resulting effects on cell behavior is an important area of cancer research [91]. A growing body of work reveals that deregulation of lipid metabolism (both structural and signaling lipids) may be one of the most definitive metabolic hallmarks of cancer, presenting powerful targets for therapeutic intervention [5,17,42,91-96]. The energy storage, structural, and cell signaling functions of lipids are fundamental components of proliferation, differentiation, autophagy, angiogenesis, and apoptotic processes [91,94,97,98]. In response to metabolic stress, the structural, bio-energetic and signaling roles of lipids can be coopted to support cancerous phenotypes (**Figure 2-1**). For example, rapidly proliferating cancer cells activate glycerophospholipid anabolism to provide structural building blocks for new plasma membrane to support rapid cell division [99]. Nutrient deprivation in the tumor microenvironment triggers oxidation of fatty acid stores to replenish ATP levels, promoting metabolism throughout various stages of tumor growth and progression [98]. Deregulation of lipid metabolic and signaling networks is an absolute requirement for cancer cells to thrive and proliferate [91], yet little is known about the details of such pathways and how they can be controlled in metabolically dynamic PDAC cells.

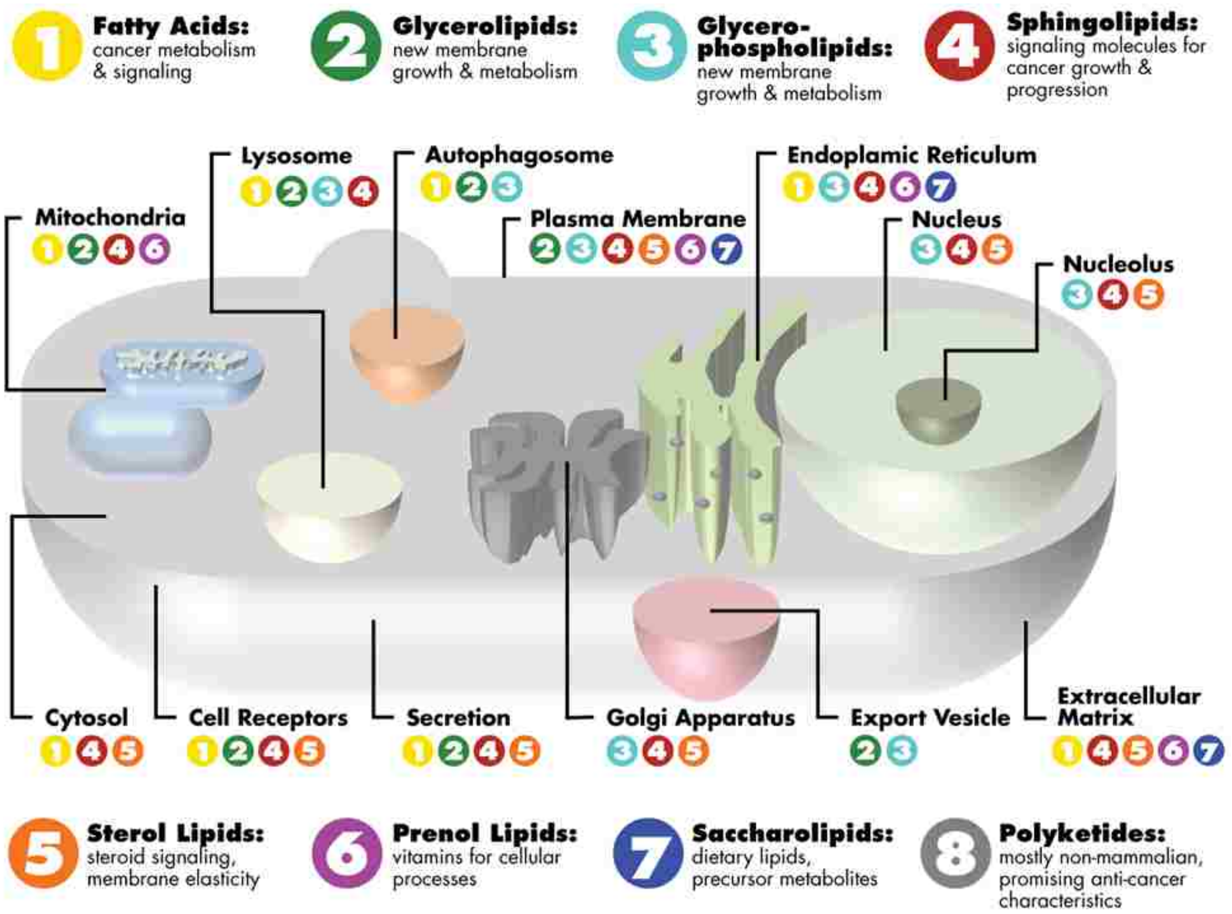

Figure 2-1 General localization of lipids and cancer-promoting roles in the cell. *At the top and bottom of this figure each lipid category/family is given a corresponding number (1–8) and brief description concerning their general involvement in supporting cancerous phenotypes. The major subcellular components have been labeled and the lipid families known to be found at each subcellular component have been listed through their corresponding numbers. The location and function of individual lipid species may change as the cell responds and adapts to stress.*

Cancer-promoting changes in lipid utilization and signaling are often traced back to the enzymes that metabolize them [16,17,94,100-102]. Altered expression and/or regulation of lipid modifying enzymes can drive pro-cancer lipid metabolism and signaling. In many tumor types, mRNA and protein expression of Fatty Acid Synthase (FASN) are activated to fuel demands for *de novo* lipid synthesis in support of new membrane formation and energy production [16,103]. FASN and other lipid-modifying enzymes are involved in complex molecular networks including both signaling and non-effector metabolites with multiple points of interplay between complimentary and competing signals. Though many substrates within these networks are structurally similar, even small modifications to a given lipid can impose vastly different physiological effects [92]. For example, although cholesterol variants like cortisol and aldosterone differ only by the position of an oxygen atom and a proton, the first promotes gluconeogenesis and anti-inflammatory processes, while the latter triggers sodium reabsorption and increased blood pressure [104]. Small changes in the expression or activity of a key lipid-modifying enzyme can lead to imbalances in inter- and extracellular lipid species leading to drastic metabolic disorders like cancer [105].

Recent literature indicates that dysregulated signaling through bioactive sphingolipids shifts the balance between pro-growth versus pro-death pathways in cancer cells [5,55,91,106]. Two interconvertible sphingolipid signals, ceramide and sphingosine-1-phosphate (S1P) play opposing roles in cancer cell fate [5,19,107-109] (**Figure 2-2**). Ceramide is metabolized to form S1P in two enzymatic steps: deacylation followed by ATP-dependent phosphorylation by Sphingosine Kinase. At basal levels, ceramide is continuously recycled from S1P by the reverse of these two reactions. The ceramide salvage pathway can also be signal-mediated to alter endogenous ceramide concentrations relative to S1P to promote stress tolerance [19]. Current research indicates that C16 Ceramide (Cer(d18:1/16:0)) (**Figure 2-2**) is a potent pro-apoptotic signal, stimulating anti-proliferative responses like cell cycle arrest, tumor suppression, and cell senescence[59-61,110]. Alternatively, S1P acts as a pro-survival signal by promoting stress tolerance, cell motility, angiogenesis, and optimal cell proliferation rates induced by growth factors [91,111]. Although endogenous S1P is generally less abundant than ceramide, it is highly mobile and suppresses ceramide-induced apoptotic phenotypes including intra-nucleosomal DNA fragmentation and altered cell morphology [64]. These findings by Cuvillier *et al.* led to the birth of the term "sphingolipid rheostat" which is used to describe the interplay between competing ceramide and S1P signals and the resulting effects on cell fate [19,64].

While several enzymes are involved in the synthesis, degradation, and turnover of C16 Cer and S1P (**Figure 2-2**), recent literature suggests that Sphingosine Kinase 1 (SK1) plays a central role in regulating the sphingolipid rheostat in many forms of cancer [112-120]. Overexpression and/or upregulation of SK1 have been reported in a wide range of tumor types, including breast, colon, lung, ovarian, kidney, and rectal tumors [119]. Elevated SK1 activity is linked to tumor angiogenesis and progression as well as resistance to radiation and chemotherapy [119]. Therefore, SK1 may serve as a powerful drug target to re-regulate the sphingolipid rheostat and restore a healthy balance between pro- and anti-apoptotic signals in drug resistant cancers.

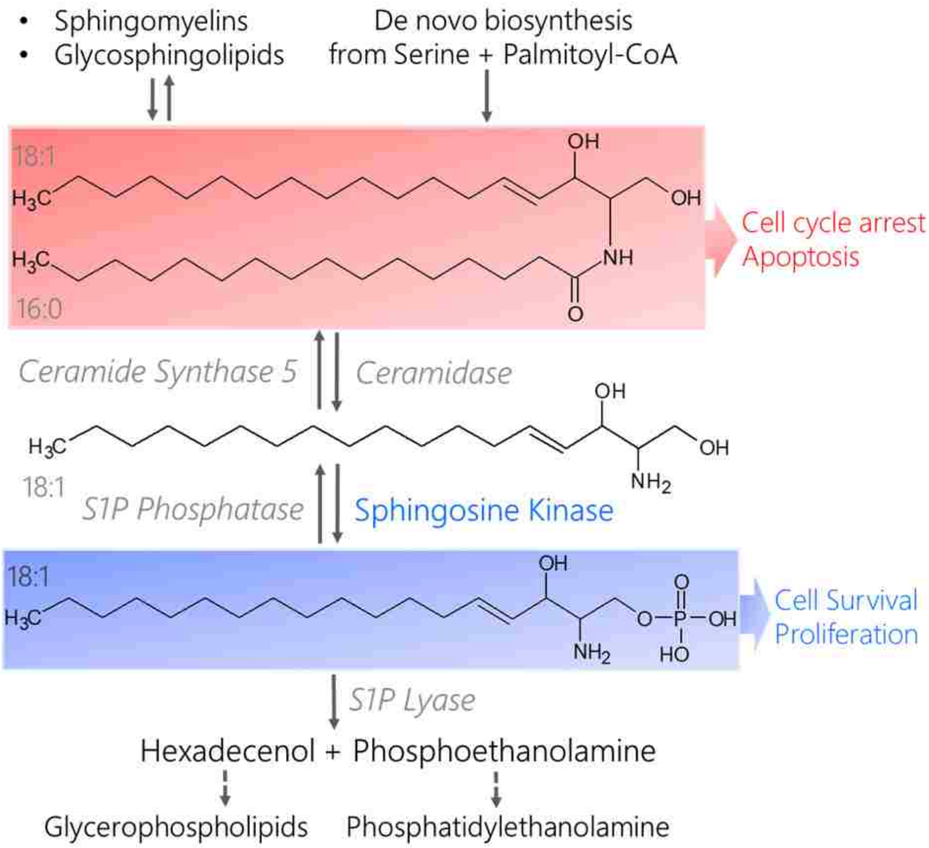

Figure 2-2 Structures and metabolism of pro-apoptotic C16 Cer and pro-survival S1P. *Ceramides result from the breakdown of more complex sphingolipids like sphingomyelins and glycosphingolipids or is biosynthesized de novo from serine and palmitoyl-CoA (C16 Cer shown in red box). Ceramidase catalyzes the de-acylation of Ceramide to form sphingosine. Sphingosine Kinase phosphorylates sphingosine in an ATP-dependent manner to generate S1P (shown in blue box). S1P is removed from the sphingolipid metabolism pathway when it is degraded by S1P Lyase, yielding precursors for phospholipid synthesis (hexadecenol and phosphoethanolamine). Ceramide can be recycled via S1P phosphatase-catalyzed dephosphorylation of S1P to reform sphingosine, which is acylated by Ceramide Synthase (CerS) to reform ceramide. The chain length of the resulting ceramide depends on the type of CerS that acts on sphingosine, e.g. CerS5 produces C16 Cer from sphingosine. C16 Cer promotes cell cycle arrest and apoptosis while S1P stimulates pro-survival and pro-proliferative signaling cascades.*

Here, we sought to explore cancer cell evolution and identify conserved pathways among differentially evolved clonal populations that underlie the aggressive and drug-resistant nature of PDAC. We developed a panel of phenotypically heterogeneous human PDAC cell populations from the same genetic origin (PSN-1) [121] to investigate how stochastic factors and microenvironmental pressures promote common and differential evolutionary paths in pancreatic cancer (**Figure 2-3**). The original PSN-1 stock was split into four isolated subcultures: psn1-A (pA), psn1-B (pB), psn1-C (pC), and psn1-D (pD). The pA and pC groups were passaged in the baseline growth conditions while pB and pD cells were subcultured in different formulations of complete growth medium for one month (**Supplemental Table 1**). The pA and pC groups were used to represent a form of "neutral evolution" since they were influenced purely by inherent stresses, such as rapid division rates which have been shown to promote spontaneous genetic and phenotypic instability [87]. In addition to "neutral" evolutionary stress, the pB and pC cells were subjected to microenvironmental cues from their diets, thereby representing subclones influenced both by stochastic internal and environmentally induced external pressures (**Figure 2-3**).

We compared genetic and metabolic profiles of the four PSN-1 subclones to one another and relative to a healthy (non-oncogenic) immortalized control cell line, hTert-HPNE (hTert) using Short Tandem Repeat (STR) profiling, Single-nucleotide Polymorphism (SNP) genotyping, RNA-Sequencing (RNA-Seq), quantitative proteomics, and lipidomics mass spectrometry (MS) techniques [122] (**Figure 2-3**). Although our genomics data suggested the four PSN-1 subclones were virtually isogenic, they exhibited consistent variations in phenotype, suggesting that each cancer group followed a unique evolutionary path driven by non-genetic variations in molecular expression and/or regulation. At the same time, all four subclones maintained similar cancer-like phenotypes relative to hTert, such as irregular cell shapes and morphology, rapid proliferation rates, altered enzyme expression and activity levels, as well resistance to apoptotic signaling. This suggests that the most important pro-cancer pathways were selectively conserved across all four cancer groups.

Despite numerous differentially expressed genes and metabolic modifications between the cancer subclones, each of our assays identified SK1 mediated S1P/C16 Cer metabolism as a key element regulating the shift between cancerous and healthy phenotypes in heterogeneous clonal populations. We propose that the selective pressure to maintain rapid growth and apoptotic resistance promotes this shift in SK1-mediated S1P/C16 Cer metabolism because it is an important component of metabolic reprogramming in human pancreatic cancer cells. This "cancerous" sphingolipid rheostat is promoted through synergistic modification of transcription, translation, and enzyme activation, yet may be corrected in any subclonal variant through selective regulation of SK1.

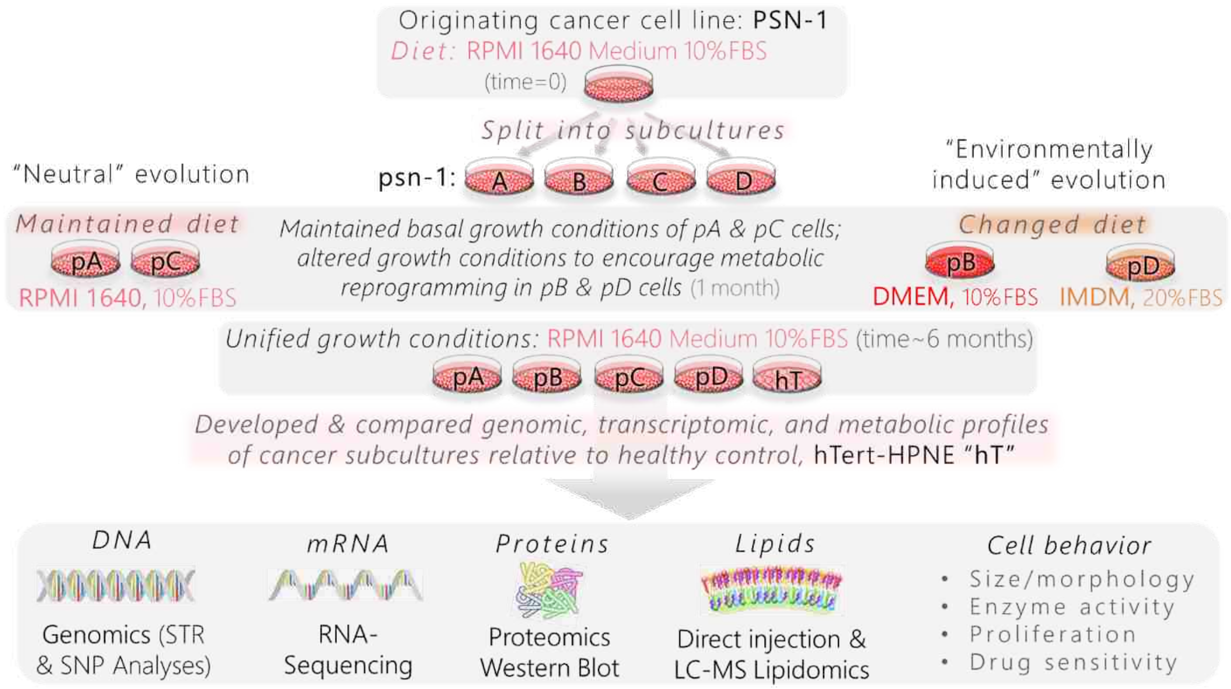

Figure 2-3 Schematic of experimental workflow used to generate isolated pancreatic cancer subclones from a common genetic origin and identify pro-survival pathways.

RESULTS

PDAC subclones and healthy controls displayed variations in cell size and morphology

The transformation from a normal to cancer cell involves characteristic changes in morphology, such as irregular cell shapes, shifts in cell size, and darker nuclei [123]. Unlike the cancer subclones, hTert cells were extremely elongated with little to no rounded centers or terminal ends (**Figure 2-4A-E**). The hT cells were lighter in appearance with much less visible nuclei compared to the cancer groups (**Figure 2-4A-E**). The four cancer subclones also were significantly smaller than the hTert cells ($P<0.01$) (**Figure 2-4F**). This suggests that the transition from a normal to malignant ductal pancreatic cell involves major shifts in cell size and morphology.

Within the cancer groups, each subclone displayed specific morphological characteristics. The pA subclones exhibited both punctate and spheroid cell shapes composed of very rounded centers with short, pursed edges (**Figure 2-4A**). The pB cells were generally thinner, less defined, and more elongated with rigid, sharp corners and darker nuclei than the other cancer groups (**Figure 2-4B**). The pC cells portrayed plumper, concave spindle shapes with both smooth and sharp edges (**Figure 2-4C**). The pD group included very punctate as well as fusiform cell shapes with well-defined, smooth edges (**Figure 2-4D**). On average, pD cells were larger than the other cancer subclones, although this difference was only significant between the pA and pD groups ($P=0.005$) (**Figure 2-4F**). Morphological phenotypes are intimately linked with shifts in cell stress, transcription, enzyme activity, and metabolism, thus serving as structural manifestations of interplay between environmental and intracellular cues [124]. We thus anticipated that these apparent phenotypic differences may be coupled with biochemical variations between cancerous and healthy cells as well as between individual PSN-1 subclones.

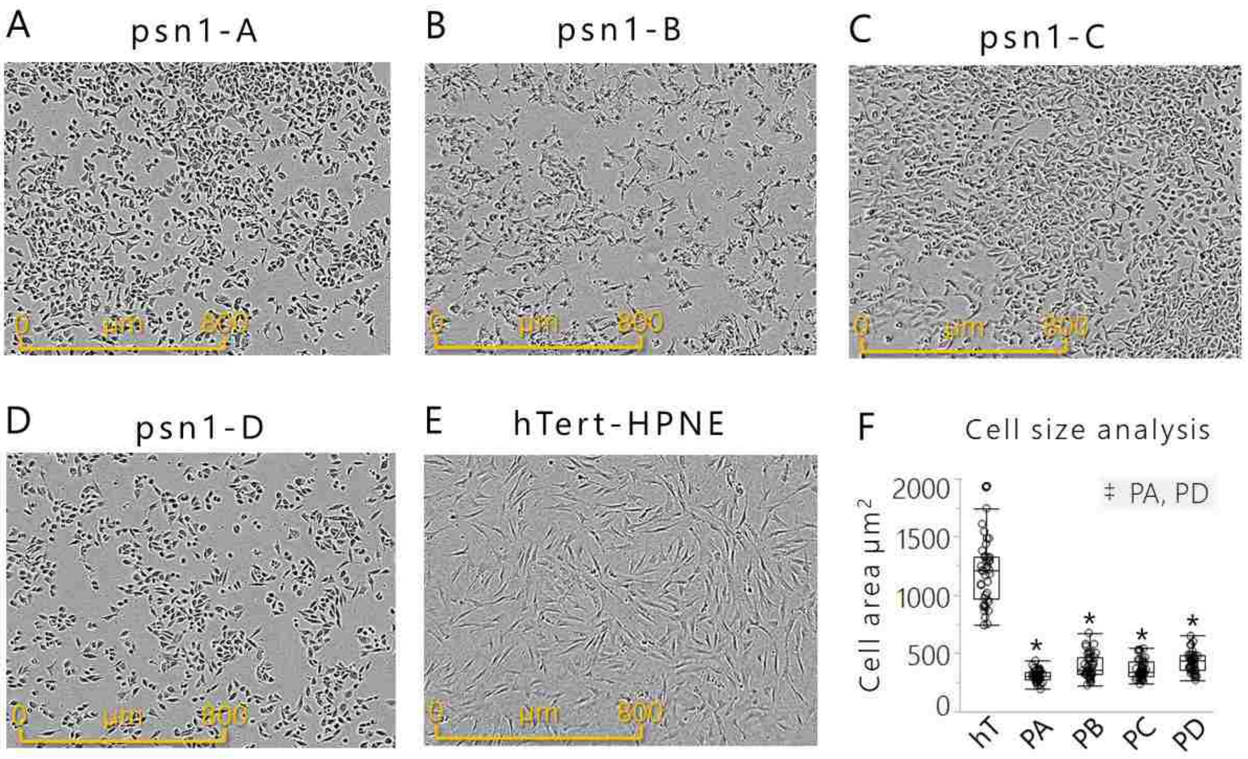

Figure 2-4 Pancreatic cancer subclones and healthy control cells displayed variations in cell size and morphology. (A-E) *Representative light microscope images of each cell group, including* ***(A)*** *psn1-A,* ***(B)*** *psn1-B,* ***(C)*** *psn1-C,* ***(D)*** *psn1-D, and* ***(E)*** *hTert cells.* ***(F)*** *Box plot of cell sizes measured by image analysis of healthy control (hT) and pancreatic cancer subculture groups. Data are represented as the cell area (μm^2) of 40 biological replicates per cell type. The Dunnett's Test was used to compare cancer groups to the healthy control, where * indicates P<01. The Tukey-Kramer Test was used to determine significant differences between the cancer subcultures; the pair found to be significantly different is highlighted in the right-hand corner of the plot, where † indicates P=0.0052.*

DNA fingerprints were identical in distinct PDAC clonal populations

STRs are short, tandemly repeated DNA sequences (~2-6bp) scattered somewhat evenly throughout the human genome [125]. Because STRs display high degrees of polymorphism between individuals, they are used to produce a unique numerical pattern made up of 8 STR markers (along with amelogenin for sex determination) known as the "DNA fingerprint" (**Supplemental Table 2A-B**) [126]. A cell line is considered authentic when there is a ≥80% match between the sample cell line and the reference STR profile [126] provided by the American Type

Culture Collection (ATCC). As a reference, there was a 100% match between our hTert cells and the ATCC hTert-HPNE reference profile (**Supplemental Table 2A**).

We compared the STR profiles of cells from each PSN-1 subculture group (pA, pB, pC, pD) collected at the end of the study (time~6 months) to cells from the original PSN-1 stock (time=0) (**Figure 2-3**). The original PSN-1 stock displayed a 92% match with the ATCC PSN-1 reference profile (**Supplemental Table 2B**), indicating that our originating PSN-1 line (**Figure 2-3**) was an authentic representation of the PSN-1 human cell line [121]. Each of the four PSN-1 subclones (pA, pB, pC, and pD) also displayed matches (92%) with the PSN-1 reference profile. Indeed, amelogenin and the eight core STR loci were unchanged in all four subculture groups relative to our original PSN-1 stock (**Supplemental Table 2B**). This indicates that any evolutionary changes that may have occurred throughout the study did not affect the DNA fingerprint nor the ability to trace each PSN-1 subclonal population back to the original tissue donor.

PDAC subclones exhibited distinct nscSNP profiles relative to healthy control cells, but were virtually isogenic relative to one another

Single nucleotide polymorphisms (SNPs) resulting from selectively maintained point mutations are the most common type of genetic variation throughout the human genome [127]. Non-synonymous SNPs in coding regions (nscSNPs) and regulatory regions of the genome tend to have the greatest effects on phenotype [128] and may provide a foundation for cancer development and tumor heterogeneity [127] [129] [130].

DNA sequencing data derived from RNA-Seq analysis was used to identify and compare the levels of nscSNPs throughout the genomes of each cell type (hT, pA, pB, pC, pD). There were numerous different non-synonymous coding SNPs detected in each sample from both hTert and cancer subclones relative to the reference genome (640,451 total nscSNPs detected in 13,657 total genes across 16 samples) (**Supplemental Database A**). Interestingly, the median nscSNP density was highest in the slower growing hT cells (0.059%), followed by pC (0.049%), pA (0.044%), pB (0.043%), and pD cells (0.039%) (**Supplemental Database A**). This indicates that the genomes of both cancer and healthy ductal pancreatic cell cultures were sensitive to nscSNP-driven genetic variation at slightly different degrees.

We used heat map clustering to visualize broad differences between gene specific nscSNP densities in each sample **(Figure 2-5A)**. All four hT biological replicates clustered together (left) and did not intermix or cluster with nscSNP profiles from any cancer sample (right) **(Figure 2-5A)**. On the other hand, nscSNP profiles of biological replicates from the four cancer groups were quite intermixed and clustered together throughout the right-hand portion of the heat map **(Figure 2-5A)**. Overall, there were no clear differences distinguishing the genome-wide nscSNP profiles of the four PSN-1 subclones **(Figure 2-5A)**.

We used a PCA of the SNP data in binary form (presence or absence of a nscSNP) to investigate genome-wide differences in these coding region SNPs between each group (**Figure 2-5B**). There was a clear separation between the nscSNP profiles of all four hTert replicates relative to the cancer samples, suggesting that there were a large number of differences in nscSNP densities per gene between the healthy and cancer groups (**Figure 2-5B**). On the other hand, all of the biological replicates derived from the four different PSN-1 clones (3 from each group) formed another fairly isolated cluster on the PCA plot (**Figure 2-5B**). This further indicates that the genome-wide nscSNPs densities between the different cancer groups did not drastically change throughout the subculturing experiment. The overlapping points of the subclone replicates (**Figure 2-5A**) suggest that there were no significant differences in global nscSNP compositions between individual PSN-1 subclones.

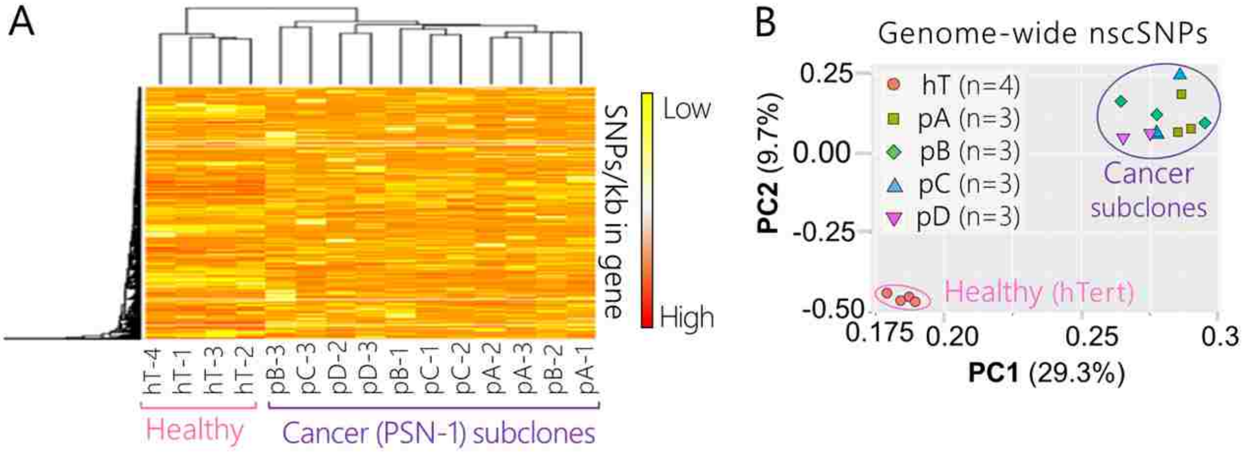

Figure 2-5 Genome-wide nscSNP Analysis PSN-1 subclones and healthy control cells. (A) *Hierarchal clustering and heat map of non-synonymous coding SNPs detected via RNA-Seq of healthy control cells (hT) and PSN-1 subclones (pA, pB, pC, pD) (n=640,451 nscSNPs). Measurements were collected in biological triplicate or quadruplicate, (all 16 shown for comparison); the group name and replicate number are shown for each sample. Rows were centered; no scaling was applied to rows; both rows and columns were clustered using Hierarchal Euclidean distance metric with complete linkage. Each row represents a different gene (n=13,657 genes). The scale from low (yellow) to high (red) represents the relative level of nscSNPs normalized to the gene length (kb) that were detected in the respective sample.* ***(B)*** *PCA of nscSNPs measured via RNA-Seq of healthy control cells (hT) and PSN-1 subclones (pA, pB, pC, pD) (n=640,451 nscSNPs). Measurements were collected in biological triplicate or quadruplicate, resulting in a total of 16 samples. SVD was used to calculate principal components; X and Y axis show principal component 1 and principal component 2, which explain 29.3% and 9.7% of the total variance, respectively. The orange circles represent hT samples, green squares represent pA samples, bright green diamonds represent pB samples, blue triangles represent pC samples, and fuchsia upside-down triangles represent pD samples. The pink open circle is shown to differentiate samples from the healthy control group (hT) from those of the cancer subculture groups (pA, pB, pC, pD) which are clustered within the purple circle. One biological replicate from the pC group and one from pD group are not visible due to overlap with points from biological replicates of the same group.*

Isogenic PDAC subclones displayed global variations in mRNA expression relative to one another and to healthy control cells

We compared the relative mRNA concentrations to identify genes that were differentially expressed across cell types using the *DESeq2* Bioconductor package and statistical criteria [131]. There were 19,946 common genes quantified in all of the groups that met the statistical criteria for quantitative mRNA analysis (See Materials and Methods) [131]. Among this list, there were a large number of significantly differentially expressed genes (66.4%; adjusted P<0.1) across the five cell groups (hT, pA, pB, pC, pD) (**Supplemental Database B**). Among the four PSN-1 subclones (excluding hT), there were about half as many significantly differentially expressed genes (31.3%; adjusted P<0.1) (**Supplemental Database C**). These results indicate that there were major differences in global mRNA expression levels between the healthy and cancer groups as well as between individual PSN-1 subgroups. In addition, these data provided our first line of evidence that although the different PSN-1 subcultures (pA, pB, pC, pD) were genetically isogenic, they were differentially modified at the level of transcription.

Hierarchal heat map clustering and PCA were used to explore general differences in the global mRNA expression profiles (n=19,946) of each group (**Figure 2-6A1-2**). Both the heat map **(Figure 2-6A1)** and PCA **(Figure 2-6A2)** displayed a very clear division between mRNA profiles of the cancer groups (pA, pB, pC, pD) relative to the healthy control (hT). There were also fewer significant differences in mRNA expression levels between the different PSN-1 subclones (**Supplemental Database C**), demonstrating that the cancer groups dysregulated transcription in slightly different ways over the course of the subculturing experiment. Based on the PCA plot (**Figure 2-6A2**), the clones most similar in terms of mRNA expression were those whose diets were unchanged (pA and pC). In contrast, cancer groups subcultured in new growth mediums (pB and pD) displayed greater degrees of variance relative to the pA and pC groups. The group subjected to the more extreme dietary change (pD) **(Figure 2-3)** displayed the greatest variation in global mRNA levels relative to the other three cancer subclones (pA, pB, pC) (**Figure 2-6A2**). This suggests that PSN-1 subclones readily altered mRNA expression levels in response to intrinsic sources of random fluctuations due to rapid cell division (as in the cases of pA and pC), and additionally in response to modified nutrient availability, as exemplified by the pD cells.

Isogenic reprogrammed PDAC subclones displayed global shifts in protein expression relative to one another and to healthy control cells

To determine whether these global shifts in transcription affected the proteome, we performed a comparative quantitative proteomics analysis of each cell group. There were 1,378 unique proteins identified across all the cell groups that met our statistical criteria for quantitative analysis and protein expression profiling (See Materials and Methods) (**Supplemental Database D**). We used hierarchal heat map clustering and a PCA to compare the protein expression profiles of each cell type (**Figure 2-6B1-2**). Similar to the RNA-Seq analysis **(Figure 2-6A1-A2)**, the heat map and PCA of our proteomics data revealed a very clear separation between the global protein expression profiles of the four cancer groups relative to the healthy control **(Figure 2-6B1-2)**. Within the fairly tight cluster of points representing cancerous protein profiles on the PCA plot, the pC cells were distant from the other three subclones **(Figure 2-6B2)**. This suggests that protein metabolism was most altered in pC cells as a result of internal (non-environmental) pressures over the course of the subculturing experiment.

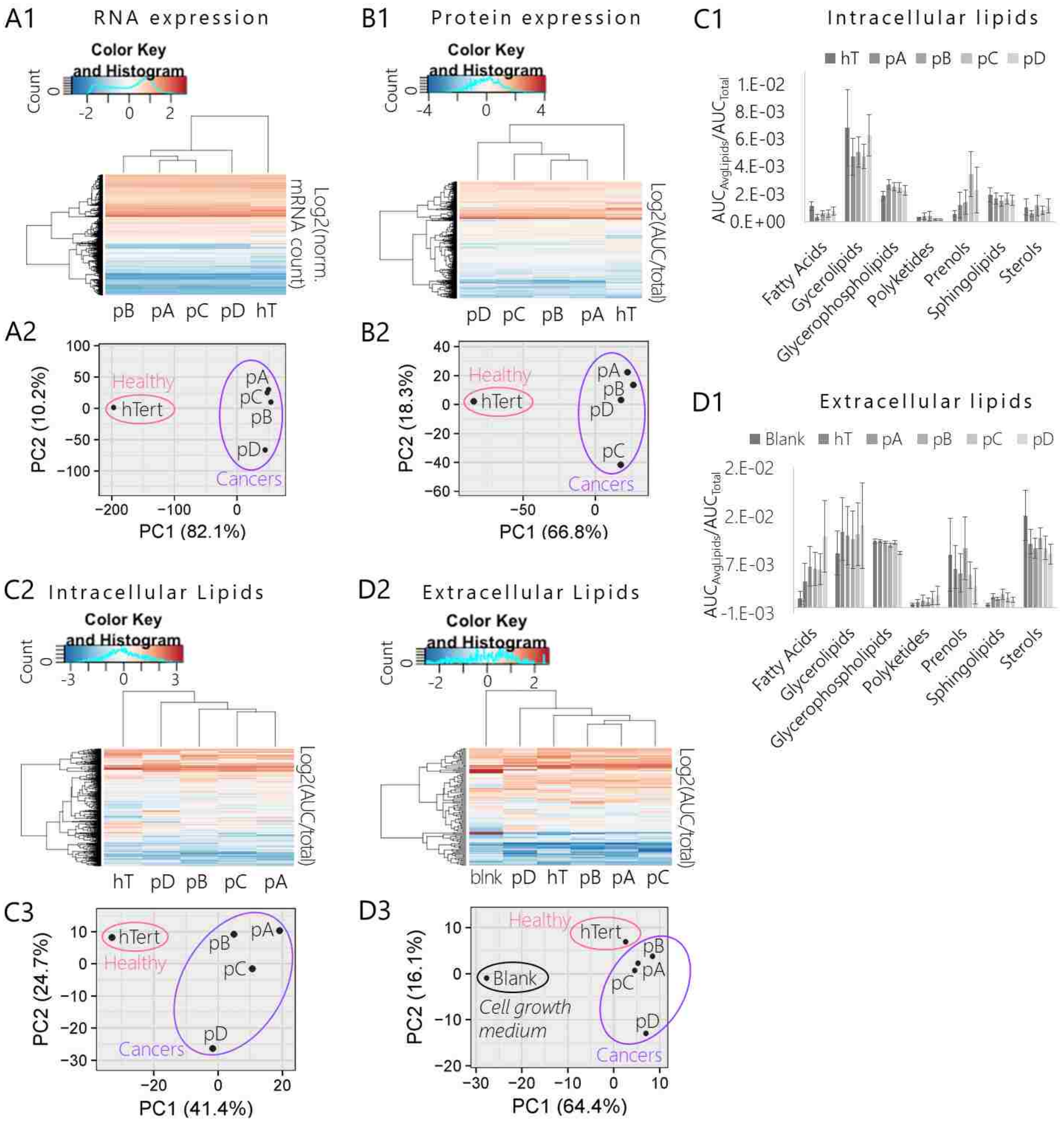

Figure 2-6 RNA, protein, and lipid expression profiling suggest global shifts in transcription and metabolism between pancreatic cancer subclones and relative to the healthy control. (A1-A2) *Results of RNA-Seq assay of global mRNA extracted from pancreatic cancer subclones and healthy control cell lysates.* ***(A1)*** *Heat map and hierarchal clustering of cancer subclone and hT transcriptomes. Rows were centered; no scaling was applied to rows; both rows and columns were clustered using Hierarchal Euclidean distance metric with complete linkage. Each row represents a unique gene (n=19,946 genes). The color scale from -2 (blue) to 2 (orange) represents the mean normalized mRNA concentration of 3-4 biological replicates per group (3 per cancer group and 4 hT) calculated for each gene as Log2(normalized mRNA Counts of gene).* ***(A2)*** *PCA of cancer*

subclone transcriptomes and healthy control. No scaling was applied to rows; SVD with imputation was used to calculate principal components; X and Y axis show principal component 1 and principal component 2 that explain 82.1% and 10.2% of the total variance, respectively. ***(B1-B2)*** *Results of global quantitative proteomics analysis of proteins extracted from whole cell lysates of pancreatic cancer subclones and hT cultures.* ***(B1)*** *Heat map and hierarchal clustering of cancer subclone and healthy control global proteomes. Rows were centered; no scaling was applied to rows; both rows and columns were clustered using Hierarchal Euclidean distance metric with complete linkage. Each row represents a unique protein identification (n=1,378 proteins). The color scale from -4 (blue) to 4 (orange) represents the mean normalized protein concentration of 3-4 biological replicates per group (4 per cancer group and 3 hT) calculated for each protein as* $Log2(AUC_{Protein}/AUC_{Total})$. ***(B2)*** *PCA of cancer subclone and healthy control cell proteomes. No scaling was applied to rows; SVD with imputation was used to calculate principal components; X and Y axis show that principal component 1 and principal component 2 explain 66.8% and 18.3% of the total variance, respectively.* ***(C1-C3)*** *Results of quantitative lipidomics analysis measured by LC-MS of lipids extracted from pancreatic cancer subclones and hT cell lysates.* ***(C1)*** *Heat map and hierarchal clustering of cancer subclone and healthy control intracellular lipidomes. Rows were centered; no scaling was applied to rows. Both rows and columns were clustered using Hierarchal Euclidean distance metric with complete linkage. Each row represents a unique lipid annotation (n=500 species). The color scale from -3 (blue) to 3 (orange) represents the mean normalized lipid concentration of three biological replicates per group calculated for each lipid as* $Log2(AUC_{Lipid}/AUC_{Total})$. ***(C2)*** *Categorized intracellular lipidome compositions of species measured via quantitative intracellular LC-MS analysis. Data are expressed as the mean (Avg) normalized concentration* $(AUC_{AvgLipids}/AUC_{Total})$ *of total lipids measured in each category +/-SEM measured in three biological replicates per cell type.* ***(C3)*** *PCA of cancer subclone and healthy control intracellular lipidomes. No scaling was applied to rows; SVD with imputation was used to calculate principal components; X and Y axis show principal component 1 and principal component 2 that explain 41.4% and 24.7% of the total variance, respectively.* ***(D1-D3)*** *Results of quantitative extracellular lipidomics analysis measured by LC-MS of lipids extracted from the complete growth medium used in cell cultures during intracellular lipidomics experiment (RPMI 1640 + 10% FBS). The negative control or "Blank" (blnk) represents the lipidome of fresh complete cell medium that was never exposed to cell cultures.* ***(D1)*** *Hierarchal clustering and heat map of cancer subclone and healthy control extracellular lipidomes. Rows were centered; no scaling was applied to rows. Both rows and columns were clustered using Hierarchal Euclidean distance metric with complete linkage. Each row represents a unique lipid annotation (n=112 lipids). The color scale from -2 (blue) to 2 (orange) represents the mean normalized lipid concentration of 3 biological replicates per group calculated for each lipid as Log2(AUC of lipid/Sum AUC of total lipids quantified in sample). Rows were centered; unit variance scaling was applied to rows. Both rows and columns were clustered using correlation distance and average linkage.* ***(D2)*** *Categorized intracellular lipidome compositions of species measured via quantitative extracellular LC-MS analysis. Data are expressed as the mean (Avg) normalized concentration* $(AUC_{AvgLipids}/AUC_{Total})$ *of total lipids measured in each category +/-SEM measured in three biological replicates per cell type.* ***(D3)*** *PCA of cancer subclones and healthy control extracellular lipidomes compared to blank. No scaling was applied to rows; SVD with imputation was used to calculate principal components. X and Y axis show principal component 1 and principal component 2 that explain 64.4% and 16.1% of the total variance, respectively.*

We performed a protein ontology analysis using David Bioinformatics Functional Annotation Tools [42] to determine whether certain types of functional proteins were differentially expressed between groups and may have driven the global phenotypic shifts between healthy and cancer cells. Among numerous significantly differentially expressed proteins in the hTert cells relative to the cancerous groups (corrected P value <0.05), ~39% were upregulated (fold change >1) and 61% were downregulated (fold change <1) (**Supplemental Database E**). We were not surprised to find that the top three significantly enriched ontologies (Benjamini score for enrichment <0.05) among proteins that were significantly upregulated in hT relative to the cancer groups were involved in actin filament binding, focal adhesion, and the cytoskeleton. A decrease in actin proteins and other cytoskeletal components may have accompanied the structural framework of the smaller, more punctate cancer cells relative to the longer, more elongated hTert cells (**Figure 2-4**). Among the list of significantly downregulated proteins in hTert relative to the cancer groups, the top three significantly enriched ontologies (Benjamini score for enrichment <0.05) were mRNA processing, mRNA splicing, and the spliceosome as a whole. This suggests that the cancer cells transcribe and process mRNA differently than hTert, which may have contributed to the severe global shift in the mRNA expression profiles of the cancer subgroups relative to hTert (**Figure 2-6A2**).

There was also some evidence for differential expression of specific protein ontologies between individual cancer subclones (**Supplemental Database F-I**). Neither the pA or pD had significant changes in recognized ontologies. The pB cells were upregulated in nucleotide binding, ATP-binding, and ATP-dependent RNA helicase activity. This suggests a difference in the way pB cells bind and use ATP, especially in regards to RNA processing and may have contributed to variations in the global mRNA profile of pB relative to other subclones (**Figure 2-**

6A1-2). The pC cells were upregulated in amino acid transport and metabolism, the extracellular exosome, and metal-binding proteins. Altered expression of amino acid metabolism networks may have affected protein metabolism and contributed to the wide separation between the pC proteome relative to the other cancer subclones depicted in the PCA plot (**Figure 2-6B2**). Among the downregulated proteins in pC, the most enriched functional groups were translation, the ribosome, and structural components of the ribosome. These results coupled with the evidence that proteins involved in amino acid metabolism were upregulated, suggest that compared to the other cancer groups the pC subclone significantly altered protein synthesis and metabolism systems relative to the proteome.

Overall, the protein ontology analysis showed that each PSN-1 subclone modified protein expression levels in unique ways to support cellular metabolism and morphology. However, we did not find any clear evidence of significant cell-fate signaling mechanisms that were conserved across the cancer subclones relative to the hTert. Because lipid metabolism and signaling play important roles in cancer cell fate (**Figure 2-1**) we next explored methods to measure and compare intracellular lipid concentrations in the healthy versus PDAC tissue models.

Isogenic reprogrammed PDAC clones displayed global shifts in lipid expression networks including altered metabolism of bioactive sphingolipids S1P and C16 Cer

We developed lipidomic profiles of each cell group in multiple stages to investigate cancer-promoting adaptations in lipid metabolism pathways. In our initial shotgun lipidomics assay, a total of 980 unique lipids that met our statistical criteria (See **Materials and Methods**) were identified among all five cell types (**Supplemental Database J**). All eight lipid categories were represented in this list, including saccharolipids (0.4%), sterols (5.1%), polyketides (5.4%), prenols (7.2%), sphingolipids (10.0%), fatty acids (19.2%), glycerolipids (21.8%), and glycerophospholipids (30.9%). Relative concentrations of the detected lipids were used to develop preliminary lipid expression profiles for each cell type (**Figure 2-7**).

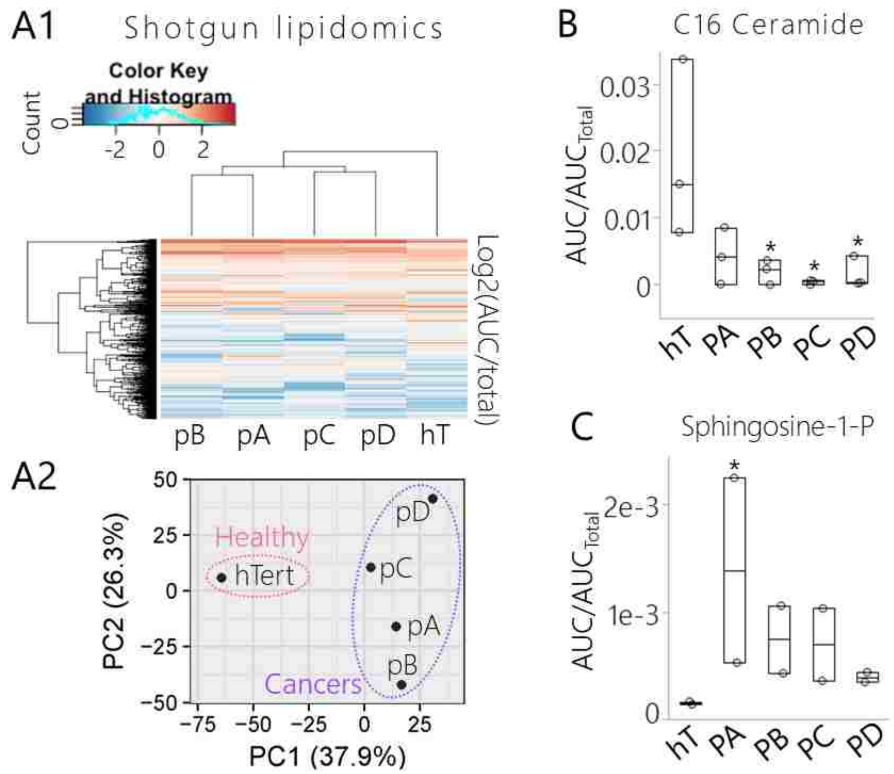

Figure 2-7 Shotgun lipidomics suggests global shifts in lipid metabolism including conserved differences in pro-survival S1P and pro-apoptotic C16 Cer levels among pancreatic cancer subclones relative to healthy control cells. (A1-A2) *Results of shotgun lipidomics analysis of pancreatic cancer subclone and healthy control cell lysates measured by direct-infusion ESI-MS.* ***(A1)*** *Hierarchal clustering and heat map of cancer subclones and healthy control lipidomes measured by direct-infusion ESI-MS. Rows were centered; no scaling was applied to rows. Both rows and columns were clustered using Hierarchal Euclidean distance metric with complete linkage. Each row represents a unique lipid annotation (n=982 species). The color scale from -2 (blue) to 2 (orange) represents the normalized lipid concentration of one sample per group calculated for each lipid as* $Log2(AUC_{Lipid}/AUC_{Total})$. ***(A2)*** *PCA of cancer subclones and healthy control lipidomes measured by direct-infusion LC-MS. No scaling was applied to rows; SVD with imputation was used to calculate principal components; X and Y axis show principal component 1 and principal component 2 that explain 37.9% and 26.3% of the total variance, respectively.* ***(B-C)*** *Box plots depicting relative concentrations of* ***(B)*** *C16 Cer and* ***(C)*** *S1P that were detected in two biological replicates of samples from each of the pancreatic cancer group and the healthy control cell line via direct-infusion ESI-MS.* ***(B-C)*** *Data are depicted as the normalized concentration of each lipid* (AUC_{Lipid}/AUC_{Total}). *The Dunnett's test was used to determine*

*significant differences between the cancer groups relative to the healthy control cell line, where * indicates $p<0.05$.*

Hierarchal heat map clustering **(Figure 2-7A1)** and PCA **(Figure 2-7A2)** illustrated a clear distinction between the cancer groups relative to hTert. This suggests that lipid concentrations and lipid metabolic networks were severely altered in relatively similar manners across the PDAC subclones compared to the healthy control. At the same time, both the heat map **(Figure 2-7A1)** and PCA **(Figure 2-7A2)** suggested that there were apparent differences in global lipid levels between the cancer groups, indicating that each cancer group altered lipid expression and/or metabolism at slightly different degrees relative to one another during the subculturing experiment.

The quantitative lipidomics analysis revealed connected differences between two interconvertible sphingolipid metabolites (**Figure 2-2**), C16 Cer (**Figure 2-7B**) and S1P (**Figure 2-7C***)*, in all four subcancer clones relative to hTert. The C16 Cer levels were *depleted* in all four cancer groups relative to hTert; this decrease was significant in pB, pC, and pD cells ($P<0.05$) (**Figure 2-7B**). On the other hand, S1P levels were *elevated* in all the cancer groups relative to hTert and this increase was statistically significant in pA cells ($p<0.05$) (**Figure 2-7C**). These results provided some evidence that S1P production from C16 Cer (C16 Cer→ sphingosine→ S1P) was suppressed in hTert cells whereas C16 Cer metabolism to S1P was upregulated to some degree in each cancer subclone (**Figure 2-2**). Despite numerous variations in expression throughout the lipidome between the different PSN-1 clones **(Figure 2-7A1-A2)**, these data suggested that altered C16 Cer and S1P levels were distinctive cancerous phenotypes conserved across all four isolated PDAC clones. Although C16 Cer and S1P levels were shifted by fairly different degrees in each subclone **(Figure 2-7B-C)**, PSN-1 cells may depend on some form of sphingolipid metabolite imbalance to regulate pro-survival pathways throughout different stages of cell progression or evolution. Our next goal was to verify these results and confirm whether this imbalance in the S1P/C16 Cer axis was indeed maintained as a pro-cancer mechanism among the PSN-1 subclones.

Sphingolipid focused LC-MS confirmed that both global lipid expression and S1P/C16 Cer metabolism were modified in PDAC subclones relative to the healthy control

Although we consistently detected C16 Cer among hundreds of other lipid species, our initial lipidomics method was limited in its ability to consistently and accurately identify S1P species. Adapting the S1P focused approach developed by Bode and Gräler (B&G) [71], we measured S1P and C16 Cer along with the global lipidome of the PSN-1 clones relative to hT cells (**Supplemental Database D**). The LC-MS improved the confidence level of each lipid annotation using RT and alignment fragmentation relative to deuterated internal standards (**Figures 2-8-10**).

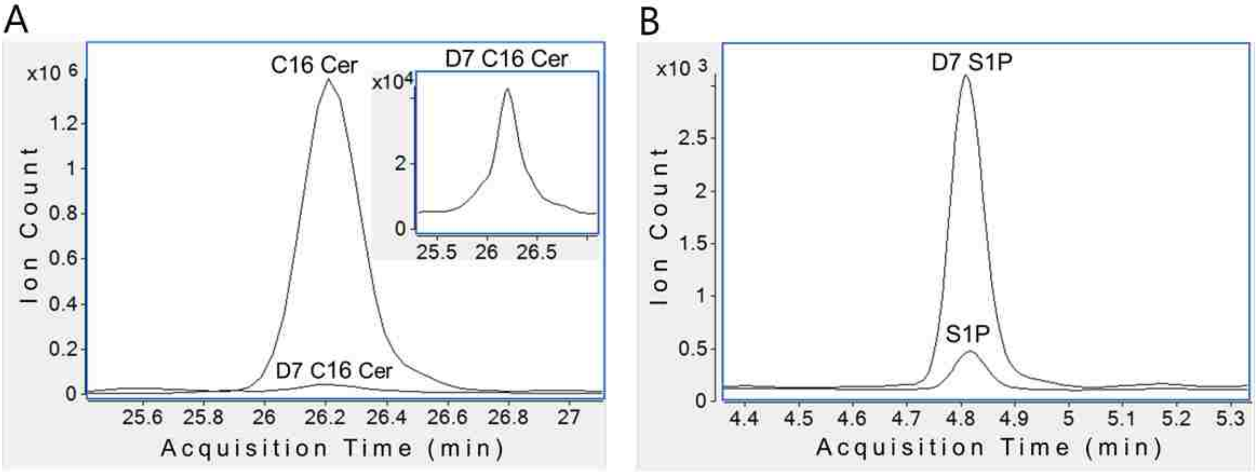

Figure 2-8 Representative elution profiles of C16 Cer, S1P, and corresponding deuterated internal standards. (A) *Representative elution profile of C16 Cer extracted from pancreatic cancer cell lysate spiked with C16 Cer-d7amide as the internal standard (inset is C16 Cer-d7 shown on a larger scale for clarity). The chromatogram shows ions for C16 Cer and C16 Cer-d7*

both eluting at 26.2 minutes. The representative chromatogram was measured by LC-MS (QTOF) in lipid extract from pA cell lysate spiked with 50 pmol of C16 Cer-d7. The normalized C16 Cer concentration was calculated using the following equation: $(50\mathrm{pmol}_{C16Cer\text{-}d7}) / (\mathrm{AUC}_{C16Cer\text{-}d7}) = (x\ \mathrm{pmol}_{C16Cer}) / (\mathrm{AUC}_{C16Cer})$*, where x = the normalized concentrations of C16 Cer. In cases where the signal:noise of the C17 Cer internal standard (not shown) was greater than C16 Cer-d7, C16 Cer was quantified by normalizing to C17 Cer instead of d7-C16 Cer.* ***(B)*** *Representative elution profile of S1P extracted from pancreatic cell lysate spiked with S1P-d7 as the internal standard. The chromatogram shows ions for S1P-d7 and S1P both eluting at 4.82 minutes. The representative chromatogram was measured by LC-MS (QqQ) in lipid extract from psn1-D (pD) cell lysate spiked with 100 pmol of S1P-d7. The area under the curve (AUC) for each compound was used to solve for S1P concentration:* $(100\mathrm{pmol}_{D7S1P}) / (\mathrm{AUC}_{D7S1P}) = (x\ \mathrm{pmol}_{S1P}) / (\mathrm{AUC}_{S1P})$*, where x = the normalized concentration of S1P.*

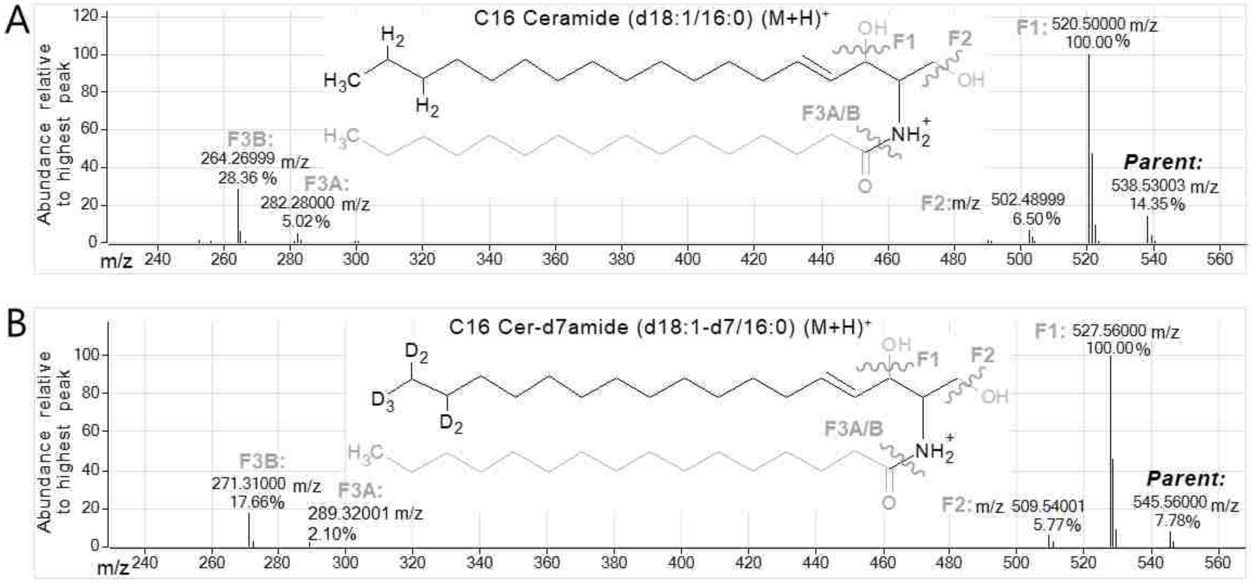

Figure 2-9 Representative MS/MS fragmentation spectra of C16 Cer and corresponding internal standard C16 Cer-d7 measured by LC-MS of pancreatic cell lipids. *Representative MS/MS spectrum of C16 Cer Parent (precursor) ion 538.53 m/z, which represents* $[C_{34}H_{67}NO_3+H]^+$*, the protonated form of C16 Cer* $(M + H)^+$ *(note: the proton can be added to multiple sites on the molecule as it is subjected to electrospray ionization, only one possibility is shown). Fragment 1 (F1) 520.5 m/z is* $[C_{34}H_{65}NO_2 + H]^+$ *which represents the parent ion with one water loss* $(M + H - H_2O)^+$*, Fragment 2 (F2) 502.5 m/z is* $[C_{34}H_{63}NO + H]^+$ *which represents the parent ion with two water losses* $(M + H - 2H_2O)^+$*, Fragment 3A (F3A) 282.28 m/z is* $[C_{18}H_{35}NO + H]^+$ *which represents the parent ion that has lost one water molecule and the C16:0 fatty acyl chain* $(M + H - H_2O$ *- fatty acyl), and Fragment 3B (F3B) 264.27 m/z is* $[C_{18}H_{33}N + H]^+$ *which represents the parent ion that has lost 2 water molecules and the acyl chain* $(M + H - 2H_2O$ *- fatty acyl).* ***(B)*** *Representative MS/MS spectrum of C16 Cer-d7 Parent ion 545.56 is* $[D_7C_{34}H_{60}NO_3 + H]^+$ *which represents the protonated form of C16 Cer-d7* $(M + H)^+$*; Fragment 1 (F1) 527.56 m/z is* $[D_7C_{34}H_{58}NO_2 + H]^+$ *which represents the parent ion with one water loss* $(M + H - H_2O)^+$*, Fragment 2 (F2) 509.54 m/z is* $[D_7C_{34}H_{56}NO + H]^+$ *which represents the parent ion with two water losses* $(M + H - 2H_2O)^+$*, Fragment 3A (F3A): 289.32 m/z is* $[D_7C_{18}H_{28}NO + H]^+$ *which represents*

the parent ion that has lost one water molecule and the C16:0 fatty acyl chain (M + H - H_2O, - fatty acyl), and Fragment 3B (F3B) 271.3 m/z is $[D_7C_{18}H_{26}N + H]^+$ which represents the parent ion that has lost 2 water molecules and the fatty acyl chain (M + H - $2H_2O$, - fatty acyl). The parent and each fragment of C16 Cer-d7 are 7 m/z units higher than the parent and corresponding fragments of C16 Cer, due to the presence of 7 deuterium atoms in place of 7 hydrogens on the 16:0 acyl tail of C16 Cer-d7. Because C16 Cer-d7 was spiked into each cell lysate prior to lipid extraction, the D7 fragmentation spectra allowed us to more accurately identify the naturally occurring C16 Cer in each cell sample. The representative spectra shown in ***(A-B)*** *were collected from psn1-A (pA) cell lysate spiked with 50pmol of C16 Cer-d7 (MS/MS Collision Energy=8). The top number in each peak label is the m/z and the bottom number is the abundance normalized to highest peak in the spectra (F1). The grayed out portions of the chemical structures represent groups that have been removed from the parent ion in each fragment and the cleavage symbols suggest where bond breakage may have occurred in succession to form the indicated fragments.*

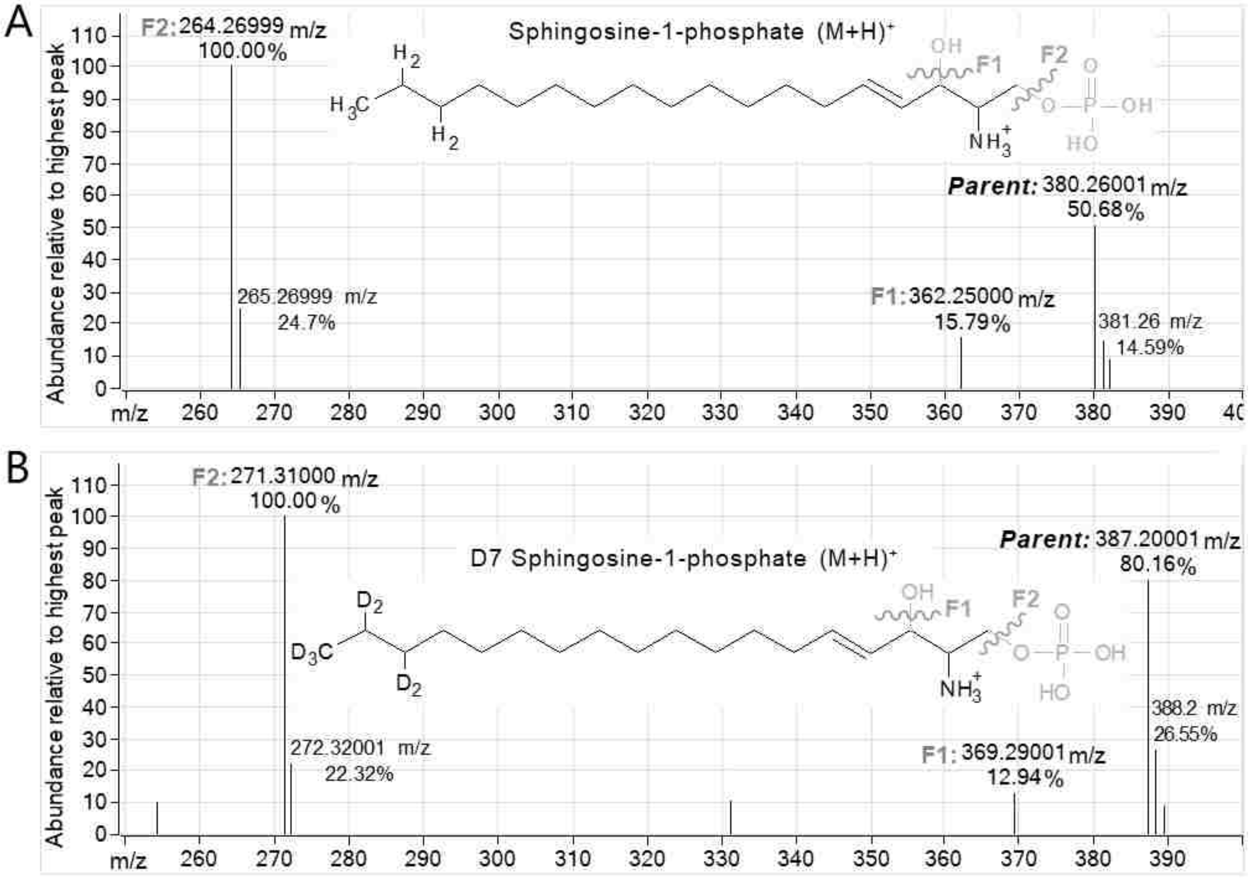

Figure 2-10 Representative MS/MS fragmentation spectra of S1P and corresponding internal standard S1P-d7 measured by LC-MS of pancreatic cell lipids. ***(A)*** *Representative MS/MS spectrum of S1P Parent (precursor) ion 380.26 m/z, which represents $[C_{18}H_{38}NO_5P + H]^+$, the protonated form of S1P $(M + H)^+$ (note: the proton can be added to multiple sites on the molecule as it is ionized in the mass spectrometer, one possibility is shown); Fragment 1 (F1) is 362.25 m/z is $[C_{18}H_{36}NO_4P + H]^+$ which represents the parent ion with a water loss $(M + H - H_2O)^+$ and Fragment 2 (F2) 264.27 m/z is $[C_{18}H_{34}N] + H]^+$ which represents the parent ion that has lost a water molecule and the phosphate group $(M + H - H2O, - phosphate)^+$.* ***(B)*** *Representative MS/MS*

spectrum of S1P-d7 Parent ion: 387.2 m/z, which is $[D_7C_{18}H_{31}NO_5P + H]^+$*, the protonated form of S1P-d7* $(M + H)^+$*, Fragment 1 (F1) 369.29 m/z is* $[D_7C_{18}H_{29}NO_4P] + H]^+$ *which represents the parent ion with a water loss* $(M + H - H2O)^+$ *and Fragment 2 (F2): 271.31 m/z is* $[D_7C_{18}H_{27}N + H]^+$ *which represents the parent ion that has lost a water molecule and the phosphate group* $(M + H - H_2O, - \text{phosphate})^+$*. Note that the parent and each fragment of S1P-d7 are 7 m/z units higher than the parent and corresponding fragments of S1P, due to the presence of the 7 deuterium atoms in place of 7 hydrogens on the acyl tail of S1P-d7. Because S1P-d7 was spiked into each cell lysate prior to lipid extraction, the D7 fragmentation spectra allowed us to more accurately identify the naturally occurring S1P in each cell-derived sample. The representative spectra were collected from psn1-A (pA) cell lysate spiked with 100pmol of S1P-d7 (MS/MS Collision Energy=8). The top number in each peak label is the respective m/z and bottom number is the abundance normalized to the highest peak in the spectra (F2). M0 and M1 isotopic peaks for the two most abundant in the spectra are also labeled (Parent and F2). The grayed out portions of the chemical structures represent groups that have been removed from the parent ion in each fragment and the cleavage symbols suggest where bond breakage successively occurred to form the indicated fragments.*

A total of 500 lipids identified across all samples (n=30) were used for quantitative lipidomic profiling after meeting our statistical criteria (see **Materials and Methods**) (**Figure 2-6C1-3; Supplemental Database K**). A wide range of lipid species were represented in this list including glycerophospholipids (32.0%), sphingolipids (30.4%), sterols (13.6%), fatty acids (12.8%), polyketides (7.2%), glycerolipids (3.2%), and prenols (0.8%) at various levels of expression across the different cell types (**Figure 2-6C1**). The heat map **(Figure 2-6C2)** and a PCA (**Figure 2-6C3**) of this analysis revealed trends similar to the shotgun lipidomics assay **(Figure 2-7A)** despite the major changes in sample preparation, LC method, and MS instrument type that were used to produce the two sets of data.

There were significant degrees of variance between the cancer subgroups, suggesting that each PSN-1 clone rerouted lipid metabolic pathways in different manners during the subculturing experiment. For example, as observed in the mRNA profiling analysis (**Figure 2-6A1-A2**), the group subjected to the most extreme diet change (pD) displayed the greatest degree of variance in lipid expression relative to the other three cancer groups on the PCA plot (**Figure 2-6C3**). The concentrations of 16% of the quantified lipids were significantly different (corrected $P<0.05$) in the pD cells relative to the other cancer groups (**Supplemental Database K**). It is interesting to note that pD cells were maintained in double the concentration of Fetal Bovine Serum (FBS; 20%) as the other groups (10%) **(Figure 2-3)** which is the main source of dietary lipids in cell culture containing high levels of cholesterol and oleic acid [132]. Among lipids that were significantly differentially expressed in the pD cells ($P<0.05$), 70% were reduced on average relative to the other cancer groups (fold change <1). This may suggest that the pD cells became dependent on the more abundant supply of dietary lipids so much so that when they were returned to the base diet for the lipidomics experiment, intracellular lipid concentrations readily dropped compared to the other subclones that were fully accustomed to 10% dietary FBS. Overall, our global lipidomics data suggests that PSN-1 cells alter global lipid metabolism in response to changes in microenvironmental resources.

Similar to what was observed in the untargeted lipidomics analysis (**Figure 2-11A**), our targeted LC-MS analysis revealed an increased S1P/C16 Cer ratio in each of the subclones (**Figure 2-12**, *blue circles*). This occurred because basal S1P concentrations were *elevated* in the cancer groups relative to the healthy control and this increase was significant in pA, pC, and pD cells ($P<0.05$) (**Figure 2-13A**, *blue circles*). In addition, C16 Cer concentrations were significantly *depleted* in pB, pC and pD cells relative to the healthy control ($P<0.05$) (**Figure 2-13B;** *blue circles*).

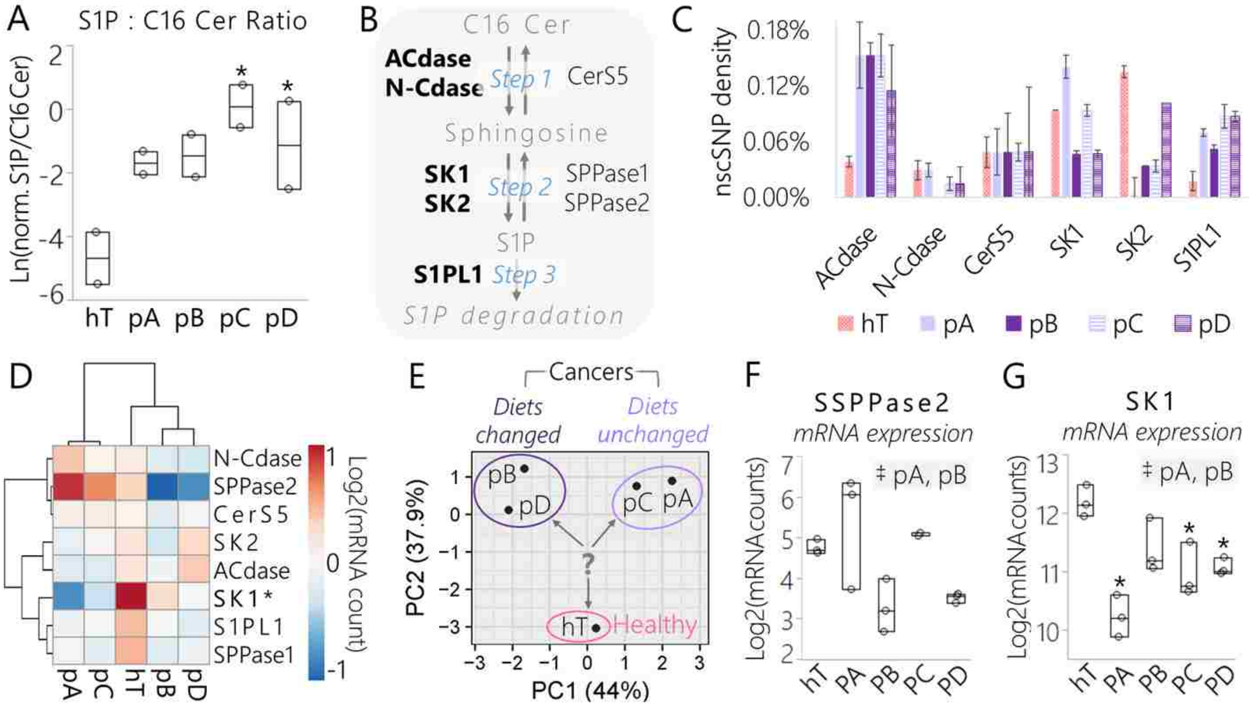

Figure 2-11 Data derived from lipidomics and RNA-Seq assays suggest a conserved shift in signaling sphingolipid metabolism in pancreatic cancer subclones relative to the healthy control driven in part by SK1. (A) *Box plot of the normalized concentration of S1P over C16 Cer measured by shotgun lipidomics assay in each cancer subclone and hT whole cell lysates. Both sphingolipids were observed within the mass accuracy cutoff in 2 biological duplicates per group and the data are represented as the log transformed ratio of the normalized (norm.) concentrations of each lipid:* $Ln[(AUC_{S1P}/AUC_{Total})/(AUC_{C16Cer}/AUC_{Total})]$. ***(B)*** *Enzymes directly involved in C16 Cer/S1P metabolism identified by RNA-Seq of cancer subclones (pA, pB, pC, pD) and hT cell lysates. Enzyme names that are* ***bolded*** *displayed nonsynonymous coding SNP(s) in one or more of the cell types.* ***(C)*** *Densities of nscSNPs detected in one or more samples from each group. Data are represented as the number of nscSNPs normalized to the corresponding mRNA transcript length in kb. Error bars represent the SEM of 3-4 biological replicates per group.* ***(D)*** *Hierarchal clustering and heat map of mRNA levels of the enzymes that participate in the S1P/C16 Cer metabolism pathway shown in panel* ***(B)*** *measured by RNA-Seq of cancer clones (pA-D) and hT cell lysates. Rows were centered; no scaling was applied to rows; both rows and columns were clustered using Hierarchal Euclidean distance metric with complete linkage. The color scale from -1 (blue) to 1 (orange) represents the mean normalized mRNA concentration of 3-4 biological replicates per group on a Log2 scale.* ***(E)*** *PCA of mRNA levels of the enzymes involved in S1P/C16 Cer metabolism shown in panel* ***(B)*** *that were detected by RNA-Seq of cancer clones and hT cell lysates. No scaling was applied to data; SVD with imputation was used to calculate principal components; X and Y axis show principal component 1 and principal component 2 that explain 44% and 37.9% of the total variance, respectively. The question mark represents the major question that arose from this analysis: which enzyme(s) were important drivers of PC2, separating the healthy control from the cancer groups?* ***(F-G)*** *Box plots of normalized* ***(F)*** *SPPase2 and* ***(G)*** *SK1 mRNA levels measured by RNA-Seq of cancer subclones and hT cells. Data are represented*

as the Log2 transformed normalized mRNA counts measured in biological triplicate or quadruplet. ***(A, F-G)*** *The * indicates $P<0.05$ with the Dunnett's Test used to compare measurements from all cancer groups to the healthy control. Tukey-Kramer Tests were used to determine significant differences between cancer subcultures; pairs that were significantly different are highlighted in the comma-separated list on the right-hand corners of each plot, where ‡ indicates $P<0.05$.*

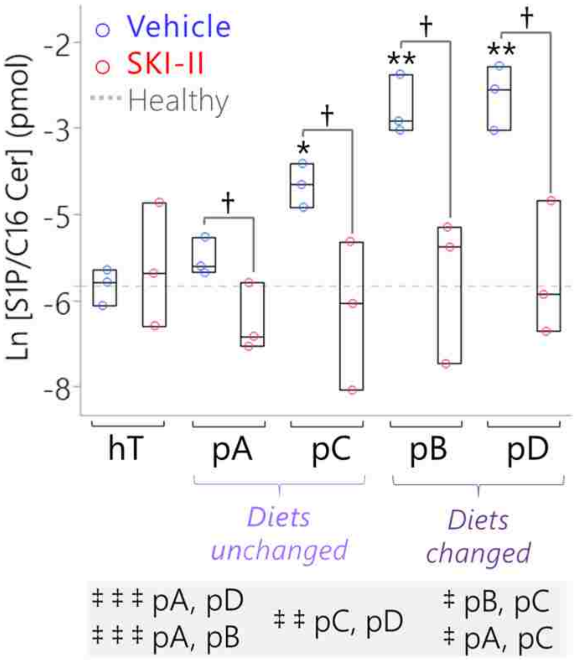

Figure 2-12 SK1 enzyme activity assay reveals SK1 as a key driver of the conserved S1P:C16 Cer imbalance in pancreatic cancer subcultures, which may be corrected by SKI-II treatment. *Box plots of S1P relative to C16 Cer concentrations measured by LC-MS of lipids extracted from pancreatic cancer subclones and hT cell lysates treated with the vehicle (1x PBS) (blue circles) versus SKI-II (13µM; red circles) for 12 hours. Both lipids were normalized to corresponding deuterated internal standards (S1P to 100 pmol of spiked S1P(d18:1-d7) and C16 Cer to 50 pmol of spiked Cer(d18:1-d7/16:0)). Data are represented as the ratio of the normalized S1P concentration (where $pmol_{S1P}/AUC_{S1P}=pmol_{S1P\text{-}d7}/AUC_{S1P\text{-}d7}$) relative to the normalized C16 Cer concentration (where $pmol_{C16Cer}/AUC_{C16Cer}=pmol_{C16Cer\text{-}d7}/AUC_{C16Cer\text{-}d7}$). The dotted gray line is the mean S1P/C16 Cer ratio of the hT Vehicle Control group, shown as a reference to represent a normal sphingolipid rheostat or the "healthy" balance between S1P and C16 Cer in non-cancerous human ductal pancreatic cells. The * indicates $P=0.002$ and ** indicates $P<0.0001$ with the Dunnett's Test used to compare the Vehicle Control groups of the cancer subclones to the healthy (hT) Vehicle Control group. The † indicates $P<0.05$ with Student's t-tests comparing each Vehicle Control group to the corresponding SKI-II-treated group of the same cell type. The Tukey-Kramer test was used to compare all of the cancer groups to one another other; pairs of groups whose baseline (Vehicle Control) ratios of S1P/C16 Cer were significantly different from each other prior to SKI-II treatment are comma-separated in the highlighted list below the plot, where ‡ ‡ ‡ indicates $P\leq0.0002$, ‡ ‡ indicates $P<0.01$, and ‡ indicates $P<0.05$.*

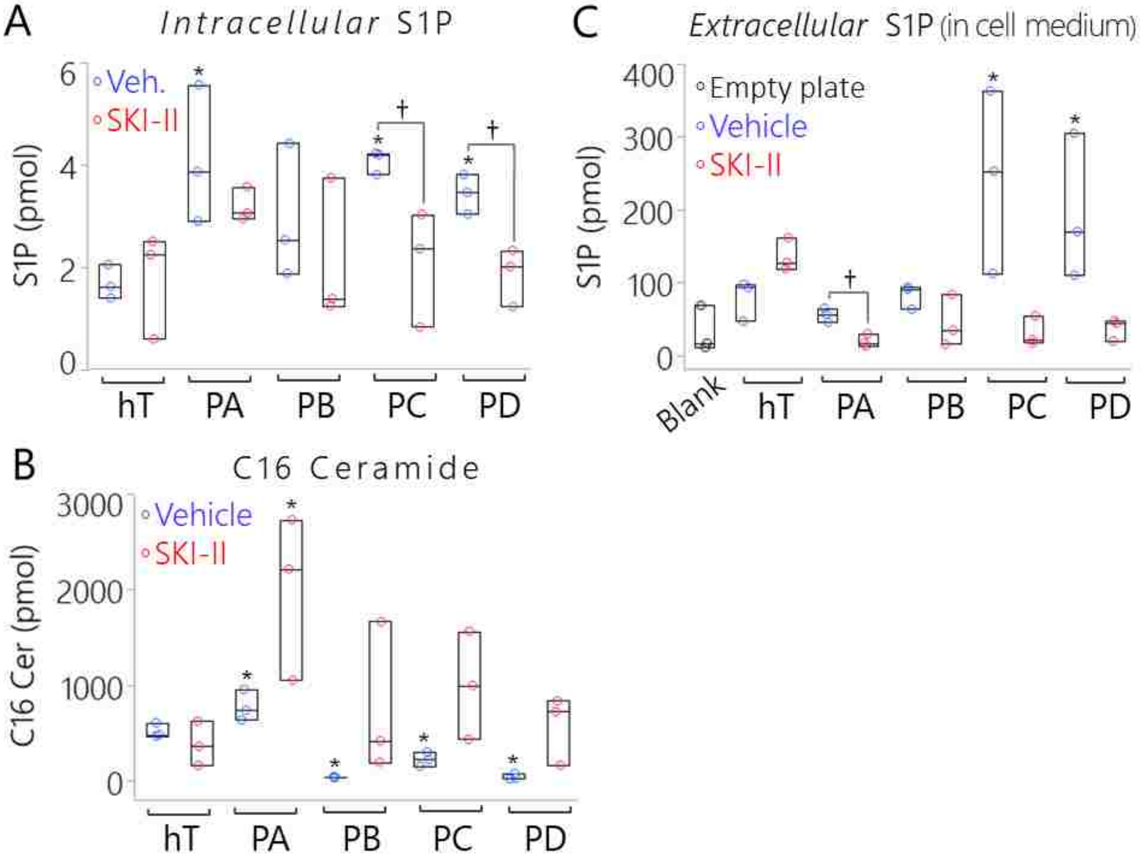

Figure 2-13 S1P and C16 Cer levels were altered in pancreatic cancer subclones relative to the healthy control but may be corrected in part by SKI-II treatment. (A,C) *Box plots of S1P concentrations measured by LC-MS of lipids extracts from* ***(A)*** *whole cell lysates and* ***(C)*** *complete cell medium from corresponding cell culture dishes after treatment with the Vehicle (1x PBS) (blue circles) or SKI-II (13µM) (red circles) for 12 hours. Note that the "Blank" in (C) represents purely FBS-derived S1P levels measured in fresh complete cell medium (RPMI 1640 + 10% FBS) that was never exposed to cell cultures.* ***(A,C)*** *Data were collected in biological triplicate and represented as the AUC of S1P normalized to the S1P-d7 internal standard.* ***(B)*** *Box plot of C16 Cer concentrations measured by LC-MS of the same samples depicted in* ***(A)****. Data are represented as the AUC of C16 Cer normalized to the C16 Cer-d7 or C17 Cer internal standard.* ***(A-C)*** *The Dunnett's Test was used to compare the lipid levels measured in the cancer groups to the healthy control under the same treatment (Vehicle or SKI-II) where * indicates $P<0.05$. Student's t-tests were used to compare the SKI-II treated group of each cell type to the respective Vehicle Control group, wherein † indicates $P<0.05$.*

Baseline C16 Cer levels were slightly, but significantly ($P<0.05$) *higher* in the pA cells compared to hTert; however, pA samples exhibited the highest basal S1P concentrations of the entire experiment, which may have helped balance signaling effects of the elevated C16 Cer levels in these cells relative to hT (**Figure 2-13A-B**, *blue circles*). Baseline S1P expression in the pB cells was not significantly higher than hTert; however, basal C16 Cer expression was lowest in the pB cells compared to all the other groups, which may have helped balance the less elevated S1P levels (**Figure 2-13A-B**, *blue circles*). The pC and pD cells displayed the highest average basal S1P levels and significantly low basal C16 Cer levels, suggesting that these groups altered S1P/C16 Cer metabolism from both ends to favor S1P production and suppress C16 Cer levels (**Figure 2-13A-B**, *blue circles*). Overall, our LC-MS method confirmed that the cancer subgroups were phenotypically distinct from one another at the level of the global lipidome. In addition, all four PSN-1 strains modified intracellular S1P and/or C16 Cer metabolite levels to some extent relative to the healthy control.

Extracellular lipid profiles of PDAC subclones mirrored the intracellular lipid profiles

If intracellular S1P is elevated, extracellular S1P levels may also be elevated [133]. The FBS in our media has high concentrations of many lipid species including S1P [68], therefore we compared the lipids extracted from growth medium samples that were exposed to cell cultures versus the fresh media as negative controls. The negative controls (blanks) were prepared by performing modified B&D extractions on fresh complete cell medium (RPMI-1640 with L-glutamine and high glucose, 10% FBS, 1x PBS) that was incubated in empty culture dishes (no cells) under the same conditions (37˚C, 5% CO_2) for the same amount of time as the cell-exposed medium samples (12 hours). There were 113 different lipid species in the resulting list of annotations that met our statistical criteria (see **Materials and Methods**) (**Supplemental Database L**) and used for a global extracellular lipid profiling (**Figure 2-6D1-D3**). A variety of lipids types were represented at different levels across the five cell types including prenols (4%), glycerolipids (6%), sphingolipids (6%), polyketides (7%), fatty acids (10%), sterols (11%), and glycerophospholipids (56%).

We used hierarchal heat map clustering and a PCA to make general comparisons between the extracellular lipid profiles of each group relative to the blank (**Figure 2-6D2-D3**). The heat map (**Figure 2-6D2**) and PCA (**Figure 2-6D3**) depicted three distinct clusters or subgroups within the dataset made up of the lipid profile(s) of (1) blanks, (2) hT cells, (3) pA, pB, and pC cells, and (3) pD cells. Above all, the heat map and PCA illustrated a considerable degree of variance between the lipid profile of the blank relative to samples exposed to cell cultures (hT, pA, pB, pC, pD) (**Figure 2-6D2-D3**). We also observed that the inter- and extracellular lipidomes of all the cell groups were correlated. Similar to the intercellular lipid profiles (**Figure 2-6C1, C3**), the pA, pB, and pC groups were more similar to each other while pD displayed the greatest degree of variance relative to the other subclones (**Figure 2-6C3**). This suggests that changes in dietary lipid levels (**Figure 2-3**) can induce adaptive lipid metabolic reprogramming that greatly affect both inter- and extracellular lipidomes, as exemplified by the pD cells (**Figure 2-6D3**).

Most importantly, this analysis provided a means to measure and compare *extracellular* S1P levels between cell types. Extracellular S1P levels from hT, pA, and pB cell cultures were slightly higher on average, but not significantly different than the S1P measured in the blank (**Figure 2-13C**, *blue circles*). On the other hand, pC and pD cells displayed significantly higher extracellular S1P concentrations compared to the blank ($P<0.05$) (**Figure 2-13C**, *blue circles*). These results suggest that S1P produced within pC and pD cells was exported at higher levels relative to the other groups, which has been shown to promote pro-survival S1P signaling in an autocrine and/paracrine fashion [67]. These results provided further evidence that each PSN-1 subclone altered lipid utilization networks in unique ways to support pro-survival S1P signaling from within and/or outside of the cell.

Pathway specific Lipidomics and RNA-Seq analyses suggest a parallel shift in S1P/C16 Cer metabolism in PDAC subclones driven by Sphingosine Kinase 1

We identified several enzymes directly involved in perturbing the S1P/C16 Cer lipid ratio by RNA-Seq, including Acid Ceramidase (ACdase), Neutral Ceramidase (N-Cdase), Ceramide Synthase 5 (Cers5), S1P Phosphatases 1 and 2 (SPPases 1 and 2), S1P Lyase 1 (S1PL1), and Sphingosine Kinases 1 and 2 (**Figure 2-11B**). Among these enzymes, there were one or more nonsynonymous coding SNPs detected in ACdase, N-Cdase, CerS5, SK1, SK2, and S1PL1 (**Supplemental Database M**). The median nscSNP densities of these five enzymes in each cell type (hT:0.043%, pA: 0.059%, pB:0.048%, pC: 0.068%, pD:0.068%) were similar to the median nscSNP densities of their corresponding genomes (hT: 0.059%, pA: 0.049%, pB:0.044%, pC: 0.043%, pD:0.039%). All four cancer groups displayed much higher SNP densities in ACdase (0.11%-0.15%), relative to ACdase enzymes in hTert (0.04%) **(Figure 2-11C**). In silico evaluations (see **Materials and Methods**) suggested two of these SNPs (C→T, G→T) in the cancer cells may have been damaging while the other three were considered benign (A→G, T→C, C→T) (**Supplemental Database M**). However, there seemed to be no major effect on ACdase expression in the cancer groups relative to hTert, since ACdase mRNA levels were not significantly different from hT in any of the cancer groups (**Figure 2-14A**).

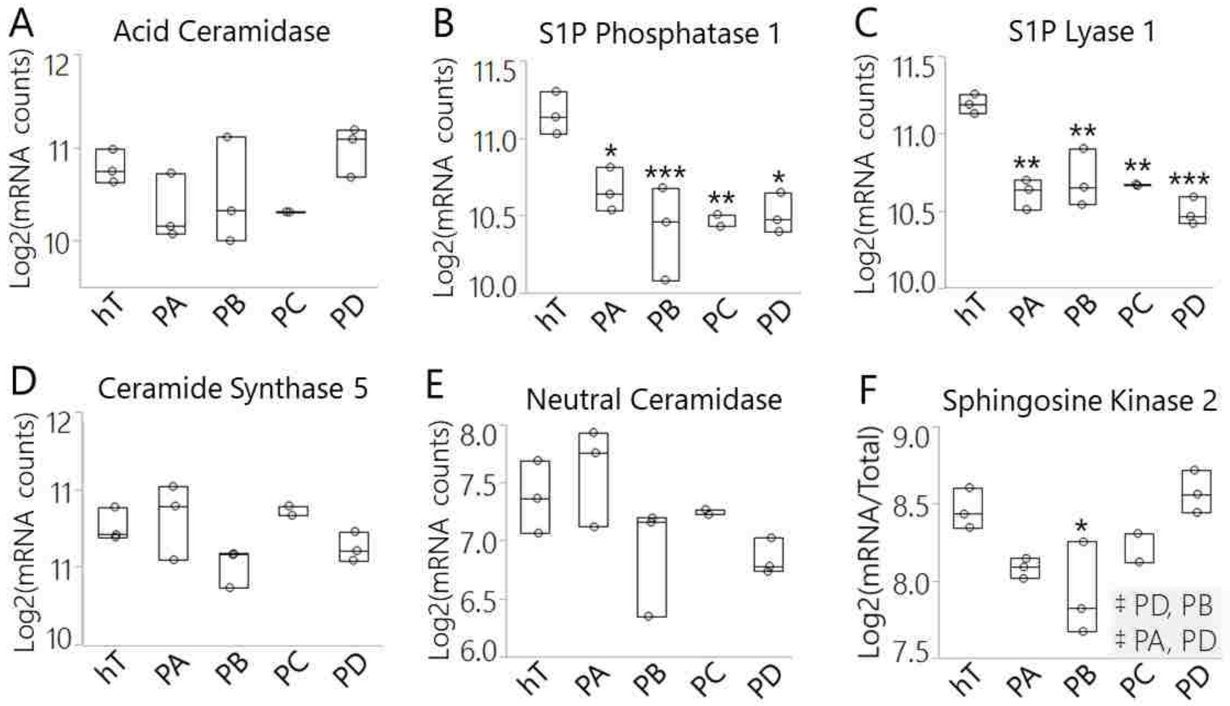

Figure 2-14 Comparison of mRNA expression of enzymes directly involved in S1P/C16 Cer metabolic pathway. (A-F) *Box plots of normalized mRNA levels of sphingolipid-modifying enzymes measured by RNA-Seq of pancreatic cancer subcultures (pA, pB, pC, pD) and healthy control cells (hT), including* ***(A)*** *Acid Ceramidase,* ***(B)*** *S1P phosphatase 1,* ***(C)*** *S1P Lyase 1,* ***(D)*** *Ceramide Synthase 5,* ***(E)*** *Neutral Ceramidase, and* ***(F)*** *Sphingosine Kinase 2.* ***(A-F)*** *Measurements were collected in biological triplicate and expressed on a Log2 scale. The Dunnett's test was used to determine differences between mRNA levels in the cancer groups relative to the healthy control; the *** indicates $P \leq 01$, ** indicates $P<0.001$, and * indicates $P<0.05$. Tukey-Kramer Tests were used to determine significant differences between cancer subcultures; pairs that were significantly different are highlighted in the comma-separated list on the right-hand corner of* ***(F)****, where ‡ indicates $P<0.05$.*

One potentially significant polymorphism seen in this analysis was an L→P polymorphism repeatedly detected in position 237 of SK1 isoform 2 (SK1-2) [134] in pA cells (**Supplemental Database M**). Residue 273 in SK1-2 is the equivalent of 187L in SK1-1, which is involved in an alpha helix in the C4 region of the C-terminal domain next to the sphingosine binding pocket [119]. The 273L→P polymorphism detected in the pA cells was predicted to be damaging. This prediction is appropriate since switching from a more flexible leucine to an inflexible proline would break the helix, potentially affecting binding or substrate affinity to the proximal sphingosine binding site. While the SNP analysis provided some evidence that pA was biochemically reprogrammed in slightly different ways with respect to the pathway of interest, it did not provide any significant evidence of genetic forces driving the major shift S1P/C16 observed across the four cancer groups relative to hTert.

We looked further into our RNA-Seq data to determine whether SK1 or any of the other sphingolipid metabolic enzymes were transcribed differently in the cancer groups relative to the healthy control. The normalized mRNA levels of the 8 sphingosine metabolic enzymes were compared on a heat map (**Figure 2-7D**) and PCA plot (**Figure 2-7E**). According to the heat map, SPPase2 and SK1 mRNA levels appeared to be most altered relative to the other 6 enzymes (**Figure 2-7D**). Interestingly, these two enzymes catalyze opposite reactions in the C16 Cer/S1P metabolic pathway; SPPase2 dephosphorylates S1P to form sphingosine whereas SK1 phosphorylates sphingosine to form S1P (**Figure 2-7B**). We hence predicted that *Step 2* (**Figure 2-7B**), wherein sphingosine was either phosphorylated or dephosphorylated, was a critical point of control in the S1P/C16 Cer metabolic pathway with respect to driving differences between the healthy and cancer cells. We used the Dunnett's test to determine significant differences in mRNA levels of each enzyme between cancer and hT cells (**Figures 2-7F-G, Figure 2-14**). There were no clear trends in SPPase2 mRNA levels among the cancer groups or significant differences relative to the healthy control (**Figure 2-7F**). On the other hand, SK1 mRNA levels were depleted in all four cancer groups relative to hTert and this difference was significant ($P<0.05$) in all but the pB cells (**Figure 2-7G**). This suggested that SK1 may be regulated differently in the PSN-1 clones relative to healthy and perhaps be linked with the shift from healthy to cancerous sphingolipid metabolism.

The PCA of [mRNA] depicted clear separations between the healthy and cancer cells as well as between cancer subclones whose diets were changed (pB, pD) versus unchanged (pA, pC) (**Figure 2-7E**). We hypothesized that SK1 plays an important role in differentiating the "healthy" phenotypes exhibited by hTert from the cancer groups by playing a key role relative to other sphingolipid modifying enzymes in regulating S1P/C16 Cer metabolism. We also anticipated that each cancer group may achieve a modified S1P/C16 Cer axis to promote clonal survival in different ways, especially since there were variations in sphingolipid enzyme expression between cancer groups subjected to different metabolic pressures (**Figure 2-7**; **Figure 2-14**).

SK1 activity is modulated by different combinations of concentration and MAPK1-mediated phospho-activation in pancreatic cancer subclones

Because SK1 was not detected in our global proteomics analysis, we used Western blotting to measure SK1 protein expression levels in each cell group (**Figure 2-15A**). SK1 concentrations varied greatly among the cancer groups, supporting our hypothesis that the different PSN-1 subclones may have used SK1 to dysregulate S1P/C16 Cer metabolism. Unlike SK1 mRNA, the average SK1 protein concentration was higher in all the cancer groups relative to hTert; this difference was significant in the pA ($P<0.0001$), pB ($P<0.0001$), and pC ($P<0.05$) cells (**Figure 2-15A**). These results suggest that SK1 protein expression was increased to some degree to promote S1P synthesis in each PDAC subclone compared to the healthy control.

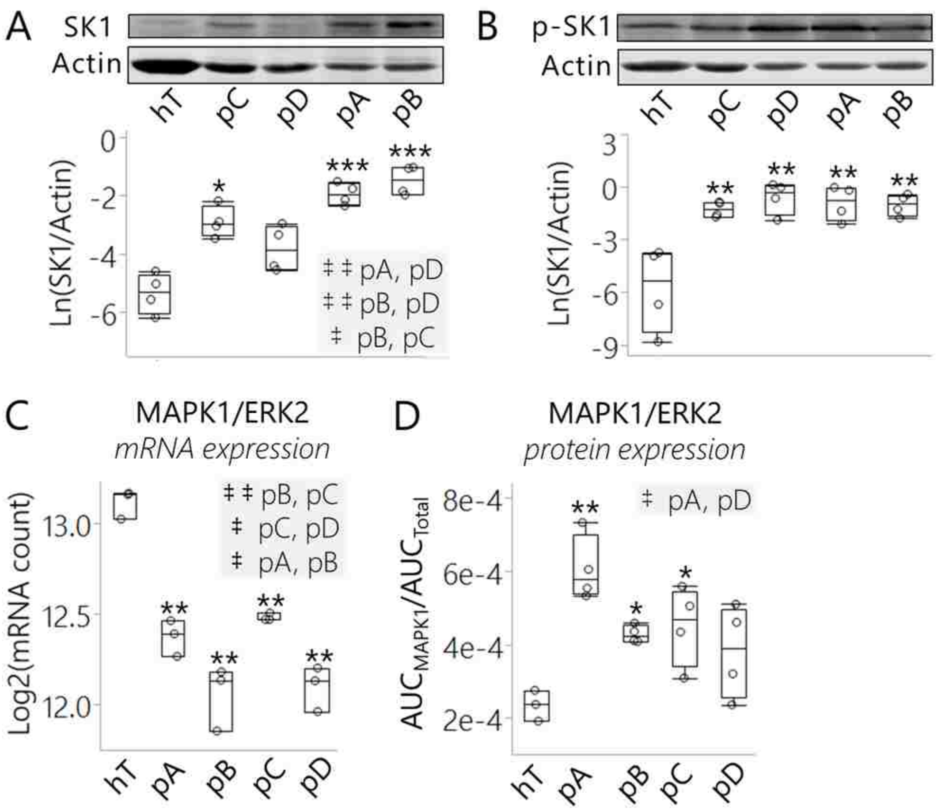

Figure 2-15 SK1 expression and/or ERK2-mediated phosphorylation was increased in pancreatic cancer subclones relative to healthy control cells. (A-B) *Representative Western blots and relative concentrations of* ***(A)*** *total SK1 and* ***(B)*** *phosphor-activated SK1 enzymes (p-SK1) in cancer subclones and hT cells lysates. Western blots were performed in biological quadruplet and actin was used for loading controls. Quantitation of each replicate is represented as* ***(A)*** *Ln(SK1/Actin) and* ***(B)*** *Ln(p-SK1/Actin) in the box plots below the respective representative Western blots****. (A-B)*** *The *** indicates $P<0.0001$, ** indicates $P<0.001$, and * indicates $P<0.05$ with the Dunnett's Test used to compare all cancer groups to the healthy control (hT). Tukey-Kramer Tests were used to determine significant differences between cancer groups; pairs that were significantly different are highlighted in the comma-separated lists on the right-hand corner of* ***(A)****, where ‡ ‡ indicates $P<0.005$ and ‡ indicates $P<0.05$.* ***(C)*** *Box plot of normalized mRNA levels of MAPK1/ERK2 in cancer subcultures and hT cells measured by RNA-Seq. Measurements were collected in biological triplicate and represented on a Log2 scale.* ***(D)*** *Box plot of normalized MAPK1 protein concentrations measured by quantitative proteomics of cancer subcultures and hT whole cell lysates. Data are represented as the mean normalized MAPK1/ERK2 protein concentration (AUC_{MAPK1}/AUC_{Total}) of 3-4 biological replicates per group.* ***(C-D)*** *The Dunnett's Test was used to compare the cancer groups to the healthy control (hT), wherein ** indicates $P\leq0.0003$ and * indicates $P<0.05$. Tukey-Kramer Tests were used to determine which cancer groups differed from each other; pairs that were significantly different are highlighted in the comma-separated lists on the top right-hand corner of each plot, where ‡ ‡ indicates $P<0.01$ and ‡ indicates $P<0.05$.*

The results of our SK1 Western blots led us to question why SK1 *protein* expression (**Figure 2-15A**) seemed to be in the opposite direction of SK1 *mRNA* expression **(Figure 2-7G**) in the cancer groups relative to hTert. Indeed, we saw that SK1 mRNA levels were depleted while SK1 protein levels were increased. This may indicate that SK1 translation was post-transcriptionally elevated. In contrast to SK1, *both* mRNA and protein levels of Beta-actin (**Figure 2-16A1-A2**) and Gamma-actin (**Figure 2-16B1-B2**) in the four cancer groups were depleted relative to hTert. This suggests that, unlike SK1, cytoplasmic actin proteins were *transcriptionally* regulated in the PDAC cells. We also checked another cancer-promoting lipid modifying enzyme, fatty acid synthase (FASN), for which we had both RNA-Seq and protein quantitation data from our proteomics analysis. Both FASN mRNA and protein levels have been shown to be overexpressed in most human cancers including PDAC, making FASN an important biomarker of the disease [135]. Consistent with other research [16,103,135] both the mRNA and protein expression levels of FASN were significantly increased in the PDAC cells relative to the healthy control (P<0.01) (**Figure 2-17A-B**). Based on these results we proposed that SK1 protein expression, as opposed to other differentially expressed species in the cancer groups like actin and FASN, was post-transcriptionally increased in the PDAC subclones relative to hTert cells.

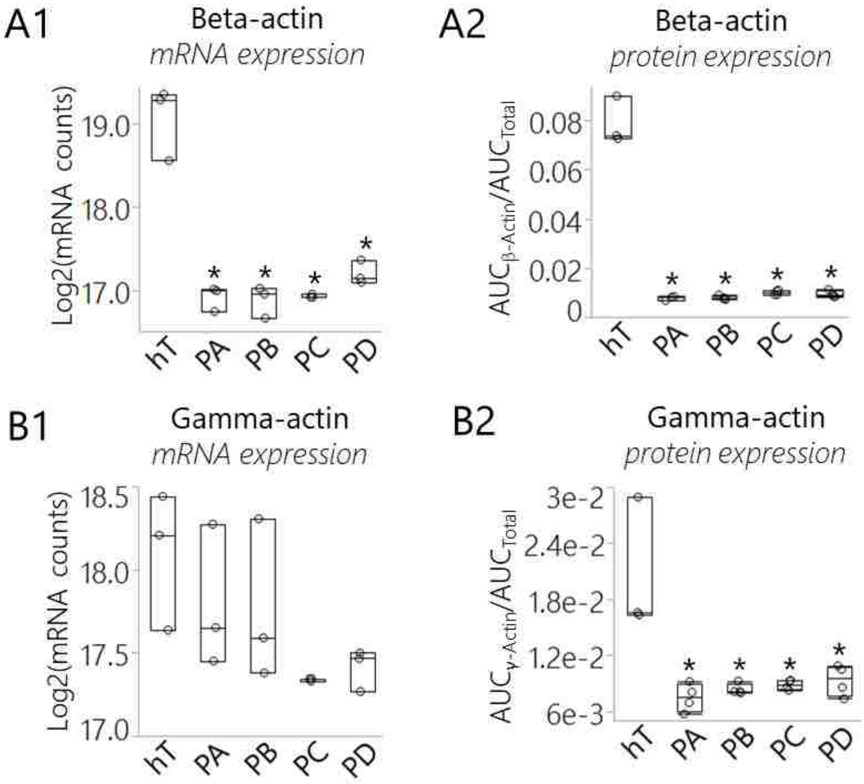

Figure 2-16 Cytoplasmic actin mRNA and protein levels were reduced in pancreatic cancer subclones relative to the healthy control. (A1, B1) *Box plots of mRNA expression levels of* ***(A1)*** *Cytoplasmic Actin 1 (Beta-actin) and* ***(B1)*** *Cytoplasmic Actin 2 (Gamma-actin) measured in biological triplicate in pancreatic cancer subclones (pA, pB, pC, pD) and healthy control cells. Data are represented as the normalized mRNA counts on a Log2 scale.* ***(A2, B2)*** *Box plots of normalized protein concentrations of* ***(A2)*** *Cytoplasmic Actin 1 (Beta-actin) and* ***(B2)*** *Cytoplasmic Actin 2 (Gamma-actin) measured in biological triplicate (hT) or quadruplet (pA-pD).* ***(A2, B2)*** *Data are represented as the mean normalized protein concentration in each sample measured in biological triplicate. The Dunnett's Test was used to compare the cancer cell groups to the healthy control; the * indicates p<01. Based on the Tukey-Kramer Test, there were no significant differences between mRNA or protein levels of actin measured in the cancer groups.*

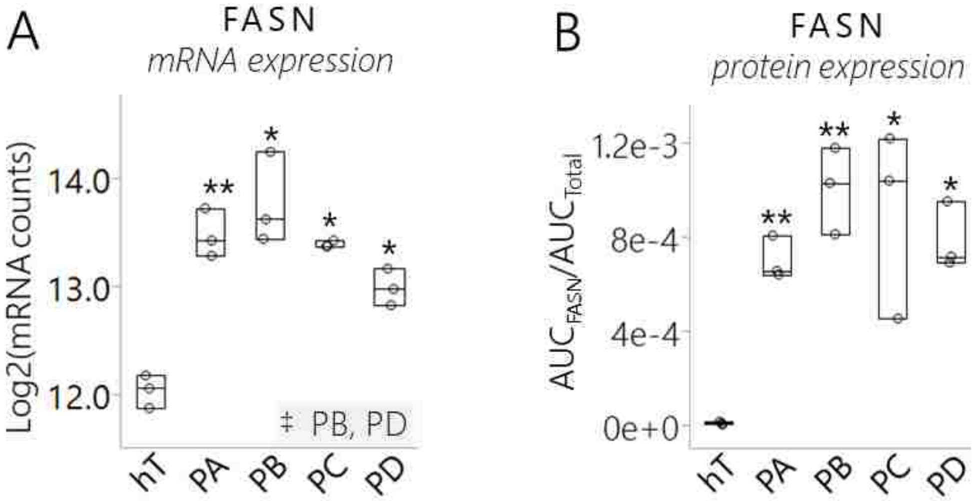

Figure 2-17 Fatty Acid Synthase mRNA and protein levels were increased in pancreatic cancer subclones relative to the healthy control. (A-B) *Box plots of* ***(A)*** *mRNA and* ***(B)*** *protein levels of Fatty Acid Synthase (FASN) measured in pancreatic cancer cell groups and the healthy control.* ***(A)*** *Data are represented as the normalized mRNA counts measured in biological triplicate in each cell type.* ***(B)*** *Data are represented as the normalized protein concentration measured in biological triplicate.* ***(A-B)*** *The Dunnett's Test was used to compare the cancer cell groups to the healthy control, where ** indicates $P<0.01$ and * indicates $p \leq 0.002$. Tukey-Kramer Tests were used to determine significant differences between the cancer groups; the pair found to be significantly different is highlighted in the right-hand corner of (A), where † indicates $P<0.05$.*

To compare activation levels of SK1 enzyme in the five cell groups, we used a phospho-SK1 (Ser225) polyclonal antibody to detect endogenous SK1 phosphorylation (**Figure 2-15B**). All cancer groups displayed a significant increase in the amount of phosphorylated SK1 relative to hTert ($P<0.001$) (**Figure 2-15B**). The pA and pB cells exhibited the highest SK1 levels as well as increased SK1 phospho-activation relative to hTert; the pC cells displayed a smaller but significant increase in SK1 expression and phosphorylation compared to hTert; in contrast, total SK1 expression was not significantly increased but the median p-SK1 concentration was highest in the pD cells relative to hTert (**Figure 2-15A-B**). This suggests the perturbed S1P/C16 Cer ratio observed across PDAC subclones (**Figure 2-11A**) was achieved in unique ways by modulating SK1 concentration and activation in each subclone. Overall, the results of our Western blots indicate that overactive SK1 may be required to maintain sphingolipid metabolic reprogramming and/or signaling in PDAC cells.

The high p-SK1 levels we observed in the cancer groups may be due to increased expression of the SK1 activating kinase, MAPK1/ERK2 (**Figure 2-15C-D**). ERK1/2 are key components of the pro-proliferative Ras/MAPK signaling pathway that is hyperactivated in many human cancers [136]. Both MAPK1 and MAPK2 (ERK1/2) activate SK1 via phosphorylation at Ser225 [133]. Although very similar in structure, ERK2 has much higher activating efficiency for human SK1 than ERK1 [133]. ERK2 was detected in all five cell groups in our RNA-Seq and proteomics analyses. These assays suggest that like SK1, ERK2 protein expression was post-transcriptionally increased in the cancer groups relative to hTert (**Figure 2-15C-D**). ERK2 mRNA expression was significantly reduced in all four cancer groups at different degrees relative to hTert ($P<0.001$) (**Figure 2-15C**). However, ERK2 protein expression was *elevated* in all the cancer groups relative to hTert and this increase was significant in pA ($P<0.001$), pB ($P<0.05$), and pC ($P<0.05$) cells (**Figure 2-15D**).

Increased p-SK1 levels (**Figure 2-15B**) may be attributed in part to this increase in the expression of its high-affinity activating kinase (ERK2) in the cancer cells relative to hTert (**Figure 2-15D**). Because protein synthesis is energetically costly, cancer cells under microenvironmental or metabolic stress can limit translation to a specific subset of mRNA’s that code proteins best suited to support survival and disease progression [136]. Based on these results, we believe that SK1 and ERK2 were among this subset of preferred mRNA molecules to promote S1P synthesis, S1P mediated pro-survival signaling, and other cancerous phenotypes in the PDAC cell groups.

SK1 inhibition effectively normalized S1P/C16 Cer levels in distinct PDAC subclones

We developed a sphingolipid targeted LC-MS based assay to quantify the specific enzyme activity of SK1 and the effects of SK1 inhibition on S1P/C16 Cer metabolism. We used this assay to assess the effect of Sphingosine Kinase Inhibitor 2 (SKI-II, 4-[[4-(4-Chlorophenyl)-2-thiazolyl]amino]phenol) a non-lipid compound displaying selective, non-ATP competitive inhibition of human SK1 [137]. Average S1P concentrations were higher in the vehicle controls of all the cancer groups relative to hTert and this difference was significant in pA ($P<0.05$), pC ($P<0.05$), and pD ($P<0.05$) cells (**Figure 2-13A**).

SKI-II treatment reduced average intracellular S1P levels in all four cancer groups relative to their corresponding vehicle controls (**Figure 2-13A**) and normalized intracellular S1P levels in all the cancer groups relative to the healthy control (**Figure 2-13A**). On the other hand, SKI-II had virtually no effect on intracellular S1P concentrations in hTert cells (**Figure 2-13A**). This suggests that SK1-mediated S1P production was initially higher in the cancer groups, but SKI-II effectively suppressed hyperactive levels of SK1 mediated S1P synthesis. This change in SK1 activity also reduced average *extracellular* S1P levels in all of the cancer groups, though this decrease was only significant in pA cells ($P<0.05$) (**Figure 2-13C**). Moreover, SKI-II treatment normalized extracellular S1P levels in the two cancer groups whose baseline extracellular S1P concentrations were significantly higher than the blank ($P<0.05$), i.e. pC and pD cells (**Figure 2-13C**). Alternatively, SKI-II treatment led to an increase in intracellular C16 Cer levels in all of the cancer cell samples relative to the corresponding vehicle controls, though this difference was only statistically significant in pA cells ($P<0.05$) (**Figure 2-9B**). This suggests that the decrease in SK1 driven S1P production from ceramide precursors allowed C16 Cer concentrations to increase in cells treated with SKI-II.

The ratio of endogenous S1P/C16 Cer is considered a key metric of the sphingolipid rheostat, thereby serving as a critical biosensor for predicting cell fate and drug sensitivity due to competing cell signaling [19,65,66,115,138]. On average, the ratio of S1P to C16 Cer was higher in all the cancer vehicle control groups relative to hTert; this increase was significant in pB ($P<0.00001$), pC ($P<0.005$), and pD ($P<0.00001$) cells (**Figure 2-12**). This indicates that the sphingolipid rheostat was perturbed in all of the cancer subclones, favoring S1P relative to C16 Cer. Note that this perturbation was displayed in significantly different degrees between different subclones (**Figure 2-12**). Baseline S1P/C16 Cer in the pB and pD vehicle control groups were significantly higher than pA and pC vehicle controls ($P<0.01$) (**Figure 2-12**). This further supports that each PSN-1 subclone adapted different ways to maintain an imbalance in sphingolipid metabolism to promote pro-survival S1P levels relative to pro-apoptotic C16 Cer.

Despite the wide variations in basal C16 Cer and S1P levels, SKI-II significantly reduced the S1P/C16 Cer ratio in all of the cancer groups relative to their respective vehicle controls ($P<0.05$) (**Figure 2-12**). Importantly, SKI-II treatment effectively normalized the average S1P/C16 Cer ratio in groups whose basal S1P/C16 Cer ratios were significantly higher than the healthy control (pB, pC, pD) (**Figure 2-12**). Overall, these results indicate that SK1 plays a significant role in regulating the perturbed sphingolipid rheostat in differentially evolved PDAC cells but may be corrected by SKI-II treatment. Next, we sought to determine whether this increase in S1P/C16 Cer in the PDAC clones contributed to cancerous phenotypes including rapid proliferation rates and resistance to apoptosis inducing drugs.

Selective inhibition of SK1 reduced PDAC cell proliferation in a dose-dependent manner

We performed a live-cell confluence assay to generate growth curves of each cell type and measure the effects of SK1 activity on PDAC cell proliferation (**Figure 2-18A-C; Figure 2-19A-E**). Cells were treated with a low (4.3µM), medium (13µM) or high (39µM) dose of SKI-II and compared to corresponding vehicle (1x PBS) controls (**Figure 2-18A-C; Figure 2-19A-E**). The vehicle control groups of all four PSN-1 subclones displayed rapid average basal growth rates, ~1.5 times faster than the healthy control (**Figure 2-18C**). The pB cells exhibited the highest average basal growth rate (1.12% confluence per hour), followed by pA (1.08% confluence per hour), pC (1.05% confluence per hour), pD (1.04% confluence per hour), and finally hTert (0.72% confluence per hour). SKI-II mediated inhibition of SK1 significantly reduced proliferation rates of all four cancer groups ($P<0.05$) in a dose-dependent manner (**Figure 2-18C**). SKI-II also reduced the average hTert cell growth rate in a dose-dependent manner though this was only statistically significant at the highest dose of SKI-II (39µM) (**Figure 2-18B-C**).

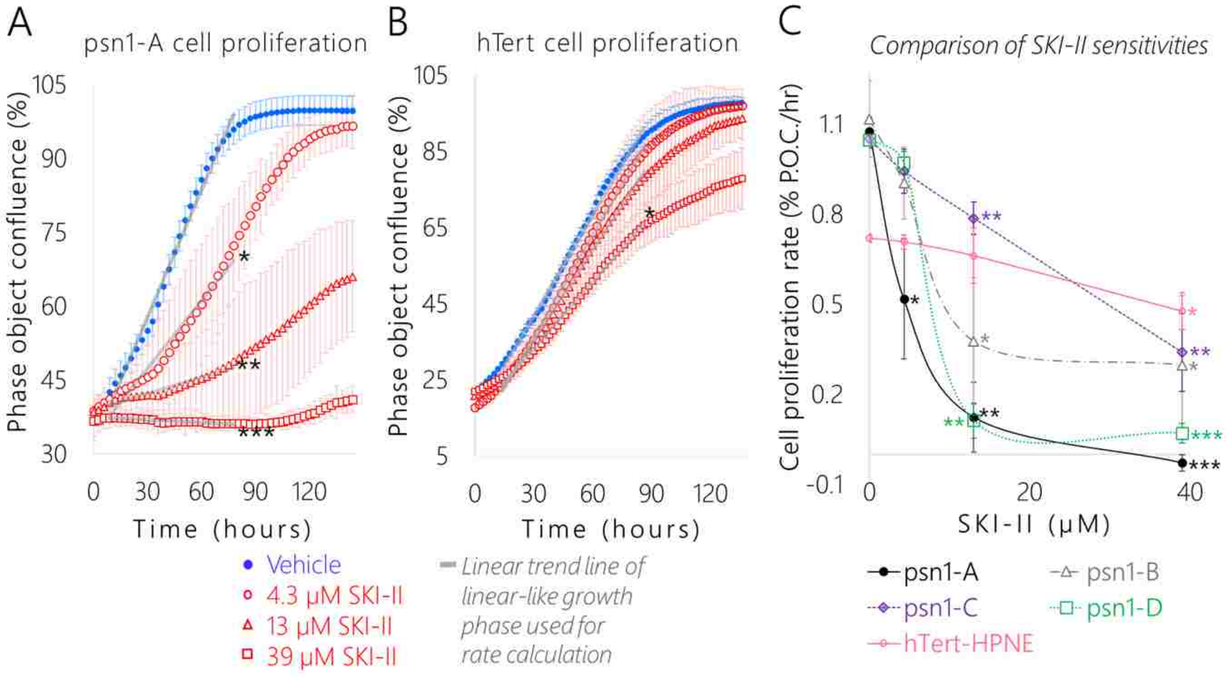

Figure 2-18 SK1 inhibition significantly slowed pancreatic cancer cell proliferation relative to the healthy control and each cancer subclones displayed a distinct level of dose-dependent SKI-II sensitivity. *Representative cell growth curves of* ***(A)*** *pA and* ***(B)*** *hT cells treated with Vehicle (1x PBS, blue dots) and the following concentrations of SKI-II: 4.3µM (red circles), 13µM (red triangles), and 39µM (red squares).* ***(A-B)*** *Data are represented as the mean phase object confluence +/- SEM of four biological replicates per group over time in hours. The gray lines are the linear trend lines of a portion of the linear-like growth period shown to illustrate how the proliferation rates for each cell group/condition were calculated.* ***(C)*** *Comparison of proliferation rates and sensitivity to increasing concentrations of SKI-II in pA (black dots), pB (gray triangles), pC (purple diamonds), pD (green squares), and hT (pink circles) cells. Growth rates were determined by calculating the slope of the linear-like growth phase of each group, where x=time (hours) and y=percent phase object confluence (% P.O.C.). Data are represented as the mean proliferation rate +/- SEM of four biological replicates per group plotted against the SKI-II concentration in µM.* ***(A-C)*** *Student's t-tests were used to compare the proliferation rates of individual cell types treated with each concentration of SKI-II to the respective Vehicle Control group of the same cell type, where *** indicates P<0.00001, ** indicates P<0.005, and * indicates P<0.05.*

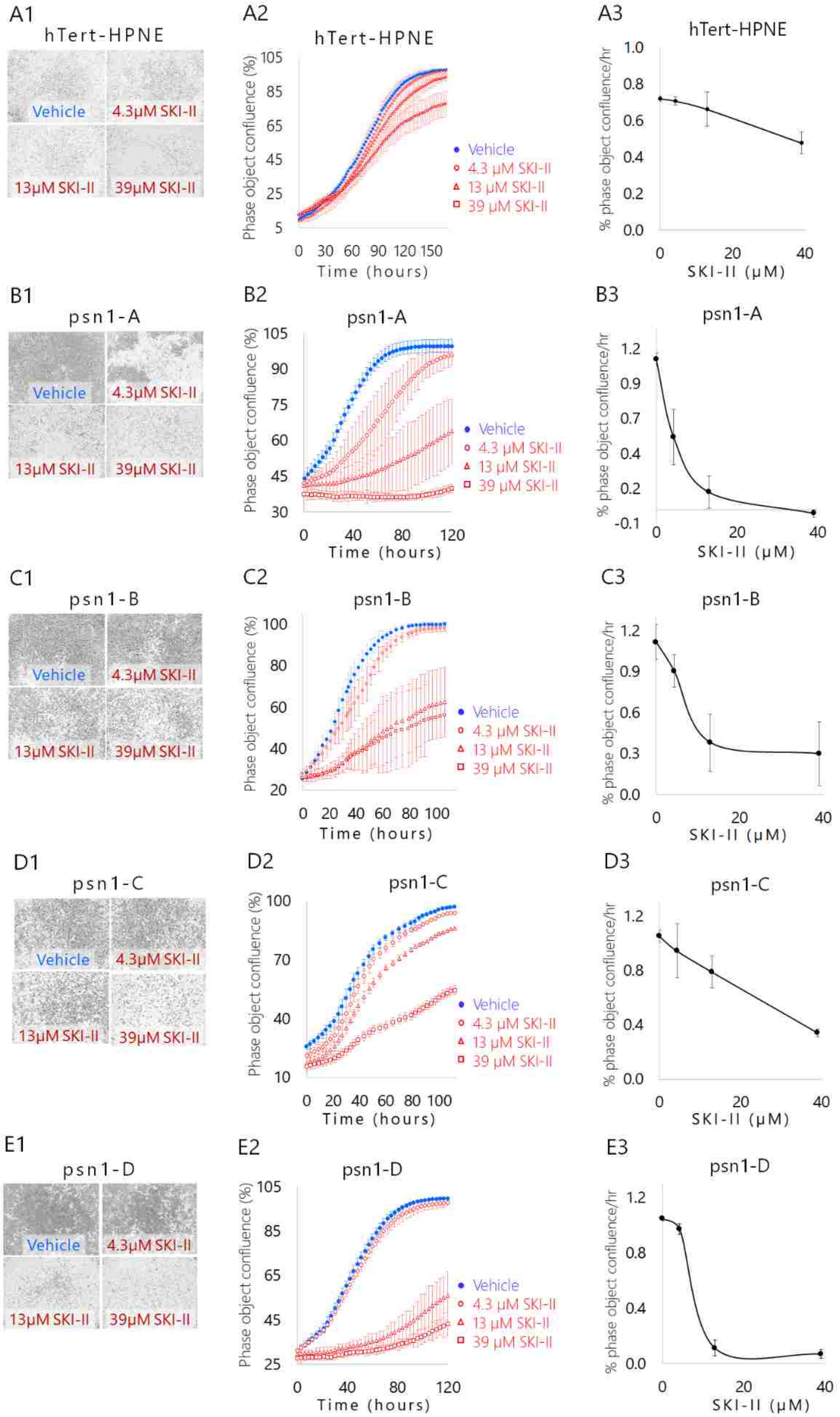
A1
hTert-HPNE
Vehicle
4.3μM SKI-II
13μM SKI-II
39μM SKI-II
A2
hTert-HPNE
Phase object confluence (%)
105
85
65
45
25
5
0 30 60 90 120 150
Time (hours)
Vehicle
4.3 μM SKI-II
13 μM SKI-II
39 μM SKI-II
A3
hTert-HPNE
% phase object confluence/hr
1.0
0.8
0.6
0.4
0.2
0.0
0 20 40
SKI-II (μM)
B1
psn1-A
Vehicle
4.3μM SKI-II
13μM SKI-II
39μM SKI-II
B2
psn1-A
Phase object confluence (%)
105
90
75
60
45
30
0 40 80 120
Time (hours)
Vehicle
4.3 μM SKI-II
13 μM SKI-II
39 μM SKI-II
B3
psn1-A
% phase object confluence/hr
1.2
0.9
0.7
0.4
0.2
-0.1
0 20 40
SKI-II (μM)
C1
psn1-B
Vehicle
4.3μM SKI-II
13μM SKI-II
39μM SKI-II
C2
psn1-B
Phase object confluence (%)
100
80
60
40
20
0 20 40 60 80 100
Time (hours)
Vehicle
4.3 μM SKI-II
13 μM SKI-II
39 μM SKI-II
C3
psn1-B
% phase object confluence/hr
1.2
0.9
0.6
0.3
0.0
0 20 40
SKI-II (μM)
D1
psn1-C
Vehicle
4.3μM SKI-II
13μM SKI-II
39μM SKI-II
D2
psn1-C
Phase object confluence (%)
100
70
40
10
0 20 40 60 80 100
Time (hours)
Vehicle
4.3 μM SKI-II
13 μM SKI-II
39 μM SKI-II
D3
psn1-C
% phase object confluence/hr
1.2
0.8
0.4
0.0
0 20 40
SKI-II (μM)
E1
psn1-D
Vehicle
4.3μM SKI-II
13μM SKI-II
39μM SKI-II
E2
psn1-D
Phase object confluence (%)
105
85
65
45
25
0 40 80 120
Time (hours)
Vehicle
4.3 μM SKI-II
13 μM SKI-II
39 μM SKI-II
E3
psn1-D
% phase object confluence/hr
1.2
0.8
0.4
0.0
0 20 40
SKI-II (μM)

Figure 2-19 Results of growth experiments of pancreatic cancer subclones and healthy control cells treated with increasing concentrations of SKI-II. (A1, B1, C1, D1, E1) *Representative confluence images of* ***(A1)*** *hT,* ***(B1)*** *pA,* ***(C1),*** *pB,* ***(D1)*** *pC, and* ***(E1)*** *pD cells after 72 hours of treatment with the Vehicle (1x PBS) (top left), 4.3 µM SKI-II (top right), 13 µM SKI-II (bottom left), and 39 µM SKI-II (bottom right).* ***(A-E)*** *Representative growth curves of* ***(A2)*** *hT,* ***(B2)*** *pA,* ***(C2),*** *pB,* ***(D2)*** *pC, and* ***(E2)*** *pD cells during treatment with the Vehicle (blue points), 4.3 µM SKI-II (red circles), 13 µM SKI-II (red triangles), and 39 µM SKI-II (red squares).* ***(A2, B2, C2, D2, E2)*** *Data are represented as the mean phase object confluence +/- SEM of four biological replicates over time (hours).* ***(A3, B3, C3, D3, E3)*** *Dose-dependent effects of SKI-II on the growth rates of* ***(A3)*** *hT,* ***(B3)*** *pA,* ***(C3),*** *pB,* ***(D3)*** *pC, and* ***(E3)*** *pD cells. Growth rates were determined by calculating the slope of the linear-like growth phase of each cell type, where x = time (hours) and y = percent phase object confluence. Data are represented as the mean proliferation rate +/- SEM of four biological replicates per group plotted against the SKI-II concentration used to treat each sample (µM).*

Each cancer subclone displayed different levels of sensitivity to SKI-II treatment (**Figure 2-18C**). The pC cells seemed to be less sensitive to SKI-II; pC cells displayed the lowest average change in growth rate in response to the medium (13µM) and high (39µM) SKI-II doses compared to the other three cancer groups (**Figure 2-18C**). On the other hand, the pA cells were significantly more sensitive to SKI-II treatment relative to the other cancer subclones. Although the average proliferation rates of all four cancer groups dropped in response to the lowest dose of SKI-II (4.3µM), this drop was only statistically significant in the pA cells ($P<0.05$) (**Figure 2-18A, C**). In addition, the pA cells exhibited the greatest drop in proliferation in response to the high SKI-II dose (39µM) ($P<0.00001$) relative to the other cell types (**Figure 2-18C**). This increased sensitivity may be due to the lower basal S1P/C16 Cer ratio displayed in the pA cells relative to the other cancer groups (**Figure 2-12**); a less extreme level of basal pro-proliferative S1P relative to C16 Cer may have made it so a lower concentration of SK1 inhibitor was sufficient to restore the healthy “hTert-like” balance in the sphingolipid rheostat in the pA cells compared to the other cancer groups whose S1P/C16 Cer ratios were significantly higher

($P<0.05$) (**Figure 2-12**). This suggests that the cancer subclones adapted different levels of dependence on SK1 mediated S1P synthesis to support proliferation rates.

Treating with SKI-II was sufficient to either normalize or significantly lower the growth rates of all four PSN-1 clones relative to hT (**Figure 2-18C**). Indeed, just 4.3μM SKI-II was sufficient to normalize pA cell proliferation (0.52 +/- 0.1% confluence per hour) to the rate of the hT vehicle control (0.72 +/- 0.01% confluence per hour) (**Figure 2-18C**). The medium SKI-II dose (13μM) was sufficient to significantly lower pB cell proliferation (0.38 +/- 0.2% confluence per hour) and pD cell proliferation (0.11 +/- 0.06% confluence per hour) relative to rate of the hT vehicle control (0.72 +/- 0.01% confluence per hour) (**Figure 2-18C**). Even for the pC cells which seemed to be the most resistant to SKI-II treatment, the medium SKI-II dose (13μM) was sufficient to nearly normalize pC cell growth (0.78 +/- 0.05% confluence per hour) relative to the growth rate of hT cells treated with the low (4.3μM) SKI-II dose (0.71 +/- 0.02% confluence per hour) (**Figure 2-18C**). Finally, the average proliferation rates of all four cancer groups treated with the high SKI-II dose (39μM) (pA: -0.03, pB: 0.30, pC: 0.34, pD: 0.13% confluence per hour) were considerably lower than hT cells treated with the same dose (0.48% confluence per hour) (**Figure 2-18C**). These results suggest that each cancer subclone was dependent to some extent on SK1 activity to support their rapid basal proliferation rates. Overall, our cell proliferation assay revealed that SK1 may be used as a drug target to reduce proliferation rates of differentially evolved PDAC clonal populations.

PDAC subclones displayed different levels of drug resistance but selective SK1 inhibition sensitized all subclones to mitochondria mediated apoptotic signals

We performed a flow cytometric cell death assay with Propidium Iodide (PI) staining on PDAC and hT cells treated with SKI-II, BH3I-1, or BH3I-1 combined with SKI-II (**Figures 2-20; Figure 2-21**). BH3I-1 is a BH3 domain-only peptide activator of mitochondria-mediated apoptosis [139,140]. We hypothesized that the SKI-II driven increase in C16 Cer levels and decrease in S1P/C16 Cer (**Figure 2-12**) would enhance sensitivity to BH3I-1 induced mitochondria-mediated apoptosis in the PSN-1 clones. As a positive control, we compared against cells treated with a non-mitochondria mediated pro-apoptotic drug, the nucleoside mimetic Gemcitabine (Gem). Unlike BH3I-1, Gem promotes apoptosis by inducing DNA damage [141]. Gem was selected as the control against BH3I-1 not only because it acts by a different mechanism but also because it is currently the most common chemotherapeutic used to treat PDAC but has strikingly low success rates [141].

We determined the half-maximal effective concentrations (EC_{50}) of compounds in the control (Gem) and mitochondria mediated apoptosis (BH3I-1) inducer alone and in combination with SKI-II by performing multiple cell death assays on PDAC subclones and hT cells (**Figure 2-20A-B**). The EC_{50} of each subclone was distinct from the others for both combinatorial treatments (**Figure 2-20A-B**). The pA and pB cells required a higher dose of Gem (9µM) combined with a lower dose of SKI-II (1-3µM) compared to pC (5µM Gem + 6µM SKI-II) and pD cells (5µM Gem + 4µM SKI-II) (**Figure 2-20A**). This suggests that the pA and pB clones were more resistant to DNA damage-induced apoptosis compared to pD and pC clones and more sensitive to SK1 inhibition in the context of this treatment. Gem treatment was ineffective in the hTert cells. This is likely due to the fact that hTert-HPNE is a slower growing cell line (**Figure 18C**) and Gem specifically targets fast-growing cells [142].

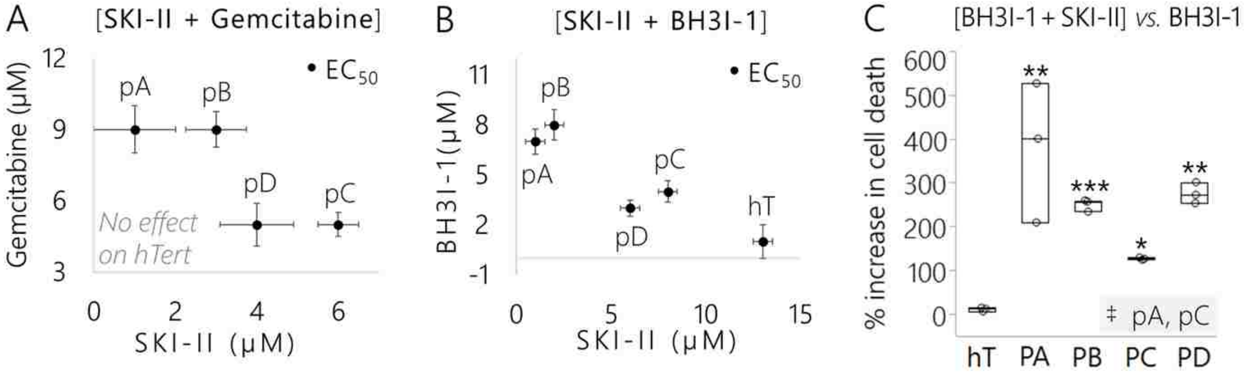

Figure 2-20 Pancreatic cancer subclones displayed different drug sensitivities yet SKI-II effectively sensitized each subclone to mitochondria-mediated apoptotic signals. (A) *Concentrations of control apoptosis-inducing treatment (SKI-II + Gemcitabine) that were required to achieve the EC_{50} of each cell group (with the exception of the slower growing hT cells where treatment was ineffective). Data are represented as the mean EC_{50} concentration of 3 biological replicates per group and error bars are drug tolerance (+/-) in µM.* ***(B)*** *Concentrations of targeted mitochondria-mediated apoptosis inducing treatment (SKI-II + BH3I-1) that were required to achieve the EC_{50} of each cell group. Data are represented as the mean EC_{50} concentration of 3 biological replicates per group and error bars are drug tolerance (+/-) in µM.* ***(C)*** *Comparison of the efficacy of SKI-II in enhancing cell death in response to mitochondria-mediated apoptotic signals across cancer subclones and healthy control. Data are represented as the percent increase in cell death of each group treated with SKI-II + BH3I-1 versus BH3I-1 alone (3 biological replicates per cell group/treatment). The Dunnett's test was used to compare between the percent increase in cell death of the cancer subclones to the healthy control (hT), wherein *** indicates $P=0.0004$, ** indicates $P<0.008$, and * indicates $P<0.05$. The Tukey-Kramer test was used to determine whether the percent increase in cell death of any of the cancer subcultures was different than any of the other cancer groups; the only pair found to be significantly different is highlighted in the bottom right-hand corner of the plot, where ‡ indicates $P=0.011$.*

On the other hand, the BH3I-1 served as an effective apoptosis inducer in the hTert cells. The hT cells required the highest dose of SKI-II (13µM) combined with the lowest dose of BH3I-1 (1µM) to achieve the EC$_{50}$ (**Figure 2-20B**). Overall, much lower concentrations of SKI-II (1-8µM) coupled with higher doses of BH3I-1 (3-8µM) were required to achieve the EC$_{50}$ in the PDAC strains relative to the hTert cells (**Figure 2-20B**). One interpretation of this could be that the PDAC clones were more resistant to mitochondria-mediated apoptosis, but more sensitive to SK1 inhibition compared to healthy cells during the combinatorial treatment. The pA and pB cells seemed to be the most resistant to BH3I-1, with an EC_{50} ranging from 7-8μM, and required the least amount of SKI-II (1-2μM) in the combinatorial treatment compared to pC (4μM BH3I-1 + 8μM SKI-II) and pD cells (3μM BH3I-1 + 6μM SKI-II) (**Figure 2-20B**). This may mean that pA cells were more resistant to mitochondria-mediated apoptosis compared to pC and pD cells but more sensitive to SK1 inhibition in the context of this combinatorial treatment. The pD cells required the least amount of BH3I-1 to achieve the EC_{50}, suggesting that pD cells were more sensitive to apoptosis in the presence of SKI-II relative to the other cancer clones.

Using the doses determined for each cell line in our EC_{50} assay, we performed another set of cell-death experiments to test whether SK1 inhibition specifically enhanced sensitivity to BH3I-1 induced apoptosis. SKI-II induced a non-significant, but reproducible increase up to 10% in cell death across all of the cell groups in response to Gem treatment (**Figure 2-21A-E**). This may have been due to a counterproductive relationship between the mechanisms of action for Gem and SKI-II, since Gem targets fast growing cells and SK1 inhibition slows PDAC cell growth rates (**Figure 2-18C**).

The percent of cell death in response to BH3I-1 alone was much lower compared to the response to the non-combinatorial Gem treatment in all the cancer groups compared to hTert (**Figure 2-21A-E**). However, sensitivity to BH3I-1 was significantly increased in each cancer subclone treated with SKI-II relative to those treated with BH3I-1 alone ($P \leq 0.001$) (**Figure 2-21B-E; Figure 2-20C**). The BH3 domain is a direct inducer of apoptosis via activation of pro-death Bcl-2 family members and does not rely on DNA damage checkpoint activation to kill the cell [140]. Therefore, the significant increases in cell death of the PDAC groups treated with BH3I1

+ SKI-II was likely driven by an increase in intracellular signaling of pro-apoptotic C16 Cer relative to S1P (**Figure 2-12**). Meanwhile, there was no significant change in cell death of hT cells treated with BH3I-1 versus hT cells treated with the [BH3I-1 + SKI-II] combination treatment (**Figure 2-20C; Figure 2-21A**). Indeed, the percent increase in cell death measured in all four cancer groups treated with the [BH3I-1 + SKI-II] combination versus BH3I-1 alone was significantly higher compared to the healthy control ($P<0.05$) (**Figure 2-20C**).

There also were slight differences in the percent increases in cell death between each cancer subclone treated with [BH3I-1 + SKI-II] versus BH3I-1 alone (**Figure 2-20C**). Based on our Western blots and SK1 activity assay, this is likely due to variations in SK1 expression (**Figure 2-15A**) and activity (**Figure 2-12**) between the different PSN-1 subclones and provides further evidence that each subclone adapted different methods to defend themselves against apoptotic signaling via SK1. Despite such modifications in SK1 expression and regulation between the cancer groups, our cell death assay indicates that SKI-II treatment effectively sensitized all of the cancer groups to mitochondria mediated apoptotic signals (**Figure 2-21B-F**). SK1 may serve as a powerful therapeutic drug target to ubiquitously enhance mitochondria mediated apoptosis in differentially reprogrammed PDAC subclones.

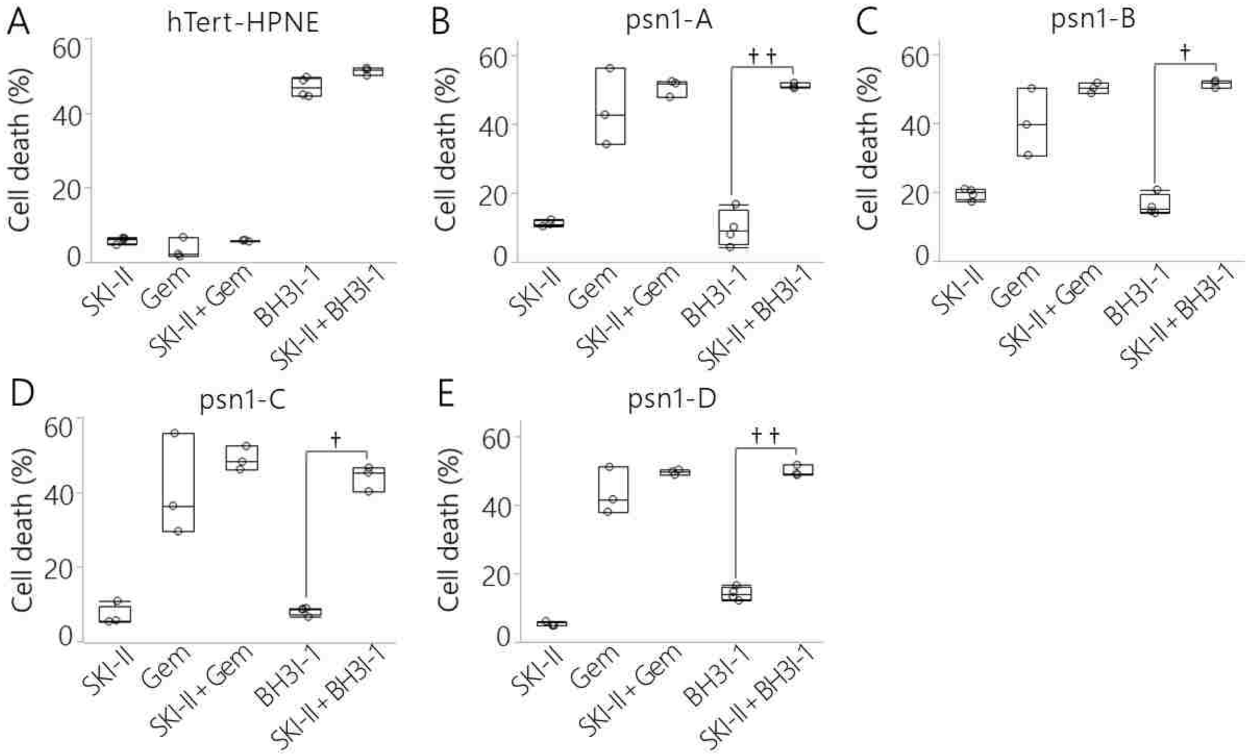

Figure 2-21 SK1 inhibition significantly sensitized pancreatic cancer subclones to mitochondria-mediated apoptotic signals. (A-F) *Results of Cell Death Assay of cancer subclones (pA, pB, pC, and pD) and hT cells treated with the following drug combinations: (1) SKI-II only, (2) control apoptosis inducer Gemcitabine (Gem) only, (3) SKI-II combined with Gem, (4) mitochondria-mediated apoptosis inducer BH3I-1, and (5) SKI-II combined with BH3I-1 for 12 hours at the following concentrations based on the combinatorial* EC_{50} *of each group:* ***(A)*** *hTert: (1) 13 µM SKI-II, (2) 10 µM Gem, (3) 13 µM SKI-II + 10 µM Gem, (4) 1 µM BH3I-1, and (5) 13 µM SKI-II + 1 µM BH3I-1;* ***(B)*** *psn1-A: (1) 1 µM SKI-II, (2) 9 µM Gem, (3) 1 µM SKI-II + 9 µM Gem, (4) 7 µM BH3I-1, and (5) 1 µM SKI-II + 7 µM BH3I-1;* ***(C)*** *psn1-B: (1) 2 µM SKI-II, (2) 9 µM Gem, (3) 3 µM SKI-II + 9 µM Gem, (4) 8 µM BH3I-1, and (5) 2 µM SKI-II + 8 µM BH3I-1;* ***(D)*** *psn1-C: (1) 8 µM SKI-II, (2) 5 µM Gem, (3) 6 µM SKI-II + 5 µM Gem, (4) 4 µM BH3I-1, and (5) 8 µM SKI-II + 4 µM BH3I-1;* ***(E)*** *psn1-D: (1) 6 µM SKI-II, (2) 5 µM Gem, (3) 4 µM SKI-II + 5 µM Gem, (4) 3 µM BH3I-1, and (5) 6 µM SKI-II + 3 µM BH3I-1.* ***(A-E)*** *After the 12-hour treatment, dead cells were stained with propidium iodide and quantified by flow cytometry. Samples were measured in biological triplicate and depicted as percent cell death normalized to vehicle controls. Student's t-tests were used to compare between cell death responses of groups treated with an apoptosis inducer alone (Gem or BH3I-1) versus those treated with an apoptosis inducer combined with SKI-II, wherein † indicates* $P<0.0001$ *and †* $P\leq0.001$.

DISCUSSION

To promote stress tolerance, isogenic clones derived from the same originating cancer cell can adopt distinct phenotypic profiles leading to inter- and intra-tumor heterogeneity, disease progression, and drug resistance [6,27,143]. Identifying pro-cancer pathways that are selectively preserved throughout stochastic and environmentally induced biochemical reprogramming is necessary to improve treatment outcomes in aggressive and therapeutically unresponsive cancers like PDAC [27,144]. This study was designed to measure global and specific shifts in gene expression and metabolism that contribute to stress tolerance mechanisms in four PDAC subclones from a common ancestry (PSN-1) (**Figure 2-3**).

The four "adaptations" of PSN-1 were compared to each other and to a 'healthy' control at the levels of DNA (STR and SNP Analyses), mRNA (RNA-Seq), protein (quantitative proteomics and Western blot analyses), and lipid (quantitative lipidomics) expression. Differences in cell behavior resulting from biochemical reprogramming were assessed using cell size/morphology, enzyme activity, cell proliferation, and drug sensitivity assays. The results of each assay are summarized in a divergence tree depicting commonalities and differentiations in the global genotypic and phenotypic profiles between individual cell groups (**Figure 2-22A**). Although there were no significant changes in DNA sequence between PSN-1 subclones, they exhibited multiple levels of phenotypic variation, including shifts in mRNA, protein, and lipid expression as well as sensitivity to anti-cancer drugs relative to one another. In addition, the mRNA, protein, and lipid data identified a pro-cancer sphingolipid metabolism pathway mediated predominantly by the enzyme Sphingosine Kinase 1 (**Figure 2-22B**). SK1 modified S1P/C16 Cer metabolism was conserved in different manners across the four differentially reprogrammed cancer subclones. Most importantly, SK1 served as an equally effective therapeutic target of SKI-II in each isolated subclone by suppressing proliferation and enhancing mitochondria mediated apoptosis with no damaging effects on healthy control cells.

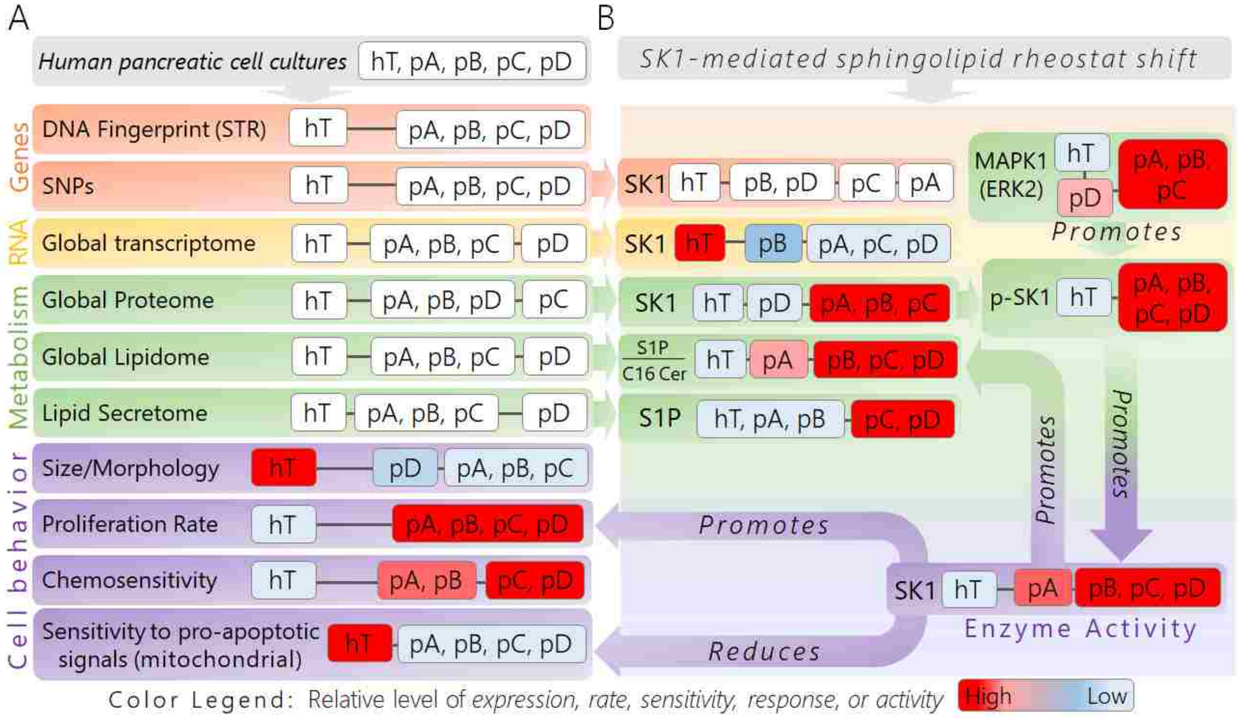

Figure 2-22 Divergence tree of genotypic and phenotypic analyses of isolated pancreatic cancer subcultures (pA, pB, pC, pD) and healthy control cells (hT) revealing nongenetic heterogeneity and a conserved, pro-cancer sphingolipid metabolic pathway mediated by SK1. (A) *The experimental groups used to investigate pro-cancer adaptations in this study are shown in the gray box (top). This is followed by each parameter used to broadly compare genotypes and phenotypes of each cell group, as well as to determine at which level of expression common pro-cancer adaptations were present. The orange boxes, labeled "Genes", represent assays performed to investigate genetic differences between each group. The yellow box, denoted "RNA", represents our RNA-Seq analysis used to compare mRNA expression levels between groups. The green boxes, labeled "Metabolism", represent assays to investigate metabolic features of each cell group, including protein and lipid (intra/extracellular) expression levels. The purple boxes, labeled "Cell Behavior", represent assays performed to measure major physical cancerous phenotypes/responses resulting from biochemical influences.* ***(B)*** *Boxes in this panel represent specific measurements of compounds that emerged from each global/omics assay related to the SK1-driven shift in S1P/C16 Cer metabolism observed to some degree in each cancer subclone. Relative to the healthy control, these biochemical influences promote SK1 activity in the cancer subclones in different manners in order to regulate cancerous behaviors, including proliferation and response to pro-mitochondria mediated apoptotic signals.* ***(A-B)*** *The distance between cell groups denoted by the black linker lines between each white box represent how closely the groups in each box were related with respect to the indicated assay. The color legend is shown to summarize general observations made in each assay, where appropriate; the boxes with groups showing high levels of expression, rate, sensitivity, response, or activity relative to the other cells*

are colored bright red; those cells showing very low levels of the respective assay metric relative to the other groups are colored light blue, while groups that were somewhere in between are colored with shades of red or blue toward the middle of the red→blue color spectrum.

Multiple lipid extraction and mass spectrometry techniques confirmed that all four subclones displayed an increase in the ratio of intracellular S1P relative to C16 Cer, but at different levels (**Figure 2-11A, Figure 2-12**). This result was intriguing not only because C16 Cer and S1P are interconvertible metabolites (**Figure 2-2**), but also because they have been shown to exhibit competing bioactive capacities in cancer [19]. Together, C16 Cer and S1P make up a critical rheostat between pro-survival versus pro-apoptotic signaling pathways in the differentially modified PDAC subclones (**Figure 2-23**) [19]. An increase in the level of pro-survival S1P molecules relative to pro-apoptotic C16 Cer has been shown to promote cancerous phenotypes like proliferation, stress tolerance, and resistance to ceramide-mediated apoptosis by activating intracellular targets including TRAF2, an essential E3 ubiquitin ligase in the pro-proliferative TNF- α/NF-κB signaling pathway [19]. In addition, S1P can accumulate in the nucleus and has been shown to bind and inhibit histone deacetylases 1 and 2 (HDAC1-2), resulting in increased histone acetylation and gene suppression [56]. Prohibitin 2 (PHB2), a conserved protein responsible for mitochondrial membrane assembly and integrity, is also known to bind S1P; this interaction may indirectly support mitochondrial respiration and pro-survival metabolism [56]. We considered the increased S1P/C16 Cer ratios in the cancer groups representative of a cancer-promoting a shift in the sphingolipid rheostat (**Figure 2-12**). We hypothesized that this shift in S1P/C16 Cer metabolism was used as a crucial stress tolerance mechanism of PSN-1 that was selectively conserved at various degrees in each isolated subclone (**Figure 2-12**).

The mRNA expression data suggested that differences in cancer subclone behavior were driven by changes in S1P formation by Sphingosine Kinase (**Figure 2-11D**). SK1 catalyzes the final step of S1P synthesis from ceramide precursors (**Figure 2-2**) and has been shown to play an important oncogenic role [120]. Surprisingly, the mRNA expression levels of SK1 were reduced in all four cancer groups (**Figure 2-11G**). We used Western blots to measure relative levels of total SK1 (**Figure 2-15A**) as well as active p-SK1 enzymes phosphorylated at Serine-225 (**Figure 2-15B**). SK1 protein concentrations reproducibly varied between the four subclones and were significantly different between certain pairs, including pA/pD ($P<0.005$), pB/pD ($P<0.005$), and pB/pC ($P<0.05$) groups (**Figure 2-15A**). All four cancer groups displayed higher levels of SK1 protein relative to the healthy control, though this difference was only statistically significant in pA ($P<0.0001$), pB ($P<0.0001$), and pC ($P<0.05$) cells (**Figure 2-15A**). These data suggest that SK1 protein expression was post-transcriptionally increased to promote S1P synthesis in the cancer groups relative to hT cells. SK1 mRNA levels may have been reduced (**Figure 2-11G**) due to continual translation/overuse to maintain high SK1 protein levels in the cancer cells relative to hTert. Elevated SK1 protein levels may trigger a cell sensing system or negative feedback loop to suppress unnecessary SK1 mRNA production which could have also contributed to the reduced SK1 mRNA levels in the cancer groups compared to hTert (**Figure 2-11G**).

Inactive SK1 is generally found in the cytosol away from its lipid substrates [133]. After activation through MAPK1/ERK2 mediated phosphorylation at Ser-225, SK1 relocates to the plasma membrane where it localizes onto functional lipid-raft subdomains for its catalytic activity [133]. Activating levels of SK1 (p-SK1) were significantly higher in all the cancer groups relative to the healthy control ($P<0.001$) (**Figure 2-15B**). Correspondingly, MAPK1/ERK2 protein expression was also higher in all of the cancer groups relative to hTert; this difference was significant in pA ($P<0.001$), pB ($P<0.05$), and pC ($P<0.05$) cells (**Figure 2-15D**). We propose that each cancer subclone achieved lower pro-apoptotic C16 Cer and higher pro-inflammatory S1P signaling (**Figure 2-12; Figure 2-13**) through a combination of greater SK1 protein expression and/or increased SK1 activity levels (**Figure 2-15A-B**).

To investigate this hypothesis, we tested how modified SK1 enzyme activity would change S1P/C16 ratios and cell behavior. We measured the concentrations of S1P and C16 Cer by targeted LC-MS in each cell group treated with a selective SK1 inhibitor (SKI-II), versus corresponding vehicle controls. The ratio of S1P relative to C16 Cer was higher at different degrees in all of cancer vehicle control groups relative to the hT vehicle control; this increase was significant in pB ($P<0.0001$), pC ($P=0.002$), and pD ($P<0.0001$) cells (**Figure 2-12**). This suggests that S1P production was elevated to some degree in the cancer groups. There was strong evidence for a potentially damaging nscSNP in SK1 of pA (**Supplemental Database M**), which may have affected SK1 activity and in turn lowered the basal S1P/C16 Cer ratio in pA cells. The 273L→P polymorphism in the helix near the sphingosine binding site of SK1 may have affected the Kd, leading to a reduction in the S1P/C16 Cer ratio in pA cells relative to the other cancer groups. Nonetheless, the highly variable S1P/C16 Cer levels observed in the other subclones did not seem to have a genetic origin (**Figure 2-12; Figure 2-13**). On average, *extra*cellular S1P levels were also higher in the cancer groups compared to the blank, though this difference was only significant in pC and pD groups (**Figure 2-13C**). This suggest that S1P may be exported from pC and pD cells, which has been shown to promote autocrine/paracrine proliferative signaling [67]. Overall, these initial implications from our SK1 activity assay data confirmed that the sphingolipid rheostat was perturbed to some extent in each of cancer subclone and S1P may be used to activate both intra- and extracellular pro-proliferative targets. SKI-II mediated inhibition of SK1 significantly reduced the S1P/C16 Cer ratio in all four cancer groups ($P<0.05$)

and normalizing S1P/C16 Cer levels relative to the healthy control. This indicates that SK1 is an important driver of the S1P/C16 Cer imbalance and other cancerous phenotypes in metabolically dynamic PDAC subclones.

Variations in S1P/C16 Cer levels (**Figure 2-12**) resulting from an SK1 mediated drive for increased proliferation may be linked to changes in cell size, shape, and production of membrane lipids to accommodate rapid growth rates of the cancer subclones (**Figure 2-18C; Figure 2-6C1; Figure 2-4**). While the cancer groups grew at nearly equivalent rapid rates ranging from 1.04 to 1.12% confluence per hour (**Figure 2-18C**), there were modest but consistent variations in the general morphology and average sizes of individual subclones (**Figure 2-4A-D**). For example, pB cells tended to be thinner with sharper corners and darker nuclei compared to the other groups (**Figure 2-4B**). Meanwhile, the pD cells were slightly larger on average relative to the other subclones, although this difference was only significant between the pA and pD cells (P=0.005) (**Figure 2-5D**). These morphological differences may be considered structural manifestations of the variations in mRNA and protein expression levels (**Figure 2-6A-B**), lipid metabolism (**Figure 2-6C-D**), and SK1 activity (**Figure 2-12, Figure 2-15B**) induced by different internal and environmental stimuli that occurred during the subculturing experiment. For example, the slight increase in pD cell size may be linked to the shift in intra- and extracellular lipidomic profiles in the pD cells relative to the other cancer groups (**Figure 2-6C-D**). The 2-fold increase in dietary serum lipids (**Figure 2-3**) may have allowed pD cells to produce more lipids to accommodate larger plasma membranes. Indeed, the pD cells exhibited the highest average concentration of cellular glycerolipids relative to the other cancer groups (**Figure 6C1**) which can be used to support new membrane growth (**Figure 2-1**).

The general reduction in PDAC cell size may also be correlated with the reduced cytoplasmic actin mRNA and protein expression levels (**Figure 2-16A-B**). The relative mRNA (**Figure 2-23A2**) and protein (**Figure 2-23B2**) concentrations of Beta-actin and Gamma-actin were depleted in all the cancer groups relative to the healthy control ($P<0.01$). Considerably higher actin mRNA and protein levels are likely required in hT cells to support their significantly larger cytoplasmic areas relative to the cancer groups. In addition, the pD cells were generally the largest of the four cancer groups (**Figure 2-4F**) and also exhibited the highest average actin concentrations relative to the other cancer groups (**Figure 2-16A2, B2**). These data suggest that shifts in mRNA, protein, and lipid expression resulting from intrinsic and microenvironmental influences are intimately linked with hallmark cancer phenotypes like cell size and shape abnormalities. Increased SK1 mediated S1P signaling may provide a pro-survival signaling environment to support such behaviors in metabolically unstable PDAC subclones.

To explore this concept further, we measured the effects of SK1 on PDAC cell growth rates. SKI-II mediated SK1 inhibition significantly reduced the growth rates of each cancer group in a unique dose-dependent manner relative to the healthy control (**Figure 2-18; Figure 2-19A-E**). These results suggest that SK1 activity was required to maintain rapid growth rates of all four PSN-1 subclones. In addition, these data suggest that SK1 may be used as a therapeutic target to regulate overwhelming levels of PDAC cell proliferation.

Up until this point, we focused mainly on the pro-proliferative effects of SK1 driven S1P synthesis in our panel of heterogeneous PDAC cells. We next shifted our focus toward its competing metabolic precursor, C16 Cer. We wondered whether SK1 inhibition was sufficient to enhance C16 Cer mediated pro-apoptotic signaling and drug sensitivity in the PDAC clones. Along with structural functions in cell membranes, ceramides serve as vital second messengers in response to stressful stimuli subjected to cancer cells, e.g. oxidative stress, anti-cancer drugs, cytokines (e.g. TNFα, IL-1β), pro-apoptotic cell surface receptors (e.g. FasR), and ionizing radiation [145]. In fact, endogenous ceramide synthesis is an essential component of apoptotic signaling in both TNFα- and FasR (CD95)- treated conditions [146]. On the other hand, reducing ceramide levels through targeted inhibition of the ceramide-producing sphingomyelinase (SMase) blocks apoptosis [147-149].

How could a membrane-bound sphingolipid mediate programmed cell death? One common mechanism by which ceramides communicate extracellular stress signals to the cell is by forming ordered, ceramide-enriched microdomains or lipid rafts. These domains serve as signaling platforms by drawing receptors and other bioactive compounds to a central location on the plasma membrane [54]. Rafts on the outer layer can induce changes in the inner layer of the membrane, thereby transducing extracellular stress signals to pro-apoptotic effector molecules in the cytosol [19,54]. In response to apoptotic stimuli, ceramides located in the outer mitochondrial membrane can form ordered channels or pores, causing protein leakage from the intermembrane space and cytochrome c release, an initial step in the mitochondria-mediated apoptotic pathway [110]. Through such mechanisms, membrane-bound ceramides have been shown to perform key functions in anti-proliferative responses to stress, e.g. senescence modulation, cell growth inhibition, ER stress response, extrinsic and intrinsic pathways of apoptosis, and autophagy [150-154].

Ceramide species have specifically been shown to regulate pro-apoptotic Bcl-2 family proteins and/or splice variants through multiple mechanisms [150,155]. Such regulatory systems are often linked to ceramide-induced activation of serine/threonine protein phosphatases, such as PP1 or PP2A [19]. For example, ceramide-driven activation of PP1 leads to increased pro-apoptotic splice variants of Bcl-x family members as well as caspase 9 proteins [156]. Following ceramide-mediated activation, PP2A dephosphorylates several key targets involved in anti-proliferative signaling events, e.g. dephosphorylation of Bax, which activates its potent pro-apoptotic functions [54]. On the other hand, ceramide has inhibitory effects on the pro-survival Akt pathway through its interaction with protein kinase Cζ [157]. Without the second-messenger properties of ceramide, the ability of the cell to undergo programmed cell death becomes severely impaired or in some cases disabled entirely [112,158]. Thus, active levels of ceramide are necessary to maintain healthy cell populations by minimizing the accumulation of damaged and oncogenic cells. There is an increased interest and need for research in ceramide metabolism due to its apparent roles in age-related diseases including cancer [145]. Although the pathophysiological effects of ceramides in general have been reviewed thoroughly, the biological functions and techniques to measure specific ceramide species are less implicit [145], yet increasingly important for uncovering potential therapeutic applications [59].

Based on current literature, we hypothesized that the increase in intracellular C16 Cer levels (**Figure 2-13B**) induced by SKI-II may enhance PDAC cell sensitivity to mitochondria mediated apoptosis while suppressing S1P driven anti-apoptotic signaling. We performed a series of cell death assays to compare drug sensitives between the different cell types and evaluate whether SK1 inhibition affected therapeutic responses to BH3I-1, a peptide activator of mitochondria mediated apoptosis relative to a standard chemotherapeutic, Gemcitabine (**Figure 2-20; Figure 2-21**). Our cell death assays suggested that the SK1 mediated shift in the S1P/C16 Cer ratio provides some defense against mitochondria-mediated apoptosis in the cancer groups. Much lower concentrations of SKI-II (1-8μM) coupled with higher doses of BH3I-1 (3-8μM) were required to achieve the EC_{50} in the PDAC lines relative to that in hTert cells (**Figure 2-**

20B). One interpretation of this could be that the PDAC cells were more resistant to mitochondria-mediated apoptosis but more sensitive to SK1 inhibition compared to healthy cells during the combinatorial treatment. The pA and pB cells seemed to be the most resistant to BH3I-1, with an EC_{50} ranging from 7-8µM, and required the least amount of SKI-II (1-2µM) in the combinatorial treatment compared to pC (4µM BH3I-1 + 8µM SKI-II) and pD cells (3µM BH3I-1 + 6µM SKI-II) (**Figure 2-20B**). This may mean that pA and pB cells were more resistant to mitochondria-mediated apoptosis compared to pC and pD cells but more sensitive to SK1 inhibition in the context of this combinatorial treatment. The pD cells required the least amount of BH3I-1 to achieve its EC_{50}, suggesting they were more sensitive to apoptosis in the presence of SKI-II relative to other PDAC subclones (**Figure 2-20B**). Another way to interpret our EC_{50} results is to consider the individual concentrations of the two treatment components as less important compared to the total [SKI-II µM + BH3I-1µM]. This may be the more definitive determinant of the EC_{50} since the two compounds are administered simultaneously and work toward the same general effect: an increase in apoptotic signaling. In this case, hTert required the highest combined sum total of SKI-II/BH3I-1 concentrations (14µM), followed by pC (12µM), pA (10µM), pD (9µM), and pA (8µM) to achieve their individual EC_{50} levels (**Figure 2-20B**).

In the presence of SKI-II, there was a very modest increase in cell death resulting from Gem treatment (**Figure 2-21**). In order for a nucleoside analogue like Gemcitabine to have maximal effect, cells should be proliferating rapidly [159]. Since SKI-II treatment extorted a potent anti-proliferative effect on the cancer groups (**Figure 2-18C; Figure 2-19B-E**) it may have had a counterproductive effect since slower cell growth may have reduced the efficacy of the Gemcitabine. On the other hand, BH3I-1 was a significantly more effective companion to SKI-II than Gem. SKI-II significantly enhanced the percent cell death of each cancer subclone exposed to BH3I-1 ($P<0.05$) (**Figure 2-20; Figure 2-21B-E**). This result may be explained by the role of C16 Cer in increasing the ratio of pro-apoptotic to anti-apoptotic Bcl-2 family proteins at the mitochondria [112,158]. Our data suggest that increased C16 Cer levels resulting from SKI-II treatment (**Figure 2-13B**) enhanced BH3 mimetic-induced mitochondrial outer membrane permeabilization and apoptosis in each PDAC subclone.

Pancreatic cancer has historically been difficult to treat compared to other cancers [160,161]. Traditional chemotherapeutics have only offered limited success due to the resistant nature of PDAC and the unique treatment-refractory environments established by individual tumors [162,163]. Although Gemcitabine is the most common chemotherapeutic used to treat pancreatic cancer, the tumor response rate is just 12% [141]. Resistance to Gem presents major clinical challenges and new strategies to enhance PDAC drug sensitivity are in high demand [141]. In addition, inter- and intra-tumor heterogeneity resulting from differential cellular evolution reduces the predictability of individual treatment outcomes between isogenic experimental models and individual patients [25].

We showed that SK1 served as the "master switch" of the perturbed sphingolipid rheostat in metabolically reprogrammed PDAC cells and may be used as a ubiquitous drug target among isogenic PDAC subclones. Consistent with previous research [133], the model established in this study states that MAPK1/ERK2 initiates a pro-survival positive feedback loop by phosphorylating and activating SK1, thereby promoting S1P synthesis and suppressing relative levels of C16 Cer; S1P in turn stimulates intra- and extracellular pro-inflammatory targets such as MAPK1/ERK, leading to increased pancreatic cancer cell proliferation and drug resistance (**Figure 2-23,** *left panel*). SKI-II mediated SK1 inhibition increases pro-apoptotic C16 Cer levels relative to S1P, interrupting the S1P pro-inflammatory feedback loop, reducing proliferation, and minimizing anti-apoptotic defense systems (**Figure 2-23,** *right panel*). Concomitant suppression of S1P and enhancement of intracellular C16 Cer levels by inhibition of SK1 activity may serve as a powerful strategy to restore a healthy balance between pro- and anti-apoptotic signaling in metabolically dynamic pancreatic cancers.

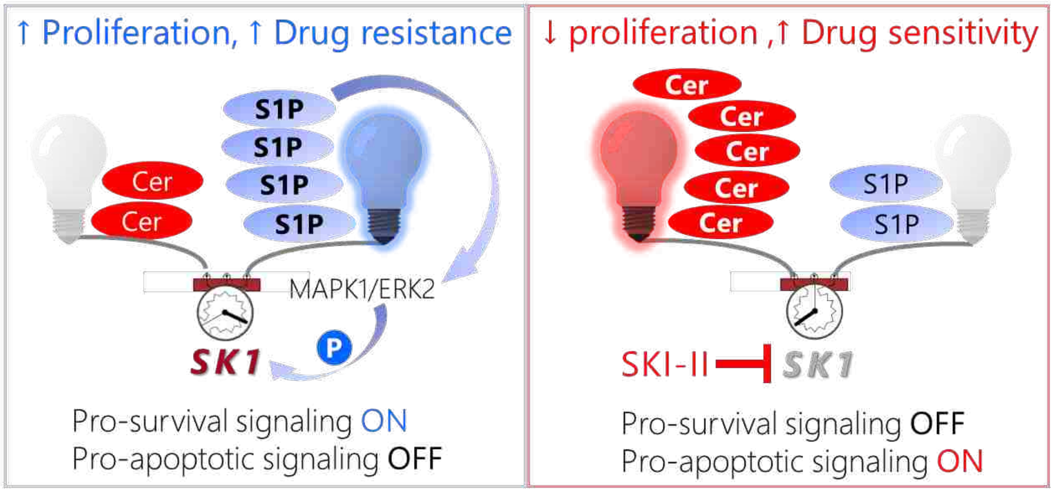

Figure 2-23 Schematic model of pro-survival S1P signaling in pancreatic cancer cells (left) followed by a shift in the sphingolipid rheostat toward C16 Cer-driven pro-apoptotic signaling induced by SKI-II treatment (right).

MATERIALS AND METHODS

Experimental Design

The originating PSN-1 cell line and hTert cell line were obtained from Dr. David Bearss at Tolero Pharmaceuticals and were not tested for mycoplasma contamination after arrival. We developed a panel of differentially reprogrammed human ductal pancreatic cancer cells originating from the same genetic origin (PSN-1) [121] (**Figure 2-3**). The original PSN-1 cells were authenticated using the ATCC human cell line short tandem repeat (STR) profiling analysis [126] (**Supplemental Table 2B**). These original cells were subcultured into four different randomly assigned groups: psn1-A (pA), psn1-B (pB), psn1-C (pC) and psn1-D (pD).

The first set of groups, pA and pC, were used to investigate stochastic, time-dependent factors influencing cancer evolution and were cultured separately in the baseline growth conditions in RPMI-1640 cell medium (Thermo Fisher cat # 11875093) with L-glutamine, high glucose, 10% Fetal Bovine Serum (FBS), and penicillin/streptomycin (PS) (1x) at 37ºC and 5% CO_2. The other groups, pB and pD, were cultured in new combinations of randomly assigned growth conditions during the same month to encourage environment-induced adaptions and metabolic reprogramming. The pB cells were maintained in DMEM cell medium with 10% FBS and 1x PS at 37ºC and 5% CO_2. The pD cells underwent the greatest dietary change as they were cultured in IMDM cell culture medium with double the concentration of FBS (20%) and 1x PS at 37ºC and 5% CO_2. All three cell mediums used in this portion of the study (RPMI-1640, DMEM, IMDM) contained the same concentration of D-Glucose (25 mM). RPMI is generally the most different of the three in terms of contents and concentrations while DMEM and IMDM are more similar formulations **(Supplemental Table 1).** The formulations differ the most in amino acid **(Supplemental Table 1A)** and vitamin content **(Supplemental Table 1B)**. RPMI contains the greatest variety of amino acids; however, their concentrations tend to be lower than those in DMEM and IMDM. RPMI also contains the greatest variety of vitamins **(Supplemental Table 1B)** and is the only one of the three mediums to include Glutathione, an antioxidant that promotes cell growth and viability [164]. After the month-long evolutionary period of culturing the cancer groups in these different cell culture mediums, frozen stocks of each group were prepared and stored in liquid nitrogen.

The growth conditions of each group were unified to the original growth medium (RPMI-1640 with L-glutamine and high glucose, 10% FBS, 1x PS) to obtain consistency of experimental conditions across all groups during the *in vitro* assays that followed. To minimize further cancer evolution/adaptive changes in each cell group from occurring throughout the study *after* the 1-month evolutionary period (**Figure 2-3**), cells from each group were passaged no more than 10 times before returning to an original frozen stock of the respective group.

Cell Size/Morphology Analysis

Light microscope imaging was used to compare cell shapes and sizes. ImageJ image analysis software was used to measure the cell areas of 40 different randomly selected cells in each group.

STR Profiling

Cell samples from each group were collected and STR profiles were generated using the ATCC Human Cell Line Authentication Service. Eight STR markers (plus amelogenin for gender determination) were amplified from cellular DNA via Polymerase Chain Reaction (PCR) and converted to the respective alleles by comparing to allelic ladders [126] (**Supplemental Table 2**). These alleles were then converted to corresponding numeric values which were used to generate an STR profiles of each group [126]. The STR Profiles of each group were then compared to the corresponding reference profiles to determine the degree of relatedness to the original tissue [126].

RNA-Seq Analysis

The mRNA extracts were prepared from cell cultures of each group using the Direct-zol™ RNA MiniPrep Plus Kit. Samples were stored at -80°C for 1 week-1 month. Three to four samples from each group with RQN values ≥8.0 and were selected for sequencing at the DNA

Sequencing Center (DNASC) at Brigham Young University. There was a Poly-A enrichment prior to the library construction and libraries were sequenced using the HiSeq 250 Cycle Paired-End (125 cycles from each end) sequencing method.

Resulting sequencing data was downloaded and quality analyzed using the fastqc package [165]. All samples passed the major sequencing quality parameters. Reads were then aligned to the human genome (GRCh38) and assigned to features using an R script based on the Rsubread package [166].

SNP Analysis/SNP Profiling and Data Analysis

Variant analysis of the RNA-seq data was conducted using custom R scripts based on the VariantTools Bioconductor package. Variants were first called individually for each sample and then results for all samples collated into a single table with presence or absence of a variant at every genomic position with a variant in at least one sample. PCA analysis comparing samples was then conducted using logisticPCA, which is designed for binary datasets [167]. Nonsynonymous mutations were identified using the VariantAnnotation package [168] and their effects predicted using Polyphen2 [169].

RNA Expression Profiling and Data Analysis

The *DESeq2* R/Bioconductor package was used to filter and normalize raw RNA-Seq data as well as to identify differentially expressed genes between groups [131]. The hierarchal heat map of the normalized RNA-Seq data was created using *DESeq2* and the PCA plot was made using *ClustVis* [170].

Protein Expression Profiling and Data Analysis

Proteomics samples were prepared from whole cell lysates collected from cell cultures of each group using an on-filter trypsin digest procedure. Cells were first grown to 70-80% confluence on 15cm tissue culture dishes. The cell medium was aspirated and cells were washed with 1x PBS. Cells were trypsinzed and pelleted by centrifugation for 5 minutes at 1200rpm. The pellet was gently washed with 1x PBS. Pelleted cells were lysed and protein was denatured in 6 M guanidine/HCl 100 mM Tris/HCl (pH 8.5) on a tissue homogenizer for 30 sec. Total protein was quantified using a bicinchoninic acid (BCA) assay. 50 µg of protein from the sample was transferred to a 30 kD spin filter and washed 2–3 times with 6 M guanidine/HCl 100 mM Tris/HCl (pH 8.5). Disulfide bonds were reduced using dithiothreitol and alkylated using iodoacetamide. The filter was washed twice with 25 mM ammonium bicarbonate. Proteins were re-suspended in 25 mM ammonium bicarbonate (pH~8) and digested overnight using Pierce MS-Grade Trypsin. The trypsin digest was quenched and peptides were spun through 30kDa filters via centrifugation. Samples were dried in a vacuum evaporator and re-suspended in 50 µL of 3% acetonitrile, 0.1% formic acid. Proteomics data was collected from each sample on a Lumos Orbitrap (Thermo) mass spectrometer. To reduce the influence of time-dependent fluctuation or cross contamination from run to run, the sample analysis schedule was randomized using a random number generator.

PEAKS Studio software was used for *de novo* sequencing to identify proteins in our raw MS data as well as to quantify, filter (quality-control) and normalize our label-free quantitation data for each protein [171]. Peptides were identified from MS/MS spectra by searching against the Swiss-Prot human database. Protein annotations with at least 2 unique peptides and a false discovery rate less than 1% were included in the comparative quantitative analysis. We used t-tests corrected for multiple comparisons using the Benjamini-Hochberg method to determine significant differences in protein concentrations between groups. The hierarchal heat map of the normalized protein concentrations was created using *DESeq2* [131] and the PCA plot was made using *ClustVis* [170]. We used t-tests to determine significant differences between protein concentrations in each group; p-values were corrected for multiple comparisons using the Benjamini-Hochberg procedure. Protein concentrations were considered significantly differentially expressed if both the p-value and corrected p-value were <0.05. The concentrations of differentially expressed proteins were compared between groups by calculating the fold change in concentration (mean concentration of each individual group relative to the mean concentration in the other groups). If the fold change was >1 the protein was considered upregulated and if the fold change was <1 the protein was considered downregulated.

DAVID Bioinformatics Functional Annotation Tools were used identify enriched functional-related gene groups in each list of significantly differentially expressed proteins [42]. The top three gene ontologies with the highest enrichment scores were considered relevant but only considered significantly enriched if the Benjamini score for enrichment calculated by the functional analysis tool was <0.05 [42].

Shotgun Lipidomics Assay Development and Data Analysis

Lipids with mass difference from LMSD <50ppm were used in quantitative analysis Several extraction methods were evaluated to determine which method would best sample each of the major lipid classes and introduce the least amount of bias into our mass spectrometry analysis. All methods had differential extraction efficiency with differences in the observed lipid categories and classes. One complication with mass spectrometry techniques is that it requires a charged molecule to make measurements. Many lipids do not have an intrinsic charge, but addition of ammonium acetate in the extraction protocol increased the coverage of lipids from all categories in both positive and negative ion modes. Based on the initial lipid classifications we determined that a modification to Bligh and Dyer extraction with addition of isopropanol and an ammonium acetate adduct [172] resulted in the most reproducible, broad coverage of the major lipid categories. Total unique lipid identifications that met our criteria were compared for each of the extraction methods. We repeatedly identified the largest number of lipid species using the modified Bligh and Dyer technique [172]. The sample preparation procedure used in this shotgun lipidomics assay is explained in the following paragraph.

Cell pellets were re-suspended in 1.5 mL cell lysis buffer (0.1M Tris-HCl @ pH 7.6) and homogenized by circular cut tissue homogenizer (Omni) and vortex (30 seconds at 850 RPM). The homogenate was then transferred to glass vial (4.5 dram) where a two-phase extraction was completed to remove the lipid constituents [172]. Sample collection and homogenization steps were performed under cold collection environments and under nitrogen to reduce oxidation. The final extraction mixture contained the 1.5 mL aqueous homogenate and then an additional 3 mL of chloroform/methanol/isopropanol (3:1:1.25, v/v/v). A larger extraction batch with the Bligh and Dyer was extracted over 24 hours with shaking gave the closest match to a spiked standard. The organic lipid containing layer was then concentrated under reduced pressure at room temperature. The concentrated lipid extract was divided into two separate samples for comparison of adduct effects. The half sample analyzed without adduct was diluted with organic phase solution chloroform/methanol/isopropanol (3:1:1.25, v/v/v) with 0.1% formic acid (Thermo) at a 9-fold dilution by volume (9:1, solution: organic layer extraction) to a total volume of 250 μL immediately prior to data collection. The half sample analyzed with adduct was diluted with the same organic phase solution with 0.1% formic acid and ammonium acetate (1.5 mM) to promote ionization of some of the neutral lipid species. The sample (with and without adduct) was run in both positive and negative instrument modes to increase specificity and variety of lipids through intra-source selection of differentially ionizable species.

To reduce the influence of time-dependent fluctuation or cross contamination from run to run, the sample analysis schedule was randomized using a random number generator. In this way if the wash cycle between sample runs did not remove all the contaminants from the capillary line, the contaminated peak should not appear more than once in the technical replicates and is thereby removed by the data analysis filters. Sample (250 µL) was infused at 10 µL/min onto a Thermo LTQ-Orbitrap XL mass spectrometer using an IonMax ESI soft-ionization direct inject technique. During the infusion a high resolution (≥100,000) MS1 survey scan cycled through m/z "windows" (75-250 m/z, 250-400 m/z, 400-600 m/z, 600-800 m/z, and 800-1800 m/z). The top 5 most intense ions from each scan were selected for fragmentation, after an ion had been selected for fragmentation twice it was excluded from further MS/MS selection.

The typical data acquisition measured approximately 2000 different ions. Initial lipid identifications were assigned for each ion based on the parent mass of ion in the primary survey scan. To increase accuracy, the m/z of each ion was corrected according to the standard curve of the internal standards. The instrumental noise was determined as the baseline detection level across all spectra. Only those peaks that are estimated to be at least twice the level of the instrumental noise are included. The data files were analyzed using in-house developed module for the MSPIRE proteomics package [173] which compared the masses and fragmentation patterns against expected masses and fragments for the lipids within the LIPID MAPS database [174]. Ions which differed from the theoretical mass provided by the database by more than 50 ppm were removed from the data set. For quantitation comparisons across groups, MS intensity data for each lipid was normalized to the sum of all the species quantified in each sample. The normalized summed spectral intensity for each sample was considered a single quantitative data point each lipid.

Intra/extracellular Lipidomics LC-MS Analysis

We established a sphingolipid focused extraction technique and reverse-phase (RP) LC-MS method based on the procedure developed by Bode *et al.* [71]. Cell cultures were plated onto 15-cm cell culture dishes in complete RPMI 1640 Cell Medium and incubated at 37°C, 5% CO_2. Once cells reached 65-75% confluence, the cell medium was aspirated and cells were washed twice with 1xPBS. Medium was replaced with fresh, pre-warmed (37°C) complete RPMI 1640 containing 13µM of SKI-II inhibitor or an equivalent volume of 1x PBS for vehicle controls. Cell cultures were incubated for 12 hours at 37°C, 5% CO_2. After the incubation period, the medium was aspirated from the cells and transferred to a glass pear-shaped flask. Total lipids were extracted from the flask using the modified B&D technique [172], vacuum dried, dissolved in 100 µL of 4:1 (v/v) MeOH/$CHCl_3$ and sealed under argon in glass MS vials. Meanwhile, cells on the plate were washed with 1x PBS two times, trypsinized, and pelleted via centrifugation at 1200 rpm for 5 min. The supernatant was decanted and the sphingolipid modified lipid extraction technique based on the B&G method [71] was performed on wet ice, in glass centrifuge tubes under argon gas to minimize lipid oxidation (procedure detailed below).

Cells were lysed via vortex in 1 mL of NaCl for 20 seconds. 1 mL of MeOH and 200µL of 6 M HCl were added. The lysate was vortexed for 10 seconds. The organic phase lipid extraction was performed by adding 2 mL of $CHCl_3$ to the sample which were vortexed for 2 minutes and then centrifuged for 3 minutes at 1900 g. The lower organic phase was transferred to a glass test tube. The phase extraction steps were repeated on the remaining aqueous layer in the sample and the resulting organic phase was combined with the first. $CHCl_3$ was evaporated from the sample in a vacuum concentrator. The vacuum-dried lipids were dissolved in 100 µL of 4:1 (v/v) MeOH/$CHCl_3$ and sealed under argon in glass MS vials.

Samples were analyzed via RP-LC-MS on a stepwise gradient using a Luna Omega 1.6uM Polar C18 100Å LC Column, 150*2.1mm (Phenomenex Part # 00F-4748-AN). The mobile phases were 1% Formic Acid (Buffer A) and 100% Methanol (Buffer B) run on the following gradient at 100µL/min: 10%→100% Buffer B (0-5 minutes), 100% Buffer B (5-25 minutes), 100%→10% Buffer B (25-27 minutes) with a stop time of 45 minutes. Liquid chromatography was followed by positive ESI on a Dual Jetstream ESI source, MS/MS fragmentation using variable collision energy based on ion mass, and mass detection using an Agilent quadrupole-time-of-flight (QTOF) mass spectrometer. To reduce the influence of time-dependent fluctuation or cross contamination from run to run, the sample analysis schedule was randomized using a random number generator. To reduce sample carryover on the column, a blank containing 4:1 (v/v) MeOH/$CHCl_3$ was run in between each sample. The injection needle was also washed twice with 48% acetonitrile/48% H_2O/1% formic acid/1% cyclohexane followed by 99% isopropyl alcohol/1% cyclohexane to reduce sample carryover on the needle between each run.

We set up a workflow in the Agilent MassHunter Qualitative Analysis workstation to annotate signals in our raw MS data using the Metlin Lipids MS Database [175]. To verify these annotations, we measured the retention time (RT) alignment of each lipid by calculating the coefficient of variation (CV) of the respective RT across all the samples run on this method (6 per cell group = 30 samples total). We used the 500 lipids with the *lowest* CV of RT (<25%) in our global quantitative lipidomics analysis. Only 112 total lipids among the lipids identified in the cell medium samples met these criteria (CV of RT ≤25%) and were used for global extracellular lipid profiling.

Western Blot Analysis

Cell pellets were lysed with ice-cold RIPA lysis buffer supplemented with protease inhibitor (Thermo scientific #A32965) and Phosphatase inhibitor (Thermo scientific #A32957). Protein concentrations of the clarified lysates were determined with the DC Protein Assay (BioRad). 50ug of total protein from each sample were resolved on 10% SDS-PAGE. Gels were then transferred to nitrocellulose membrane and were immunoblotted for proteins of interest (SK1 and p-SK1). Actin was used for loading controls. The following antibodies were used: Actin (C-2) *(Santa Cruz Biotechnology sc-8432)*, Anti-SPHK1 antibody (*Abcam ab71700)*, and SPHK1-Phospho-Ser225 Antibody (*Proteintech 19561-1-AP).* Proteins of interest were visualized and quantified by the Li-Cor Odyssey Classic or CLx imaging system and the Image Studio software package.

Targeted S1P/C16 Cer Quantitative Analysis and SK1 Activity Assay

Cell cultures were plated onto 15-cm cell culture dishes in complete RPMI 1640 Cell Medium and incubated at 37°C, 5% CO_2. Once cells reached 65-75% confluence, the cell medium was aspirated and cells were washed twice with 1xPBS. Medium was replaced with fresh, pre-warmed (37°C) complete RPMI 1640 medium containing 13µM of SKI-II inhibitor or an equivalent volume of 1x PBS for vehicle controls. All cells were treated with an equal dose of the inhibitor to maintain sample uniformity, which was the highest concentration of SKI-II used in our EC50 estimation assay (See **Results**). We considered this dose representative of the concentration of SKI-II required to sensitize cells to a drug-induced effect on cell viability in a population of healthy pancreatic cells. Cell cultures treated with SKI-II and vehicle controls were incubated for 12 hours at 37°C, 5% CO_2. After the incubation period, total lipids were extracted from the cells and cell medium followed by RP-LC-MS analysis using positive electrospray ionization using the methods described above (see **Intra/extracellular Lipidomics LC-MS Analysis**). To increase the detection and accuracy of our S1P and C16 Cer measurements, we spiked deuterated and/or odd-chain internal standards into each sample immediately following the cell lysis step and switched to a targeted version of our RP-LC-MS method designed to specifically select protonated S1P and C16 Cer ions for MS/MS fragmentation. Diluted stock solutions of the internal standards were made by diluting in MeOH and the following volumes were spiked into each sample prior to lipid extractions: 20µL of 2.5µM C16 Cer-d7 diluted in MeOH, 20µL of 2.5µM C17 Cer diluted in MeOH, and 20µL of 5µM S1P.

Our sphingolipid optimized sample preparation and LC-MS method significantly improved the singal:noise ratio of C16 Cer ions in all of our samples, greatly increasing the confidence of our annotation and quantitation of this particular target. Yet, we were concerned that the QTOF lacked sensitivity required to detect low S1P levels because it was not observed all our cell samples. In addition, the upper pressure limit on the pumps leading to our QTOF instrument limited our ability to run at pressures high enough to potentially increase the S1P signal:noise ratio. To further improve the consistency and accuracy of our S1P detection and quantitation, we reran our samples using an S1P targeted method with higher pressure pumps and a more sensitive triple-quadrupole (qQq) mass spectrometer at the Metabolomics Core

Facility at the University of Utah [72]. This method significantly improved the chromatography, signal intensity, fragment verification, and overall consistency of our S1P measurements in all our samples **(Figure 2-8B; 10A-B)**.

The identities of our two sphingolipid targets, C16 Cer and S1P, were confirmed by retention time alignment **(Figure 2-8A-B)** and MS/MS fragment verification **(Figures2- 9-10)** with the corresponding internal standards. Quantitation of S1P and C16 Cer was performed by normalizing to the AUC of the corresponding internal standards initially spiked into the cell lysates (50 pmol of C16 Cer-d7, 50 pmol of C17 Cer, and 100 pmol of S1P-d7). The following equation was used for C16 Cer quantitation: $(50\text{pmol}) / (\text{AUC}_{\text{C16Cer-d7 or C17 Cer}}) = (x \text{ pmol}) / (\text{AUC}_{\text{D7C16Cer}})$, where x=[C16 Cer] (**Figure 8A**). Note that C16 Cer was normalized to whichever internal standard had higher a signal:noise ratio in the MS run (C16 Cer-d7 or C17 Cer). The following equation was used for S1P quantitation: $(100\text{pmol}) / (\text{AUC}_{\text{D7S1P}}) = (x \text{ pmol}) / (\text{AUC}_{\text{S1P}})$, where x=[S1P] (**Figure 2-8B**).

Cell Proliferation Assay

Cells from each group were plated evenly on a 24-well tissue culture dishes and incubated overnight at 37°C, 5% CO_2. Each dose of SKI-II inhibitor (*Santa Cruz Biotechnology cas 312636-16-1*) was prepared by serial dilution in complete RPMI 1640 Cell Medium (Thermo Fisher cat # 11875093). The SKI-II treated volumes of cell medium were sterilized on 0.2µm filters and heated to 37°C. Wells containing adhered cells in the tissue culture dishes were aspirated and washed twice with 1x PBS. 1 mL of SKI-II treated medium was added to each well. Real-time phase object confluence was monitored over time using an Incucyte ZOOM® Live-Cell Analysis System at 37°C, 5% CO_2 and quantitative data were analyzed using the

Incucyte ZOOM® data analysis software to generate cell growth curves. Proliferation rates were determined by calculating the mean slope of the linear-like growth phases of 3-4 biological replicates per group.

Flow cytometry cell death assays

Cell death assays were completed by plating cells in T-75 flasks (~10,000 cells/cm^2) in log-phase growth and allowing a minimum of 6 hours for growth and adhesion before drug treatment. Growth media was replaced with fresh media prior to injection of drugs into culture flasks or plates. Cells were then treated for 12-24 hours with drugs. At the end of drug treatment, dead cells were removed and collected in a new plate. Cells were washed with 1x PBS and this was collected and combined into the new plate. Living adhered cells were removed from growth plates using 0.05% pH balanced trypsin at 37°C and then transferred to the new plate. Under dark conditions on ice a 1 mg/100 mL solution of propidium iodide (PI) was mixed with light shaking into the cell mixture and allowed 15 minutes to stain. PI is a DNA-binding fluorescent dye used to distinguish between live cells with intact membranes versus dead cells whose membranes are permeable to the dye [176]. Cell counts were then collected on a red/blue acoustically focused Applied Biosciences Attune flow cytometer at a scan rate of 200 µL/min using BL2-PI blue laser and BL1 blue laser. Data was analyzed with the Attune software.

Quantitation and statistical tests

If not otherwise specified, figure development as well as data quantitation and statistical tests were conducted in Excel (dot plots, bar graphs, t-tests, Benjamini-Hochberg procedure) and JMP (box plots, t-tests, Dunnett’s tests, Tukey-Kramer tests).

SUPPLEMENTAL TABLES

Supplemental Table 2-1 Comparison of components in cell growth mediums used to feed pancreatic cancer groups (pA, pB, pC, pD) during subculturing experiment. *Concentrations of* ***(A)*** *amino acids,* ***(B)*** *vitamins and* ***(C)*** *salts and other components in RPMI 1640, DMEM and IMDM cell culture mediums in the concentrations between each component in the three different formulations.* ***(A-C)*** *Cells in the table shaded red indicate differences between formulations while those shaded green indicate the concentrations of the component in the respective row are the same among the formulations.*

A

Amino acid (mM)	**RPMI (pA, pC)**	**DMEM (pB)**	**IMDM (pD)**
Glycine	0.133	0.400	0.400
L-Alanine	0	0	0.281
L-Arginine hydrochloride	0	0.398	0.398
L-Arginine	1.149	0	0
L-Asparagine (freebase)	0	0	0.189
L-Asparagine	0.379	0	0
L-Aspartic Acid	0.150	0	0.226
L-Cystine 2HCl	0.208	0.201	0.292
L-Glutamic Acid	0.136	0	0.510
L-Glutamine	2.055	4.000	4.000
L-Histidine hydrochloride-H2O	0	0.200	0.200
L-Histidine	0.097	0	0
L-Hydroxyproline	0.153	0	0
L-Isoleucine	0.382	0.802	0.802
L-Leucine	0.382	0.802	0.802
L-Lysine hydrochloride	0.219	0.798	0.798
L-Methionine	0.101	0.201	0.201
L-Phenylalanine	0.091	0.400	0.400
L-Proline	0.174	0	0.348
L-Serine	0.286	0.400	0.400
L-Threonine	0.168	0.798	0.798
L-Tryptophan	0.025	0.078	0.078
L-Tyrosine disodium salt dihydrate	0.111	0.398	0
L-Tyrosine disodium salt	0	0	0.462
L-Valine	0.171	0.803	0.803

B

Vitamin (mM)	**RPMI**	**DMEM (pB)**	**IMDM (pD)**
Biotin	8.20×10^{-4}	0	5.33×10^{-5}
Choline Chloride	0.021	0.029	0.029
D-Calcium pantothenate	0.001	0.008	0.008
Folic Acid	0.002	0.009	0.009
Niacinamide	0.008	0.033	0.033
Para-Aminobenzoic Acid	0.007	0	0
Pyridoxine hydrochloride	0.005	0.019	0.020
Riboflavin	5.32×10^{-4}	0.001	0.001
Thiamine hydrochloride	0.003	0.012	0.012
Vitamin B12	3.69×10^{-6}	0	9.59×10^{-6}
i-Inositol	0.194	0.040	0.040

C

Salt/ Miscellaneous (mM)	**RPMI**	**DMEM (pB)**	**IMDM (pD)**
Calcium Chloride	0	1.802	1.486
Calcium nitrate	0.424	0	0
Ferric Nitrate	0	2.48×10^{-4}	0
Magnesium Sulfate	0.407	0.814	0.814
Potassium Chloride	5.333	5.333	4.400
Potassium Nitrate	0	0	7.52×10^{-4}
Sodium Bicarbonate	17.857	44.048	36.000
Sodium Chloride	103.448	110.345	77.672
Sodium Phosphate monobasic	0	0.906	0.906
Sodium Phosphate dibasic anhydrous	5.634	0	0
Sodium Selenite	0	0	9.83×10^{-5}
D-Glucose (Dextrose)	25.000	25.000	25.000
Glutathione (reduced)	0.003	0	0
HEPES	10.013	0	25.034
Phenol Red	0.013	0.040	0.040
Sodium Pyruvate	1.000	0	1.000

Supplemental Table 2-2 STR Profile Reports of healthy control and pancreatic cancer cells before and after subculturing experiment. (A) *Results of STR profiling of healthy immortalized control cell line (hTert) relative to the ATCC reference database profile for hTert-HPNE.* ***(B)*** *Results of STR profiling of originating cell line at time=0 (PSN-1) as well as the four different isolated subculture groups (psn1-A, psn1-B, psn1-C, psn1-D) from the originating PSN-1 cell line after subculturing experiment, genotypic and phenotypic profiling (time~6 months) relative to the ATCC reference database profile of PSN-1.*

A	Test Results *Healthy Control cells*		**ATCC Reference**	
Locus	Query Profile: **hTert**		Database Profile: hTert-HPNE	
TH01	8	9	8	9
D5S818	11		11	
D13S317	12	13	12	13
D7S820	9	10	9	10
D16S539	12	13	12	13
CSF1PO	12		12	
Amelogenin	X	Y	X	Y
vWA	17		17	
TPOX	8	11	8	11
Total # of alleles in database profile	15			
# of shared alleles b/t query sample & database profile	15			
% match between sample & hTert-HPNE database profile	**100%**			

B

	Test Results *Originating cells*		Test Results *Subculture A*		Test Results *Subculture B*		Test Results *Subculture C*		Test Results *Subculture D*		**ATCC Reference**	
Locus	Query Profile: **PSN-1**		Query Profile: **psn1-A**		Query Profile: **psn1-B**		Query Profile: **psn1-C**		Query Profile: **psn1-D**		**Database Profile: PSN-1**	
TH01	6		6		6		6		6		**6**	
D5S818	11	13	11	13	11	13	11	13	11	13	**11**	**13**
D13S317	10		10		10		10		10		**10**	
D7S820	10		10		10		10		10		**10**	
D16S539	11		11		11		11		11		**10**	**11**
CSF1PO	12		12		12		12		12		**12**	
Amelogenin	X		X		X		X		X		**X**	
vWA	17		17		17		17		17		**17**	
TPOX	8	11	8	11	8	11	8	11	8	11	**8**	**11**
Total # of alleles in database profile	11		11		11		11		11			
# of shared alleles b/t query sample & database profile	12		12		12		12		12			
% match between sample & PSN-1 database profile	**92%**		**92%**		**92%**		**92%**		**92%**			

ABBREVIATIONS

hTert-HPNE: (hTert or hT); psn1-A or pA: PSN-1 subclone group A; psn1-B or pB: PSN-1 subclone group B; psn1-C or pC: PSN-1 subclone group C; psn1-D or pD: PSN-1 subclone group D; SK1: Sphingosine Kinase 1; C16 Cer: Ceramide(d18:1/16:0); C16 Cer-d7: Ceramide(d18:1-d7/16:0); C17 Cer: Ceramide(d18:1/17:0); S1P: Sphingosine-1-phosphate (d18:1); S1P-D7: Sphingosine-1-phosphate (d18-d7:1); SKI-II: Sphingosine Kinase Inhibitor 2; Gem: Gemcitabine.

ACKNOWLEDGEMENTS

We sincerely thank: Dr. David Bearss for the generous gift of the pancreatic cancer lines; Dr. Bearss and Dr. Daniel D. Von Hoff for helpful conversations; BYU RIC facility for assistance in the cell death assay; The Brigham Young University DNASC in the Department of Biology under the direction of Dr. Michael F. Whiting and managed by Dr. Edward Wilcox; Ryan Sheaparé for assistance in figure design, and the following individuals for their helpful advice and kind support throughout the duration of this study: Kyle Speirs, Bradley Naylor, Bruce Jackson, Lavender Hsien-Jung Lin, Daniel Mortensen, Colten McEwan, Nathan Rotriguez, and Rusty Denton.

FUNDING

This study was supported by BYU Department of Chemistry and Biochemistry, Ronald K. Robins Graduate Research Fellowship, Fritz B. Burns Funds for cancer research at BYU, and the BYU Simmons Center for Cancer Research.

3. Autophagy targets mitochondria specifically in tumors, but not the liver of HCT116 xenograft mice

Chapter Summary

This chapter is the final manuscript demonstrating our novel kinetic proteomics based *in vivo* autophagy assay in an animal model of colorectal cancer. It was submitted to *Molecular & Cellular Proteomics* in October 2018 and is currently under review for publication.

Authors in Order of Contribution

Monique Merilyn Paré Speirs*[1], Bradley C. Naylor[1], Frederick F. Peelor III[2], Karyn Hamilton[2], Benjamin F. Miller[3], Joshua L. Andersen[1], John C. Price[1]

Author affiliations: 1. Department of Chemistry and Biochemistry, Brigham Young University, Provo, Utah 84602. 2. Aging and Metabolism Research Program, Oklahoma Medical Research Foundation, Oklahoma City, OK 73104. 3. Department of Health and Exercise Science, Colorado State University, Fort Collins, Colorado 80523.

Contributions of Authors

I carried out all stages of the *in vitro* experiments, including cell culture maintenance, experimental design, sample collection and preparation, instrument maintenance, *in vitro* cell proliferation assays, as well as *in vitro* data analysis and interpretation under the direction of John C. Price. Joshua L. Andersen and John C. Price designed the mouse experiment and all live mouse handling and dissections were performed at the Huntsman Cancer Institute (HCI) at the University of Utah under the direction of Dr. David H. Lum (HCI Preclinical Research Resource

Director). I subsequently performed all mouse tissue handling, developed protocols for sample preparation and prepared all mouse tissue samples for mass spectrometry (LC-MS and GC-MS), performed all steps of the percentage blood D_2O analysis, performed all steps of the immunofluorescence assays, analyzed and interpreted all data, produced all the figures, and wrote the manuscript under the direction of John C. Price. Fredrick Peelor III, Karyn Hamilton, Benjamin Miller conducted the GC-MS analysis of DNA samples used for the *in vivo* cell proliferation measurement. Bradley C. Naylor greatly assisted in data analysis of *in vivo* kinetic and quantitative proteomics as well as the deuterium enrichment data.

ABSTRACT

Motivation

The activation of the catabolic pathway autophagy is strongly connected to cancer stress tolerance and chemoresistance. Pharmacological inhibition of autophagy is a potential strategy to sensitize tumors to traditional chemotherapeutics. Current clinical trials are attempting to control autophagy flux using lysosomal inhibitors such as chloroquine (CQ) with limited knowledge of the side effects of these drugs on protein homeostasis and metabolism in healthy surrounding tissues. If autophagy is used differently in cancer relative to healthy tissue, then oncogenic functions and specific autophagy substrates creates opportunity for specific chemosensitizing therapies. We used D_2O-based metabolic labeling and mass spectrometry combined with standard quantitative proteomics techniques to measure CQ-dependent changes in autophagy substrate turnover and concentration in a xenograft mouse model of colon cancer.

Results

We found that autophagy substrates differ in the tumor versus liver tissue. Our results suggest that autophagy is used to selectively degrade mitochondria (mitophagy) in tumor cells, perhaps to promote mitochondrial function and biogenesis. On the other hand, autophagy is used broadly as a bulk degradation system in the liver to promote global proteostasis. These experiments support a model of modified mitochondrial metabolism, enforced in part by rapid autophagic degradation, as a pro-survival mechanism in cancer. We also observed off-target effects in the liver consistent with a toxicity response to treatment. This suggests that inhibition of substrate-specific autophagy degradation pathways may be an effective anti-cancer treatment that will be well tolerated by healthy tissues.

Data Availability

Supplemental databases are stored on the Price lab research drive. All raw data are available within the Chorus repository (Chorusproject.org, project #1534: Autophagy_Xenograft_2018).

ABBREVIATIONS

CRC: colorectal cancer; HCT116: Human Colon Tumor 116 cell line; D_2O: deuterated water; p62: Sequestosome-1/p62, LC3: microtubule associated light chain 3; TR: protein turnover rate; FC: fold change; AUC: area under the curve; TIC: total ion count; INST: internal standard; CQ: chloroquine diphosphate; Ox/Oxali: oxaliplatin.

INTRODUCTION

Cancer recurrence and chemoresistance are a frequent problem, and in some cancers can limit the 5-year survival rate to as low as 8% [177]. Metabolic adaptations that increase stress resistance are important to promote the transition to, and maintenance of, the cancerous phenotype while enhancing chemoresistance [24]. Cell metabolism and cell-fate can be modified by shifting specific protein synthesis and degradation systems [178]. As a result, the lifetimes or turnover rates of structures throughout the cellular proteome may change as cells become cancerous or drug resistant. The turnover of transiently expressed or shorter-lived proteins is generally controlled by the ubiquitin-proteasome system (UPS) [179]. Longer-lived proteins and organelles accumulate damage over time and must also be turned over periodically to minimize toxic effects of damaged structures on the cell [179]. Macroautophagy (hereafter referred to as autophagy) is an evolutionarily conserved catabolic process that can degrade whole protein complexes, organelles, and aggregated proteins. This recycles the resulting monomeric components, which can be used as metabolic intermediates to support cell survival and fitness [74,76,178].

Autophagy begins with the formation of a double membrane bound vesicle, called an autophagosome (**Figure 1**), which sequesters the soon-to-be degraded cytosolic targets [76]. Lysosomes subsequently fuse with autophagosomes (forming autophagolysosomes) to degrade the encapsulated cargo, thereby providing carbon and nitrogen sources for energy metabolism or macromolecular biosynthesis and cofactors for redox balance [76,180,181]. Basal autophagy occurs at low levels in healthy cells, has been shown to prevent chronic tissue damage over time, and contributes to multiple physiological processes such as differentiation, programmed cell death, as well as innate and adaptive immunity [76]. Long-term differences in autophagy flux impact the concentrations and biosynthesis rates of complexes, organelles, and their constituent proteins throughout the cell [178].

Metabolic stresses characteristic of the tumor microenvironment (hypoxia, nutrient deprivation, and ROS) are known to upregulate autophagy [76,182,183]. Accumulating evidence suggests that increased utilization of autophagy promotes a diverse array of survival responses including chemoresistance [24,75,80,178,180,182,184-187]. Autophagy contributes to cellular metabolism and homeostasis at multiple levels by promoting protein and organelle quality control, clearing toxic structures from the cytosol, altering intracellular concentrations of a variety of functional proteins, and boosting biosynthesis and energy metabolism [178]. These beneficial functions are presumably why many types of cancer cells display an "autophagy addiction" [188], but the exact mechanisms of autophagy-driven cell survival in cancer and chemoresistance are just emerging [76,80].

Autophagy is frequently described as a nonselective degradation system whereby autophagosomes randomly surround large portions of the cytosol to rapidly produce biofuels when nutrient levels are lacking [189]. Constitutive activation of autophagy in this manner would be bioenergetically inefficient, because it would increase demand for protein synthesis in proliferating cancer cells that are already suffering extreme basal levels of metabolic stress [6,28,143]. Recent research suggests instead that autophagy is highly regulated and may respond to intrinsic and environmental stresses by targeting *specific* proteins or organelles such as ribosomes [49,190], mitochondria [81,191], endoplasmic reticulum [192], proinflammatory signaling proteins [75], portions of the nucleus [193], or the proteasome [52]. Autophagosomal targeting of specific cytosolic substrates, a process known as "*selective* autophagy" [75,79,194] could confer a significant metabolic advantage in proliferating cancer cells by consuming excess or deleterious proteins and reusing the resulting amino acids to serve as bioenergetic precursors or building blocks for cellular structures in higher demand [191].

The specificity of autophagosome cargo selection in cancer versus healthy tissues, and whether autophagy targets certain pathways to regulate global cancer cell metabolism and function, are poorly understood [195]. Selective autophagy may be accomplished in part by autophagy adapter proteins such as Sequestosome-1/p62, which recognizes polyubiquitinated structures and forms a bridge between the targeted cargo and the establishing autophagosome [134,196]. Chaperones such as heat shock proteins have also been shown to shuttle specific substrates to autophagosomes for degradation, a process known as chaperone mediated autophagy [197]. Identifying autophagic targets in healthy versus tumor tissues is crucial to understand how autophagy provides a metabolic advantage in xenograft [23]. Targeting selective systems of autophagy rather than global autophagy may facilitate more selective tumor inhibition. However, this remains to be comprehensively explored in tumor and healthy surrounding tissues, in part due to the challenge of measuring the highly dynamic processes and biological effects of autophagy *in vivo* [83,198,199].

Traditionally, proteins associated with the autophagosome, including microtubule associated light chain 3 (LC3) and p62, have been used as autophagosomal markers and the standard for conventional autophagy detection assays, such as Western blot and immunohistochemistry [83]. While such techniques can be used to quantitate general levels of autophagosome accumulation at a given time point, they do not necessarily differentiate between the dynamic effects of increased autophagy initiation or decreased autophagosome degradation. Changes in protein degradation rates and autophagy flux have been explored using “pulse-chase” experiments to measure protein half-lives using radioactively labeled amino acids that are incorporated and subsequently removed from specific protein targets, such as p62 over time [200,201]. Recent advances in mass spectrometry have led to the birth of *in vivo* kinetic proteomics techniques that can be used to measure treatment induced effects on global and pathway-specific metabolic flux [46,47,49,202-206].

To investigate *in vivo* regulation of autophagy in a cancer mouse model, we performed time-resolved metabolic labeling using low levels of dietary heavy water (D_2O) and mass spectrometry, a cost-effective technique that is easily adapted in humans [47] (**Figure 3-1**). Nonspecific autophagy inhibitors like chloroquine diphosphate (CQ), a lysosomotropic agent that suppresses lysosomal enzyme activity, autophagolysosome formation, and autophagosome cargo degradation, have been shown to sensitize resistant cancer lines and animal models to chemotherapy at tolerable doses [182,186]. Ongoing clinical trials are currently testing CQ or its derivative hydroxy-CQ combined with conventional chemotherapeutics [207]. However, such drugs are considered “double edge swords” when it comes to cancer treatment, since surrounding healthy tissues that depend on basal autophagy to maintain protein quality and cellular metabolism may be sensitive to CQ and damaged by the combined chemotherapy [78]. We tested the effects of CQ mediated autophagy inhibition on protein concentrations and turnover in both cancerous and healthy tissues of human tumor derived xenograft mice (**Figure 3-1**).

Our results suggest that autophagy contributed to maintaining basal concentrations of the majority of the proteome in both xenograft and normal mouse tissues. Autophagy may play distinct functional roles in remodeling the proteomes of tumor versus healthy cells, since our results indicate that autophagy mediated protein degradation was selective toward different substrates in the xenograft compared to the liver. In the tumor, mitochondrial protein turnover and concentrations were significantly more sensitive to CQ-induced autophagy inhibition. In the liver, many functional protein categories were sensitive to CQ treatment. Our results suggest that selective autophagy driven turnover of mitochondria (mitophagy) may serve as a tumor-specific drug target with reduced off-target effects in healthy surrounding tissues.

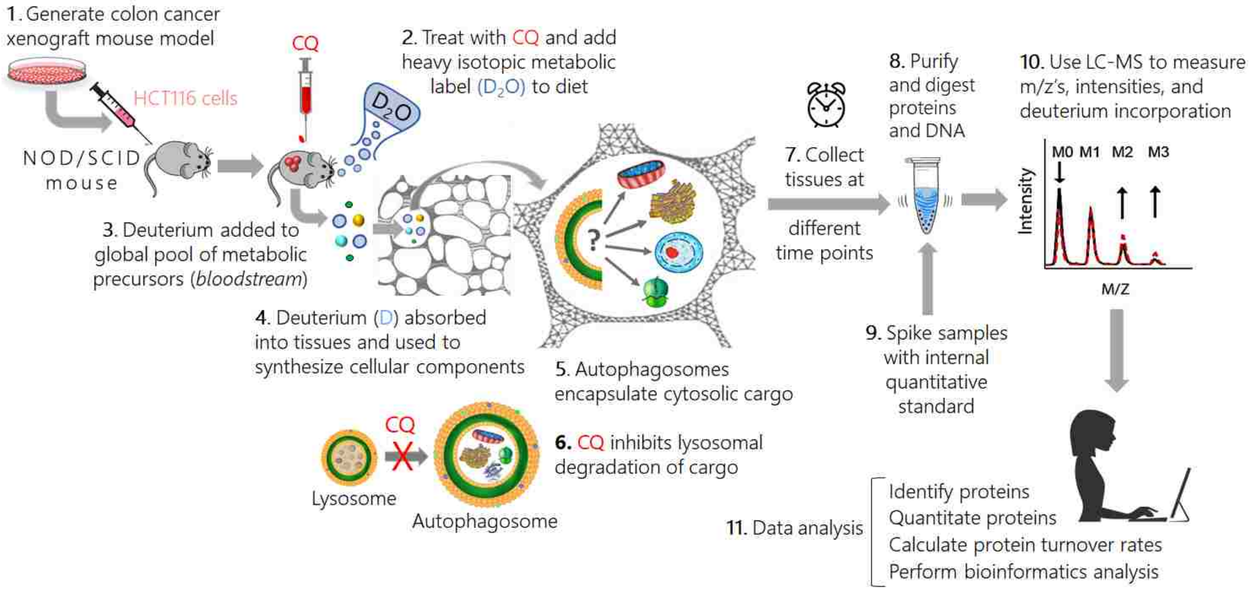

Figure 3-1 In vivo autophagy flux measurement workflow. *HCT116 xenograft mice were treated with an autophagy inhibitor (CQ) or the vehicle (H_2O) and deuterated water (D_2O) was added to the diet of mice to be used for kinetic measurements (12 biological replicates per treatment group). The heavy isotopes were absorbed into tissues and subsequently incorporated into cellular DNA and proteins over time via DNA and protein synthesis. Blood, tumor, and liver tissues were collected at different time points to monitor blood D_2O percentage and incorporation of the heavy label into cellular DNA and proteins over time, which serves as a measure of DNA and protein turnover, or the fraction of new DNA/protein produced per unit of time (hours). We used duplex peptide stable isotope dimethyl labeling for quantitative proteomics measurements of tumor tissue samples and an L-Lysine (97% 13C6) SILAM (stable isotope labeling in mammals) mouse liver tissue standard for quantitative proteomics of liver tissue samples collected at the final time point of the metabolic labeling experiment (96 hours). LC-MS was used to measure the relative intensities of each peptide and levels of isotope incorporation into nucleotides and peptides over time, which were used to calculate relative protein concentrations and molecular turnover rates (fraction of new protein or DNA replaced per hour) in each drug treated group relative to vehicle controls using PEAKS and in-house developed software tools. DNA turnover was used as a metric of in vivo cell proliferation over the course of the metabolic labeling experiment. Protein turnover and concentration measurements were used to infer changes in protein synthesis and degradation rates induced by the drug. A bioinformatics analysis was performed to investigate concentration and turnover changes of specific autophagy substrates relative to the global proteome in each tissue type.*

EXPERIMENTAL PROCEDURES

Experimental Design and Statistical Rationale

Cell culturing experiments: Human colorectal tumor derived cells (HCT116 cells [208]) were plated evenly on 12-well tissue culture dishes and incubated overnight in 2 mL of complete tissue culture medium made up of 1x Dulbecco's Modified Eagle Medium (DMEM, Gibco #11965-092) containing 10% Fetal Bovine Serum (FBS) per well at 37°C and 5% CO_2. Stock solutions of drug treatments and vehicle control conditions (drug treatments: 5µM CQ, 0.625µM oxaliplatin, or [5µM CQ + 0.625µM oxaliplatin]; vehicles: 1x PBS/DMSO) were diluted in complete tissue culture medium (DMEM + 10% FBS), thoroughly mixed on a vortex for 60 seconds, sterilized on 0.2µm filters, and heated to 37°C. Cell medium in wells containing adhered cells were aspirated and washed twice with 1x PBS. Two mL of drug or vehicle-treated complete cell medium or serum-free DMEM were added to each well. Real-time phase object confluence was monitored over time using an Incucyte ZOOM® Live-Cell Analysis System at 37°C and 5% CO_2. Quantitative cell proliferation data were analyzed using the Incucyte ZOOM® data analysis software to generate cell growth curves. Proliferation rates were determined by calculating the mean slope of the linear-like growth phases of four biological replicates per group subsequent to the addition of each treatment.

Relative concentrations of p62 in CQ treated and vehicle control cells were measured in biological triplicate using label-free quantitative proteomics (**Table S1**). The cell medium was aspirated from each well, cells were washed twice with 1x PBS and removed from the tissue culture dish by trypsinization. Cells were pelleted via centrifugation at 1200 rpm for 5 minutes. The supernatant was decanted and pellets were flash frozen in dry ice. Cell pellets were stored at

-80°C. Frozen cell pellets were lysed and prepared for mass spectrometry (see Sample preparation for quantitative and kinetic proteomics analyses).

HCT116 xenograft mouse experiment: Live mouse handling and dissections were performed in a pathogen-free facility with 12-hour light/dark cycles at the Huntsman Cancer Institute (University of Utah). All protocols were approved by the University of Utah Institutional Animal Care and Use Committee. Twenty-five 6-week-old male NOD/SCID mice (NOD/MrkBomTac-*Prkdc*^{scid}) were implanted with HCT116 cells ($3x10^6$ in 35uL matrigel) in each flank. After tumors reached sufficient size, one control (no deuterium) HCT116 xenograft mouse was sacrificed and blood was extracted via cardiac puncture for deuterium enrichment analysis. Tumor and liver tissues were removed, flash frozen, and stored at −80 °C.

The remaining HCT116 xenograft mice were divided randomly into the drug and vehicle control groups and received an intraperitoneal (IP) injection of saline (vehicle group) or 60mg per kg of body weight of chloroquine (drug group). One hour later, all mice received a second IP of D_2O saline (35ul/g body wt.) to equilibrate physiological deuterium levels and were provided 8% w/w D_2O-enriched drinking water for the remainder of the experiment. Vehicle and CQ were delivered *via* IP for 4 consecutive days (60mg/kg daily). Four mice from each group were consecutively euthanized 24, 48, and 96 hours after D_2O administration. Immediately after each euthanization, blood was extracted via cardiac puncture for deuterium enrichment analysis, and tumor and liver tissues were removed, flash frozen, and stored at −80 °C.

There were up to four biological replicates for each time point. A minimum of three, (one at each time point) were required for protein quantitation and kinetic analysis. Median concentration and the best fit turnover rates were calculated with confidence intervals around each value. If the 95% confidence interval normalized to the turnover rate was greater than or equal to 0.5, the protein was discarded. Protein turnover rates were compared between the treatment and vehicle control group based on the following criteria: turnover was considered “decreased” if the fold change in turnover (drug/vehicle) was <0.9; turnover was considered “increased” if the fold changed in turnover was greater than or equal to 1.1; turnover was considered “unchanged” if the confidence intervals overlapped significantly or fold change was between 0.9 and 1.1 in CQ treated mice relative to vehicle controls.

The average protein concentrations of 3-4 biological replicates in the treatment and vehicle control groups were compared based on the following criteria: concentration was considered “unchanged” if the absolute value of the difference between averages for drug treated and control mice was less than the standard deviation of biological replicates; protein concentration was considered “decreased” if the fold change in the average concentration was less than 1 and the absolute value of the average difference between concentrations in CQ and vehicle control mice was greater than the standard deviation between biological replicates; protein concentration was considered “increased” if the fold change in average concentration was greater than 1 and the absolute value of the average difference between concentrations in CQ and vehicle control mice was greater than the standard deviation between biological replicates.

Pairwise comparisons of protein concentration and turnover within ontological categories of the proteomics data were made using paired t-tests. Tests involving multiple comparisons relative to a control group (such as individual protein ontologies relative to the global proteome) were carried out using the Dunnett’s test. Grouped comparisons were made using Students t-tests. Statistical tests were performed in Excel (2016) and JMP statistics package (version 13).

Measurement of deuterium enrichment

Blood collected at each time point was cooled to 4 °C and serum was separated from cells via centrifugation (800xG for 10 minutes). Aliquots of serum were diluted 1:300 in the same unenriched water used to create the standard curve. Body water D_2O enrichments were determined by direct measurement of deuterium molar percentage excess (MPE) in diluted blood serum. Isotopic enrichments were measured in duplicate for all time points (**Table S2**). MPE was measured against a D_2O standard curve using a cavity ring-down water isotope analyzer (Los Gatos Research [LGR], Los Gatos, CA, USA) according to the published method [209].

In vivo cell proliferation assay

New DNA was measured as the incorporation of deuterium into the deoxyribose (dR) moiety of the nucleoside bases extracted from tumor and liver tissues of mice following the 4-day treatment period with the vehicle or CQ (3-4 biological replicates per group, **Table S3**), as previously described [49,210]}[211]. Briefly, cells in approximately 100mg of frozen tissue were lysed on a bead beating tissue homogenizer in 1 mL of 25mM ammonium bicarbonate (pH~8). The nucleus was separated from cytosolic proteins *via* nuclear extraction [212]. DNA in the resulting nuclear pellet was purified using the Qiagen Miniprep Kit [213]. Isolated DNA was hydrolyzed into 5′ mononucleotides overnight at 37°C with nuclease S1 and potato acid phosphatase [214]. Hydrolysates were reacted with pentafluorobenzyl hydroxylamine and acetic acid and then acetylated with acetic anhydride and 1-methylimidazole. Dichloromethane extracts were dried and resuspended in ethyl acetate.

The pentafluorobenzyl triacetyl derivative of purine dR were analyzed by GC/MS (Agilent 7890B/5877A) by negative chemical ionization. Briefly, 1 uL of sample was injected into heated injection port (280°C). Helium was used as carrier gas at a flow rate of 1mL/min through an Agilent DB-17 column (30m x 250 um x .25um). The oven had an initial temperature of 140˚C for 1 minute, then ramped at 40˚C per minute to 270 ˚C where it held for 1 minute and then ramped to 40˚C per minute to 280˚C and held for 2 minutes. Methane was used as the reactant gas and selective ion monitoring for the 435 (m+0) and 436 (m+1) ions.

Sample preparation for quantitative and kinetic proteomics analyses

Frozen HCT116 cell pellets or approximately 100mg of frozen tumor or liver tissue from each xenograft mouse were prepared for LC-MS analysis. Cells in frozen pellets and tissues were thawed at room temperature and lysed in 1 mL of 25mM ammonium bicarbonate (pH~8) containing 10 µL of protease inhibitor mixture (Sigma) on a bead beating tissue homogenizer for 30 (cells) or 60 (tissues) seconds at 6 m/s. Total protein concentrations were quantified using a bicinchoninic acid assay (Thermo). Fifty micrograms of total protein in each sample were purified and prepared for LC-MS analysis using a modified filter-aided sample preparation protocol [215]. As described previously [49], protein was denatured in 6 M guanidine/HCl 100 mM Tris/HCl (pH 8.5). Cysteines were reduced using dithiothreitol and alkylated using iodoacetamide. Samples were placed on 500 µl 30 kD filters and washed two times on the filters using 6 M guanidine/HCl 100 mᴍ Tris/HCl, pH 8.5. The guanidine solution was removed by two 25 mM ammonium bicarbonate (pH~8) washes. Proteins were resuspended in 25 mM ammonium bicarbonate (pH~8) and digested overnight at 37˚C using Pierce MS-Grade Trypsin in a 1:50 (w:w) ratio per sample. Trypsin digests were quenched using phenylmethane-sulfonylfluoride and centrifuged through the above-mentioned filters to remove the trypsin. Samples were spun through filters, placed in mass spec vials, speed vacuumed to dry, and re-suspended at ~1 μg/μl in 3% acetonitrile 0.1% formic acid. No quantitative standard was added to cell culture samples and the relative concentrations of p62 were measured via label-free quantitative proteomics by normalizing the area under the curve (AUC) of p62 ions to the total ion count (TIC) in each sample.

Tumor tissue samples collected at the last time point of the *in vivo* autophagy assay (96 hours) were prepared for quantitative proteomics measurements using duplex peptide stable isotope dimethyl labeling [85]. N-termini and side chains of lysine and arginine residues of peptides derived from control (time=0 or non-deuterated) samples using the protocol described above were dimethylated with deutero-formaldehyde (CD_2O) to serve as quantitative internal standards while drug and vehicle treated samples were dimethylated with formaldehyde (CH_2O) using the method reported by Boersema *et al.* [85]. Equal amounts of internal standard peptide were mixed with each drug and vehicle treated sample. The ratio of CH_2O labeled sample to CD_2O labeled standard was used as a measure of the relative concentration of each protein in tumor tissue samples.

Liver tissue samples collected at the last time point (96 hours) of the *in vivo* autophagy assay were prepared for quantitative proteomics measurements by mixing predigested protein samples with equal amounts of Mouse Express L-Lysine Mouse Express (97% $^{13}C_6$) Mouse Liver Tissue SILAM (Stable isotope labeling in mammals) internal standard (Cambridge Isotope Laboratories, Inc. # MT-LYSC6-ML-PK). The ratio of sample relative to $^{13}C_6$ labeled standard was used as a measure of the relative concentration of each protein in the liver.

LC-MS data acquisition

Mass spectrometry data were collected using an Orbitrap Fusion Lumos mass spectrometer (Thermo Fisher Scientific, Waltham, MA, USA) coupled to an EASY-nLC 1200 liquid chromatography (LC) pump (Thermo Fisher Scientific, Waltham, MA, USA). A capillary RSLC column (EASY-spray column pepMap ® RSLC, C18, 2 µm, 100 Å, 75 µm × 15 cm) was used for separation of peptides. The mobile phase was comprised of buffer A (0.1% formic acid in optima water) and buffer B (optima water and 0.1% formic acid in 80% acetonitrile). The peptides were eluted at 300 nL/min with the following gradients over 2 h: 3–25% B for 80 min; 25–35% B for 20 min; 35–45% B for 8 min; 45–85% B for 2 min and 85% for 8 min. Data were acquired using the top speed method (3 s cycle). A full scan MS at resolution of 120,000 at 200 m/z mass was acquired in the Orbitrap with a target value of 4e5 and a maximum injection time of 60 ms. Peptides with charge states of 2-4 were selected from the top abundant peaks by the quadrupole for high energy collisional dissociation (HCD with normalized energy 29) MS/MS, and the fragment ions were detected in the linear ion trap with target AGC value of 1e4 and a maximum injection time of 250 ms. The dynamic exclusion time was set at 40 s. Precursor ions with ambiguous charge states were not fragmented.

Kinetics data acquisitions were performed in MS-only mode and collected at 60,000 m/z resolution. These settings increase signal intensity, improve signal-to-noise, and give more scan points per elution chromatogram, greatly enhancing kinetic analysis accuracy [202]. Raw data are available for download at the Chorus Project (1534: Autophagy_Xenograft_2018).

Peptide identification

PEAKS Studio software (version 8.5) was used for *de novo* sequencing database searching to identify proteins in our raw MS data as well as to quantify, filter (quality-control), and normalize our quantitation data for each protein [171]. Peptides were identified from MS/MS spectra by searching against the Swiss-Prot human (downloaded January 2018 or May 2018, for tumor and cell culture samples, respectively) and Swiss-Prot mouse databases (for liver samples only, downloaded January 2018) with a reverse sequence decoy database concatenated (**Table S9**). Variables for the search were as follows: enzyme was set as trypsin with one missed cleavage site. Carbamidomethylation of cysteine was set as a fixed modification while N-terminal acetylation and methionine oxidation were set as variable modifications. A false positive rate of 0.01 was required for peptides and proteins. Minimum length of peptide was set to 7 amino acids. At least 2 peptides were required for protein identification. The precursor mass error of 20 ppm was set for the precursor mass, and the mass error was set as 0.3 Da for the MSMS. Label-free quantitation was enabled with MS1 tolerance ±20ppm and a MS2 tolerance ±50 ppm, carbamidomethylation of cysteine was set as a fixed modification, while N-terminal acetylation and methionine oxidation were set as variable modifications. Protein annotations with a false discovery rate less than 1% were included in comparative quantitative analyses and used to generate protein identification files for the quantitative and kinetic analyses.

Quantitative proteomics data analysis

Protein quantitation in the cell culture was done using label free quantitation (LFQ) in the PEAKS software package (Version 8.5). After the removal of contaminants, low scoring peptides and reverse matches, the LFQ values for the top three peptides were summed for each protein (**Table S1**). The biological replicates were grouped into CQ-treated and vehicle control groups. Only proteins with at least three valid LFQ values in each group were used for quantification. For quantitation in the liver (**Table S4**) and tumor (**Table S5**) isotopically labeled internal standards were used (Liver: Lys-$^{13}C_6$ from Cambridge Isotope, Tumor: deutero-demethylation [85]) and the relative concentration of each protein was determined based on the AUC of each peptide relative to the heavy isotopic internal standard (light/heavy ratio). One advantage of the PEAKS quantitation is that multiple isotope (neutromer [216]) peaks within the isotope pattern of each peptide are summed for each peptide and its internal standard. This removed any detectable bias due to deuterium incorporation shifting intensity to heavier neutromer species in the experimental samples (**Supplemental Figure 3-1**). Gene ontology terms and information about protein function, location, and pathway assignment was cross checked between Uniprot [134], PANTHER [217], Human Cell Atlas [218,219], and DAVID Bioinformatics [42]. Statistical analyses and data plots were generated using Excel and JMP.

Kinetic proteomics data analysis

MS-only isotope distribution data was analyzed as previously described [202]. Neutromer [216] intensities and spacing values for each peptide were extracted from the RAW data files based on peptide identification from MSMS acquisition using m/z (± 12 ppm) and retention time alignment (± 0.8 minutes). Briefly, neutromer peaks M0–M4 were normalized against the sum of the signal intensity, then compared to theoretical calculations based on percentage D_2O enrichment to determine fraction deuterium enriched (new) peptide [49,202]. Theoretical changes were calculated using the eMASS algorithm [220] and based on the number of possible deuterium incorporation sites per amino acid [202]. The theoretical changes in abundance of each neutromer peak M0–M4 were compared against experimental changes at each time point in order to determine a time dependent percentage of newly synthesized peptide reported for each isotope peak. Thus, for each peptide there were up to 9 semi-independent measurements of the peptide turnover (measuring M0-M4 results in 5 intensity and 4 spacing metrics), as previously described [49,202]. We used the standard deviation between these measurements as a metric of the measurement precision for that peptide. If peptide precision was low (i.e. standard deviation exceeded 0.1), the data point was removed from downstream analysis [49]. Additional filters were also applied to remove peptides with total relevant intensity below 20,000 counts and a retention time deviation greater than 0.5 minutes.

The median percent new peptide was calculated at each point and outliers (defined as greater than 1.4 the median absolute standard deviation) were removed from the calculation of the protein percent new. All peptide measurements for an individual time point that passed these filters were weighted equally in the calculation of the percent new protein at that time point. As described previously, the M0% new data from the above mentioned peptides were combined and fit using a non-linear least squares regression based on first-order rate kinetic equations [49,202] The proteins with high precision data for at least two peptides at 3 or more time points were fit according to first-order rate kinetics. We required 3 or more labeled time points in order to increase the confidence of the rate constant. For the regression fit, time point zero was set to 0% new and was given a standard deviation of 0.05 based on the accuracy during long term performance of the instrument. Protein turnover rates, confidence intervals, and number of unique peptides after filtering are reported for the liver (**Table S6**) and xenograft tumor tissue samples (**Table S7**).

Immunofluorescence analysis

Immunohistochemical techniques were used to detect LC3-II positive autophagosomes, mitochondria, and nuclei in paraffin imbedded tumor and liver tissues of HCT116 xenograft mice following the 4-day treatment period (3 biological replicates per group). Tissues were fixed in formaldehyde solution (1mL of 37% formaldehyde, 9 mL of 1x PBS pH 7.4) at room temperature in sealed glass scintillation vials for 24 hours. The formaldehyde solution was removed and tissues were washed 3 times with 1x PBS (pH 7.4). Tissues were completely submerged and incubated in 15% sucrose at room temperature and washed 3 times with 1x PBS. The same steps were then repeated using 30% sucrose. Paraffin solution was prepared by mixing 1 package of Knox Gelatin (7g 225 Bloom) and 15g of Sucrose in 100mL of 1x PBS (pH 7.4) at 37°C. Fixed tissues were placed in 12-well tissue culture dishes and completely submerged in paraffin solution. The paraffin solidified overnight at 4˚C. Paraffin embedded samples were flash frozen in $N_{(l)}$ and stored at -20˚C. Tissue slices (20µM) were prepared from frozen tissues on a tissue cryostat at -20˚C and stored at -4˚C. Tissue sections were prepared for confocal imaging using LC3B (D11) XP® Rabbit mAb (Cell Signaling #3868), COX4I-1 (mitochondrial inner membrane) pAb (Novus Biologicals #NBP2-15975) using the Cell Signaling Technologies LC3B (D11) XP® Rabbit mAb #3868 immunohistochemistry protocol [221]. Nuclei were stained using Prolong® Gold AntiFade Reagent with DAPI (Cell Signaling #8961). Tissues were imaged via confocal microscopy and analyzed using ImajeJ (2-5 images analyzed per mouse).

Calculation of individual protein degradation rates

The classically accepted kinetic mechanism for protein turnover *in vivo* (**Figure 8A**) [222] shows that the relative concentration of each protein in the cell is controlled by a balance between the individual synthesis, and the sum of the individual protein degradation and cellular proliferation rates. This assumes that protein synthesis is unaffected by individual protein concentrations and that protein folding is very fast relative to these rates.

$$\textit{Equation 1:}\quad \frac{d[P_{correct}]}{dt} = k_{Synthesis} - \left(k_{Degradation}[Protein] + k_{Cell\ Division}\right)$$

Individual protein turnover rates, like those measured in this study, are the average of these rates [222].

$$\textit{Equation 2:}\qquad Turnover = \frac{k_{synth} + \left(k_{Degradation}[Protein] + k_{Cell\ Division}\right)}{2}$$

If we assume steady state conditions, *Equation 1*=0. So we can combine *Equation 1* and *2* to get *Equation 3*.

$$\textit{Equation 3:}\qquad Turnover = \frac{2 * \left(k_{Degradation}[Protein] + k_{Cell\ Division}\right)}{2}$$

Which can be rearranged to:

$$\textit{Equation 4:}\qquad k_{Degradation} = \frac{Turnover - k_{Cell\ Division}}{[Protein]}$$

These assumptions are probably quite good for the mice in the vehicle control group, but may underestimate the degradation rate constants during CQ treatment. The unknown variable is the timeline to achieving a new CQ-dependent protein homeostasis. However, the timeline for tumor growth restricts the possible dosing and sampling period. Regardless of this uncertainty, it was a useful starting point for our data analysis by allowing us to solve for the individual protein degradation rate constants in vehicle and drug treated groups. So, we used our experimentally determined values for individual protein turnover, cell division rates, and concentration measurements for individual proteins to calculate their relative degradation rate constants using *Equation 4* (**Tables S6** and **S7**).

RESULTS AND DISCUSSION

Autophagy inhibition reduced *in vitro* cell proliferation and sensitized CRC cells to chemotherapy

We tested whether autophagy contributed to the rapid growth and chemoresistant nature of human colorectal cancer (CRC) cells by generating cell growth curves of HCT116 cells before and after treatment with CQ as an autophagy inhibitor (**Figure 3-2A**). CQ significantly reduced average HCT116 cell proliferation by 65.3% ($P<0.05$). In conjunction with the change in growth, the concentration of p62 was considerably elevated in HCT116 cells treated with CQ relative to vehicle control ($P=0.05$), suggesting that this decrease in cell proliferation occurred simultaneously with a general reduction in autophagy flux resulting from the inhibitor (**Figure 3-2B**) [52].

We also tested whether chemotherapy sensitivity was increased in these cells during CQ treatment. Oxaliplatin (Oxal), a common treatment for colorectal cancer, significantly reduced HCT116 cell proliferation relative to the vehicle control by 78.3% ($P<0.0001$) (**Figure 3-2A**). The proliferation rate of cells treated with oxaliplatin combined with CQ was significantly lower than HCT116 cells treated with oxaliplatin alone (49.0 % decrease, $P=0.033$). These results suggest that these cells are a good model for investigating how autophagy promotes cell proliferation and enhances stress resistance in cancer cells.

Autophagy inhibition did not significantly reduce *in vivo* cell proliferation

One of the benefits of using D_2O as a metabolic tracer is that time-dependent deuterium incorporation can be used to mark many types of continually biosynthesized molecules in proliferating cells, including new proteins and new DNA. Evidently, rates of DNA synthesis serve as metrics of cell proliferation [210]. The rates of cell proliferation were significantly faster ($P<0.0001$) in tumor tissues of both CQ and vehicle control mice compared to the liver (**Figure 3-2C, Table S3**). This indicates that relative to normal tissues of the mouse, HCT116 xenograft cells maintained the cancerous phenotype of rapid proliferation. There was a trend toward reduced average cell proliferation rates after four days of CQ treatment in both the tumor (12.6% decrease, $P=0.3$) and liver (11.9% decrease, $P=0.5$). This suggests that autophagy played a role in encouraging basal growth rates in both the tumor and healthy tissues, but the treatment period was not long enough to induce a *significant* effect on cell proliferation rates in either tissue.

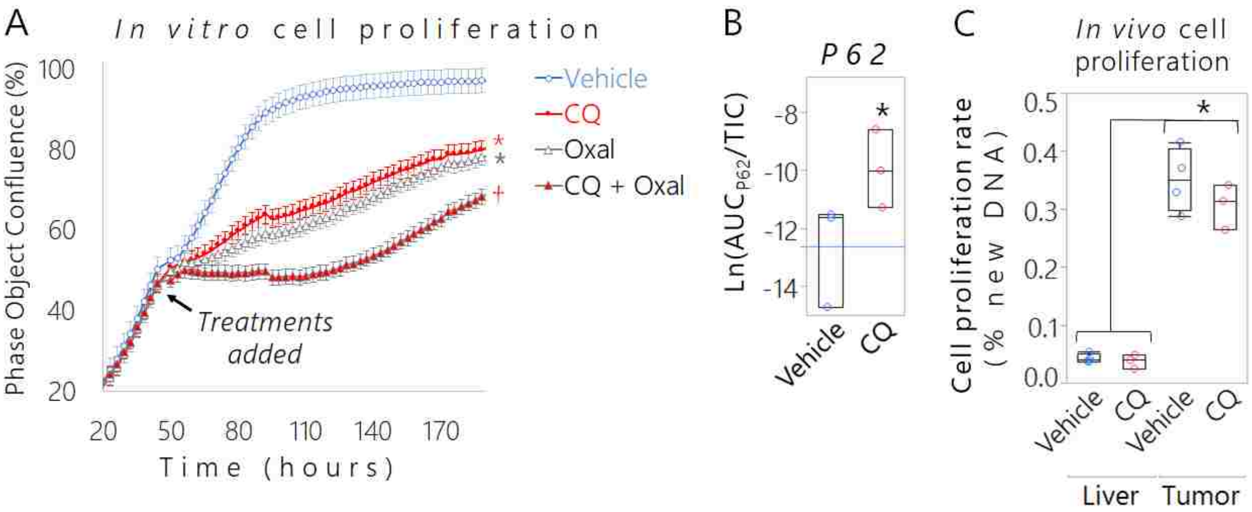

Figure 3-2 Autophagy inhibition slowed colon cancer cell proliferation and enhanced chemosensitivity. (A) *Live cell imaging was used to generate growth curves of HCT116 cells treated with the autophagy inhibitor (5µM CQ) versus vehicle controls (1x PBS) or chemotherapy (0.625µM oxaliplatin, Oxal) alone or in combination with 5µM CQ. Data are represented as the mean phase object confluence (%) of four biological replicates +/- SEM over time (hours). The * indicates $P<0.05$ using t-tests to compare the proliferation rate of individual drug treated groups (CQ or Oxal) to the vehicle control group. The † indicates $P=0.033$ using t-tests to compare the proliferation rate of the [5µM CQ + 0.625µM Oxal] combination treatment group to cells treated with 0.625µM oxaliplatin alone.* ***(B)*** *Label-free quantitative proteomics was used to measure the relative concentrations of p62 in HCT116 cells treated with the autophagy inhibitor (5µM CQ) relative to vehicle controls (1x PBS). Data are represented as the natural log of the area under the curve (AUC) of p62 normalized to total signal (total ion count, TIC) in each sample measured in biological triplicate. The * indicates $P=0.05$ based on a t-test comparison of p62 concentrations between the drug treated and vehicle control group. The blue line represents the average p62*

concentration of the vehicle control group, shown as a reference. ***(C)*** *Comparison of cell proliferation rates (% new DNA) in liver and tumor tissues of vehicle controls versus CQ treated HCT116 xenograft mice. Data are represented as the incorporation of D_2O into the deoxyribose (dR) moiety of the nucleoside bases following the 4-day treatment period. Data were collected in biological quadruplet or triplicate due to the premature death of one mouse in the CQ-treated group. The * indicates $P<0.0001$ using a t-test to compare between tissue types.*

In vivo **protein concentrations changed in response to autophagy inhibition in the tumor and liver**

In the tumor, 515 proteins met our statistical criteria for quantification with duplex peptide stable isotope dimethyl labeling [85] and were used to represent the global proteome in the tumor (**Figure 3-3A-B**). There was an 11.3% *decrease* in the median protein concentration of CQ mice relative to vehicle controls and this difference was statistically significant ($P<0.0001$) according to pair-wise comparisons for each protein measured in the CQ group relative to the same protein in the vehicle control (**Figure 3-3A-B**). The concentrations of more than half (60.8%) of the tumor proteome were not significantly changed relative to vehicle controls (the average difference between CQ and control mice was less than the standard deviation of biological replicates) (**Figure 3-3A-B**). The median concentration was reduced in the CQ tumor because almost 30% of proteins were significantly decreased relative to the vehicle control (fold change in average concentration less than 1 and the absolute value of the average difference between concentrations in CQ and vehicle control mice was greater than the standard deviation between biological replicates, **Figure 3-3A-B**).

In the liver, a total of 715 proteins met our statistical criteria for quantification against an L-Lysine mouse liver tissue SILAM (97% $^{13}C_6$) protein internal standard and were used to represent the global liver proteome (**Figure 3-3C-D**). Like in the tumor, the concentrations of over half of the liver proteome (65.6%) were unchanged by CQ treatment (**Figure 3-3C-D**). The proteome level response to autophagy inhibition was very different in the liver. Nearly 30% of liver protein concentrations were *increased* (fold change in average concentration greater than 1 and the absolute value of the average difference between concentrations in CQ and vehicle control mice was greater than the standard deviation between biological replicates) relative to vehicle controls (**Figure 3-3C-D**). Indeed, there was an 18.6% increase in the median protein concentration in liver tissue of CQ treated mice and this difference was significant (P<0.0001) according to pairwise comparisons between each protein concentration in the CQ treated group to its match in the vehicle control (**Figure 3-3C-D**).

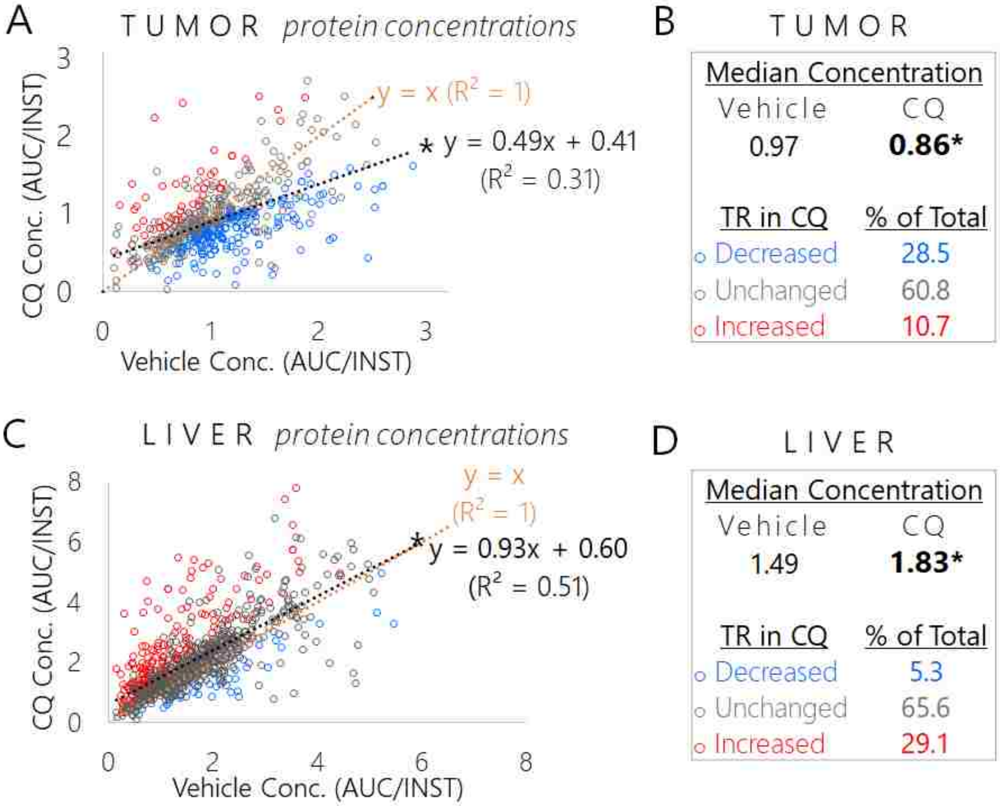

Figure 3-3 Effects of CQ induced autophagy inhibition on global protein concentrations in the tumor and liver. (A, C) *Comparison of relative protein concentrations (Conc.) in* ***(A)*** *tumor and* ***(C)*** *liver tissues of HCT116 xenograft mice treated CQ (y-axis) versus vehicle controls (x-axis) (n=515 tumor proteins common between groups and n=756 liver proteins common between groups). Each circle represents the relative concentration of a unique protein. The colors are indicative of the average concentration in the CQ group normalized to the vehicle control group measured in biological quadruplet; blue: protein concentration significantly decreased (the fold change in the average concentration was less than 1 and the absolute value of the average*

difference between concentrations in CQ and vehicle control mice was greater than the standard deviation between biological replicates), gray: protein concentration did not significantly change (the absolute value of the difference between averages for drug treated and control mice was less than the standard deviation of biological replicates), and red: protein concentration significantly increased (the fold change in average concentration was greater than 1 and the absolute value of the average difference between concentrations in CQ and vehicle control mice was greater than the standard deviation between biological replicates) in the tumor or liver tissue of CQ treated mice relative to vehicle controls. Data were collected in biological quadruplet and are represented as the AUC of each protein relative to the AUC of the respective internal standard (INST) in each tissue. The dotted black line is the linear trend line of the entire data set (Tumor: linear trend line slope=0.49, R^2*=0.41; Liver: linear trend line slope=0.93,* R^2*=0.51) shown to emphasize that protein concentrations generally decreased in the tumor and generally increased in the liver of CQ treated mice relative to vehicle controls (if the groups were identical, the fit line should have an approximate slope and* R^2 *of 1 and fall along the dotted orange line (slope=1) shown as a reference).* ***(C, D)*** *The median protein concentration of the entire quantitative dataset in the* ***(C)*** *tumor and* ***(D)*** *liver as well as the percentages of proteins whose concentrations significantly decreased (blue), were unchanged (gray), or significantly increased (red) in HCT116 xenograft mice treated with CQ versus vehicle controls for each tissue type.* ***(A-D)*** *The * indicates P<0.0001 using paired t-tests to compare each protein concentration in the vehicle control group to the corresponding concentration in the CQ treated group.* ***(A-D)*** *The * indicates P<0.0001 using paired t-tests to compare each protein concentration in the vehicle control to the corresponding concentration in the CQ treated group in each tissue type.*

In vivo protein turnover changed in response to autophagy inhibition in the tumor and liver

The turnover rates of a total of 1,652 unique proteins met our statistical criteria and were used to represent the global proteome in our kinetic analysis of the tumor (**Figure 3-4A-C**). The turnover rates (TR) of 43.3% of proteins were unchanged (fold change was 0.9 < TR <1.1 or displayed overlapping confidence intervals), the turnover rates of 37.7% were decreased (fold change in TR < 0.9), and 19.0% were increased (fold change in TR ≥ 1.1) in CQ treated mice relative to vehicle controls (**Figure 3-4A-B**). Overall, there was a 5% *decrease* in the median TR of the tumor proteome and pairwise comparisons between each protein in the CQ group relative to the vehicle control revealed that this global kinetic change was statistically significant (**Figure 3-4A-B**, P<0.0001). This decrease was less than expected if turnover rates were driven primarily by a change in cell proliferation (~12% slower) (**Figure 3-2C**).

Previous work has shown that the half-lives of short and long-lived proteins may respond to autophagy inhibition in different ways [52]. To explore this concept, we split the data set into long versus short-lived groups based on the half-life measured in vehicle control. We observed that the CQ induced reduction in turnover among proteins in the short-lived group was significantly more pronounced ($P<0.0001$) compared to those in the long half-life group (**Figure 3-4C**). The greater effect on short-lived proteins is probably not just due to the short measurement period as 30% of the cells in the tumor were new within the measurement (**Figure 3-2C**). Our results suggest that autophagy not only influences the turnover of long-lived structures, as traditionally described [179], but also plays an important role in regulating the turnover of shorter-lived proteins in this cancer model (**Figure 3-4C**).

In the liver, 1,213 proteins met our statistical criteria and were used to represent the global proteome (**Figure 3-4D-F**). Similar to the tumor, a little over half of the observed proteome was affected by CQ mediated autophagy inhibition in the liver. The turnover rates of 47.2% of proteins were unchanged (fold change in TR $\geq 0.9 <1.1$), 27.5% were decreased (fold change in TR < 0.1), and 25.2% were increased (fold change in TR ≥ 1.1) in CQ treated mice relative to vehicle controls (**Figure 3-4D-E)**. Also like in the tumor, shorter-lived proteins were significantly more sensitive to autophagy inhibition ($p<0.0001$) compared to longer-lived proteins (**Figure 3-4F**). Unlike in the tumor however, the median protein turnover rate in the liver was essentially unchanged (-1.85%, $P=0.8$) (**Figure 3-4D-E**).

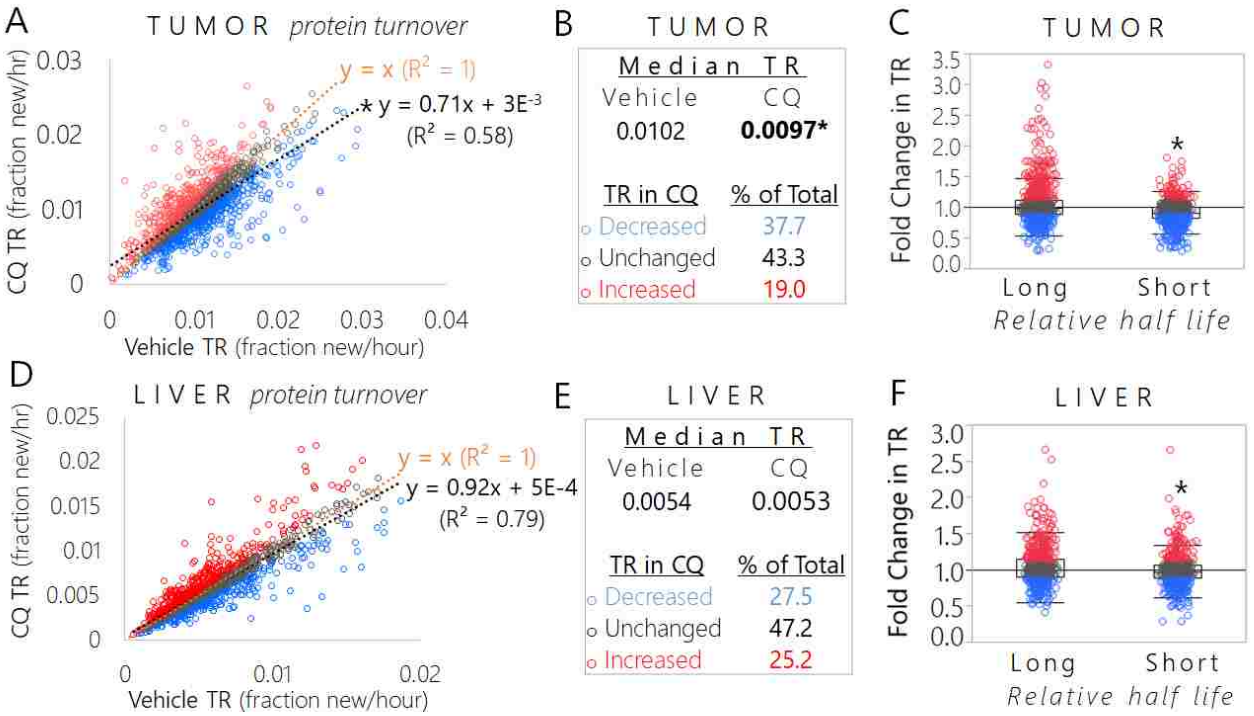

Figure 3-4 Effects of CQ induced autophagy inhibition on global protein turnover in the tumor and liver. (A, D) *Comparison of protein turnover rates (fraction of new protein per hour) in* ***(A)*** *tumor and* ***(D)*** *liver tissue of HCT116 xenograft mice treated CQ (y-axis) versus vehicle controls (x-axis) (n=1652 tumor proteins common between groups and n=1213 liver proteins common between groups). Each circle represents the turnover rate of a unique protein normalized to the vehicle control group; blue: protein turnover significantly decreased (fold change (FC)* < 0.9*), gray: protein turnover did not significantly change (FC* $\geq 0.9 < 1.1$*), and red: protein turnover significantly increased (FC* ≥ 1.1*) in the tumor or liver tissue of CQ treated xenograft mice relative to vehicle controls. The dotted black line is the linear trend line of the entire data set (Tumor: liner trend line slope=0.71,* R^2*=0.58; Liver: liner trend line slope=0.92,* R^2*=0.79) shown to emphasize that protein turnover generally decreased in the tumor and liver of CQ treated mice relative to vehicle controls (if the groups were identical, the fit line should have an approximate slope and* R^2 *of 1 and fall along the dotted orange line (slope=1) shown as a reference).* ***(B, E)*** *The median turnover rate of the entire kinetic dataset in the* ***(B)*** *tumor and* ***(E)*** *liver as well as the percentages of proteins whose turnover rates significantly decreased (blue), were unchanged (gray), or significantly increased (red) in HCT116 xenograft mice treated with CQ versus vehicle controls for each tissue type.* ***(A-E*** *(excluding* ***C))*** *The * indicates if there was a significant difference in global protein turnover using paired t-tests to compare each protein turnover rate in the vehicle control relative to the corresponding rate in the CQ treated group of each tissue type (* is* $P<0.0001$*).* ***(C,F)*** *Comparison of turnover rates of relatively long and relatively short-lived proteins from kinetic analysis of the observed* ***(C)*** *tumor and* ***(F)*** *liver proteomes of HCT116 xenograft mice.* ***(C,F)*** *The * indicates* $P < 0.0001$ *using Student's t-tests to compare the mean fold change in turnover rates of long versus short-lived proteins in each tissue.*

Protein functional categories responded to CQ treatment differently in the tumor and liver

We tested whether CQ treatment affected turnover (**Figure 3-5**) and concentration (**Figure 3-6**) of functionally associated protein groups in the tumor and liver of HCT116 xenograft mice. CQ treatment had greater effects on the turnover (**Figure 3-5A-B**) and concentration **(Figure 3-6A)** of specific substrates relative to the global tumor proteome. Longer-lived components of tumor cell mitochondria exhibited the most *reduced* mean fold change relative to other autophagy substrates and a multiple comparison test evaluating fold change in turnover of each long-lived category relative to the long-lived global proteome gave a suggestive *p value* for this difference (P=0.072) (**Figure 3-5A**). Even so, there was a *significant* reduction in average turnover of short-lived mitochondrial proteins relative to the short-lived tumor proteome (P=0.033) (**Figure 3-5B**). Note that approximately 70% of the mitochondrial proteins for which we measured kinetic data ended up in the long-lived group while 30% were considered short-lived. Pairwise comparisons between all these mitochondrial proteins in CQ versus vehicle control tumors revealed that there was a statistically significant reduction in mitochondrial protein turnover in the tumor (P=0.017). No significant differences in turnover were observed in any other functional category relative to the long or short-lived proteome of the tumor (**Figure 3-5A-B**). No functional categories within the mitochondria were changed significantly more than others (**Figure 3-8D**). However, the TR of 58% of proteins displaying a significant decrease in turnover (fold change <0.1) were found in the inner mitochondrial membrane. This suggests that general dynamics of the entire mitochondria changed relative to the global tumor proteome including other autophagy substrates in response to CQ treatment (**Figure 3-5A-B**). Moreover, the mitochondria may be *selectively* turned over via autophagy in the tumor, a process known as mitophagy [81,191].

Interestingly, the only short-lived group exhibiting a lower mean fold change in turnover compared to the mitochondria was made up of proteins characteristic of endosomes and/or lysosomes (**Figure 3-5B**). This may indicate that CQ treatment led to a reduction in the turnover of lysosomes since they were not being used to perform the late stages of autophagy. In addition, the fact that the mean fold change of lysosomal proteins was closest to that of the mitochondria suggests that the mitochondria and lysosomes were turned over at similar rates under normal conditions in the tumor, perhaps because lysosomes were used to selectively degrade the mitochondria via mitophagy (**Figure 3-5B**).

In the liver, the mean fold change in mitochondrial protein turnover was no different than the global proteome in the short and long-lived groups (**Figure 3-5C-D**). Long-lived chaperones were the only group displaying a significant difference in turnover relative to the global long-lived proteome (**Figure 3-5C**). The average TR of chaperones was significantly *increased* relative to the global proteome (P=0.015). This connected with the non-significant increase in chaperone concentration (**Figure 3-6B**) suggests that synthesis increased for these proteins. We suspect this was related to the significant increase in *global* protein concentrations in the liver (**Figure 3-3C-D**). Increased synthesis and activity of chaperones may be used to maintain quality of the significantly increased protein concentrations in the liver during CQ treatment. Moreover, short-lived ribosomal proteins exhibited the most dramatic *decrease* in turnover relative to the short-lived proteome (P=0.05) (**Figure 3-5D**). Selective degradation of ribosomes (ribophagy) has long been considered one of the primary roles of autophagy in healthy tissues [223], and reduced protein synthesis would help balance a reduction in protein degradation capacity.

We also compared the effects of CQ treatment on the *concentrations* of distinct autophagy substrates and related ontologies in the tumor and liver. Interestingly, there was general trend towards reduced protein concentrations in the tumor (P<0.0001) (**Figure 3-3A, Figure 3-6A**). In spite of this, the concentrations of most mitochondrial proteins were *elevated* (fold change in average concentration was greater than 1) (**Figure 3-6A**). Due to this significant *increase* in mitochondrial protein concentration, the mitochondria was the only autophagy substrate that displayed a significant difference in mean fold change relative to the global proteome based on our test for multiple comparisons (P<0.0001) (**Figure 3-6A**).

In the liver, the mitochondria displayed the *lowest* mean fold increase in concentration among all other substrates and this difference was significant relative to the global proteome (P=0.038) (**Figure 3-6B**). CQ has been shown to accumulate at high concentrations in rat liver, where it inhibits mitochondrial metabolism and significantly impairs availability and utilization of energy [224]. The less dramatic increase in mitochondrial protein expression may thus be attributed to reduced mitochondrial biosynthesis as CQ accumulates and is metabolized in the liver [224,225]. The mean fold increase in ribosomal protein concentrations was not significantly different than the global proteome. Indeed, there were no other autophagy substrates that had significantly *increased* in concentration relative to the global liver proteome (**Figure 3-6B**). This suggests that although autophagy may be used in part to selectively control the *turnover* of the ribosome in the liver (**Figure 3-5C-D**), the quantitative effects of autophagy inhibition were reflected quite evenly across the liver proteome (**Figure 3-6B**). As discussed previously, the only exception to this was the mitochondria, which was quantitively *lower* than the global proteome (opposite of our expectation based on autophagy inhibition, **Figure 3-6B**). We thus conclude that the less dramatic increase in mitochondrial protein concentrations in the liver was more likely due to a drug-induced reduction in mitochondrial protein synthesis, rather than loss of autophagy-mediated degradation. Overall, our results suggest that autophagy inhibition did not selectively alter the turnover of any substrate in the liver enough to induce a change in concentration; however, *both* the turnover and concentrations of mitochondrial proteins were significantly altered relative to the global proteome in the tumor (**Figure 3-5A-B, Figure 3-6A**).

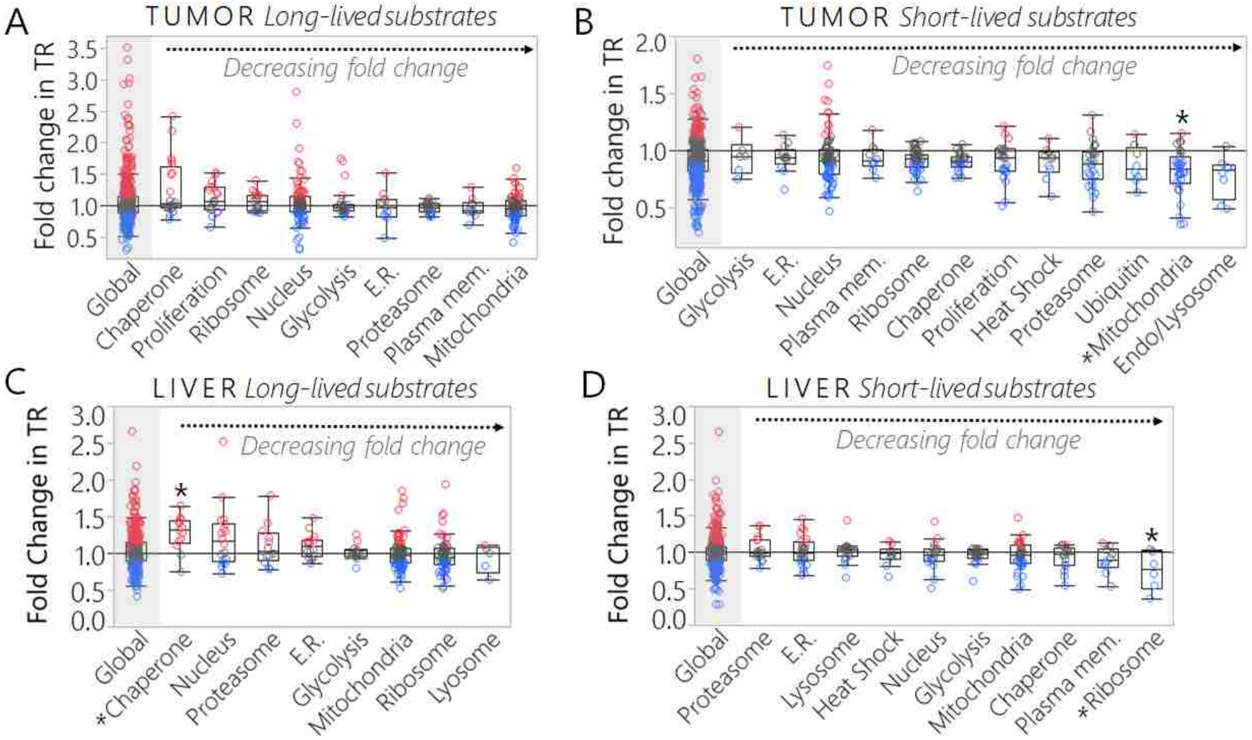

Figure 3-5 Effects of CQ treatment on turnover of autophagy related proteins and substrates relative to the observed global proteome in the tumor and liver. ***(A-D)*** *Comparison of changes in turnover rates (fraction of new protein per hour) of protein ontology groups relative to the observed proteomes (made up of remaining proteins from corresponding kinetic datasets) of* ***(A-B)*** *tumor tissue and* ***(C-D)*** *liver tissue of HCT116 xenograft mice treated with CQ versus vehicle controls. Data are represented as the fold change in protein turnover (fraction of new protein replaced per hour) in CQ treated mice relative to vehicle controls in order of decreasing fold change from left to right.* ***(A, C)*** *depicts proteins that were long-lived and* ***(B, D)*** *depicts proteins that were short-lived relative to the observed proteomes of the respective tissue types.* ***(B)*** *The * indicates P=0.033 using the Dunnett's test to compare each protein ontology to the global proteome (Note that the Dunnett's test provided a suggestive P-value of 0.072 for the mitochondria relative to the global proteome in the long-lived tumor protein analysis depicted in* ***(A)****). In* ***(C)*** *the * indicates P=0.015 and in* ***(D)*** *the * indicates P=0.05 using the Dunnett's test to compare each protein ontology to the global proteome.* ***(A-D)*** *Each circle represents the turnover rate of a unique protein. The colors are indicative of the fold change in turnover in the CQ group normalized to the vehicle control group; blue: turnover significantly decreased (FC < 0.9), gray: turnover did not significantly change (FC ≥ 0.9 <1.1), and red: turnover significantly increased (FC ≥ 1.1) in the tumor or liver tissue of CQ treated mice relative to vehicle controls.*

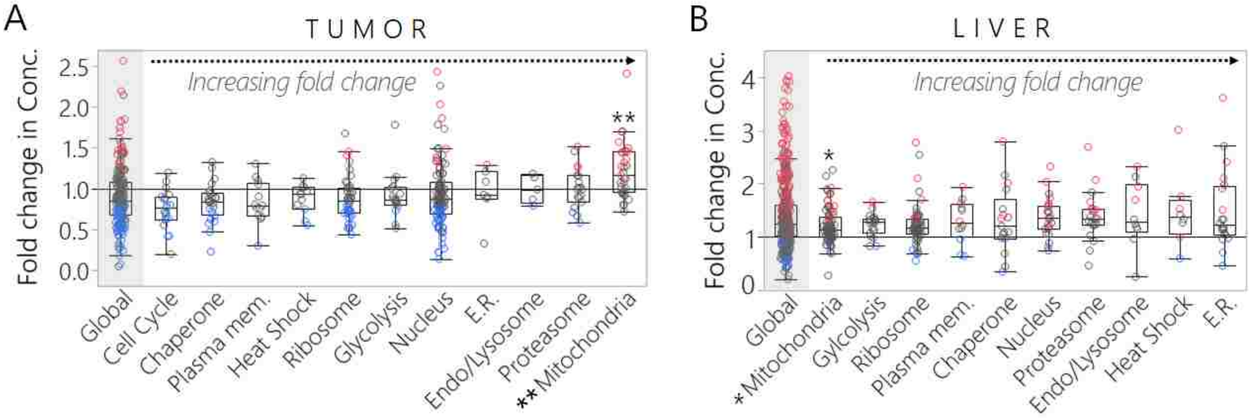

Figure 3-6 Effects of CQ treatment on concentrations of autophagy related proteins and substrates relative to the observed global proteome in the tumor and liver. *Comparison of changes in concentrations (conc.) of protein ontology groups relative to the observed proteomes (made up of remaining proteins from corresponding quantitative datasets) of* ***(A)*** *tumor tissue and* ***(B)*** *liver tissue of HCT116 xenograft mice treated with CQ versus vehicle controls.* ***(A-B)*** *Data are represented as the mean fold change in protein concentration (AUC/INST) in CQ treated mice relative to vehicle controls in order of increasing mean fold change from left to right. Each circle represents a unique protein. The color of the circle is indicative of the fold change in concentration of that protein in the CQ group normalized to the vehicle control group; blue: concentration significantly decreased (the fold change in the average concentration was less than 1 and the absolute value of the average difference between concentrations in CQ and vehicle control mice was greater than the standard deviation between biological replicates), gray: concentration did not significantly change (the absolute value of the difference between averages for drug treated and control mice was less than the standard deviation of biological replicates), and red: concentration significantly increased (the fold change in average concentration was greater than 1 and the absolute value of the average difference between concentrations in CQ and vehicle control mice was greater than the standard deviation between biological replicates) in the tumor or liver tissue of CQ treated mice relative to vehicle controls. In* ***(A)*** *the ** indicates $P<0.0001$ and in* ***(B)*** *the * indicates $P=0.0385$ using the Dunnett's test to compare each protein ontology to the global proteome.*

Immunofluorescence supported mitochondrial targeting by autophagy in the xenograft

LC3 is a common marker for autophagy because it is processed from an unlipidated (LC3-I) to a lipidated form (LC3-II) and localized to the autophagosomal membrane, where it is required for membrane expansion and the formation of the established autophagosome [52,226]. During the late stages of autophagy, LC3-II is degraded along with encapsulated cargo upon fusion with the lysosome [83]. We performed an immunofluorescence analysis to visualize LC3-II positive autophagosomes and mitochondria in the tumor. Our confocal images of xenograft tissue suggested that LC3-II positive autophagosomes colocalized with the mitochondria (**Figure 3-7A**). This supports the results of our proteomics analysis by suggesting that the mitochondria were selectively targeted by autophagosomes in the tumor.

Because CQ treatment inhibits lysosomes from fusing with autophagosomes, an accumulation of autophagosomes containing the LC3-II marker is considered evidence of reduced autophagy flux [83]. The ratio of LC3-II positive autophagosomes relative to nuclei (used to represent the total number of cells) was significantly elevated ($P<0.0001$) in tumor and liver tissues of xenograft mice treated with CQ relative to vehicle controls (**Figure 3-7B-C**). This suggests that although the early stages of autophagy including autophagosomal formation and maturation continued to occur in both the tumor and liver, CQ treatment delayed the later stages of autophagy, including autophagosome-lysosome fusion and substrate degradation.

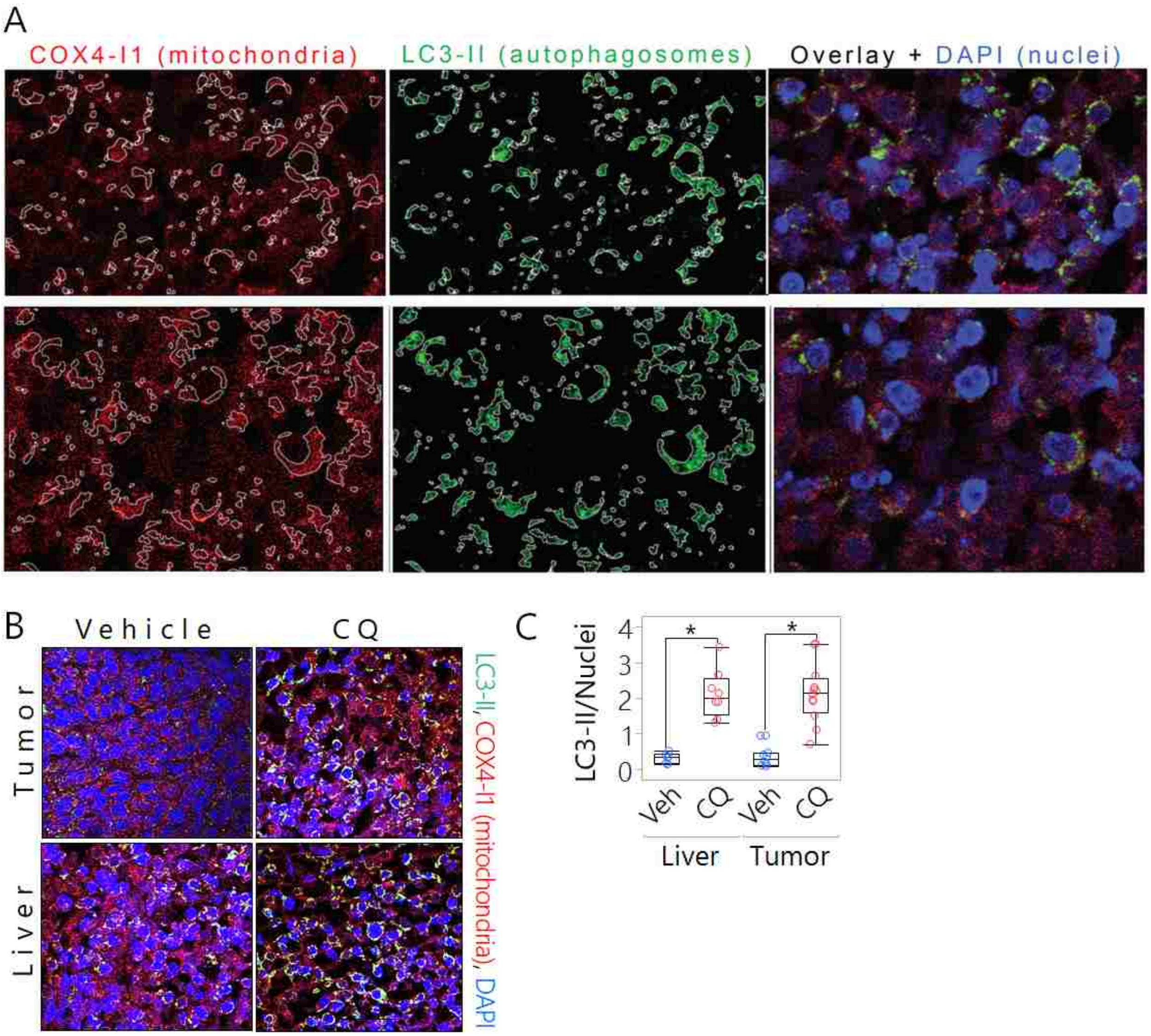

Figure 3-7 Accumulation of LC3-II autophagy markers in tumor and liver tissues of HCT116 xenograft mice treated with CQ relative to vehicle controls. (A-B) *Representative images of immunofluorescence analysis of LC3-II autophagosomal marker and mitochondria in cryoprotected mouse tissues. Red: COX4-I1 (mitochondria), Green: LC3-II (autophagosomes), Blue: DAPI (Nuclei).* ***(A)*** *Representative immunofluorescence images depicting overlap of fluorescently labeled mitochondria with LC3-II puncta in HCT116 xenograft mouse xenograft tumor tissue. Dotted lines around concentrated regions of red and green fluorescence are shown to illustrate the overlap of mitochondria and autophagosomal structures.* ***(B)*** *Representative images and* ***(C)*** *quantitation of immunofluorescence analysis of LC3-II accumulation in tumor and liver tissues of mice treated with CQ versus vehicle controls. Data are represented as the number of LC3-II positive puncta (green dots) relative to the number of cells or nuclei (blue) per image (3 mice per group, 2-5 images analyzed per mouse). The * indicates P<0.0001 with a t-test comparison between CQ treated groups relative to the respective vehicle controls in each tissue type.*

Drug metabolism enzymes increased in the liver during CQ treatment

We were unable to collect a fourth biological replicate for the *in vivo* cell proliferation assay because one of the mice in the CQ group unexpectedly died thirty minutes before tissue harvesting. We suspect this was related to systemic treatment-induced toxicity. To investigate this hypothesis, we compared the concentrations and turnover rates of CQ related drug metabolism enzymes between the two treatment groups (**Figure 3-8**). CQ is metabolized through the N-dealkylation pathway in the liver by cytochrome P450 enzymes (CYP) in both humans and mice [225,227]. Elevated expression of CYP proteins and related metabolic pathway components are indicative of cellular responses to treatment-induced cytoxicity [225,227].

A total of six CYP enzymes were detected in our quantitative proteomics analysis of the liver. Collectively, the concentrations of these CYP enzymes were significantly increased in mice treated with CQ relative to vehicle controls (P=0.046) and pairwise comparisons indicated that there were also significant differences in concertation between individual CYPs in CQ treated mice versus vehicle controls (P=0.0008). In addition, the turnover rates of all six CYPs were elevated during CQ treatment (**Figure 3-8**). This suggests that CQ treatment intended to suppress oncogenic metabolism in the tumor also induced a significant metabolic response that required increased synthesis and utilization of CYP enzymes in the liver. These off target responses suggest CQ may be more damaging than therapeutic, since short-term CQ treatment reduced cell proliferation in both the tumor and liver (**Figure 3-2C**), triggered expression of enzymes that function to reduce cytotoxicity in the liver (**Figure 3-8**), and may have induced premature death of one of our lab animals.

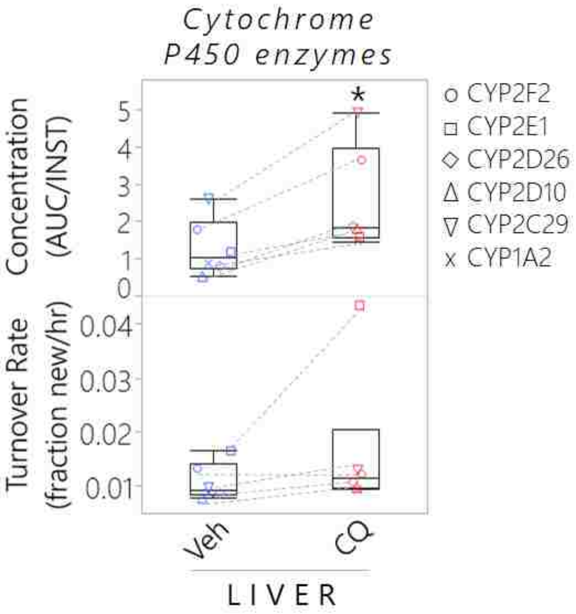

Figure 3-8 Effects of CQ treatment on drug metabolism in the liver. *Turnover rates (bottom) and concentrations (top) of cytochrome P450 enzymes in liver tissue of vehicle controls and CQ treated mice. Concentration data (AUC/INST) are represented as the median protein concentration of 3-4 biological replicates per group for each enzyme. Turnover data are represented as the fraction of new protein per hour. Student's and paired t-tests were used to make group and pairwise comparisons between Vehicle and CQ treated mice; * indicates P<0.05 for both the student's and paired t-tests.*

Degradation of mitochondria is sensitive to autophagy inhibition in xenograft tumors

To test whether autophagy driven degradation could be the cause of the changed concentration and turnover in the tumor (**Figure 3-5A-B, 3-6A**), we calculated the degradation rate constants (*Equation 4*) for proteins where we had both turnover and concentration measurements (**Table S6, S7**). Analysis of these degradation rates (**Figure 3-9B-C**) suggests that the observed changes in protein concentration and turnover during CQ treatment are because autophagy is used to control cellular protein degradation quite differently in the liver versus the tumor.

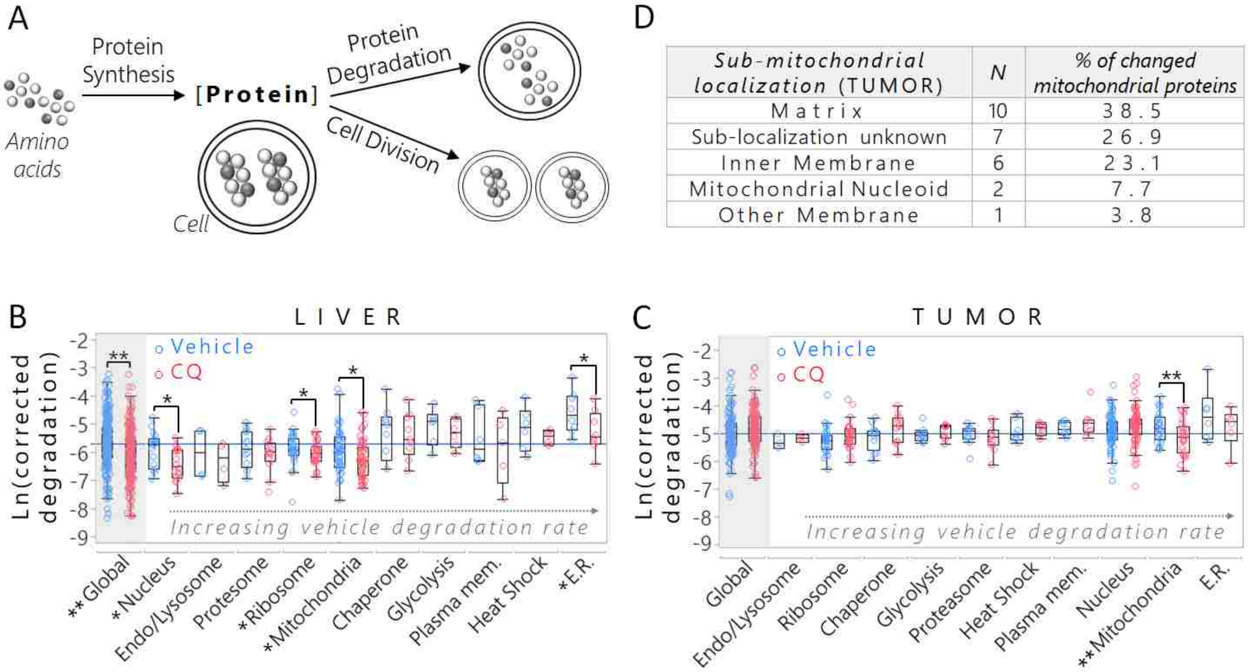

Sub-mitochondrial localization (TUMOR)	N	% of changed mitochondrial proteins
Matrix	10	38.5
Sub-localization unknown	7	26.9
Inner Membrane	6	23.1
Mitochondrial Nucleoid	2	7.7
Other Membrane	1	3.8

Figure 3-9 Protein degradation rates in the tumor and liver of xenograft mice. (A) *Protein concentration is maintained by the dynamic balance of synthesis against degradation and dilution into new cells.* ***(B-C)*** *Comparison of degradation rates normalized to cell division rates of proteins for which we observed either turnover and/or concentration was significantly changed in the* ***(B)*** *liver and* ***(C)*** *tumor of CQ-treated mice versus vehicle controls.* ***(B-C)*** *Each circle represents a unique protein. Data points are represented as the degradation rate corrected by the cell division rate (percent new DNA per hour) calculated using the formula: (Protein turnover rate (hours) - Cell division rate (hours))/Protein concentration). Blue circles represent measurements of proteins in vehicle control mice and red circles represent the same proteins whose measurements were collected in CQ treated mice. The blue line represents the mean degradation rate of the global proteome in the vehicle control group shown as a reference for each tissue type. Box plots are ordered by increasing mean degradation rate of the vehicle control group for each category from left to right. The * indicates P<0.05 and ** indicates P<0.0001 using paired t-tests to compare the degradation rate of each protein in the CQ group relative to the vehicle control.* ***(D)*** *Sub-mitochondrial localization of mitochondrial tumor proteins depicted in* ***(C)*** *(n=26 proteins generally found in the mitochondria of human cells).*

In the liver, inhibition of autophagy reduced individual protein degradation rates across the proteome (*Global*, **Figure 3-9B,** $P<0.001$) as well as in multiple canonical autophagy substrates at significant levels ($P<0.05$), including the ER [192], mitochondria [81,191,228-230], nuclear proteins [193], and ribosome [190]. In the tumor, protein degradation rates were relatively unchanged *with exception* to the mitochondria (**Figure 3-9C**). Mitochondrial proteins were the only group including the global proteome that displayed a significant reduction in degradation rate based on pairwise comparisons ($P<0.0001$). Every location in the mitochondria seemed to be affected similarly (**Figure 3-9D**). This suggests that in the liver, autophagy plays a complex, multifaceted role across the proteome, probably by selecting multiple specific targets as well as untargeted maintenance of the proteome [194,231]. On the other hand, targeted degradation of the mitochondria or mitophagy may be the primary role of autophagy in the CRC xenograft tumor. Neither degradation of the general tumor proteome nor any of the other canonical autophagy substrates were significantly perturbed by autophagy inhibition (**Figure 3-9C**). This suggests that in the tumor, dilution of other canonical substrates into new cells may be fast enough that proteasomal degradation is adequate to balance synthesis.

CONCLUSION

Under normal conditions, protein concentrations within a cell remain relatively constant due to a balance between protein synthesis and degradation or dilution into new cells (**Figure 3-9A**). In cancer, the rapid proliferation of new cells causes a higher demand for protein synthesis [6,232] that could minimize the contribution of protein degradation in balancing the equation (**Figure 3-9A,** *Equation 1*). Yet, it has been shown many times that the autophagy pathway, which rapidly degrades cellular proteins, is an important component of cancer biology [76,80,182,183,233]. In an effort to understand how autophagy function differs in cancer tissue, we measured individual concentrations (**Table S4, S5**) and individual turnover rates (**Table S6, S7**) for a large number of proteins, as well as the cell proliferation rate (**Table S3**) in liver and xenograft tumor tissues. We monitored the change in each of these values during treatment with chloroquine diphosphate, a traditional autophagy inhibitor [78,182,234]. We found that the xenograft seems to focus autophagy specifically on targeted degradation of the mitochondria while autophagy plays multi-functional roles supporting more general proteome maintenance in the liver.

Our results support recent studies promoting inhibition of mitophagy as a chemosensitizing drug target. Silencing of the mitophagy regulator gene BNIP3L (BCL2 interacting protein 3 like) was shown to significantly enhance sensitivity of xenograft stem cells to doxorubicin-induced DNA damage by unclear mechanisms [230]. Mitochondrial division inhibitor-1 (mvidi-1), a cell-permeable quinazolinone which attenuates mitochondrial fission preceding mitophagy, prevents cell cycle progression in lung cancer [235]. While mdivi-1 may serve as an important research tool and a leading compound for further optimization, due to its undesired effects such as prevention of mitochondrial outer membrane permeabilization, modified cell membrane potential, and relatively high IC_{50} in mammalian cells (IC50 » 50 µM), more potent and specific mitophagy inhibitors are in high demand [229,236]. Further studies are necessary to fully understand how mitophagy is regulated and used to support pro-survival metabolism different tumor types [229,236].

Loss of autophagy has been shown to reduce the ability of cancer cells to adapt to cytotoxic stress [182,183] and deregulation of autophagy has been shown to reduce key substrates of mitochondrial metabolism including free amino acids, consequently inhibiting mitochondrial respiratory activity [185,233]. In tumor cells, increased autophagy mediated degradation of mitochondrial proteins through mitophagy may promote mitochondrial biogenesis, a phenomenon that has been shown to "fuel" tumor cell growth and migration [237]. Rapid degradation of mitochondria may also be a method to protect cancer cells against mitochondria mediated apoptosis [228].

A therapeutic advantage of specifically inhibiting targeted degradation of mitochondria in the tumor is that it may reduce the toxicity of anti-autophagy treatments in other tissues. This study suggests that basal liver proteome maintenance via autophagy may cause major toxicity issues with systemic, nonselective anti-autophagy drugs. Although mitochondrial degradation is still a function of autophagy in the liver, our data suggest the slower proliferating tissues may be able to cope with the targeted inhibition more easily by reducing mitochondrial biogenesis, and increasing proteome wide folding capacity and synthesis.

Future Directions

Using *in vivo* monitoring of protein turnover and concentration, we can specifically test whether synthesis or degradation rates change in response to drug treatment in different tissue types (**Figure 3-1**). We show that inhibition of autophagy slows protein degradation rates and that mitochondria are one of the primary targets for autophagy in this tumor model (**Figure 3-10**). This method is easily applicable to *in vivo* monitoring in humans and could be useful for investigating patient-specific tumor metabolism as well as treatment efficacy.

Figure 3-10 Schematic model of autophagy substrate selection in the tumor versus liver tissue in colon cancer xenograft mouse. *Our kinetic and quantitative data suggest that autophagy generally served as a bulk degradation system to improve global proteostasis by promoting quality control of organelles and complexes such as the ribosome in the liver (left). Our results further suggest that autophagy played a different functional role in xenograft tumor tissue (right), whereby the mitochondria were significantly targeted (indicated by the *) for autophagy-mediated*

degradation relative to the global proteome to promote energy metabolism, stress tolerance, and rapid proliferation (left). Treating HCT116 xenograft mice with CQ altered autophagy-mediated proteome remodeling and cell proliferation in both the tumor and healthy liver tissue.

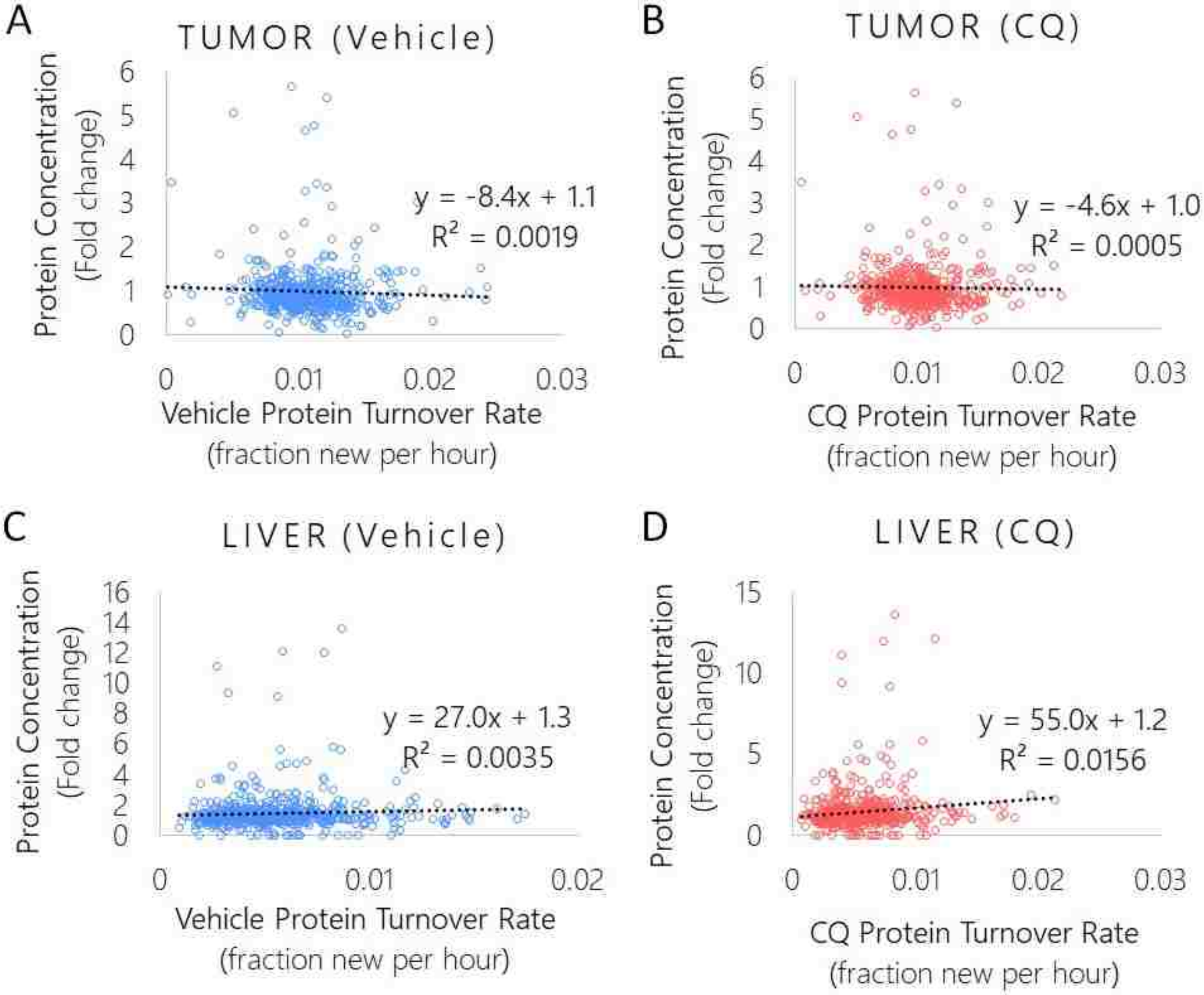

Supplemental Figure 3-1 Comparison of quantitative and kinetic proteomics data in the tumor and liver. *Scatterplot and linear trend line of protein concentration data (fold change in CQ relative to vehicle control) plotted against the protein turnover rate in the tumor (n=498 total proteins)* ***(A-B)*** *and the liver (n=626 total proteins) of* ***(A,C)*** *vehicle control and* ***(B,D)*** *CQ treated HCT116 xenograft mice.*

ACKNOWLEDGEMENTS

This research was funded by the Fritz B. Burns Foundation (JCP and JLA), Ronald K. Robins Graduate Research Fellowship (MMPS and BCN), the Brigham Young University Simmons Center for Cancer Research (MMPS), and the National Institutes of Health Grant (JLA, R15CA202619). We thank Dr. David H. Lum and the Huntsman Cancer Institute Preclinical Research Resource at the University of Utah for generating the HCT116 xenograft mouse and for carrying out live mouse handling procedures, euthanizations, and dissections. We sincerely thank Ryan Sheaparé for developing the mitophagosome colocalization figure. We are grateful to Nathan Rotriguez, Vajira Weerasekara, Colten McEwen, Richard Carson, Dr. Kenneth A. Christensen, and Courtney Banks for constructive insights and helpful conversations.

4. Conclusions and future directions toward understanding metabolic mechanisms of cancer and chemoresistance

Chapter Summary

This chapter provides general conclusions from the published studies and results of studies I have initiated which have not yet fully developed. I summarize these unfinished studies here to ensure that they can be referenced after the conclusion of my graduate work and hopefully lay a foundation for future cancer research in the Price lab and beyond.

CONCLUSIONS FROM PUBLISHED WORK

Epigenetic or metabolic adaptations by cancer cells are significant contributors to cancer's competitive advantages. Just eighteen years ago, experts believed that the primary source of cancer was genome instability and the complexity of cancer pathogenesis resulting from this genetic diversity could be reduced to just six underlying principles known as the "Hallmarks of Cancer" [238,239]. First introduced by Douglas Hanahan and Robert A. Weinberg in 2000, the original hallmarks of cancer include sustaining proliferative signaling, evading growth suppressors, resisting cell death, enabling replicative immortality, inducing angiogenesis, and activating invasion and metastasis [239]. It was once anticipated that this complex set of principles in time could be further reduced to either fewer or simpler core concepts [238,239]. However, recent discoveries facilitated by new technologies have revealed that carcinogenesis is even more complex than ever imagined, requiring the addition of "next generation Hallmarks of Cancer", including evading immune destruction and metabolic reprogramming [238].

Improvements in mass spectrometry in recent years have been part of the improved understanding of cancer biology through contributions in proteomics, lipidomics, and metabolomics. These investigations have enhanced traditional genomics assays by increasing our understanding of *nongenetic* drivers of cancer metabolism [240]. Despite rapid advances in these fields of study, significant technological challenges still hinder further progression in our understanding of specific metabolic pathways and intermediates involved in cancer evolution and drug resistance.

Studying cell metabolism is challenging because many metabolites are derived from common precursors and exhibit similar chemical structures making it difficult to differentiate between them [232]. This is further complicated by rapid rates of change and the challenge of consistently and accurately quantifying the expression levels of such metabolites in a complex mixture. Often, the most biologically influential metabolites are expressed at very low levels relative to other components in a cancer cell. For a mass spectrometrist, this often makes it very difficult to detect, nevertheless to accurately quantify such metabolites using traditional bioanalytical techniques. I have shown that minute changes in the expression and metabolism of bioactive lipids have significant biological effects in pancreatic cancer cells. Therefore, developing methods capable of monitoring small shifts in metabolite concentrations and pathways are imperative for fully understanding cancer pathogenesis and improving treatment efficacy. Throughout my research, I have learned that even the most sophisticated analytical instruments are useless if they cannot be utilized to identify and measure the compounds or biological processes of interest. Much innovation and countless hours of troubleshooting are often required to answer even the simplest biological questions.

When I began my work on the pancreatic cancer study (Chapter 2), we had one seemingly simple objective: to quantify just *two* lipids out of the thousands of metabolites expressed in the cell, S1P and C16 ceramide. S1P is a classic example of a metabolite that, although expressed at picomolar concentrations, has significant biological effects and is very difficult to detect in human pancreatic cells even with the assistance of high-resolution mass spectrometers. Although we could easily identify thousands of other lipids and proteins in these cells using various LC-MS methods and instruments, we simply could not find an effective way to monitor intracellular S1P levels. On the rare occasions when S1P ions *were* detected, the chromatography and fragmentation patterns were insufficient in providing confident identifications or concentration measurements.

Ultimately we established an LC-MS method to accurately quantify S1P and C16 ceramide, along with thousands of other lipids to compare against in our metabolically reprogrammed cancer lines. Through this method, we were also able to discover an important oncogenic pathway of pancreatic cancer with promising therapeutic effects. The knowledge we gained about the effects of this pathway on cell behavior and how it is differentially regulated to support pro-survival phenotypes in metabolically dynamic PDAC cells may lead to future treatment development and drug discoveries. In addition, the LC-MS based SK1 enzyme activity assay I developed may serve as a companion diagnostic to track disease progression and treatment efficacy.

My doctoral research also addressed issues concerning cell culture-based studies that are significantly affecting researchers and funding organizations. Despite the important role of cell culture in foundational and clinical research, cancer cell lines can also lead to greater levels of confusion through the research community. Misidentified cell lines resulting from microbial or cross contamination between cell lines and differences in growth medium compositions create problems at many levels of cancer research [241]. Even when all preventative steps are accounted for, cultured cells are inevitably subject to change over time without any external contamination due to chromosomal duplications or rearrangements, mutations, and epigenetic changes that can greatly modify cellular phenotypes including responses to treatments [241]. This is a key concern of the U.S. National Institutes of Health (NIH) because inconsistencies between experimental models make it difficult to replicate data and apply the results of basic research to clinical trials [241]. If a drug is proven successful in the wrong model or phenotypically altered cells exhibit variations in behavior, discoveries and progress toward the most effective treatments can be delayed [241]. Evidently, more effort is needed to evaluate both genotypic and phenotypic variations between cell lines [241].

My work in pancreatic cancer models (Chapter 2) addresses these concerns by showing global and specific biochemical changes at multiple levels that contribute to behavioral differences between PDAC subclones derived from a common originating line. While STR Profiling is traditionally the standard for distinguishing between human cell lines, recent research indicates that both genetic and nongenetic factors contribute to severe changes in cancer cell lines and tumors [4,25,26,30]. For example, metabolic adaptations can be clonally selected to promote tumorigenesis and phenotypic diversity between cells from a common origin [232]. Thus, assays beyond the level of the genome may serve as more accurate representations of cellular responses to drug treatments. I demonstrated a multifunctional workflow that can be used to monitor both genetic and phenotypic heterogeneity between cell lines, track evolutionary changes, and discover conserved pathways of significance. The pro-survival SK1 mediated sphingolipid pathway we identified served as an effective drug target in all the PDAC subclones despite variations in global and pathway-specific gene expression and metabolism. This is an important finding not only because it suggests that SK1 is important driver of cancerous phenotypes among heterogeneous *in vitro* subclones, but also suggests that this pathway may contribute to solving research and clinical problems such as cancer stem cell evolution, diversions between cell culture systems, and inter/intra-tumor heterogeneity.

Another major challenge of cancer metabolism research I focused on throughout my graduate work lies in the quantitative measurement of metabolic flux; i.e., monitoring the movement of atoms through metabolic pathways rather than simply measuring steady-state conditions. The fluxes of critical metabolic pathways such as the TCA cycle, glutaminolysis, and autophagy have been quantified in cultured cell lines using innovative applications of SILAC (Stable isotopic labeling with amino acids in cell culture), radioactive tracer amino acids, and ^{13}C NMR spectroscopy [52,80,201,242]. While such approaches have provided important insight into fundamental components of cancer metabolism, they are not necessarily representative of *in vivo* metabolic flux and do not provide a comprehensive understanding of how these fluxes change in the context of a living organism.

The ability to measure global autophagy and identify selective forms of autophagy has been greatly challenging due to the highly dynamic nature of this process and limited technology [83]. Through my novel application of kinetic and quantitative proteomics techniques in HCT116 xenograft mice, I demonstrated an entirely new method to measure autophagy flux *in vivo* that can potentially be used in humans (Chapter 3). I showed how autophagy is used to remodel the proteome of cancer and healthy tissues and identified a specific form of autophagy used to selectively control degradation rates of the mitochondria relative to other substrates in xenograft colon tumor tissue. While intrinsic and extrinsic stresses promote the accumulation of damaged mitochondria in cancer cells, research has shown that much of the metabolic reprogramming required for tumor growth and clonal selection depends on utilizing mitochondria as functional bioenergetic systems [232]. My research suggests that mitophagy may be used to support global energy metabolism by improving mitochondrial quality control in colon tumor cells. Thus, mitophagy may serve as a more tumor specific anti-autophagy drug target compared to conventional inhibitors like chloroquine, which have severe off target effects [78,224]. Overall, my discoveries regarding the functional role of autophagy in CRC may provide insight for improving diagnostic tools and developing personalized treatment strategies.

Recent reviews suggest that metabolic reprogramming is perhaps the most pivotal emerging hallmark of cancer [6,28,143,232,238]. I have further showed that metabolic signatures and flux are not simply passive effects of genetic mutations but serve as active drivers of the classic hallmarks of cancer, including proliferative signaling, evading growth suppressors, and resisting cell death [239]. Both small and large shifts in the regulation and flux of metabolic pathways such as the conversion of ceramide to S1P and selective autophagy promote cancerous phenotypes like rapid proliferation and drug resistance. These findings and my contributions toward expanding applications of bioanalytical techniques will pave the way for future discoveries to improve our understanding and treatment of cancer.

FUTURE DIRECTIONS

Amino acid metabolism is a potential chemosensitizing drug target in triple negative breast cancer cells

My interest in cancer metabolism and the effects of the mitochondria on pro-survival pathways originated from my work involving a panel of chemoresistant triple negative breast cancer (TNBC) cells. TNBC treatment options are limited due to the lack of a therapeutic hormone receptor target and high tendency for tumors to develop chemoresistance [234]. Resistant cell lines were originally generated by exposing MDA231 and SUM159 TNBC cells that were initially sensitive to epirubicin (epi), a DNA-damage inducing chemotherapeutic, to varying concentrations of epi for approximately one year [234]. My first observations were that the sensitive cells required splitting about twice as often as the resistant cells due their considerably faster growth rates (**Figure 4-1**). While epi treatment had no major effect on resistant SUM159 cell proliferation, even a low concentration of epi (1 μM) in the cell medium significantly slowed sensitive SUM159 cell growth ($P<0.05$) (**Figure 4-1**). We hypothesized that energy and metabolic intermediates initially used to fuel cell division in their "sensitive" state were redirected toward an adaptive stress response against epi-induced stress in their "resistant" state.

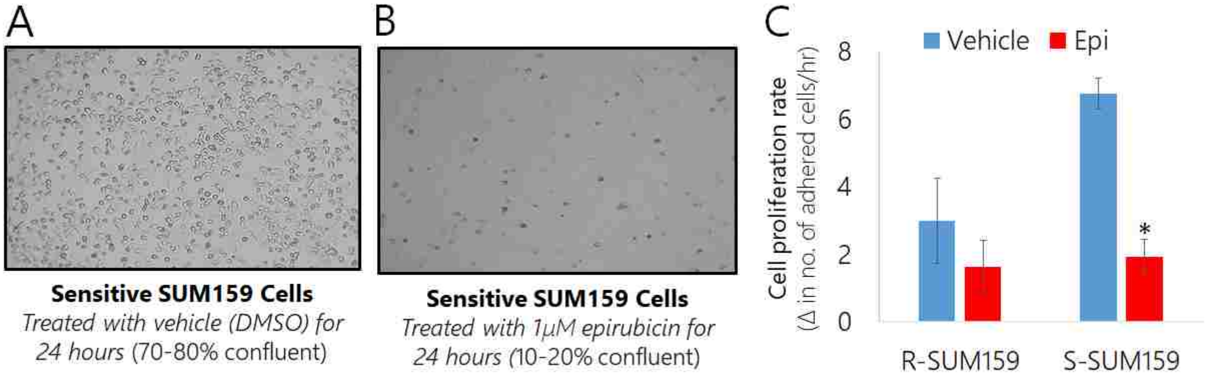

Figure 4-1 Effects of chemotherapy on sensitive versus resistant TNBC cells. (A-B) *Representative light microscope images of sensitive SUM159 TNBC cells treated with **(A)** 1μM epirubicin for 24 hours relative to the **(B)** vehicle control. **(C)** Comparison of cell proliferation rates of sensitive and resistant SUM159 cells treated with 1μM epirubicin for 24 hours relative to vehicle controls. Data are represented as the mean cell proliferation rate (change/increase in number of adhered cells counted per hour) of two biological replicates +/- SEM. The * indicates P<0.05 using t-tests to compare growth rates of epi-treated cells relative to vehicle controls.*

We also observed considerable differences in mitochondrial morphology between sensitive and resistant TNBC cells treated with epirubicin (**Figure 4-2**). Resistant MDA231 and SUM159 and cells had small, punctate mitochondria and displayed no major changes in mitochondrial morphology after 24-hour exposure to chemotherapy. On the other hand, sensitive MDA231 and SUM159 cells initially exhibited long, tubular networks of mitochondria. After epi treatment, both sets of sensitive TNBC cells displayed shorter, more punctate mitochondria, much like their resistant counterparts (**Figure 4-2**). This suggests that mitochondrial biogenesis and activity was increased in sensitive TNBC cells relative to the resistant cells and that epi may induce mitochondrial fission and suppress mitochondrial metabolism.

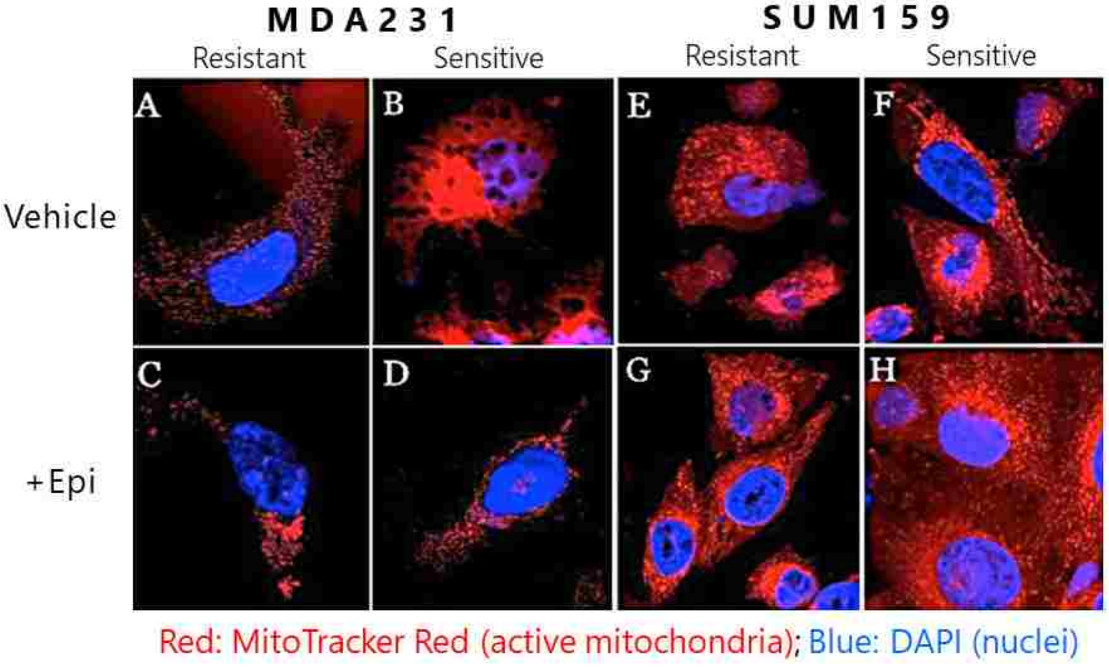

Figure 4-2 Effects of chemotherapy on mitochondrial morphology in sensitive and resistant TNBC cells. *Representative immunofluorescence images of active mitochondria stained with MitoTracker Red and nuclei stained with DAPI (blue) in sensitive and resistant MDA231* ***(A-D)*** *and SUM159* ***(E-H)*** *cells treated with the vehicle (DMSO) or 1µM epirubicin for 24 hours.*

We investigated this hypothesis by measuring respiratory oxygen flux, which serves as a metric of mitochondrial activity [243], in sensitive and resistant SUM159 cells under basal conditions and after exposure to epi (**Figure 4-3**). Substrate-uncoupler-inhibitor titration was used to measure oxygen consumption in each group immediately after 24 hour treatments relative to vehicle controls [49,243]. Average levels of aerobic respiration were consistently reduced in resistant relative to sensitive SUM159 cells. This suggests that mitochondrial oxidative phosphorylation was suppressed in the resistant cells. Chemotherapy significantly reduced oxygen utilization in sensitive SUM159 cells ($P<0.05$) but had no measurable effect on aerobic respiration in resistant cells.

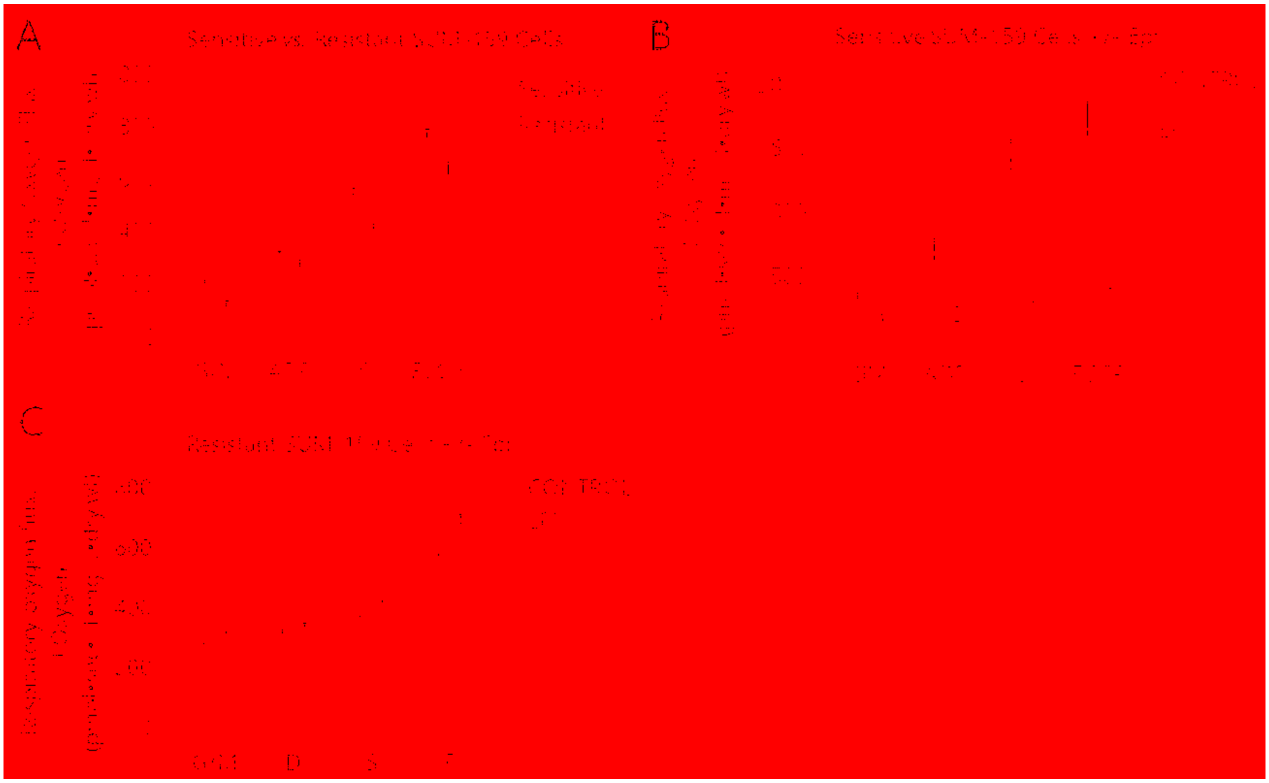

Figure 4-3 Chemoresistance and chemotherapy reduced respiratory oxygen flux (mitochondrial activity) in TNBC cells. *Mitochondrial oxygen consumption measured in* ***(A)*** *sensitive versus resistant SUM159 cells,* ***(B)*** *sensitive SUM159 cells treated with 1µM epi for 24 hours relative to vehicle controls, and* ***(C)*** *resistant SUM159 cells treated with 1µM epi for 24 hours relative to*

*vehicle controls using substrate-uncoupler-inhibitor titration. G/M: Mitochondrial Complex I-linked substrates glutamate/malate; ADP: Adenosine diphosphate (ATP synthase substrate); S: Mitochondrial Complex II-linked substrate succinate; FCCP: Oxidative phosphorylation uncoupler. Data are represented as the mean respiratory oxygen flux in response to each substrate measured in biological triplicate +/- SDM. The * indicates P<0.05 using t-tests to compare between treatment and control groups.*

Because mitochondria contain their own genome (mtDNA), we believe they were major targets of DNA damage resulting from chemotherapy in the TNBC cells. Moreover, the resistant cells may have increased mitochondrial fission and reduced mitochondrial aerobic activity as an effect of epi-induced mtDNA damage, causing them to depend on other sources of energy to support metabolism, macromolecular biosynthesis, and stress tolerance. Perhaps due to the loss of the abundant sources of ATP and metabolic intermediates normally supplied the TCA cycle and oxidative phosphorylation in the mitochondria, the resistant cells could no longer divide and proliferate as rapidly as their chemosensitive counterparts that displayed fully functional mitochondria (**Figure 4-1**).

We also identified a significant difference in amino acid utilization between sensitive and resistant TNBC cells that may be used to support survival and compensate for the loss of mitochondrial metabolism in the resistant cells. Sensitive and resistant SUM159 cells were treated with 5% dietary D_2O and collected after approximately 1/3, ½ and 1 doubling period. Mass spectrometry was used to detect changes in protein mass as deuterium from the diet was incorporated into proteins over time (**Figure 4-4**). Although the sensitive cells were dividing rapidly throughout the course of the metabolic labeling experiment, they lacked deuterium incorporation into proteins. On the other hand, our data clearly showed that resistant SUM159 cells incorporated the heavy isotopic label into proteins over time. This indicates that the sensitive cells did not produce any of their own nonessential amino acids, but instead relied solely on amino acids provided in the growth medium to support cell viability and division. On the other hand, the resistant cells adapted the ability to generate their own nonessential amino acids *via* transamination (**Figure 4-5**). Cancer cells have been shown to rely heavily on amino acid metabolism to support survival and drug resistance [8,20,21,244,245]. Because of the loss of mitochondrial function, the resistant TNBC cells may have increased utilization and metabolism of amino acids to support cell viability and growth. On the other hand, sensitive cells seemed to direct more energy and metabolic precursors toward mitochondrial biogenesis and activity to facilitate the overwhelming biosynthetic demands required to fuel their more rapid division rates (**Figure 4-1**).

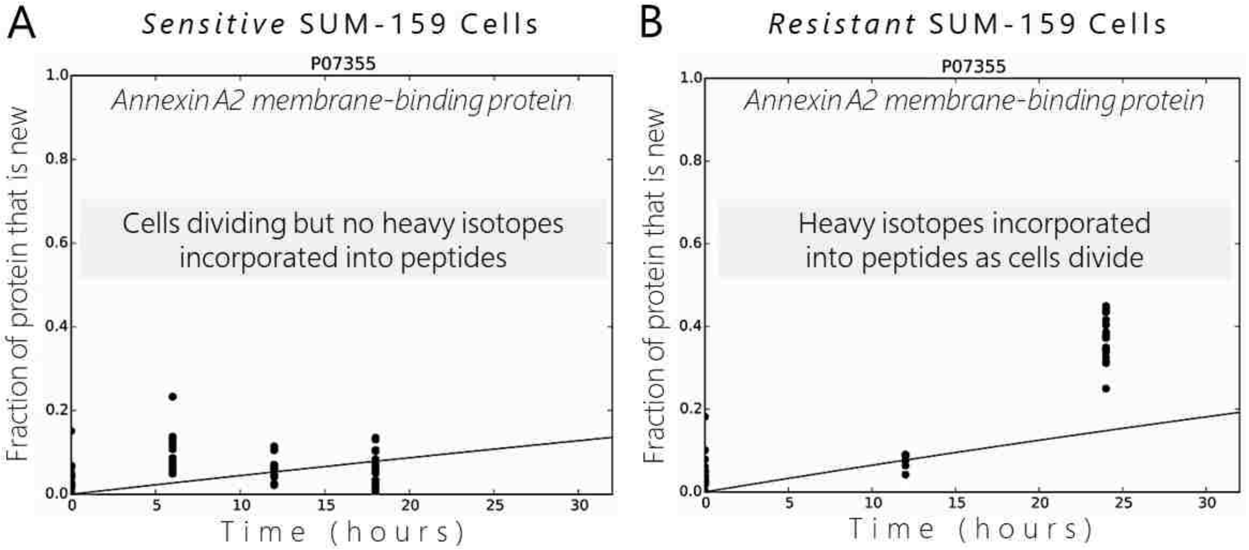

Figure 4-4 Amino acid metabolism was modified in chemoresistant TNBC cells. (A-B) *Representative profiles of deuterium incorporation into protein over time in* ***(B)*** *resistant SUM159 cells and lack of deuterium incorporation in* ***(A)*** *sensitive SUM159 cells treated with 5% dietary* D_2O*. Each black dot represents a different tryptic peptide in the Annexin A2 calcium-regulated membrane-binding protein (P07355). Mass spectrometry was used to calculate the deuterium-induced mass change in each peptide over time in the resistant cells, which was used to calculate the fraction of new protein or turnover rate. Sensitive cells lacked deuterium incorporation, indicating they do not synthesize nonessential amino acids. However, resistant cells adapted some transamination capacity to produce their own nonessential amino acids.*

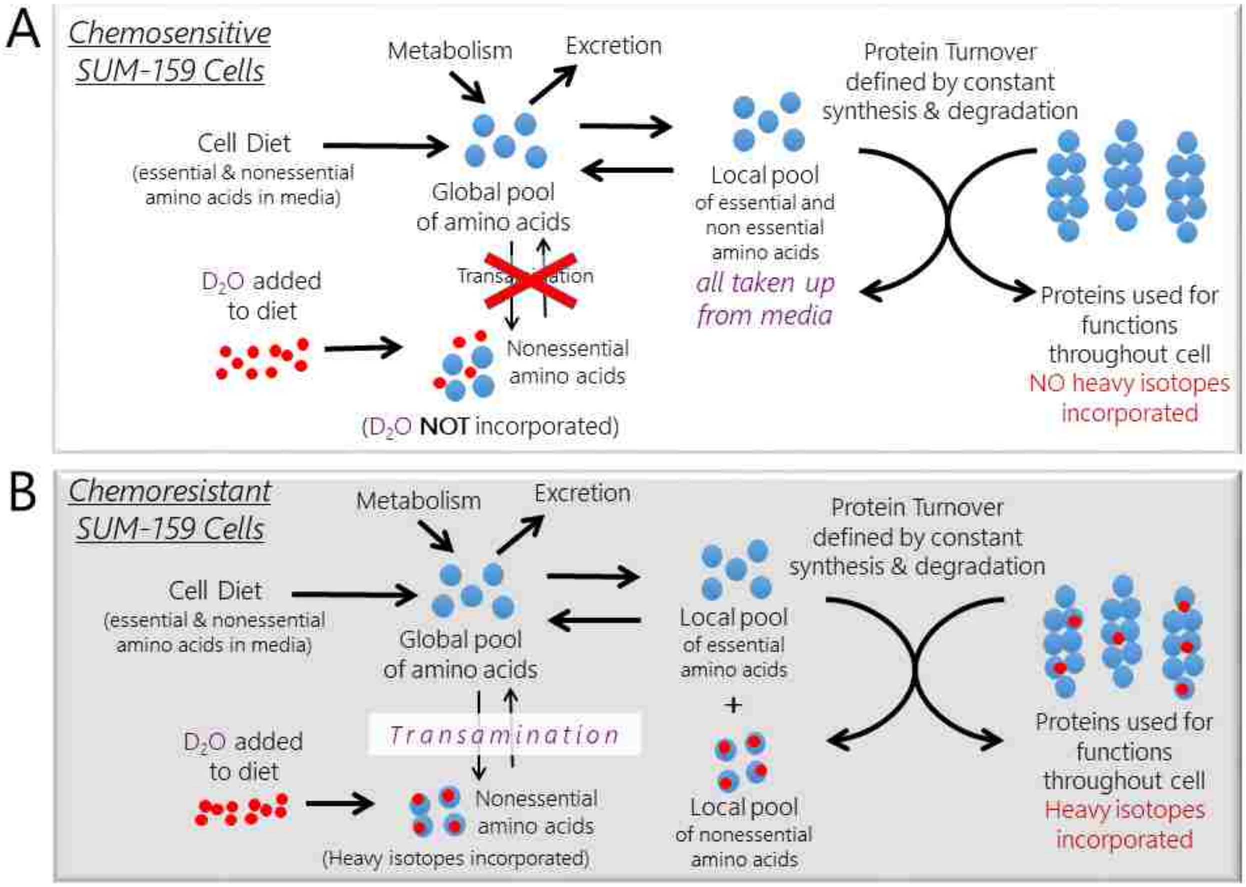

Figure 4-5 Kinetic model of amino acid and protein metabolism in sensitive versus resistant TNBC cells.

Although D_2O-based metabolic labeling of nonessential amino acids provided interesting insight into general metabolic pathway shifts between sensitive and resistant cell states, our results also indicated that we could not use this method to measure *protein* turnover in the sensitive TNBC cells. We attempted exposing sensitive SUM159 cells to other heavy isotopic labels to overcome this limitation, including ^{15}N Arginine and D4 arginine SILAC standards as well as a mixture of heavy ^{15}N algal amino acids. Our MS data revealed that sensitive SUM-159 cells were fully capable of incorporating these heavy amino acids into protein, as illustrated by the clear shift in the isotopic distribution of masses over time in the γ-actin peptide (**Figure 4-6**).

While we were able to use the change in the isotope pattern to calculate the turnover rate of γ-actin by hand, the generally low signal to noise ratio in the remainder of our data and lack of analysis tools to handle such complex MS data hindered our ability to perform a wide-scale kinetic proteomics analysis of these cells. For this reason, we shifted our focus to a different cancer cell line, HCT116, which enabled us to complete the wide-scale kinetic proteomics study described in Chapter 3.

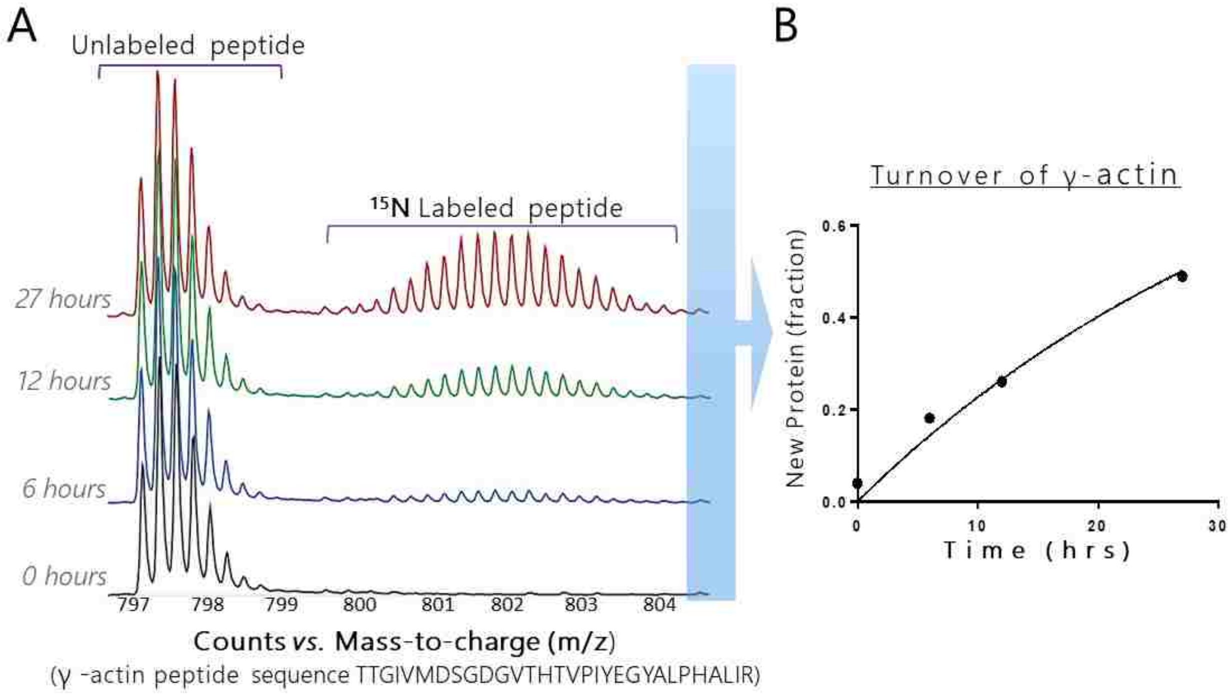

Figure 4-6 Protein turnover measurement in TNBC cells using 15N-based metabolic labeling. ***(A)*** *Raw mass spectral data of γ -actin peptide after metabolic labeling of sensitive SUM-159 cells with a mixture of heavy (^{15}N) algal amino acids. Over time,^{15}N is incorporated into proteins and the isotopic distribution of masses increases.* ***(B)*** *The change in the isotope pattern was used to calculate the relative difference in isotopic intensity and fraction of new protein (turnover rate) of the γ -actin protein.*

This work provides further evidence that metabolic pathways are readily altered to support stress tolerance in cancer and lays a foundation for future TNBC research. These data also further emphasize the importance of mitochondrial metabolism in fueling cancer cell proliferation, as exemplified by the sensitive SUM159 cells. On the other hand, loss of mitochondrial function or biogenesis may have contributed to the lower proliferation rates of the resistant cells. Based on our results, nonessential amino acid metabolism via transamination may serve as a potential therapeutic drug target and enhance the effects of chemotherapy in resistant TNBC cells.

Generation of chemoresistant colon cancer cell line

Despite recent advances in surgical restriction and chemotherapy, 50% of colorectal cancer patients experience disease recurrence [246]. An increased understanding of cellular mechanisms driving CRC recurrence and resistance to current chemotherapeutics is essential to improve clinical outcomes. We generated a chemoresistant CRC cell line to study potential metabolic mechanisms of treatment resistance in colon cancer. F-Fluorouracil and oxaliplatin are currently the standards of CRC chemotherapeutics [246]. Oxaliplatin is a platinum-based compound that exerts its cytotoxic effect mostly through DNA damage. We generated an oxaliplatin-resistant CRC cancer cell line derived from wild type HCT116 cells which we refer to as "ROXY-HCT116" cells.

ROXY cells were generated by exposing HCT116 cells to oxaliplatin at clinically relevant doses and schedules [246]. Cells were maintained in 10 mL of Dulbecco's modified Eagle medium (DMEM; 4.5 g/L $_d$-glucose) supplemented with 10% FBS and 1% penicillin streptomycin in 10 cm tissue culture dishes at 37°C, 5% CO_2. Once a week, cells were gently washed with 1x PBS and the cell medium was exchanged for 10 mL of fresh medium pre-warmed to 37°C. The cell medium was consecutively treated with intermediate, high, or low doses of oxaliplatin followed by recovery periods during which surviving cells were harvested.

Cells were first exposed to the intermediate dose of oxaliplatin (0.625 μM) for one week. The surviving cells were then allotted a one-week recovery period in drug-free medium. This cycle was repeated fifteen times. The surviving cells were then split and exposed to the highest dose of oxaliplatin (1.25 μM) for one-week periods, each followed by a one-week recovery phase. This cycle was repeated over the course of two months. Finally, the resistant cells were maintained in the complete culture medium (DMEM + 10% FBS/1% penicillin streptomycin) containing a low dose oxaliplatin (0.125 μM) at 37°C, 5% CO_2.

To confirm that the ROXY-HCT116 cells had achieved chemoresistance status, we performed a cell proliferation assay of our newly generated line compared to the original wild type HCT116 line using live-cell imaging on an Incucyte system. Cells were split evenly onto 12-well tissue culture dishes and allowed to adhere overnight at 37°C, 5% CO_2 in the complete DMEM cell culture medium (10% FBS and 1% penicillin streptomycin). The cell medium was subsequently removed, cells were washed with 1x PBS, and the cell medium was exchanged for fresh complete medium pre-warmed to 37°C. Cell proliferation was monitored for 39 hours at 37°C, 5% CO_2 after which cells were again washed with 1x PBS and the cell medium was exchanged for fresh complete medium (DMEM + 10% FBS/1% penicillin streptomycin) containing the medium dose of oxaliplatin (0.625 μM) or the vehicle (DMSO) pre-warmed to 37°C. Monitoring of cell proliferation immediately resumed until the vehicle control cells reached maximum confluence (**Figure 4-7**).

Oxaliplatin treatment significantly reduced wild type HCT116 cell proliferation by nearly 80% ($P<0.05$). On the other hand, oxaliplatin only reduced ROXY-HCT116 cell proliferation by an average of approximately 18%. Interestingly, the average growth rate of the control ROXY cells was even higher (~32%) than the control wild type cells. Unlike the resistant TNBC cells, these resistant colon cancer cells not only adapted the capacity to withstand oxaliplatin-induced stress, but also seemed to develop an enhanced growth capacity. We suspected that the ROXY cells significantly altered gene expression and metabolism to overcome the cytotoxic effects of chemotherapy.

To test this, we performed a quantitative proteomics analysis comparing ROXY to wild type HCT116 cells using duplex peptide stable dimethyl isotope labeling and mass spectrometry [85]. We identified a total of 964 proteins and quantified 660 proteins containing at least two unique peptides. Surprisingly, there were only five significantly differentially expressed genes between ROXY and wild type cells among these 660 and all five were *upregulated* in the wild type cells (**Figure 4-8**). There were no major functional relationships between any of these proteins based on our ontology analysis of these five proteins using DAVID Bioinformatics tools [42]. However, based on the functions of these proteins, each could be related to known oncogenic pathways that may have contributed to the resistance phenotype in ROXY cells.

The serrate RNA effector molecule homolog is known to be involved cell cycle progression at the S phase, suggesting that ROXY cells altered regulation of the cell cycle relative to wild type [134]. In addition, Glycine-tRNA ligase serves as universal pleiotropic signaling molecule needed for cell regulation pathways [134]. Modified expression of these two regulatory proteins may have allowed ROXY cells to bypass cell cycle checkpoints and continue to divide rapidly during chemotherapy. Palladin is a cytoskeletal protein that plays a role in cell adhesion, control of cell morphology, and cell motility [134], indicating that the ROXY cells may have altered their general shape and structure to support the transition from the sensitive to the resistant state, a common feature of proliferating cells [124,247]. Our data also suggests that peptide metabolism was modified in the ROXY cells because Aminopeptidase B is responsible for selectively removing excess arginine and lysine from the N-termini of peptide substrates [134]. Our current hypothesis is that the ROXY cells used these proteins (**Figure 4-8**) to upregulate and sustain stress resistance pathways over the course of their long-term exposure to the chemotherapy. The work we put towards generating this highly resistant colorectal cancer line will lay a foundation for future research by students in the Price Lab that will help further increase our understanding of chemoresistance mechanisms in colorectal cancer.

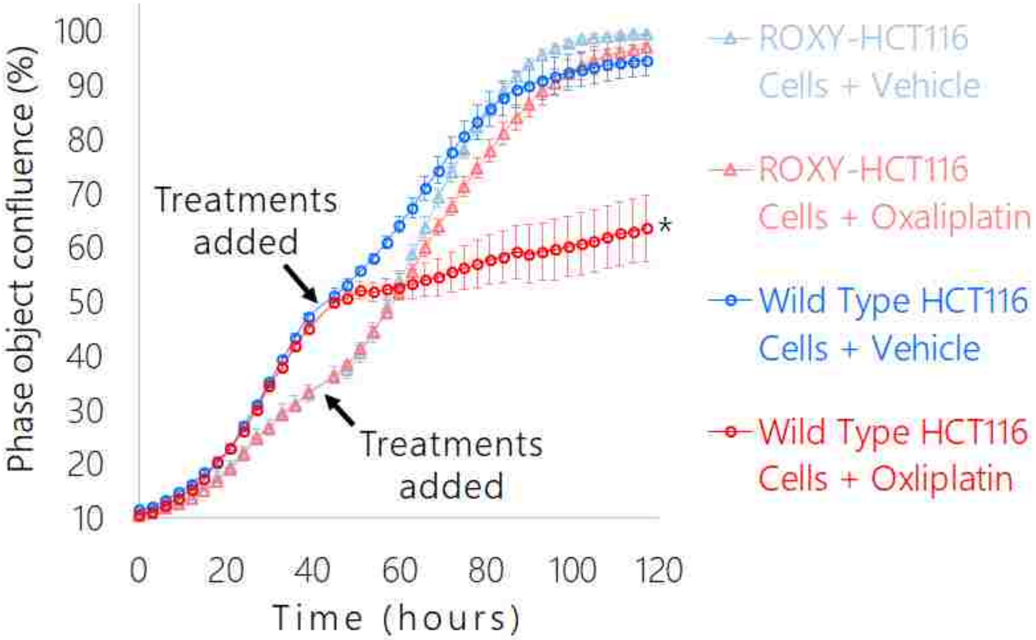

Figure 4-7 Comparison of cell proliferation rates of Wild-Type versus oxaliplatin resistant cell line (ROXY-HCT116) treated with 0.625µM oxaliplatin. *Data are represented as the mean phase object confluence (%) of four biological replicates +/-SEM. The * indicates $P<0.05$ using t-tests to compare the proliferation rate of oxaliplatin treated cells relative to the corresponding vehicle (DMSO) control.*

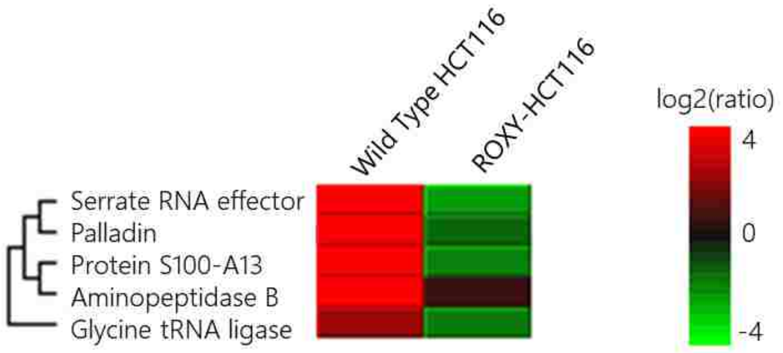

Figure 4-8 Differentially expressed genes in chemoresistant versus wild type CRC cells. *Protein profile heat map of significantly different protein concentrations in oxaliplatin resistant (ROXY-HCT116) versus wild type HCT116 cells based on signal to noise ratio >20 (log2[light-heavy ratio/average]) measured by quantitative proteomics.*

Each of the studies I performed during my graduate research adds another piece to the increasingly intricate puzzle of cancer metabolism. Much more research is required to fully comprehend the underlying mechanisms of metabolic reprogramming and chemoresistance. I pray that my novel applications of proteomics and lipidomics technologies will aid other researchers and clinicians, enabling them to further our knowledge of this debilitating disease, increase survival rates, and improve quality-of-life of cancer patients and their loved ones.

Bibliography

1 Rahman, M. & Hasan, M. R. Cancer Metabolism and Drug Resistance. *Metabolites* **5**, 571-600, doi:10.3390/metabo5040571 (2015).

2 Vander Heiden, M. G. & DeBerardinis, R. J. Understanding the Intersections between Metabolism and Cancer Biology. *Cell* **168**, 657-669, doi:10.1016/j.cell.2016.12.039 (2017).

3 Prasasya, R. D., Tian, D. & Kreeger, P. K. Analysis of cancer signaling networks by systems biology to develop therapies. *Semin Cancer Biol* **21**, 200-206, doi:10.1016/j.semcancer.2011.04.001 (2011).

4 Sharma, S., Kelly, T. K. & Jones, P. A. Epigenetics in cancer. *Carcinogenesis* **31**, 27-36, doi:10.1093/carcin/bgp220 (2010).

5 Beloribi-Djefaflia, S., Vasseur, S. & Guillaumond, F. Lipid metabolic reprogramming in cancer cells. *Oncogenesis* **5**, e189, doi:10.1038/oncsis.2015.49 (2016).

6 Pavlova, N. N. & Thompson, C. B. The Emerging Hallmarks of Cancer Metabolism. *Cell Metab* **23**, 27-47, doi:10.1016/j.cmet.2015.12.006 (2016).

7 Mason, E. F. & Rathmell, J. C. Cell metabolism: an essential link between cell growth and apoptosis. *Biochimica et biophysica acta* **1813**, 645-654, doi:10.1016/j.bbamcr.2010.08.011 (2011).

8 Keibler, M. A. *et al.* Metabolic requirements for cancer cell proliferation. *Cancer Metab* **4**, 16, doi:10.1186/s40170-016-0156-6 (2016).

9 Fiaschi, T. & Chiarugi, P. Oxidative stress, tumor microenvironment, and metabolic reprogramming: a diabolic liaison. *Int J Cell Biol* **2012**, 762825, doi:10.1155/2012/762825 (2012).

10 Hess, J. A. & Khasawneh, M. K. Cancer metabolism and oxidative stress: Insights into carcinogenesis and chemotherapy via the non-dihydrofolate reductase effects of methotrexate. *BBA Clin* **3**, 152-161, doi:10.1016/j.bbacli.2015.01.006 (2015).

11 Ozaki, T. & Nakagawara, A. Role of p53 in Cell Death and Human Cancers. *Cancers (Basel)* **3**, 994-1013, doi:10.3390/cancers3010994 (2011).

12 Ward, P. S. & Thompson, C. B. Signaling in control of cell growth and metabolism. *Cold Spring Harb Perspect Biol* **4**, a006783, doi:10.1101/cshperspect.a006783 (2012).

13 WARBURG, O. On respiratory impairment in cancer cells. *Science* **124**, 269-270 (1956).

14 Vidal, R. S., Quarti, J., Rumjanek, F. D. & Rumjanek, V. M. Metabolic Reprogramming During Multidrug Resistance in Leukemias. *Front Oncol* **8**, 90, doi:10.3389/fonc.2018.00090 (2018).

15 Patra, K. C. & Hay, N. The pentose phosphate pathway and cancer. *Trends Biochem Sci* **39**, 347-354, doi:10.1016/j.tibs.2014.06.005 (2014).

16 Flavin, R., Peluso, S., Nguyen, P. L. & Loda, M. Fatty acid synthase as a potential therapeutic target in cancer. *Future Oncol* **6**, 551-562, doi:10.2217/fon.10.11 (2010).

17 Menendez, J. A. & Lupu, R. Fatty acid synthase and the lipogenic phenotype in cancer pathogenesis. *Nat Rev Cancer* **7**, 763-777, doi:10.1038/nrc2222 (2007).

18 Liu, Y. Fatty acid oxidation is a dominant bioenergetic pathway in prostate cancer. *Prostate Cancer Prostatic Dis* **9**, 230-234, doi:10.1038/sj.pcan.4500879 (2006).

19 Newton, J., Lima, S., Maceyka, M. & Spiegel, S. Revisiting the sphingolipid rheostat: Evolving concepts in cancer therapy. *Exp Cell Res* **333**, 195-200, doi:10.1016/j.yexcr.2015.02.025 (2015).

20 Wise, D. R. & Thompson, C. B. Glutamine addiction: a new therapeutic target in cancer. *Trends Biochem Sci* **35**, 427-433, doi:10.1016/j.tibs.2010.05.003 (2010).

21 Yang, L., Venneti, S. & Nagrath, D. Glutaminolysis: A Hallmark of Cancer Metabolism. *Annu Rev Biomed Eng* **19**, 163-194, doi:10.1146/annurev-bioeng-071516-044546 (2017).

22 Commisso, C. *et al.* Macropinocytosis of protein is an amino acid supply route in Ras-transformed cells. *Nature* **497**, 633-637, doi:10.1038/nature12138 (2013).

23 Burada, F. *et al.* Autophagy in colorectal cancer: An important switch from physiology to pathology. *World J Gastrointest Oncol* **7**, 271-284, doi:10.4251/wjgo.v7.i11.271 (2015).

24 Galluzzi, L. *et al.* Autophagy in malignant transformation and cancer progression. *EMBO J* **34**, 856-880, doi:10.15252/embj.201490784 (2015).

25 Cros, J., Raffenne, J., Couvelard, A. & Poté, N. Tumor Heterogeneity in Pancreatic Adenocarcinoma. *Pathobiology* **85**, 64-71, doi:10.1159/000477773 (2018).

26 Easwaran, H., Tsai, H. C. & Baylin, S. B. Cancer epigenetics: tumor heterogeneity, plasticity of stem-like states, and drug resistance. *Mol Cell* **54**, 716-727, doi:10.1016/j.molcel.2014.05.015 (2014).

27 Lipinski, K. A. *et al.* Cancer Evolution and the Limits of Predictability in Precision Cancer Medicine. *Trends Cancer* **2**, 49-63, doi:10.1016/j.trecan.2015.11.003 (2016).

28 Yoshida, G. J. Metabolic reprogramming: the emerging concept and associated therapeutic strategies. *J Exp Clin Cancer Res* **34**, 111, doi:10.1186/s13046-015-0221-y (2015).

29 Nowell, P. C. The clonal evolution of tumor cell populations. *Science* **194**, 23-28 (1976).

30 McGranahan, N. & Swanton, C. Clonal Heterogeneity and Tumor Evolution: Past, Present, and the Future. *Cell* **168**, 613-628, doi:10.1016/j.cell.2017.01.018 (2017).

31 Saito, T. *et al.* A temporal shift of the evolutionary principle shaping intratumor heterogeneity in colorectal cancer. *Nat Commun* **9**, 2884, doi:10.1038/s41467-018-05226-0 (2018).

32 Nguyen, L. V., Vanner, R., Dirks, P. & Eaves, C. J. Cancer stem cells: an evolving concept. *Nat Rev Cancer* **12**, 133-143, doi:10.1038/nrc3184 (2012).

33 Tamburrino, A., Piro, G., Carbone, C., Tortora, G. & Melisi, D. Mechanisms of resistance to chemotherapeutic and anti-angiogenic drugs as novel targets for pancreatic cancer therapy. *Frontiers in pharmacology* **4**, 56, doi:10.3389/fphar.2013.00056 (2013).

34 Tiligada, E. Chemotherapy: induction of stress responses. *Endocrine-related cancer* **13 Suppl 1**, S115-124, doi:10.1677/erc.1.01272 (2006).

35 Viale, A. *et al.* Oncogene ablation-resistant pancreatic cancer cells depend on mitochondrial function. *Nature* **514**, 628-632, doi:10.1038/nature13611 (2014).

36 Kalluri, R. & Zeisberg, M. Fibroblasts in cancer. *Nat Rev Cancer* **6**, 392-401, doi:10.1038/nrc1877 (2006).

37 Cimino, G. D., Pan, C. X. & Henderson, P. T. Personalized medicine for targeted and platinum-based chemotherapy of lung and bladder cancer. *Bioanalysis* **5**, 369-391, doi:10.4155/bio.12.325 (2013).

38 Joo, W. D., Visintin, I. & Mor, G. Targeted cancer therapy--are the days of systemic chemotherapy numbered? *Maturitas* **76**, 308-314, doi:10.1016/j.maturitas.2013.09.008 (2013).

39 Mardis, E. R. & Wilson, R. K. Cancer genome sequencing: a review. *Hum Mol Genet* **18**, R163-168, doi:10.1093/hmg/ddp396 (2009).

40 Johnson, C., Warmoes, M. O., Shen, X. & Locasale, J. W. Epigenetics and cancer metabolism. *Cancer Lett* **356**, 309-314, doi:10.1016/j.canlet.2013.09.043 (2015).

41 Oliveira A.P., J. M. C., Nielsen J. *From Gene Expression to Metabolic Fluxes*. (The Humana Press Inc, 2007).

42 Huang, d. W., Sherman, B. T. & Lempicki, R. A. Systematic and integrative analysis of large gene lists using DAVID bioinformatics resources. *Nat Protoc* **4**, 44-57, doi:10.1038/nprot.2008.211 (2009).

43 Sud, M., Fahy, E., Cotter, D., Dennis, E. A. & Subramaniam, S. LIPID MAPS-Nature Lipidomics Gateway: An Online Resource for Students and Educators Interested in Lipids. *Journal of chemical education* **89**, 291-292, doi:10.1021/ed200088u (2012).

44 Bradley N , P. M., Wilson E , Herring A , Lofthouse S , Hannemann A , Piccolo S , Rockwood A and Price J. (ed Brigham Young University Dept of Chemistry and Biochemistry) (Bioinformatics, 2017).

45 Guan, S., Price, J. C., Ghaemmaghami, S., Prusiner, S. B. & Burlingame, A. L. Compartment modeling for mammalian protein turnover studies by stable isotope metabolic labeling. *Anal Chem* **84**, 4014-4021, doi:10.1021/ac203330z (2012).

46 Price, J. C., Guan, S., Burlingame, A., Prusiner, S. B. & Ghaemmaghami, S. Analysis of proteome dynamics in the mouse brain. *Proc Natl Acad Sci U S A* **107**, 14508-14513, doi:10.1073/pnas.1006551107 (2010).

47 Price, J. C. *et al.* Measurement of human plasma proteome dynamics with (2)H(2)O and liquid chromatography tandem mass spectrometry. *Anal Biochem* **420**, 73-83, doi:10.1016/j.ab.2011.09.007 (2012).

48 Duckwall, C. S., Murphy, T. A. & Young, J. D. Mapping cancer cell metabolism with(13)C flux analysis: Recent progress and future challenges. *J Carcinog* **12**, 13, doi:10.4103/1477-3163.115422 (2013).

49 Mathis, A. D. *et al.* Mechanisms of In Vivo Ribosome Maintenance Change in Response to Nutrient Signals. *Mol Cell Proteomics* **16**, 243-254, doi:10.1074/mcp.M116.063255 (2017).

50 Price, J. C. *et al.* The effect of long term calorie restriction on in vivo hepatic proteostatis: a novel combination of dynamic and quantitative proteomics. *Mol Cell Proteomics* **11**, 1801-1814, doi:10.1074/mcp.M112.021204 (2012).

51 Sallam, R. M. Proteomics in cancer biomarkers discovery: challenges and applications. *Dis Markers* **2015**, 321370, doi:10.1155/2015/321370 (2015).

52 Zhang, T. & Ghaemmaghami, S. Global analysis of cellular protein flux quantifies the selectivity of basal autophagy. *Autophagy* **12**, 1411-1412, doi:10.1080/15548627.2016.1190891 (2016).

53 Pisco, A. O. & Huang, S. Non-genetic cancer cell plasticity and therapy-induced stemness in tumour relapse: 'What does not kill me strengthens me'. *Br J Cancer* **112**, 1725-1732, doi:10.1038/bjc.2015.146 (2015).

54 Bieberich, E. Ceramide signaling in cancer and stem cells. *Future Lipidol* **3**, 273-300, doi:10.2217/17460875.3.3.273 (2008).

55 Furuya, H., Shimizu, Y. & Kawamori, T. Sphingolipids in cancer. *Cancer metastasis reviews* **30**, 567-576, doi:10.1007/s10555-011-9304-1 (2011).

56 Maceyka, M., Harikumar, K. B., Milstien, S. & Spiegel, S. Sphingosine-1-phosphate signaling and its role in disease. *Trends Cell Biol* **22**, 50-60, doi:10.1016/j.tcb.2011.09.003 (2012).

57 Osawa, Y. *et al.* Roles for C16-ceramide and sphingosine 1-phosphate in regulating hepatocyte apoptosis in response to tumor necrosis factor-alpha. *The Journal of biological chemistry* **280**, 27879-27887, doi:10.1074/jbc.M503002200 (2005).
58 Patwardhan, G. A., Beverly, L. J. & Siskind, L. J. Sphingolipids and mitochondrial apoptosis. *J Bioenerg Biomembr* **48**, 153-168, doi:10.1007/s10863-015-9602-3 (2016).
59 Hartmann, D. *et al.* Long chain ceramides and very long chain ceramides have opposite effects on human breast and colon cancer cell growth. *Int J Biochem Cell Biol* **44**, 620-628, doi:10.1016/j.biocel.2011.12.019 (2012).
60 Rénert, A. F. *et al.* The proapoptotic C16-ceramide-dependent pathway requires the death-promoting factor Btf in colon adenocarcinoma cells. *J Proteome Res* **8**, 4810-4822, doi:10.1021/pr9005316 (2009).
61 Eto, M., Bennouna, J., Hunter, O. C., Lotze, M. T. & Amoscato, A. A. Importance of C16 ceramide accumulation during apoptosis in prostate cancer cells. *Int J Urol* **13**, 148-156, doi:10.1111/j.1442-2042.2006.01249.x (2006).
62 Thomas, R. L., Matsko, C. M., Lotze, M. T. & Amoscato, A. A. Mass spectrometric identification of increased C16 ceramide levels during apoptosis. *The Journal of biological chemistry* **274**, 30580-30588 (1999).
63 Chalfant, C. E. & Spiegel, S. Sphingosine 1-phosphate and ceramide 1-phosphate: expanding roles in cell signaling. *J Cell Sci* **118**, 4605-4612, doi:10.1242/jcs.02637 (2005).
64 Cuvillier, O. *et al.* Suppression of ceramide-mediated programmed cell death by sphingosine-1-phosphate. *Nature* **381**, 800-803, doi:10.1038/381800a0 (1996).
65 Fyrst, H. & Saba, J. D. An update on sphingosine-1-phosphate and other sphingolipid mediators. *Nat Chem Biol* **6**, 489-497, doi:10.1038/nchembio.392 (2010).
66 Guillermet-Guibert, J. *et al.* Targeting the sphingolipid metabolism to defeat pancreatic cancer cell resistance to the chemotherapeutic gemcitabine drug. *Mol Cancer Ther* **8**, 809-820, doi:10.1158/1535-7163.MCT-08-1096 (2009).
67 Kunkel, G. T., Maceyka, M., Milstien, S. & Spiegel, S. Targeting the sphingosine-1-phosphate axis in cancer, inflammation and beyond. *Nat Rev Drug Discov* **12**, 688-702, doi:10.1038/nrd4099 (2013).
68 Obinata, H. & Hla, T. Assessment of sphingosine-1-phosphate activity in biological samples by receptor internalization and adherens junction formation. *Methods Mol Biol* **874**, 69-76, doi:10.1007/978-1-61779-800-9_6 (2012).
69 Taha, T. A., Mullen, T. D. & Obeid, L. M. A house divided: ceramide, sphingosine, and sphingosine-1-phosphate in programmed cell death. *Biochimica et biophysica acta* **1758**, 2027-2036, doi:10.1016/j.bbamem.2006.10.018 (2006).
70 Takabe, K. & Spiegel, S. Export of sphingosine-1-phosphate and cancer progression. *Journal of lipid research* **55**, 1839-1846, doi:10.1194/jlr.R046656 (2014).
71 Bode, C. & Gräler, M. H. Quantification of sphingosine-1-phosphate and related sphingolipids by liquid chromatography coupled to tandem mass spectrometry. *Methods Mol Biol* **874**, 33-44, doi:10.1007/978-1-61779-800-9_3 (2012).
72 Utah, M. C. F. a. t. U. o.
73 McShane, E. *et al.* Kinetic Analysis of Protein Stability Reveals Age-Dependent Degradation. *Cell* **167**, 803-815.e821, doi:10.1016/j.cell.2016.09.015 (2016).

74 White, E., Mehnert, J. M. & Chan, C. S. Autophagy, Metabolism, and Cancer. *Clinical cancer research : an official journal of the American Association for Cancer Research* **21**, 5037-5046, doi:10.1158/1078-0432.CCR-15-0490 (2015).

75 Mathew, R. & White, E. Eat this, not that! How selective autophagy helps cancer cells survive. *Mol Cell Oncol* **2**, e975638, doi:10.4161/23723556.2014.975638 (2015).

76 White, E. The role for autophagy in cancer. *J Clin Invest* **125**, 42-46, doi:10.1172/JCI73941 (2015).

77 Thorburn, A., Thamm, D. H. & Gustafson, D. L. Autophagy and cancer therapy. *Mol Pharmacol* **85**, 830-838, doi:10.1124/mol.114.091850 (2014).

78 Kimura, T., Takabatake, Y., Takahashi, A. & Isaka, Y. Chloroquine in cancer therapy: a double-edged sword of autophagy. *Cancer Res* **73**, 3-7, doi:10.1158/0008-5472.CAN-12-2464 (2013).

79 Johansen, T. & Lamark, T. Selective autophagy mediated by autophagic adapter proteins. *Autophagy* **7**, 279-296 (2011).

80 Mathew, R. *et al.* Functional role of autophagy-mediated proteome remodeling in cell survival signaling and innate immunity. *Mol Cell* **55**, 916-930, doi:10.1016/j.molcel.2014.07.019 (2014).

81 Chourasia, A. H., Boland, M. L. & Macleod, K. F. Mitophagy and cancer. *Cancer Metab* **3**, 4, doi:10.1186/s40170-015-0130-8 (2015).

82 Yang, X. *et al.* The role of autophagy induced by tumor microenvironment in different cells and stages of cancer. *Cell Biosci* **5**, 14, doi:10.1186/s13578-015-0005-2 (2015).

83 Barth, S., Glick, D. & Macleod, K. F. Autophagy: assays and artifacts. *J Pathol* **221**, 117-124, doi:10.1002/path.2694 (2010).

84 Williamson, C. D., Wong, D. S., Bozidis, P., Zhang, A. & Colberg-Poley, A. M. Isolation of Endoplasmic Reticulum, Mitochondria, and Mitochondria-Associated Membrane and Detergent Resistant Membrane Fractions from Transfected Cells and from Human Cytomegalovirus-Infected Primary Fibroblasts. *Curr Protoc Cell Biol* **68**, 3.27.21-33, doi:10.1002/0471143030.cb0327s68 (2015).

85 Boersema, P. J., Raijmakers, R., Lemeer, S., Mohammed, S. & Heck, A. J. Multiplex peptide stable isotope dimethyl labeling for quantitative proteomics. *Nat Protoc* **4**, 484-494, doi:10.1038/nprot.2009.21 (2009).

86 Heaney, L. M., Jones, D. J. & Suzuki, T. Mass spectrometry in medicine: a technology for the future? *Future Sci OA* **3**, FSO213, doi:10.4155/fsoa-2017-0053 (2017).

87 Stratton, M. R., Campbell, P. J. & Futreal, P. A. The cancer genome. *Nature* **458**, 719-724, doi:10.1038/nature07943 (2009).

88 Gottesman, M. M. Mechanisms of cancer drug resistance. *Annu Rev Med* **53**, 615-627, doi:10.1146/annurev.med.53.082901.103929 (2002).

89 Oberstein, P. E. & Olive, K. P. Pancreatic cancer: why is it so hard to treat? *Therap Adv Gastroenterol* **6**, 321-337, doi:10.1177/1756283X13478680 (2013).

90 Labi, V. & Erlacher, M. How cell death shapes cancer. *Cell Death Dis* **6**, e1675, doi:10.1038/cddis.2015.20 (2015).

91 Baenke, F., Peck, B., Miess, H. & Schulze, A. Hooked on fat: the role of lipid synthesis in cancer metabolism and tumour development. *Disease models & mechanisms* **6**, 1353-1363, doi:10.1242/dmm.011338 (2013).

92 Wymann, M. P. & Schneiter, R. Lipid signalling in disease. *Nature reviews. Molecular cell biology* **9**, 162-176, doi:10.1038/nrm2335 (2008).

93 Menendez, J. A. Fine-tuning the lipogenic/lipolytic balance to optimize the metabolic requirements of cancer cell growth: molecular mechanisms and therapeutic perspectives. *Biochimica et biophysica acta* **1801**, 381-391, doi:10.1016/j.bbalip.2009.09.005 (2010).

94 Liu, Q., Luo, Q., Halim, A. & Song, G. Targeting lipid metabolism of cancer cells: A promising therapeutic strategy for cancer. *Cancer Lett* **401**, 39-45, doi:10.1016/j.canlet.2017.05.002 (2017).

95 Huang, J. *et al.* Tumor-Induced Hyperlipidemia Contributes to Tumor Growth. *Cell Rep* **15**, 336-348, doi:10.1016/j.celrep.2016.03.020 (2016).

96 Daniëls, V. W. *et al.* Cancer cells differentially activate and thrive on de novo lipid synthesis pathways in a low-lipid environment. *PLoS One* **9**, e106913, doi:10.1371/journal.pone.0106913 (2014).

97 Magtanong, L., Ko, P. J. & Dixon, S. J. Emerging roles for lipids in non-apoptotic cell death. *Cell Death Differ* **23**, 1099-1109, doi:10.1038/cdd.2016.25 (2016).

98 Luo, X. *et al.* Emerging roles of lipid metabolism in cancer metastasis. *Mol Cancer* **16**, 76, doi:10.1186/s12943-017-0646-3 (2017).

99 Carracedo, A., Cantley, L. C. & Pandolfi, P. P. Cancer metabolism: fatty acid oxidation in the limelight. *Nat Rev Cancer* **13**, 227-232, doi:10.1038/nrc3483 (2013).

100 Chen, J. *et al.* Ceramide synthase-4 orchestrates the cell proliferation and tumor growth of liver cancer in vitro and in vivo through the nuclear factor-κB signaling pathway. *Oncol Lett* **14**, 1477-1483, doi:10.3892/ol.2017.6365 (2017).

101 Haddadi, N., Lin, Y., Simpson, A. M., Nassif, N. T. & McGowan, E. M. "Dicing and Splicing" Sphingosine Kinase and Relevance to Cancer. *Int J Mol Sci* **18**, doi:10.3390/ijms18091891 (2017).

102 Hatoum, D., Haddadi, N., Lin, Y., Nassif, N. T. & McGowan, E. M. Mammalian sphingosine kinase (SphK) isoenzymes and isoform expression: challenges for SphK as an oncotarget. *Oncotarget* **8**, 36898-36929, doi:10.18632/oncotarget.16370 (2017).

103 Bauerschlag, D. O. *et al.* Fatty acid synthase overexpression: target for therapy and reversal of chemoresistance in ovarian cancer. *J Transl Med* **13**, 146, doi:10.1186/s12967-015-0511-3 (2015).

104 Gabitova, L., Gorin, A. & Astsaturov, I. Molecular pathways: sterols and receptor signaling in cancer. *Clinical cancer research : an official journal of the American Association for Cancer Research* **20**, 28-34, doi:10.1158/1078-0432.CCR-13-0122 (2014).

105 Zhang, F. & Du, G. Dysregulated lipid metabolism in cancer. *World J Biol Chem* **3**, 167-174, doi:10.4331/wjbc.v3.i8.167 (2012).

106 Chipuk, J. E. *et al.* Sphingolipid metabolism cooperates with BAK and BAX to promote the mitochondrial pathway of apoptosis. *Cell* **148**, 988-1000, doi:10.1016/j.cell.2012.01.038 (2012).

107 Hannun, Y. A. & Obeid, L. M. Principles of bioactive lipid signalling: lessons from sphingolipids. *Nature reviews. Molecular cell biology* **9**, 139-150, doi:10.1038/nrm2329 (2008).

108 Gault, C. R., Eblen, S. T., Neumann, C. A., Hannun, Y. A. & Obeid, L. M. Oncogenic K-Ras regulates bioactive sphingolipids in a sphingosine kinase 1-dependent manner. *The Journal of biological chemistry* **287**, 31794-31803, doi:10.1074/jbc.M112.385765 (2012).

109 Gault, C. R., Obeid, L. M. & Hannun, Y. A. An overview of sphingolipid metabolism: from synthesis to breakdown. *Advances in experimental medicine and biology* **688**, 1-23 (2010).

110 Siskind, L. J., Kolesnick, R. N. & Colombini, M. Ceramide channels increase the permeability of the mitochondrial outer membrane to small proteins. *The Journal of biological chemistry* **277**, 26796-26803, doi:10.1074/jbc.M200754200 (2002).

111 Pyne, N. J. & Pyne, S. Sphingosine 1-phosphate and cancer. *Nat Rev Cancer* **10**, 489-503, doi:10.1038/nrc2875 (2010).

112 Bektas, M. *et al.* Sphingosine kinase activity counteracts ceramide-mediated cell death in human melanoma cells: role of Bcl-2 expression. *Oncogene* **24**, 178-187, doi:10.1038/sj.onc.1208019 (2005).

113 Hait, N. C., Oskeritzian, C. A., Paugh, S. W., Milstien, S. & Spiegel, S. Sphingosine kinases, sphingosine 1-phosphate, apoptosis and diseases. *Biochimica et biophysica acta* **1758**, 2016-2026, doi:10.1016/j.bbamem.2006.08.007 (2006).

114 Olivera, A. *et al.* Sphingosine kinase expression increases intracellular sphingosine-1-phosphate and promotes cell growth and survival. *The Journal of cell biology* **147**, 545-558 (1999).

115 Ponnusamy, S. *et al.* Sphingolipids and cancer: ceramide and sphingosine-1-phosphate in the regulation of cell death and drug resistance. *Future Oncol* **6**, 1603-1624, doi:10.2217/fon.10.116 (2010).

116 Sarkar, S. *et al.* Sphingosine kinase 1 is required for migration, proliferation and survival of MCF-7 human breast cancer cells. *FEBS letters* **579**, 5313-5317, doi:10.1016/j.febslet.2005.08.055 (2005).

117 Schnitzer, S. E., Weigert, A., Zhou, J. & Brune, B. Hypoxia enhances sphingosine kinase 2 activity and provokes sphingosine-1-phosphate-mediated chemoresistance in A549 lung cancer cells. *Molecular cancer research : MCR* **7**, 393-401, doi:10.1158/1541-7786.MCR-08-0156 (2009).

118 Taha, T. A., Hannun, Y. A. & Obeid, L. M. Sphingosine kinase: biochemical and cellular regulation and role in disease. *Journal of biochemistry and molecular biology* **39**, 113-131 (2006).

119 Wang, Z. *et al.* Molecular basis of sphingosine kinase 1 substrate recognition and catalysis. *Structure* **21**, 798-809, doi:10.1016/j.str.2013.02.025 (2013).

120 Xia, P. *et al.* An oncogenic role of sphingosine kinase. *Current biology : CB* **10**, 1527-1530 (2000).

121 Yamada, H., Yoshida, T., Sakamoto, H., Terada, M. & Sugimura, T. Establishment of a human pancreatic adenocarcinoma cell line (PSN-1) with amplifications of both c-myc and activated c-Ki-ras by a point mutation. *Biochem Biophys Res Commun* **140**, 167-173 (1986).

122 Lee, K. M., Nguyen, C., Ulrich, A. B., Pour, P. M. & Ouellette, M. M. Immortalization with telomerase of the Nestin-positive cells of the human pancreas. *Biochem Biophys Res Commun* **301**, 1038-1044 (2003).

123 Baba AI, C. C. *Comparative Oncology.* (The Publishing House of the Romanian Academy, 2007).

124 D'Anselmi, F. *et al.* Metabolism and cell shape in cancer: a fractal analysis. *Int J Biochem Cell Biol* **43**, 1052-1058, doi:10.1016/j.biocel.2010.05.002 (2011).

125 Fan, H. & Chu, J. Y. A brief review of short tandem repeat mutation. *Genomics Proteomics Bioinformatics* **5**, 7-14, doi:10.1016/S1672-0229(07)60009-6 (2007).

126 Reid Y, S. D., Riss T, et al. *Authentication of Human Cell Lines by STR DNA Profiling Analysis*. (Eli Lilly & Company and the National Center for Advancing Translational Sciences, 2013

127 Deng, N., Zhou, H., Fan, H. & Yuan, Y. Single nucleotide polymorphisms and cancer susceptibility. *Oncotarget* **8**, 110635-110649, doi:10.18632/oncotarget.22372 (2017).

128 Ramensky, V., Bork, P. & Sunyaev, S. Human non-synonymous SNPs: server and survey. *Nucleic acids research* **30**, 3894-3900 (2002).

129 Hirshfield, K. M., Rebbeck, T. R. & Levine, A. J. Germline mutations and polymorphisms in the origins of cancers in women. *J Oncol* **2010**, 297671, doi:10.1155/2010/297671 (2010).

130 Gerstung, M. *et al.* Reliable detection of subclonal single-nucleotide variants in tumour cell populations. *Nat Commun* **3**, 811, doi:10.1038/ncomms1814 (2012).

131 Love, M. I., Huber, W. & Anders, S. Moderated estimation of fold change and dispersion for RNA-seq data with DESeq2. *Genome Biol* **15**, 550, doi:10.1186/s13059-014-0550-8 (2014).

132 William Whitford, J. M. *Lipids in Cell Culture Media*, <https://static.fishersci.com/cmsassets/downloads/segment/Scientific/pdf/Cell_Culture/Application_Notes/Lipids_Media.pdf> (

133 Pitson, S. M. *et al.* Activation of sphingosine kinase 1 by ERK1/2-mediated phosphorylation. *EMBO J* **22**, 5491-5500, doi:10.1093/emboj/cdg540 (2003).

134 The UniProt Consortium. UniProt: the universal protein knowledgebase. *Nucleic acids research* **45**, D158-D169, doi:10.1093/nar/gkw1099 (2017).

135 Walter, K. *et al.* Serum fatty acid synthase as a marker of pancreatic neoplasia. *Cancer Epidemiol Biomarkers Prev* **18**, 2380-2385, doi:10.1158/1055-9965.EPI-09-0144 (2009).

136 Jewer, M., Findlay, S. D. & Postovit, L. M. Post-transcriptional regulation in cancer progression : Microenvironmental control of alternative splicing and translation. *J Cell Commun Signal* **6**, 233-248, doi:10.1007/s12079-012-0179-x (2012).

137 French, K. J. *et al.* Discovery and evaluation of inhibitors of human sphingosine kinase. *Cancer Res* **63**, 5962-5969 (2003).

138 Baran, Y. *et al.* Alterations of ceramide/sphingosine 1-phosphate rheostat involved in the regulation of resistance to imatinib-induced apoptosis in K562 human chronic myeloid leukemia cells. *The Journal of biological chemistry* **282**, 10922-10934, doi:10.1074/jbc.M610157200 (2007).

139 Roa, W. *et al.* Enhancement of radiation sensitivity with BH3I-1 in non-small cell lung cancer. *Clin Invest Med* **28**, 55-63 (2005).

140 van Delft, M. F. *et al.* The BH3 mimetic ABT-737 targets selective Bcl-2 proteins and efficiently induces apoptosis via Bak/Bax if Mcl-1 is neutralized. *Cancer Cell* **10**, 389-399, doi:10.1016/j.ccr.2006.08.027 (2006).

141 Giroux, V. *et al.* p8 is a new target of gemcitabine in pancreatic cancer cells. *Clinical cancer research : an official journal of the American Association for Cancer Research* **12**, 235-241, doi:10.1158/1078-0432.CCR-05-1700 (2006).

142 Plunkett, W. *et al.* Gemcitabine: metabolism, mechanisms of action, and self-potentiation. *Semin Oncol* **22**, 3-10 (1995).

143 DeBerardinis, R. J. & Chandel, N. S. Fundamentals of cancer metabolism. *Sci Adv* **2**, e1600200, doi:10.1126/sciadv.1600200 (2016).
144 Chand, S., O'Hayer, K., Blanco, F. F., Winter, J. M. & Brody, J. R. The Landscape of Pancreatic Cancer Therapeutic Resistance Mechanisms. *International journal of biological sciences* **12**, 273-282, doi:10.7150/ijbs.14951 (2016).
145 Grösch, S., Schiffmann, S. & Geisslinger, G. Chain length-specific properties of ceramides. *Prog Lipid Res* **51**, 50-62, doi:10.1016/j.plipres.2011.11.001 (2012).
146 Kolesnick, R. N., Haimovitz-Friedman, A. & Fuks, Z. The sphingomyelin signal transduction pathway mediates apoptosis for tumor necrosis factor, Fas, and ionizing radiation. *Biochemistry and cell biology = Biochimie et biologie cellulaire* **72**, 471-474 (1994).
147 Schwandner, R., Wiegmann, K., Bernardo, K., Kreder, D. & Kronke, M. TNF receptor death domain-associated proteins TRADD and FADD signal activation of acid sphingomyelinase. *The Journal of biological chemistry* **273**, 5916-5922 (1998).
148 Lin, T. *et al.* Role of acidic sphingomyelinase in Fas/CD95-mediated cell death. *The Journal of biological chemistry* **275**, 8657-8663 (2000).
149 Garcia-Ruiz, C. *et al.* Defective TNF-alpha-mediated hepatocellular apoptosis and liver damage in acidic sphingomyelinase knockout mice. *J Clin Invest* **111**, 197-208, doi:10.1172/JCI16010 (2003).
150 Morales, A., Lee, H., Goni, F. M., Kolesnick, R. & Fernandez-Checa, J. C. Sphingolipids and cell death. *Apoptosis : an international journal on programmed cell death* **12**, 923-939, doi:10.1007/s10495-007-0721-0 (2007).
151 Smyth, M. J., Obeid, L. M. & Hannun, Y. A. Ceramide: a novel lipid mediator of apoptosis. *Advances in pharmacology* **41**, 133-154 (1997).
152 Schiffmann, S. *et al.* Activation of ceramide synthase 6 by celecoxib leads to a selective induction of C16:0-ceramide. *Biochemical pharmacology* **80**, 1632-1640, doi:10.1016/j.bcp.2010.08.012 (2010).
153 Kitatani, K., Idkowiak-Baldys, J. & Hannun, Y. A. The sphingolipid salvage pathway in ceramide metabolism and signaling. *Cellular signalling* **20**, 1010-1018, doi:10.1016/j.cellsig.2007.12.006 (2008).
154 Olivera, A. & Spiegel, S. Sphingosine kinase: a mediator of vital cellular functions. *Prostaglandins & other lipid mediators* **64**, 123-134 (2001).
155 Bose, R. *et al.* Ceramide synthase mediates daunorubicin-induced apoptosis: an alternative mechanism for generating death signals. *Cell* **82**, 405-414 (1995).
156 Chalfant, C. E. *et al.* De novo ceramide regulates the alternative splicing of caspase 9 and Bcl-x in A549 lung adenocarcinoma cells. Dependence on protein phosphatase-1. *The Journal of biological chemistry* **277**, 12587-12595, doi:10.1074/jbc.M112010200 (2002).
157 Bourbon, N. A., Sandirasegarane, L. & Kester, M. Ceramide-induced inhibition of Akt is mediated through protein kinase Czeta: implications for growth arrest. *The Journal of biological chemistry* **277**, 3286-3292, doi:10.1074/jbc.M110541200 (2002).
158 Colie, S. *et al.* Disruption of sphingosine 1-phosphate lyase confers resistance to chemotherapy and promotes oncogenesis through Bcl-2/Bcl-xL upregulation. *Cancer Res* **69**, 9346-9353, doi:10.1158/0008-5472.CAN-09-2198 (2009).
159 de Sousa Cavalcante, L. & Monteiro, G. Gemcitabine: metabolism and molecular mechanisms of action, sensitivity and chemoresistance in pancreatic cancer. *European journal of pharmacology* **741**, 8-16, doi:10.1016/j.ejphar.2014.07.041 (2014).

160 Lennon, A. M. *et al.* The early detection of pancreatic cancer: what will it take to diagnose and treat curable pancreatic neoplasia? *Cancer Res* **74**, 3381-3389, doi:10.1158/0008-5472.CAN-14-0734 (2014).
161 Siegel, R. *et al.* Cancer treatment and survivorship statistics, 2012. *CA Cancer J Clin* **62**, 220-241, doi:10.3322/caac.21149 (2012).
162 Ireland, L. *et al.* Chemoresistance in pancreatic cancer is driven by stroma-derived insulin-like growth factors. *Cancer Res*, doi:10.1158/0008-5472.CAN-16-1201 (2016).
163 Takeuchi, S. *et al.* Chemotherapy-Derived Inflammatory Responses Accelerate the Formation of Immunosuppressive Myeloid Cells in the Tissue Microenvironment of Human Pancreatic Cancer. *Cancer Res* **75**, 2629-2640, doi:10.1158/0008-5472.CAN-14-2921 (2015).
164 Sigma-Aldrich, I. *Importance and uses of glutathione in serum-free eucaryotic, including hybridoma and Chinese Hamster Ovary (CHO) cell, cultures*, <https://www.sigmaaldrich.com/life-science/cell-culture/learning-center/media-expert/glutathione.html> (
165 Andrews, S. *FastQC: a quality control tool for high throughput*

sequence data, <http://www.bioinformatics.babraham.ac.uk/projects/fastqc> (2010).
166 Liao, Y., Smyth, G. K. & Shi, W. The Subread aligner: fast, accurate and scalable read mapping by seed-and-vote. *Nucleic acids research* **41**, e108, doi:10.1093/nar/gkt214 (2013).
167 Andrew J. Landgraf, Y. L. (Cornell University Library, 2015).
168 Obenchain, V. *et al.* VariantAnnotation: a Bioconductor package for exploration and annotation of genetic variants. *Bioinformatics* **30**, 2076-2078, doi:10.1093/bioinformatics/btu168 (2014).
169 Adzhubei, I., Jordan, D. M. & Sunyaev, S. R. Predicting functional effect of human missense mutations using PolyPhen-2. *Curr Protoc Hum Genet* **Chapter 7**, Unit7.20, doi:10.1002/0471142905.hg0720s76 (2013).
170 Metsalu, T. & Vilo, J. ClustVis: a web tool for visualizing clustering of multivariate data using Principal Component Analysis and heatmap. *Nucleic acids research* **43**, W566-570, doi:10.1093/nar/gkv468 (2015).
171 Zhang, J. *et al.* PEAKS DB: de novo sequencing assisted database search for sensitive and accurate peptide identification. *Mol Cell Proteomics* **11**, M111.010587, doi:10.1074/mcp.M111.010587 (2012).
172 Bligh, E. G. & Dyer, W. J. A rapid method of total lipid extraction and purification. *Canadian journal of biochemistry and physiology* **37**, 911-917, doi:10.1139/o59-099 (1959).
173 Prince, J. T. & Marcotte, E. M. mspire: mass spectrometry proteomics in Ruby. *Bioinformatics* **24**, 2796-2797, doi:10.1093/bioinformatics/btn513 (2008).
174 Sud, M. *et al.* LMSD: LIPID MAPS structure database. *Nucleic acids research* **35**, D527-532, doi:10.1093/nar/gkl838 (2007).
175 Smith CA, O. M. G., Want EJ, Qin C, Trauger SA, Brandon TR, Custodio DE, Abagyan R, Siuzdak G. *METLIN: a metabolite mass spectral database*, 2005).
176 Crowley, L. C., Chojnowski, G. & Waterhouse, N. J. Measuring the DNA Content of Cells in Apoptosis and at Different Cell-Cycle Stages by Propidium Iodide Staining and Flow Cytometry. *Cold Spring Harb Protoc* **2016**, pdb.prot087247, doi:10.1101/pdb.prot087247 (2016).

177 Thomassen, I., van Gestel, Y. R., Lemmens, V. E. & de Hingh, I. H. Incidence, prognosis, and treatment options for patients with synchronous peritoneal carcinomatosis and liver metastases from colorectal origin. *Dis Colon Rectum* **56**, 1373-1380, doi:10.1097/DCR.0b013e3182a62d9d (2013).

178 Kimmelman, A. C. The dynamic nature of autophagy in cancer. *Genes Dev* **25**, 1999-2010, doi:10.1101/gad.17558811 (2011).

179 Ciechanover, A. Intracellular protein degradation: from a vague idea thru the lysosome and the ubiquitin-proteasome system and onto human diseases and drug targeting. *Cell Death Differ* **12**, 1178-1190, doi:10.1038/sj.cdd.4401692 (2005).

180 Mathew, R. & White, E. Autophagy, stress, and cancer metabolism: what doesn't kill you makes you stronger. *Cold Spring Harb Symp Quant Biol* **76**, 389-396, doi:10.1101/sqb.2012.76.011015 (2011).

181 Rabinowitz, J. D. & White, E. Autophagy and metabolism. *Science* **330**, 1344-1348, doi:10.1126/science.1193497 (2010).

182 Selvakumaran, M., Amaravadi, R. K., Vasilevskaya, I. A. & O'Dwyer, P. J. Autophagy inhibition sensitizes colon cancer cells to antiangiogenic and cytotoxic therapy. *Clinical cancer research : an official journal of the American Association for Cancer Research* **19**, 2995-3007, doi:10.1158/1078-0432.CCR-12-1542 (2013).

183 Zheng, H. Y., Zhang, X. Y., Wang, X. F. & Sun, B. C. Autophagy enhances the aggressiveness of human colorectal cancer cells and their ability to adapt to apoptotic stimulus. *Cancer Biol Med* **9**, 105-110, doi:10.3969/j.issn.2095-3941.2012.02.004 (2012).

184 Weerasekara, V. K. *et al.* Metabolic-stress-induced rearrangement of the 14-3-3ζ interactome promotes autophagy via a ULK1- and AMPK-regulated 14-3-3ζ interaction with phosphorylated Atg9. *Mol Cell Biol* **34**, 4379-4388, doi:10.1128/MCB.00740-14 (2014).

185 Guo, J. Y. *et al.* Activated Ras requires autophagy to maintain oxidative metabolism and tumorigenesis. *Genes Dev* **25**, 460-470, doi:10.1101/gad.2016311 (2011).

186 Sui, X. *et al.* Autophagy and chemotherapy resistance: a promising therapeutic target for cancer treatment. *Cell Death Dis* **4**, e838, doi:10.1038/cddis.2013.350 (2013).

187 Hu, F. *et al.* Docetaxel-mediated autophagy promotes chemoresistance in castration-resistant prostate cancer cells by inhibiting STAT3. *Cancer Lett* **416**, 24-30, doi:10.1016/j.canlet.2017.12.013 (2018).

188 Degenhardt, K. *et al.* Autophagy promotes tumor cell survival and restricts necrosis, inflammation, and tumorigenesis. *Cancer Cell* **10**, 51-64, doi:10.1016/j.ccr.2006.06.001 (2006).

189 Stolz, A., Ernst, A. & Dikic, I. Cargo recognition and trafficking in selective autophagy. *Nat Cell Biol* **16**, 495-501, doi:10.1038/ncb2979 (2014).

190 Kraft, C., Deplazes, A., Sohrmann, M. & Peter, M. Mature ribosomes are selectively degraded upon starvation by an autophagy pathway requiring the Ubp3p/Bre5p ubiquitin protease. *Nat Cell Biol* **10**, 602-610, doi:10.1038/ncb1723 (2008).

191 Lu, H. *et al.* Regulation and function of mitophagy in development and cancer. *Autophagy* **9**, 1720-1736, doi:10.4161/auto.26550 (2013).

192 Bernales, S., Schuck, S. & Walter, P. ER-phagy: selective autophagy of the endoplasmic reticulum. *Autophagy* **3**, 285-287 (2007).

193 Fu, N., Yang, X. & Chen, L. Nucleophagy plays a major role in human diseases. *Curr Drug Targets*, doi:10.2174/1389450119666180518112350 (2018).
194 Reggiori, F., Komatsu, M., Finley, K. & Simonsen, A. Autophagy: more than a nonselective pathway. *Int J Cell Biol* **2012**, 219625, doi:10.1155/2012/219625 (2012).
195 Mizushima, N. & Komatsu, M. Autophagy: renovation of cells and tissues. *Cell* **147**, 728-741, doi:10.1016/j.cell.2011.10.026 (2011).
196 Vadlamudi, R. K. & Shin, J. Genomic structure and promoter analysis of the p62 gene encoding a non-proteasomal multiubiquitin chain binding protein. *FEBS letters* **435**, 138-142 (1998).
197 Kaushik, S. & Cuervo, A. M. Chaperone-mediated autophagy. *Methods Mol Biol* **445**, 227-244, doi:10.1007/978-1-59745-157-4_15 (2008).
198 Chatterjee, A., Mambo, E. & Sidransky, D. Mitochondrial DNA mutations in human cancer. *Oncogene* **25**, 4663-4674, doi:10.1038/sj.onc.1209604 (2006).
199 Galluzzi, L., Larochette, N., Zamzami, N. & Kroemer, G. Mitochondria as therapeutic targets for cancer chemotherapy. *Oncogene* **25**, 4812-4830, doi:10.1038/sj.onc.1209598 (2006).
200 GARFINKEL, D. A metabolic inhomogenity of glycine in vivo. II. Computer simulation. *The Journal of biological chemistry* **238**, 2435-2439 (1963).
201 Bjørkøy, G. *et al.* Monitoring autophagic degradation of p62/SQSTM1. *Methods Enzymol* **452**, 181-197, doi:10.1016/S0076-6879(08)03612-4 (2009).
202 Naylor, B. C. *et al.* DeuteRater: a tool for quantifying peptide isotope precision and kinetic proteomics. *Bioinformatics* **33**, 1514-1520, doi:10.1093/bioinformatics/btx009 (2017).
203 Claydon, A. J. & Beynon, R. Proteome dynamics: revisiting turnover with a global perspective. *Mol Cell Proteomics* **11**, 1551-1565, doi:10.1074/mcp.O112.022186 (2012).
204 Dai, D. F. *et al.* Altered proteome turnover and remodeling by short-term caloric restriction or rapamycin rejuvenate the aging heart. *Aging Cell* **13**, 529-539, doi:10.1111/acel.12203 (2014).
205 Kasumov, T. *et al.* Assessment of cardiac proteome dynamics with heavy water: slower protein synthesis rates in interfibrillar than subsarcolemmal mitochondria. *Am J Physiol Heart Circ Physiol* **304**, H1201-1214, doi:10.1152/ajpheart.00933.2012 (2013).
206 Lam, M. P. *et al.* Protein kinetic signatures of the remodeling heart following isoproterenol stimulation. *J Clin Invest* **124**, 1734-1744, doi:10.1172/JCI73787 (2014).
207 Institute, N. C. *NCI Supported Clinical Trials*, <https://www.cancer.gov/about-cancer/treatment/clinical-trials/search/r?q=autophagy&t=&z=&a=> (2017).
208 Schroy, P. C. *et al.* Detection of p21ras mutations in colorectal adenomas and carcinomas by enzyme-linked immunosorbent assay. *Cancer* **76**, 201-209 (1995).
209 Lis, G., Wassenaar, L. I. & Hendry, M. J. High-precision laser spectroscopy D/H and 18O/16O measurements of microliter natural water samples. *Anal Chem* **80**, 287-293, doi:10.1021/ac701716q (2008).
210 Neese, R. A. *et al.* Measurement in vivo of proliferation rates of slow turnover cells by 2H2O labeling of the deoxyribose moiety of DNA. *Proc Natl Acad Sci U S A* **99**, 15345-15350, doi:10.1073/pnas.232551499 (2002).
211 Bruns, D. R. *et al.* Differential effects of vitamin C or protandim on skeletal muscle adaptation to exercise. *J Appl Physiol (1985)* **125**, 661-671, doi:10.1152/japplphysiol.00277.2018 (2018).

212 Scientific, T. F. *Nuclear Extraction Protocol*, <https://www.thermofisher.com/us/en/home/references/protocols/cell-and-tissue-analysis/elisa-protocol/elisa-sample-preparation-protocols/nuclear-extraction-method-.html#prot5> (2007).
213 QIAGEN. *Plasmid DNA isolation (Qiagen Miniprep kit)*, <http://www.uni-tuebingen.de/fileadmin/Uni_Tuebingen/Fakultaeten/Biologie/Institut_fuer_Evolution_und_Oekologie/Evolutionsoekologie_der_Tiere/Dokumente/research/methods/Plasmid_180706.pdf> (2016).
214 Scientific, T. F. *S1 nuclease manuals and protocols*, <https://tools.thermofisher.com/content/sfs/manuals/S1_nuclease_man.pdf> (2016).
215 Wiśniewski, J. R., Zougman, A., Nagaraj, N. & Mann, M. Universal sample preparation method for proteome analysis. *Nature methods* **6**, 359-362, doi:10.1038/nmeth.1322 (2009).
216 Smith, R., Taylor, R. M. & Prince, J. T. Current controlled vocabularies are insufficient to uniquely map molecular entities to mass spectrometry signal. *BMC Bioinformatics* **16 Suppl 7**, S2, doi:10.1186/1471-2105-16-S7-S2 (2015).
217 Mi, H., Muruganujan, A., Casagrande, J. T. & Thomas, P. D. Large-scale gene function analysis with the PANTHER classification system. *Nat Protoc* **8**, 1551-1566, doi:10.1038/nprot.2013.092 (2013).
218 Regev, A. *et al.* The Human Cell Atlas. *Elife* **6**, doi:10.7554/eLife.27041 (2017).
219 Rozenblatt-Rosen, O., Stubbington, M. J. T., Regev, A. & Teichmann, S. A. The Human Cell Atlas: from vision to reality. *Nature* **550**, 451-453, doi:10.1038/550451a (2017).
220 Rockwood, A. L. & Haimi, P. Efficient calculation of accurate masses of isotopic peaks. *J Am Soc Mass Spectrom* **17**, 415-419, doi:10.1016/j.jasms.2005.12.001 (2006).
221 Technology, C. S. *LC3B (D11) XP Rabbit mAb #3868 IHC Protocol*, <https://www.cellsignal.com/products/primary-antibodies/lc3b-d11-xp-rabbit-mab/3868?site-search-type=Products&N=4294956287&Ntt=lc3b+antibody+ihc&fromPage=plp> (2016).
222 Waterlow, J. C. *Protein turnover in mammalian tissues and the whole body*. (North-Holland Publishing Company, 1978).
223 ASHFORD, T. P. & PORTER, K. R. Cytoplasmic components in hepatic cell lysosomes. *The Journal of cell biology* **12**, 198-202 (1962).
224 Deepalakshmi, P. D., Parasakthy, K., Shanthi, S. & Devaraj, N. S. Effect of chloroquine on rat liver mitochondria. *Indian J Exp Biol* **32**, 797-799 (1994).
225 Kim, K. A., Park, J. Y., Lee, J. S. & Lim, S. Cytochrome P450 2C8 and CYP3A4/5 are involved in chloroquine metabolism in human liver microsomes. *Arch Pharm Res* **26**, 631-637 (2003).
226 Nakatogawa, H., Ichimura, Y. & Ohsumi, Y. Atg8, a ubiquitin-like protein required for autophagosome formation, mediates membrane tethering and hemifusion. *Cell* **130**, 165-178, doi:10.1016/j.cell.2007.05.021 (2007).
227 Wauthier, V., Verbeeck, R. K. & Calderon, P. B. The effect of ageing on cytochrome p450 enzymes: consequences for drug biotransformation in the elderly. *Curr Med Chem* **14**, 745-757 (2007).
228 Meyer, J. N., Leuthner, T. C. & Luz, A. L. Mitochondrial fusion, fission, and mitochondrial toxicity. *Toxicology* **391**, 42-53, doi:10.1016/j.tox.2017.07.019 (2017).

229 Yan, C. & Li, T. S. Dual Role of Mitophagy in Cancer Drug Resistance. *Anticancer Res* **38**, 617-621, doi:10.21873/anticanres.12266 (2018).

230 Yan, C. *et al.* Doxorubicin-induced mitophagy contributes to drug resistance in cancer stem cells from HCT8 human colorectal cancer cells. *Cancer Lett* **388**, 34-42, doi:10.1016/j.canlet.2016.11.018 (2017).

231 Deschênes-Simard, X., Lessard, F., Gaumont-Leclerc, M. F., Bardeesy, N. & Ferbeyre, G. Cellular senescence and protein degradation: breaking down cancer. *Cell Cycle* **13**, 1840-1858, doi:10.4161/cc.29335 (2014).

232 Ward, P. S. & Thompson, C. B. Metabolic reprogramming: a cancer hallmark even warburg did not anticipate. *Cancer Cell* **21**, 297-308, doi:10.1016/j.ccr.2012.02.014 (2012).

233 Rao, S. *et al.* A dual role for autophagy in a murine model of lung cancer. *Nat Commun* **5**, 3056, doi:10.1038/ncomms4056 (2014).

234 Chittaranjan, S. *et al.* Autophagy inhibition augments the anticancer effects of epirubicin treatment in anthracycline-sensitive and -resistant triple-negative breast cancer. *Clinical cancer research : an official journal of the American Association for Cancer Research* **20**, 3159-3173, doi:10.1158/1078-0432.CCR-13-2060 (2014).

235 Rehman, J. *et al.* Inhibition of mitochondrial fission prevents cell cycle progression in lung cancer. *FASEB J* **26**, 2175-2186, doi:10.1096/fj.11-196543 (2012).

236 Qian, W., Wang, J. & Van Houten, B. The role of dynamin-related protein 1 in cancer growth: a promising therapeutic target? *Expert Opin Ther Targets* **17**, 997-1001, doi:10.1517/14728222.2013.823160 (2013).

237 Wang, J., Wen, X., Liu, J. & Sun, H. Mitochondrial Biogenesis Inhibitors for Anticancer Therapy: A Review of Recent Patents. *Recent Pat Anticancer Drug Discov* **11**, 332-341 (2016).

238 Hanahan, D. & Weinberg, R. A. Hallmarks of cancer: the next generation. *Cell* **144**, 646-674, doi:10.1016/j.cell.2011.02.013 (2011).

239 Hanahan, D. & Weinberg, R. A. The hallmarks of cancer. *Cell* **100**, 57-70 (2000).

240 Jeon, S. M. & Hay, N. Expanding the concepts of cancer metabolism. *Exp Mol Med* **50**, 32, doi:10.1038/s12276-018-0070-9 (2018).

241 Lorsch, J. R., Collins, F. S. & Lippincott-Schwartz, J. Cell Biology. Fixing problems with cell lines. *Science* **346**, 1452-1453, doi:10.1126/science.1259110 (2014).

242 DeBerardinis, R. J. *et al.* Beyond aerobic glycolysis: transformed cells can engage in glutamine metabolism that exceeds the requirement for protein and nucleotide synthesis. *Proc Natl Acad Sci U S A* **104**, 19345-19350, doi:10.1073/pnas.0709747104 (2007).

243 Nelson, M. B. *et al.* Cardiomyocyte mitochondrial respiration is reduced by receptor for advanced glycation end-product signaling in a ceramide-dependent manner. *Am J Physiol Heart Circ Physiol* **309**, H63-69, doi:10.1152/ajpheart.00043.2015 (2015).

244 Ananieva, E. Targeting amino acid metabolism in cancer growth and anti-tumor immune response. *World J Biol Chem* **6**, 281-289, doi:10.4331/wjbc.v6.i4.281 (2015).

245 Son, J. *et al.* Glutamine supports pancreatic cancer growth through a KRAS-regulated metabolic pathway. *Nature* **496**, 101-105, doi:10.1038/nature12040 (2013).

246 Yu, Y. *et al.* Elimination of Colon Cancer Stem-Like Cells by the Combination of Curcumin and FOLFOX. *Transl Oncol* **2**, 321-328 (2009).

247 Picard, M., Shirihai, O. S., Gentil, B. J. & Burelle, Y. Mitochondrial morphology transitions and functions: implications for retrograde signaling? *Am J Physiol Regul Integr Comp Physiol* **304**, R393-406, doi:10.1152/ajpregu.00584.2012 (2013).